SYNTHESIS AND PHOTOPHYSICAL STUDIES OF NAPHTHALIMIDE-BASED CHEMOSENSORS

Thesis Submitted for the Award of the Degree of

DOCTOR OF PHILOSOPHY

in

CHEMISTRY

By

Gurdeep Kaur

Registration Number: 12207855

Supervised By

Dr. Iqubal Singh (26211)

(Assistant Professor)

Department of Pharmaceutical Sciences

Lovely Professional University

Co-Supervised by

Dr. Paul P.I. Elliot

(Professor)

Department of Physical & Life Sciences

University of Huddersfield, U.K.



LOVELY PROFESSIONAL UNIVERSITY, PUNJAB 2025

DECLARATION

I hereby declared that the presented work in the thesis entitled "SYNTHESIS AND

PHOTOPHYSICAL STUDIES OF NAPHTHALIMIDE-BASED CHEMOSENSORS" in

fulfilment of degree of **Doctor of Philosophy** (**Ph. D.**) is outcome of research work carried out by

me under the supervision Dr. Iqubal Singh, working as Assistant Professor in the Department

of Pharmaceutical Chemistry, School of Pharmaceutical Sciences of Lovely Professional

University, Punjab, India. In keeping with the general practice of reporting scientific observations,

due acknowledgements have been made whenever work described here has been based on findings

of other investigator. This work has not been submitted in part or full to any other University or

Institute for the award of any degree.

(Signature of Scholar)

Ms. Gurdeep Kaur

Registration No.: 12207855

Department of Chemistry

Lovely Professional University

Punjab, India

CERTIFICATE

This is to certify that the work reported in the Ph. D. thesis entitled "SYNTHESIS AND PHOTOPHYSICAL STUDIES OF NAPHTHALIMIDE-BASED CHEMOSENSORS" submitted in fulfillment of the requirement for the award of degree of Doctor of Philosophy (Ph.D.) in the Department of Chemistry, School of Chemical Engineering & Physical Sciences, is a research work carried out by Ms Gurdeep Kaur, 12207855, is bonafide record of her original work carried out under my supervision and that no part of thesis has been submitted for any other degree, diploma or equivalent course.

(Signature of Supervisor)

Dr. Iqubal Singh Assistant Professor (26211) Department of Pharmaceutical Sciences Lovely Professional University Punjab, India

(Signature of Co-supervisor)

Dr. Paul P.I. Elliot Professor Department of Physical & Life Science University of Huddersfield United Kingdom

SYNTHESIS AND PHOTOPHYSICAL STUDIES OF NAPHTHALIMIDE-BASED CHEMOSENSORS

Thesis Submitted for the Award of the Degree of

DOCTOR OF PHILOSOPHY

in

CHEMISTRY

By

Gurdeep Kaur

Registration Number: 12207855

Supervised By

Dr. Iqubal Singh (26211)

(Assistant Professor)

Department of Pharmaceutical Sciences

Lovely Professional University

Co-Supervised by

Dr. Paul P.I. Elliot

(Professor)

Department of Physical & Life Sciences

University of Huddersfield, U.K.



LOVELY PROFESSIONAL UNIVERSITY, PUNJAB 2025

DECLARATION

I hereby declared that the presented work in the thesis entitled "SYNTHESIS AND

PHOTOPHYSICAL STUDIES OF NAPHTHALIMIDE-BASED CHEMOSENSORS" in

fulfilment of degree of **Doctor of Philosophy** (**Ph. D.**) is outcome of research work carried out by

me under the supervision Dr. Iqubal Singh, working as Assistant Professor in the Department

of Pharmaceutical Chemistry, School of Pharmaceutical Sciences of Lovely Professional

University, Punjab, India. In keeping with the general practice of reporting scientific observations,

due acknowledgements have been made whenever work described here has been based on findings

of other investigator. This work has not been submitted in part or full to any other University or

Institute for the award of any degree.

(Signature of Scholar)

Ms. Gurdeep Kaur

Registration No.: 12207855

Department of Chemistry

Lovely Professional University

Punjab, India

CERTIFICATE

This is to certify that the work reported in the Ph. D. thesis entitled "SYNTHESIS AND PHOTOPHYSICAL STUDIES OF NAPHTHALIMIDE-BASED CHEMOSENSORS" submitted in fulfillment of the requirement for the award of degree of Doctor of Philosophy (Ph.D.) in the Department of Chemistry, School of Chemical Engineering & Physical Sciences, is a research work carried out by Ms Gurdeep Kaur, 12207855, is bonafide record of her original work carried out under my supervision and that no part of thesis has been submitted for any other degree, diploma or equivalent course.

(Signature of Supervisor)

Dr. Iqubal Singh Assistant Professor (26211) Department of Pharmaceutical Sciences Lovely Professional University Punjab, India

(Signature of Co-supervisor)

Dr. Paul P.I. Elliot Professor Department of Physical & Life Science University of Huddersfield United Kingdom

CHAPTER - 1

Introduction and Review of Literature

This chapter provides an overview of naphthalimide-based chemosensors and an in-depth discussion of the detection mechanism of different ions. It thoroughly explores the synthetic route and evaluates their sensing ability concerning optical alterations and their ability to detect a particular analyte with a low detection limit.

ChemistrySelect

Review doi.org/10.1002/slct.202301661



www.chemistryselect.org

1,8-Naphthalimide-Based Chemosensors: A Promising Strategy for Detection of Metal Ions in Environmental and Biological Systems

Gurdeep Kaur, [a] Iqubal Singh, [b] Nitin Tandon, *(a) Runjhun Tandon, [a) and Aeyaz Ahmad Bhat [a]

The advancement of optical chemosensors has achieved success with the advent of Supramolecular Chemistry. Unlike other scaffolds, the 1,8-naphthalimide motif has emerged as an excellent fluorescent chemosensor due to its photophysical properties like thermostability, cytotoxicity, membrane permability, selectivity, and sensitivity. The naphthalimide scaffold is distinctive in its ways of tracking biological analytes and diagnosing its role in various diseases. This review provides

insight into current developments in the synthesis and designing of 1,8-naphthalimide-based chemosensors for the recognition of metal ions, its mechanistic approach for its sensitivity, selectivity, and practical applications in a real environment. We hope that this review will aid to develop a novel approach to sense toxic analytes in real water samples and improve real-time applications.

1. Introduction

The research arena in the 21st century has witnessed a revolution in the field of design and facile synthesis of chemosensors with commendable results for their selective and subtle tracking of analytes such as metal ions, anions, biomolecules, etc.11-31 A probe comprises various subunits such as a receptor, spacer, and photoactive units which are capable of transducing the molecular level changes into analytical signals via color or fluorescence and is known as a chemosensor. IN A major attempt in this field is to develop optical chemosensors as a dynamic tool for sensing various analytes having facile synthesis, selectivity, sensitivity, and exhibition of the broad range of emission characteristics.⁽⁹⁻¹⁰⁾ Moreover, these tools are distinctive in their way of sensing various biological analytes and diagnosing their role in a given disease state. Recent years have witnessed tremendous research in supramolecular chemistry with incredible outcomes in terms of sensitivity and the working of chemosensors. Also, scientific research is paying attention to the development of a molecular marker for selectively detecting biologically important cations.[11-12] The molecular scaffold displaying metal-induced turn-on emission is organism by offering less interference from background fluorescence, photobleaching, light scattering, etc. thereby causing less injury to tissue with enhanced three-dimensional spatial localization, resolution, observation time and penetration depth. [25-26] Further, these versatile photo-physical properties can be refined by varying the substituents on its aromatic ring. [25-26]

Such intriguing properties of 1,8-napthalimide derivatives make it an excellent marker for displaying vibrant potential in the field of bioinorganic chemistry, material chemistry, analytical chemistry, medical science communities, etc.²⁹¹ These captivating properties of the naphthalimide motif mark them as exceptional moiety for displaying wide application in the fields of biological and medical science, analytical chemistry, materials chemistry, bioorganic chemistry, etc.²⁹⁰ and are employed as metal ion sensors.¹⁹⁰ pH sensors, ^{10,120} cellular imaging agents, ¹⁰¹ optoelectronic materials, ¹⁹¹ light emitting diodes¹⁹¹ and as well as solar energy collectors.¹⁹⁰ The sensory features of 1,8-naphthalimide-based derivatives are attributed to several processes, including Photoinduced Electronic Transfer (PET), ¹⁹¹ intra-molecular Charge Transfer (ICT), ¹⁹¹ Foster-Resonance Energy Transfer (IFRET), ¹⁹¹ and Aggregation Induced Emission/

With the advent of industrialization and modernization, the research fraternity has also undoubtedly evolved, enhancing the quality of life. Scientists have substantially developed ubiquitous technological tools with efficient research efforts in various fields. Supramolecular Chemistry is one such field that deals with the advancement of superlative optical sensors for the selective detection of harmful analytes in the ecosystem. There are a significant number of ions and small molecules that hold a supreme place in human life, various physiological processes, as well as in the environment. Despite being benign, the analytes exceeding the threshold values produce catastrophic effects, therefore, their recognition in a particular system is of relevant interest¹. The research arena in the 21st century has witnessed a revolution in the field of design and facile synthesis of chemosensors with commendable results for their selective and subtle tracking of analytes such as metal ions, anions, biomolecules, etc.²

There are several traditional methods for the detection of metal ions, like Atomic absorption spectroscopy (AAS), Inductively coupled plasma mass spectroscopy (ICP-MS), inductively coupled atomic plasma emission spectroscopy (ICP-AES), voltammetry, and anodic strip voltammetry³⁻⁶ are used which generally require high cost and specialized man-power without recovery of samples. On the other hand, chemosensors are regarded as a suitable option for detecting ions owing to their properties, including high sensitivity, specificity, selectivity, low response time, versatility, colorimetric, and fluorescence response. A chemosensor is a molecular device comprising a receptor unit that transforms the chemical modification occurring at the molecular level into electrical signals⁷. Amongst the sensors, fluorescent and colorimetric chemosensors can afford real-time information along with quantification of the target analyte of particular interest^{8, 9}. In general, it is a cost-effective analytical device designed with excellent selectivity and sensitivity towards a specific analyte in an organic, semi-aqueous, or aqueous medium to yield electrical signals at a particular concentration^{10, 11}. Hence, it is of paramount importance to develop colorimetric or fluorometric sensors for the detection of anions, cations, and other molecules of biological relevance.

A major attempt in this field is to develop optical chemosensors as a dynamic tool for sensing various analytes having facile synthesis, selectivity, sensitivity, and exhibiting a broad range of emission characteristics¹²⁻¹⁶. Moreover, these tools are distinctive in their way of sensing various biological analytes and diagnosing their role in a given disease state^{17, 18}. Recent years

have witnessed tremendous research in supramolecular chemistry with incredible outcomes in terms of sensitivity and the working of chemosensors. Also, scientific research is paying attention to the development of a molecular marker for selectively detecting biologically important cations 19, 20

1.1. Why Naphthalimide Only?

Several photophysical properties must be taken into consideration for designing the molecular chemosensor, such as sensitivity, selectivity²¹, photostability²², cytotoxicity, membrane permeability^{23,24}, and solvatofluorochromism²⁵. The derivatives of numerous structural moieties, such as boron dipyrromethene difluoride, cyanide, fluorescein, squaraine, and 1,8-napthalimide, have been used for the selective detection of various chemical species^{26, 27}. Amongst these structural motifs, 1,8-napthalimide possesses remarkable properties and was found to be chemically stable. It exhibits excellent optical, electrochemical, photophysical, and thermal properties, which mark the basis for its synthesis and the design of novel fluorescent chemosensors^{12, 15}. The property of high two-photon absorption cross-section displayed by 1,8-naphthalimide is a uniquely beneficial property for the imaging of analytes in bio-organisms by offering less interference from background fluorescence, photobleaching, light scattering, etc., thereby causing less injury to tissue with enhanced three-dimensional spatial localization, resolution, observation time, and penetration depth^{28, 29}. Further, these versatile photo-physical properties can be refined by varying the substituents on its aromatic ring (**Figure 1.1**)³⁰.

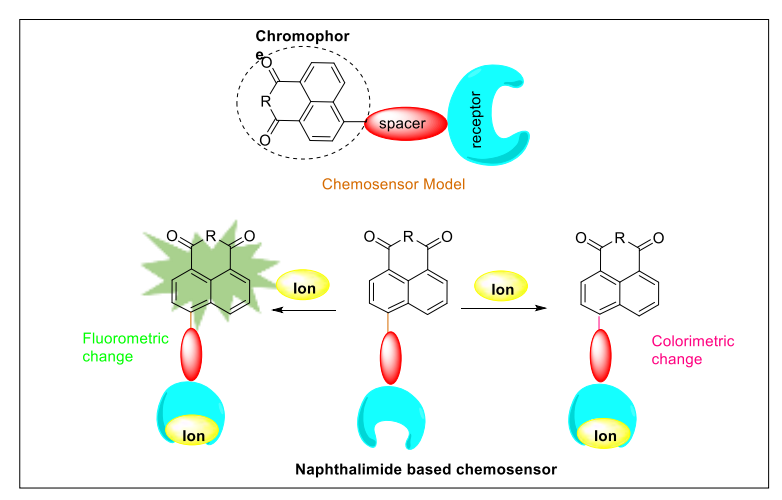


Figure 1.1: Naphthalimide as a chemosensor model displaying fluorometric and colorimetric change

Such intriguing properties of 1,8-napthalimide derivatives make it an excellent marker for displaying vibrant potential in the field of bioinorganic chemistry, material chemistry, analytical chemistry, medical science communities, etc. These captivating properties of the naphthalimide motif mark them as exceptional moiety for displaying wide application in the fields of biological and medical science, analytical chemistry, materials chemistry, bioorganic chemistry, etc. 31 and are employed as metal ion sensors², pH sensors^{32, 33}, cellular imaging agents³⁴, optoelectronic materials³⁵, light emitting diodes³⁶, and as well as solar energy collectors³⁷. The sensory features of 1,8-naphthalimide-based derivatives are attributed to several processes, including Photoinduced Electronic Transfer (PET)³⁸, Intra-molecular Charge Transfer (ICT)³⁹, Foster-Resonance Energy Transfer (FRET)⁴⁰, and Aggregation Induced Emission/Quenching (AIEE/AIEO)⁴¹. In addition to these, naphthalimides have exceptional pharmacological capabilities, making them important scaffolds in a variety of anti-inflammatory, antiprotozoal, antibacterial, anticancer, and antidepressant medicines, among other things^{42, 43}. Numerous derivatives based on the 1,8naphthalimide moiety have been created and used for the sensing of various types of substances due to the myriad benefits that this moiety offers. 1,8-napthalimide and its derivatives have played a significant role in supramolecular chemistry, and with the continuous structural modification in the naphthalimide motif, it has become possible to achieve a considerable detection value^{7, 44, 45}. In addition, in the case of 1,8-naphthalimide derivatives, two approaches are generally employed for the detection of analytes i.e. binding site signaling approach and the other is the chemodosimeter approach. In the former approach, the analyte transforms the signaling subunit into chemical modification via various interactions and forces occurring at the molecular level that transforms them into signals (color or fluorescent change)⁴⁶ while in the later approach, the chemosensor and analyte interaction leads to breaking of bonds and formation of new bonds forming a chemically new moiety having different optical properties than initial molecule⁴⁷.

1.2. Review of Literature

The recent advancement in the development of the 1,8-naphthalimide-based chemosensor for the detection of ions has been studied and covered for the optical transformations that involve broad and real-time applications.

1.2.1. Detection of cations

Metal ions are present widely in the environment and contribute to various chemical and biological systems to perform numerous functions in all life forms. These metal ions are split into two types from a physiological perspective, *i.e.* non-essential metal ions and essential metal ions. The non-essential metal ions, which are generally harmful to health, came into existence through volcanic eruptions, soil erosion, geological weathering, etc., while these are also the result of many anthropogenic activities like mining, smelting, waste dumping, livestock, automobiles, *etc.*, ^{48, 49}. On the other hand, the essential metal ions play a pivotal role in the ecosystem by regulating transcription, electron chain transport, intra- and inter-cellular communications, Krebs' cycle, photosynthesis, etc.⁵⁰. However, if both non-essential and essential metal ions are present above the threshold value, they could result in serious health issues. Therefore, detecting metal ions has gained serious concern and encouraged researchers to design a fluorogenic and colorimetric chemosensor to detect their presence even in trace amounts.

The accumulation of toxic metal ions in the environment is a growing concern due to their aggravating toxicological effects on sustaining life forms⁵¹. Heavy metal ions like mercury, cobalt, lead, palladium, and chromium are hazardous metal ions even in trace concentrations^{52, 53}. These are ubiquitously distributed in the biosphere, posing a threat to mankind and the environment if present above the threshold values⁵⁴. These are non-biodegradable and their accumulation in living forms occurs through an alimentary chain, thereby leading to severe health impacts⁵⁵. These metal ions are contemplated as "Environmental Health Hazards" as they rank in the top ten in listing from "Agency of Toxic Substances and Disease Registry Priority List of Hazardous Substances" based on their exposure to water, soil, and air, and their toxicity. Its toxicity is being assessed by several international organizations, including the World Health Organization (WHO)⁵⁶, the Center for Disease Control (CDC)⁵⁷, the Joint Food and Agricultural Organization (FAO), and the International Agency for Research on Cancer (IARC)⁵⁸.

Therefore, its detection even in trace amounts plays a very crucial role in the environment and also in biological systems. If we were able to maintain a certain limit on these metal ions, then various serious diseases like Alzheimer's, renal toxicity, lung cancer, Minamata, impaired neurologic development, reproductive toxicity, carcinogenicity etc., can be controlled to a certain extent^{59, 60}. So, fluorescent chemosensors play a significant role in the detection of metal ions in an environment as well as in human cells for the detection of various diseases.

1.2.1.1. Detection of mercury (Hg²⁺) ions

Mahata *et al.* synthesized a fluorescent chemosensor (5) possessing hydrazine carbothioamide and 1,8-napthalimide moieties as skeleton structures, which were evaluated for sensing Hg²⁺ and Ag⁺ ions. Its synthesis followed three steps in which 6-bromo-1,8-naphthalic anhydride (1) reacted with 2-aminoethanol at high temperature, forming a white solid intermediate 2 in moderate yield in the first step, which was further reacted with hydrazine hydrate, forming a yellow solid compound 3. Finally, an acetonitrile solution of 1-isothiocyanatonaphthalene (4) was added to compound 3 at a high temperature to afford compound 5 in good yield (Scheme 1.1).

Scheme 1.1: Synthetic route of 5

According to the UV-Vis studies, free chemosensor 5 exhibited an absorption band at 410 nm, while no change was seen in the presence of other metal ions. In addition, the gradual addition of Hg²⁺ caused a drop in absorption intensity and the formation of a new peak at 452 nm with an isosbestic point at 446 nm. On the other hand, a similar decrease was observed at 410 nm with the addition of Ag⁺, while two new peaks were observed at 432 nm and 528 nm. In addition, the emission studies revealed that upon excitation with 410 nm, weak fluorescence at 529 nm was observed. The addition of Hg²⁺ ions led to an increase in fluorescent intensity imparting a yellowgreen color with a gradual shift in emission spectra at 213 nm (Figure 1.2). On the other hand, the Ag⁺ exhibits a similar increase in intensity, imparting an orange color with the shift in emission peak to 527 nm. This increase in the intensity in the presence of Hg²⁺ and Ag⁺ did not exhibit any significant effect in the presence of other metal ions such as Li⁺, Na⁺, K⁺, Ca²⁺, Mg²⁺, Al³⁺, Cr³⁺, Mn^{2+} , Fe^{2+} , Co^{2+} , Ni^{2+} , Cu^{2+} , Zn^{2+} , Cd^{2+} , Pb^{2+} , Pd^{2+} , Pt^{2+} , Au^{3+} and Fe^{3+} . Further, the 1HNMR gave insight into the interaction between the chemosensor and targeted metal ions. The findings of Density Functional Theory (DFT) studies supported the PET mechanism, which is responsible for the switch-on response of chemosensor 5. In addition, the Job's plot analysis revealed a 1:1 binding ratio between chemosensor 5 and the tested metal ions. Further, the association for the metal-ligand was found to be $1.9 \times 10^5 \, \text{M}^{-1}$ and $0.9 \times 10^5 \, \text{M}^{-1}$ towards Hg^{2+} and Ag^+ ions, respectively. The turnon fluorescence response of the chemosensor marked its practical utility for the intercellular detection of metal ions⁶¹.

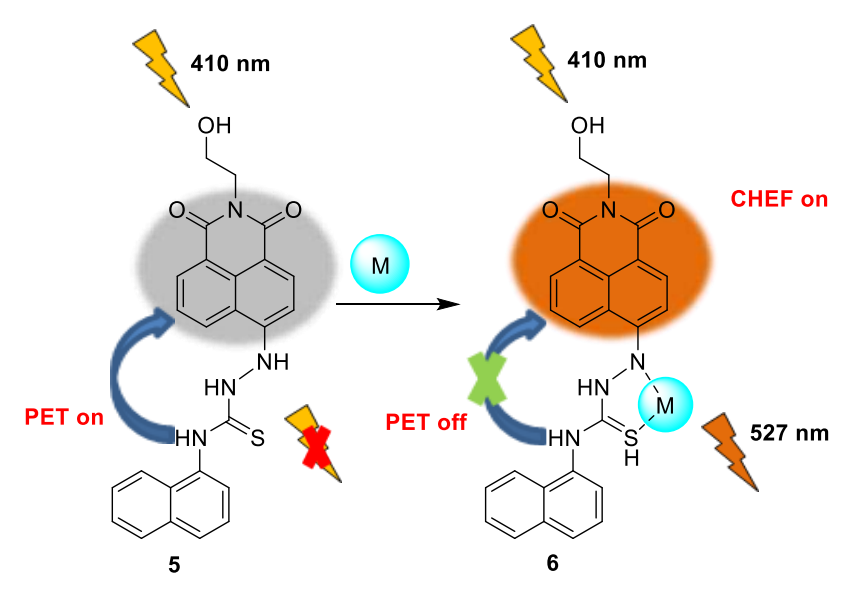


Figure 1.2: Sensing mechanism of 5 towards Hg²⁺ and Ag⁺

Jothi *et al.* synthesized a naphthalimide-based fluorescent chemosensor (11) for the recognition of Hg²⁺ ions. The chemosensor was synthesized in a three-step reaction initially reacting 6-bromo-1,8-naphthalic anhydride (1) with 4-(2-aminoethyl)morpholine (7) at a high temperature to afford intermediate 8 in good yield. Further, the Suzuki reaction between 8 and 4-formylphenylboronic acid (9) produced compound 10 in moderate yield, which on reaction with 1,3-propanedithiol (11) at high temperature afforded targeted chemosensor 12 (Scheme 1.2).

Scheme 1.2: Synthesis of chemosensor 12

The chemosensor **12** exhibited peak originally at 370 nm causing a blue shift of the absorption maxima with substantial changes that were only seen in the absorption and emission spectra in the presence of Hg²⁺ while other metal ions (Cu²⁺, Al³⁺, Ba²⁺, Bi³⁺, Ca²⁺, Cd²⁺, Ce³⁺,

Co²⁺, Li⁺, Mg²⁺, Mn²⁺, Fe³⁺, Ni²⁺, Pb²⁺, Ru³⁺, Se²⁺, Sr²⁺, Pd²⁺, Th⁴⁺, Zr²⁺, Zn²⁺, Ag⁺ and Hg²⁺) did not significantly alter the absorption spectra of the chemosensor **12**. In addition, the emergence of a new peak at 451 nm was observed with an isosbestic point at 409 nm. The fluorescence emission of **12** was observed at 429 nm, which was gradually enhanced with the addition of Hg²⁺ ions, while the presence of other metal ions produced no effect. The addition of Hg²⁺ ions to **12** exposed its turn-on behaviour by changing color from colorless to blue when viewed under a UV lamp, which could be attributed to the ICT process (**Figure 1.3**). Further, the DFT studies and ¹HNMR spectroscopy support and illustrate the mechanism of formation of **13** in the presence of Hg²⁺ ions. The detection limit of **12** for Hg²⁺ was found to be 3.3 nM with an association constant of 3.429 × 57 M⁻¹. Moreover, the chemosensor was efficiently applied for bioimaging Hg²⁺ ions in the liver cells of *Escherichia coli* ⁶².

Tian *et al.* synthesized and reported a fluorescent marker (18) for the detection of Hg²⁺ ions. In the first step, 6-bromo-1,8-naphthalic anhydride (1) was reacted with n-butylamine to introduce a non-polar tail on the moiety, forming compound 14, which on further reaction under basic conditions in the presence of methanol at high temperature, produced compound 15. Deprotection of 15 in strongly acidic conditions yielded 16, which was converted to formyl

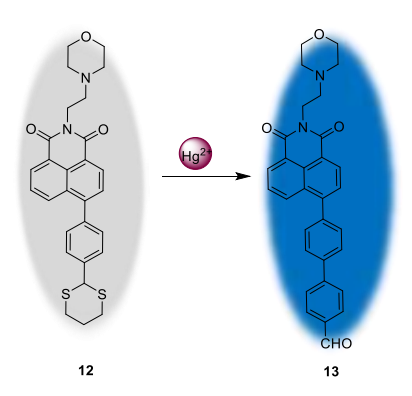


Figure 1.3: Sensing mechanism of 12 towards Hg^{2^+}

derivative (17) under oxidizing conditions. Finally, compound 17 was reacted with 1,2-ethanedithiol under acidic conditions to give target compound 18 in good yield (Scheme 1.3).

Scheme 1.3: Synthetic route of chemosensor 18

The spectroscopic performance of chemosensor 18 revealed a 20-fold enhancement of fluorescence emission intensity at 510 nm with the addition of Hg²⁺ ions. The co-existence of Hg²⁺ ions with other metal ions exhibited almost no change in the fluorescence intensity. It was further observed that the presence of Hg²⁺ ions leads to the deprotection of chemosensor 18, which triggers the transformation of the disulfide group into an aldehyde group, forming compound 17 (Figure 1.4). Chemosensor 18 depicted an absorption peak at 461 nm, while compound 17 exhibited a peak at 417 nm. Meanwhile, the color of the chemosensor solution changed from pale yellow to light green which could be attributed to the formation of compound 17 due to the deprotection reaction of dithioacetal triggered by Hg²⁺. The limit of detection for 18 was found to be 4×10⁻⁸ M. The non-cytotoxicity of compounds 17 and 18 found its practical application in confocal imaging of Hg²⁺ in PC-12 cells⁶³.

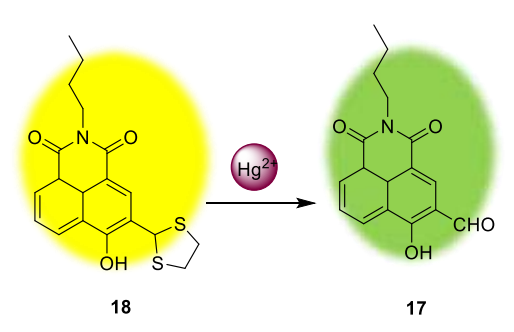


Figure 1.4: Sensing mechanism of 18 towards Hg²⁺

1.2.1.2. Detection of cobalt (Co²⁺) ions

Li *et al.* developed a new fluorescent complex (20) to efficiently sense Co²⁺ ions. Synthesis of the targeted compound was achieved by the reaction of compound 6-bromo-1,8-naphthalic anhydride (1) with butylamine under acidic conditions to afford intermediate 14 in good yield, followed by a reaction with hydrazine at reflux temperature to give compound 19. Finally, compound 19 was reacted with methyl-isothiocyanate (20) to afford the target compound 21 in moderate yield (Scheme 1.4).

Scheme 1.4: Synthetic route of chemosensor 21

In the case of chemosensor **21** spectrum analysis found the highest absorption peak at 390 nm, which underwent a 16 nm blue shift in the presence of Co²⁺. Interestingly, the presence of additional metal ions had no impact on the spectra. On the other hand, the fluorescence spectrum of **21** exhibited a switch-on response with negligible influence of other metal ions on the introduction of Co²⁺ metal ions (**Figure 1.5**). Further evaluation of the **21** with anions *viz*. F⁻, Cl⁻, Br⁻, I⁻, NO₃⁻, ClO₄⁻, SO₄²⁻, HSO₄⁻, NO₂⁻ and SCN⁻ did not elicit any response keeping the chemosensor in an off state confirming its selectivity and sensitivity towards Co²⁺ ions. In addition, Job's plot indicated 1:1 stoichiometric binding between chemosensor **21** and Co²⁺. Further the chemosensor metal association was confirmed by ¹HNMR titrations and DFT studies. The detection limit of **21** was calculated as low as 7.82 nM. Also, the chemosensor-metal complex exhibited remarkable detection ability for tri-ketone 4-hydroxyphenylpyruvate dioxygenase (HPPD) inhibitor⁶⁴.

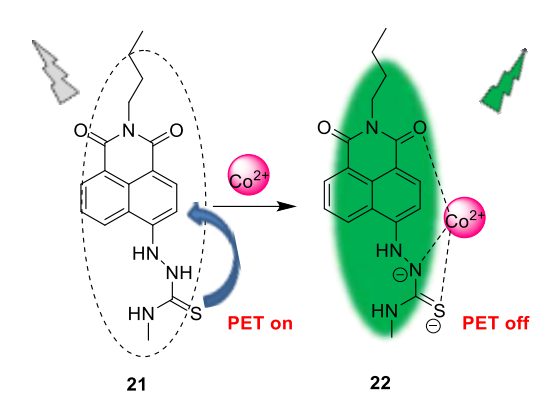


Figure 1.5: Sensing mechanism of 21 towards Co²⁺

1.2.1.3. Detection of palladium (Pd^{2+}) ions

Kumar *et al.* designed and synthesized a bis-naphthalimide-based crown ether chemosensor (25) for the detection of Pb²⁺ and tris(2-aminoethylamine) (TAEA). The chemosensor 25 was synthesized in a three-step reaction in which the first step involved an electrophilic aromatic substitution reaction of compound 23 under basic conditions at high temperature, followed by reaction with cyclohexylamine at room temperature to afford compound 24. Compound 24 was further refluxed in the presence of pentamethylene glycol at 100 °C to give 25 (Scheme 1.5). Further, the treatment of 25 with Pb²⁺ (25 equiv.) generated ensemble 26.

Scheme 1.5: Synthesis of chemosensor 25

Chemosensor **25** revealed a drastic change in fluorescent spectra in the presence of Pd²⁺/Pd⁰ and Fe³⁺/Fe²⁺ with quenching of 65% in the case of Pd²⁺, whereas 25-30% quenching was observed in the case of Pd⁰, Fe³⁺, and Fe²⁺ ions. On the other hand, less than 20% quenching was observed in the case of other metal ions (Hg²⁺, Pb²⁺, Cs⁺, K⁺, Co²⁺, Ca²⁺, Zn²⁺, Cd²⁺, Li⁺, Ni²⁺, Ba²⁺, La³⁺, Cu²⁺). In addition, the studies of non-fluorescent ensemble **26** revealed turn-on perturbations with the gradual addition of TAEA (**Figure 1.6**). However, ligand-to-metal charge transfer (LMCT) from naphthalimide to Pb²⁺ was observed, which further quenches the complex.

Further, this "on-off" switching aids in studying its bio-imaging in MG-31 cells. The sensing of the TAEA ensemble was proved with experimental methods such as optical and DLS techniques. Furthermore, the limit of detection of 25 towards Pd^{2+} was found to be 0.1 μ M, and the ensemble (26) exhibited a 0.8 μ M detection limit towards TAEA⁶⁵.

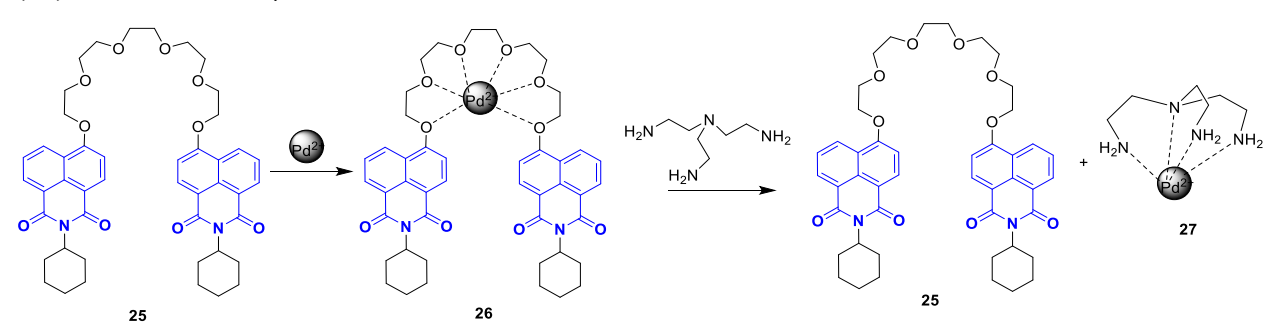


Figure 1.6: Sensing mechanism of 25 towards Pb²⁺

1.2.1.4. Detection of lead (Pb2+) ions

Jiang *et al.* synthesized a novel fluorescent chemosensor, a thiosemicarbazide-appended naphthalimide derivative (30), in three steps of synthesis (Scheme 1.6). In the first step, 6-bromo-1,8-naphthalicanhydride (1) was treated with n-butylamine in ethyl alcohol at a high temperature to give compound 14 in moderate yield. Further reaction with hydrazine under nitrogen atmosphere led to the formation of compound 28 in good yield through nucleophilic aromatic substitution of Br. The compound 28 was further reacted with 1-methoxy-1-thionitrosoethene (29) to give fluorescent chemosensor 30 in moderate yield. The fluorescent chemosensor 30 revealed the excitation wavelength at 390 nm. The presence of Pb²⁺ ions augments fluorescence, while the co-existence of other metal ions (K⁺, Na⁺, Mn²⁺, Mg²⁺, Zn²⁺, Hg²⁺, Cu²⁺, Ni²⁺, Ca²⁺, Fe³⁺, Al³⁺, Sn²⁺, Ba²⁺, Ag⁺ and Cr³⁺) produces a negligible response. Meanwhile, a notable color change from weak green to yellow was observed at 365 nm under a UV lamp exhibiting a "turn-on" response (Figure 1.7). The Job's plot analysis revealed 1:1 stoichiometric binding of the complex. In addition, the detection limit of 30 was found to be 4.7 nM. The remarkable sensitivity, selectivity, and lower cellular toxicity of chemosensor 30 found its practical applicability in environmental samples and bio-imaging of HSC cells⁶⁶.

Scheme 1.6: Synthetic route to chemosensor 30

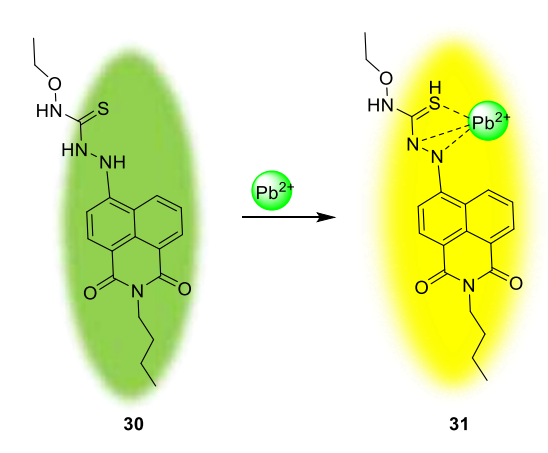


Figure 1.7: Sensing mechanism of 30 towards Pb²⁺

1.2.1.5. Detection of bismuth (Bi^{3+}) ions

Treto-Suárez *et al.* reported an optical dual-selective chemosensor **(31)** for the detection of Bi³⁺. Chemosensor **31** revealed two absorption bands at 342 nm and 233 nm. The turn-on behaviour of the chemosensor was observed after interaction with Bi³⁺ and it was found that the variation in the intensity of the absorption band was pH dependent. In an alkaline medium, a slight blue shift was observed at 338 nm with the emergence of a new absorption band at 406 nm. Also, **31** exhibited a red shift in the absorption band and Chelation Enhanced Fluorescence (CHEF) effect in response to Bi³⁺ (**Scheme 1.7**). This enhancement in the spectrum could be attributed to the inhibition of PET after the coordination of the metal ion with the N atom of the sensor. The presence of other metal ions does not exhibit any variation in the fluorescence intensity of the sensor. The stoichiometric ratio between metal-ligand was found to be 1:1. However, a slight change in the concentration of metal-sensor implies a decrease in the emission intensity of the chemosensor⁶⁷.

Scheme 1.7: Proposed sensing mechanism of the chemosensor 31 in the presence of metal ions [109] 1.2.1.6. Detection of copper (Cu^{2+}) ions

Liu *et al.* designed and synthesized a novel turn-off fluorescent 1,8-napthalimide-based chemosensor (36) for the selective detection of Cu²⁺ ions employing a hydrolysis mechanism in three steps (Scheme 1.8). The first step involved the treatment of compound 6-bromo-1,8-naphthalic anhydride (1) with n-butylamine in ethanol at reflux temperature to form compound 14 followed by nucleophilic aromatic substitution of Br in the presence of hydrazine to form compound 34. Finally, target compound 36 was synthesized in good yield by reaction of 34 with thiophene-2-carbaldehyde (35) under nucleophilic reaction conditions.

Scheme 1.8: Synthetic route of chemosensor 36

Chemosensor **36** exhibited two bands at 452 nm and 328 nm, while a sharp decline in intensity was observed in the former with the addition of Cu²⁺ ions, accompanied by a red shift of the absorption peak at 328 nm to 338 nm. This could be attributed to the decomposition of **36** in the presence of Cu²⁺ ions to compound **38**. In addition, the absorption peak of compound **36** was found to emerge at 340 nm, which could be ascribed to the π-π* transition of the naphthalimide core unit. Other cations such as K⁺, Na⁺, Ag⁺, Cu⁺, Mn²⁺, Mg²⁺, Zn²⁺, Co²⁺, Hg²⁺, Pb²⁺, Ni²⁺, Cd²⁺, Ca²⁺, Ba²⁺, Sn²⁺, Fe²⁺, Fe³⁺, Al³⁺ and Cr³⁺ have exiguous effects on the absorption spectra. In addition, the fluorescent studies revealed an evident yellow emission of the independent chemosensor (**36**) when excited at 450 nm. The subsequent presence of Cu²⁺ ions, along with other

metal ions quenched the fluorescence significantly, making the chemosensor act as a turn-off chemosensor with noticeable color change visible to the naked eye which could further pave the way for calorimetric detection of Cu²⁺ ions (**Figure 1.8**). The binding stoichiometric of the complex determined by the Job's plot analysis was found to be 1:1, and the limit of detection was as low as 9.15 nM. Further, the binding mechanism was supported by FT-IR and ¹H-NMR spectroscopic techniques. In addition, chemosensor **36** was useful in determining the quantity of Cu²⁺ ions present in environmental samples⁶⁸.

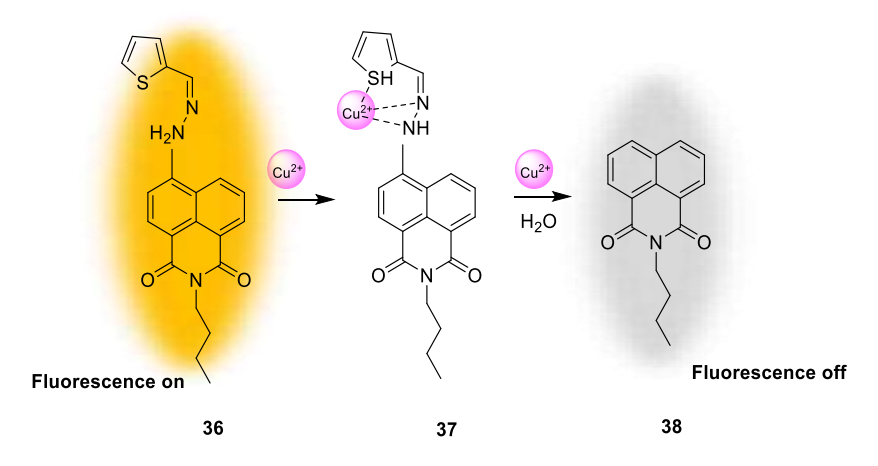


Figure 1.8: Sensing mechanism of 36 towards Cu²⁺

Li *et al.* synthesized a 1,8-phthalimide-based hydrazone fluorescent turn-on chemosensor **41** for the detection and imaging of Cu²⁺ ions in lysosomes. The synthesis of chemosensor **41** took place in a step reaction in which compound **39** reacted with compound **40** via a condensation reaction (**Scheme 1.9**). The free solution of chemosensor **41** displayed absorption bands at 500 and 343 nm. Further, the absorption and fluorescent studies revealed vivid enhancement in fluorescence with the addition of Cu²⁺ ions with the shift in the band from 550 to 210 nm while spectrum interferences from other metal ions (Ag⁺, Al³⁺, Ca²⁺, Cd²⁺, Co²⁺, Cr³⁺, Cu²⁺, Fe³⁺, Hg²⁺, K⁺, Mg²⁺, Mn²⁺, Na⁺, Ni²⁺, Pb²⁺, and Zn²⁺) were barely noticeable. Also, as the concentration of Cu²⁺ ions increased, bands with centers at 480 and 343 nm gradually decreased; this could be attributable to the suppression of the PET process. In addition, the emergence of two isosbestic points at 440 and 345 nm revealed the formation of new chemical species. The detection limit of chemosensor **41** was found to be 68 nM, which could be attributed to the formation of the **41**-Cu²⁺ complex with a 1:1 stoichiometric binding ratio, and the binding constant was calculated to be 2.88 × 54 M⁻¹ (**Figure 1.9**). Moreover, the low toxicity of the chemosensor found its application in the bioimaging of the HeLa cells for monitoring Cu²⁺ in lysosomes⁶⁹.

Scheme 1.9: Synthetic route to chemosensor 41

Figure 1.9: Sensing mechanism of 41 towards Cu²⁺

Nur *et al.* designed and synthesized a 1,8-napthalimide-based fluorescent chemosensor 44 for the detection of Cu²⁺ ions in environmental samples. In the first step, 6-bromo-1,8-naphthalic anhydride (1) was reacted with n-butylamine under acidic conditions, forming compound 14, which, on further reaction with hydrazine at high temperature, yielded compound 34 via nucleophilic substitution reaction. Finally, 34 reacted with 2-hydroxy-1-naphthaldehyde (43) at high temperature, yielding target chemosensor 44 (Scheme 1.10).

Scheme 1.10: Synthetic route of chemosensor 44

The colorimetric and fluorescence response of **44** revealed the presence of two absorption bands at 325 nm and 460 nm and an emission band at 550 nm and 551 nm when excited at 290 nm. The fluorescent studies showed a remarkable blue shift from 550 to 545 nm was observed with a visible color change from yellow to blue in the presence of Cu²⁺ ions, (**Figure 1.10**). The

colorimetric studies exhibited a substantial decrease in absorbance at 325 and 460 nm in the presence of Cu^{2+} ions which could be attributed to the π - π^* and n- π^* transitions. The presence of various cations (Ni^{2+} , Mg^{2+} , Co^{2+} , Pb^{2+} , Ca^{2+} , Cd^{2+} , Fe^{2+} , Zn^{2+} , Hg^{2+} , Ba^{2+} , K^+ , Ag^+ , Al^{3+} and Fe^{3+}), anions (ClO^- , NO_2^- , $H_2PO_4^-$, HCO_3^- , NO_3^- , OH^- , Br^- , F^- and Cl^-), and amino acids (L-valine (Val), L-arginine (Arg), L-phenylalanine (Phe), L-threonine (Pro), L-methionine (Pro), L-methionine (Pro)) exhibited no significant difference in the intensity of the spectra supporting the excellent performance of 44 and its affinity towards Cu^{2+} ions. In addition, Proventorian by Proventorian and Proventorian supported by mass spectrometry. Also, the DFT findings further corroborate with the experimental results. The limit of detection of 44 was found to be 9.21 nM. Further, the chemosensor was also used to detect the Proventorian corresponds to the support of the complex of bottled drinking water and real food samples Proventorian and Proventorian in experimental samples of bottled drinking water and real food samples Proventorian and Proventorian in experimental samples of bottled drinking water and real food samples Proventorian in the presence of Proventorian and <math>Proventorian and Proventorian and Proventorian and Proventorian and <math>Proventorian and Proventorian and <math>Proventorian

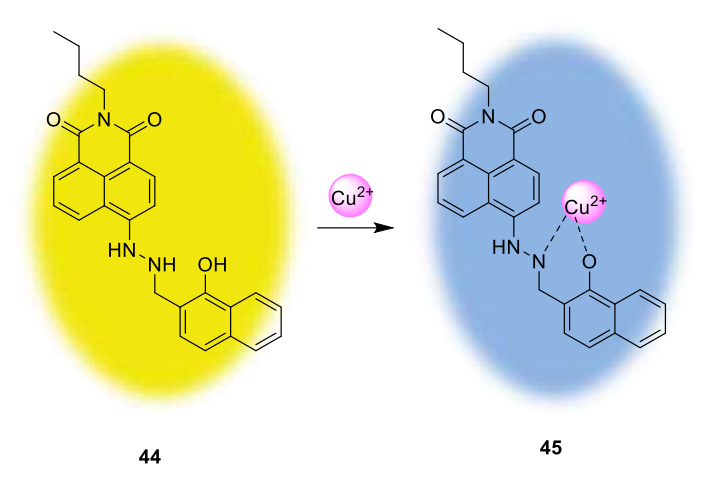


Figure 1.10: Sensing mechanism of 44 towards Cu²⁺

1.2.1.7. Detection of aluminum (Al^{3+}) ions

Zhang *et al.* designed and synthesized a new turn-on napthalimide picolinohydrazide fluorescent chemosensor **48** for the selective detection of Al³⁺ ions in a real water sample. The synthesis of the chemosensor was carried out by reacting compounds **46** and **47** in methanol at reflux temperature to give **48** in good yield (**Scheme 1.11**). Chemosensor **48** exhibited an absorption band at 470 nm, which was shifted to 403 nm with a visual color change on the addition of Al³⁺ ions. At 10 μM concentration of metal ion, the intensification of the absorption band at 350 and 403 nm was observed along with the consistent decrease in intensity of bands at 310 and 470 nm. In addition, the fluorescent studies revealed an increase in the emission intensity at 500 nm with an increase in the concentration of Al³⁺, with a change in color from dodger blue to spring

green, which was accompanied by the formation of a 1:1 complex between **48** and Al³⁺. This distinctive color change of the chemosensor could be attributed to the C=N isomerization and inhibition of the PET process, which were supported by ¹H-NMR spectroscopy and DFT studies. The detection limit of chemosensor **48** was found to be 39 nM (**Figure 1.11**). Furthermore, the chemosensor could be used efficiently for the detection and quantification of Al³⁺ ions in real and biological samples⁷¹.

Scheme 1.11: Synthetic route to chemosensor 48

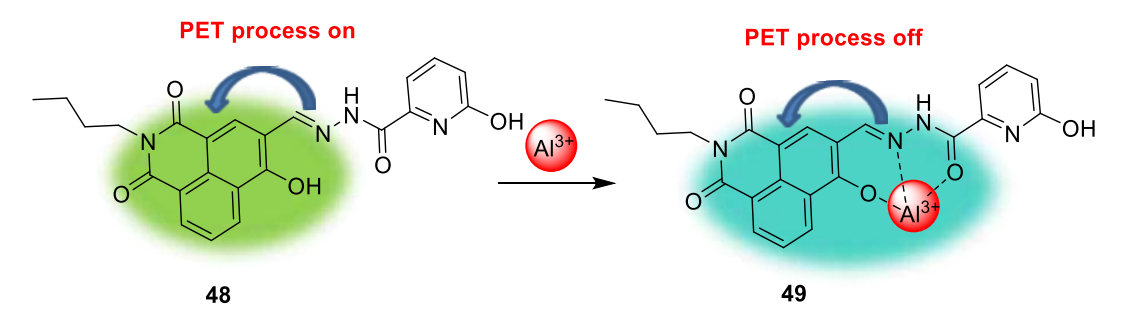


Figure 1.11: Sensing mechanism of 48 towards Al³⁺

Xu *et al.* developed a naphthalimide appended isoquinoline "switch-on" fluorescent chemosensor **51** for the detection of Al³⁺ ions. Chemosensor **51** was fabricated as a Schiff base in good yield by reacting compounds **46** and isoquinoline-1-carbohydrazide (**50**) in methanol (**Scheme 1.12**). The fluorescent spectroscopic studies revealed weak fluorescence of **51** at 510 nm when excited at 394 nm, which could be ascribed to C=N isomerization and the ESIPT process. The sensing behaviour of chemosensor **51** revealed that the addition of Al³⁺ ions caused a progressive increase in intensity at 510 nm and a colorimetric shift from colorless to bright greenish under UV light. This switch-on response could be ascribed to the formation of a complex between **51** and Al³⁺ with the stoichiometric binding ratio of 1:1 as indicated by Job's plot with binding constant of 3.27×10⁵ M⁻¹ (**Figure 1.12**). Moreover, the detection limit of **51** was found to

be 52 nM. Furthermore, this turn-on behaviour of the chemosensor (51) found its practical applicability in bio-imaging the Al³⁺ ions in living cells⁷².

Scheme 1.12: Synthetic route to chemosensor 51

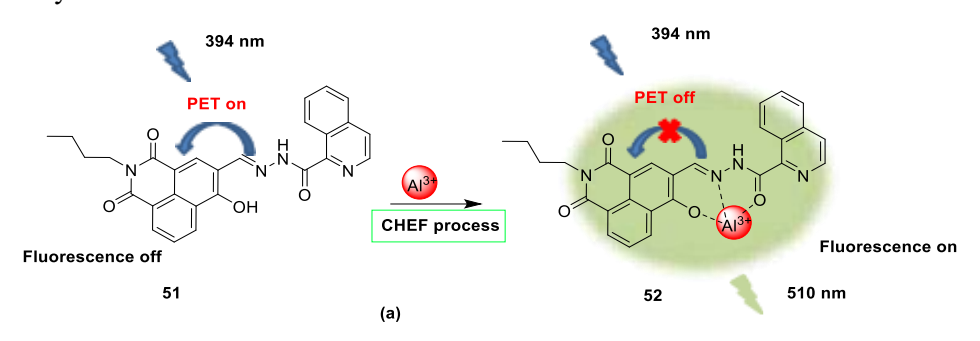


Figure 1.12: Sensing mechanism of 51 towards Al³⁺

1.2.1.8. Detection of zinc (Zn^{2+}) ions

Xiang *et al.* synthesized a novel Schiff base turn-on fluorescent chemosensor **54** for selective detection of Zn²⁺ ions. The chemosensor was synthesized by the condensation reaction of compounds **46** and furan-2-carbohydrazide (**53**) in methanol at high temperature to afford pure pale-yellow compound **54** in good yield (**Scheme 1.13**). Chemosensor **54** exhibited very weak fluorescence emission when excited at 404 nm. Further, the UV-Vis experiments showed an increase in intensity at 400 nm with a decrease in absorbance at 500 nm of **54** on the addition of Zn²⁺. Also, the fluorescence intensity at 506 nm exhibited an increment with the addition of Zn²⁺, accompanied by a distinctive colorimetric change from green to bright greenish visible to the naked eye at 365 nm under the UV lamp, which could be ascribed to inhibition of the PET and ESIPT process (**Figure 1.13**). The experimental results agreed with the findings of the DFT studies that revealed a decreased HOMO-LUMO energy gap, suggesting a more stable metal ligand complex (**104**). In addition, Job's plot revealed a 1:1 binding ratio of the complex between **54** and Zn²⁺ and association constant of 1.18×10⁵ M⁻¹. Interestingly, the practical usefulness of

chemosensor **54** in detecting Zn²⁺ in actual environmental samples as well as test strips was supported by its low limit of detection of 39 nM⁷³.

Scheme 1.13: Synthetic route of chemosensor 54

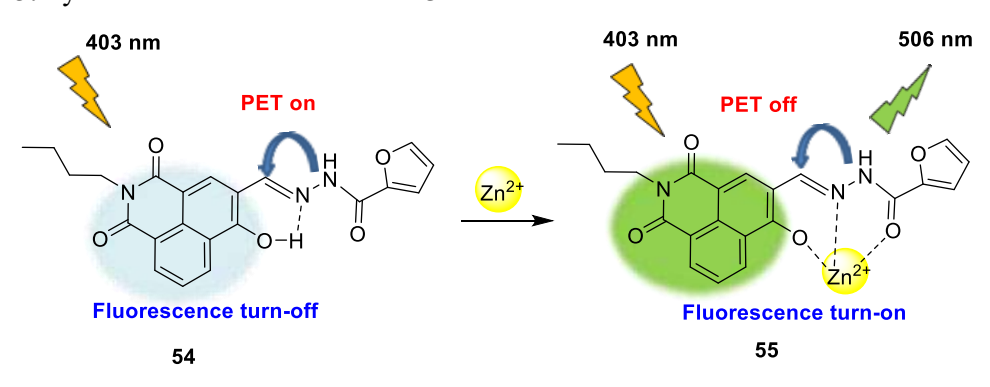


Figure 1.13: Sensing mechanism of 54 towards Zn²⁺

Das *et al.* designed and synthesized a new "turn-on" fluorescent chemosensor 57 for the recognition of Zn²⁺ ions. The chemosensor was synthesized by a one-pot amidation reaction between compound 56 and hydrazine at a high temperature, which yielded brownish-yellow solid compound 57 in moderate yield (Scheme 1.14).

Scheme 1.14: One-pot synthesis of 57

The fluorescent studies revealed that the chemosensor (57) displayed weak fluorescent emission at 508 nm when excited at 430 nm. The addition of metal ions (Cd²⁺, Co²⁺, Fe²⁺, Cu²⁺, Mg²⁺, Ni²⁺, Mn²⁺, Ba²⁺, Al³⁺, Ce³⁺, Sn²⁺, Pb²⁺, Cr³⁺, and Ca²⁺) exhibited no change in intensity except for Cd²⁺ and Co²⁺ that showed little fluorescence, however, Zn²⁺ caused a dramatic change in fluorescence

intensity and a change in color from light green to fluorescent green. Further, with an increase in the concentration of Zn²⁺ ions, no significant changes were observed for absorption bands at 268 nm and 429 nm. Further, the interference studies revealed no major perturbations except for Co²⁺, Cd²⁺, and Al³⁺ ions in the presence of the target ion. However, a slight increase in the intensity was observed in the former band, accompanied by a decrease in the intensity of the latter band with an isosbestic point at 325 nm. Additionally, the PET process was inhibited which could be attributed to the binding of Zn²⁺ with the chemosensor, thereby restoring the emission intensity with the ICT process (**Figure 1.14**). Further, the binding ratio between the Zn²⁺ and **57** was found to be 1:2, and chemosensor **57** found its practical utility in the mapping of Zn²⁺ ions in biological systems in the nanomolar range. Also, the association constant was found to be 62.007 M⁻¹ indicating weak binding of chemosensor **57** with Zn²⁺ in the ground state⁷⁴.

Figure 1.14: Sensing mechanism of 57 towards Zn²⁺

1.2.2. Detection of anions

1.2.2.1. Detection of fluoride (F) ions

Chen *et al.* synthesized a chemosensor comprising 3-hydroxy-4-cyano-1,8-naphthaleneimide (59), and 4-(tert-butyl-diphenylsilyloxy) benzyl bromide (60) in the presence of potassium carbonate and was allowed to reflux for 24 hours in acetonitrile (Scheme 1.15). The residue obtained was treated with dilute hydrochloric acid, followed by its extraction with ethyl acetate. After the removal of the solvent, the crude product was purified using column chromatography to obtain the desired chemosensor 61. The synthesized chemosensor acts as a chromogenic and fluorescent chemosensor to detect F⁻ ions. The chemosensor exhibits remarkable absorption spectra at 345 and 390 nm in THF. On addition of F⁻ ions, the new peaks formed at 270 and 510 nm accompanied by a color change from colorless to yellow. Further, upon excitation at 410 nm, the chemosensor shows significant emission at 250 nm while other ions (F⁻, CN⁻, AcO⁻, H₂PO₄⁻, I⁻, Cl⁻, NO₃⁻,

HSO₄⁻, ClO₄⁻, BF₄⁻, Br⁻, and OH⁻) revealed no changes. To study the sensing mechanism, ¹H-NMR titrations were performed, which revealed that the synthesized chemosensor follows chemodosimetric approach. The results revealed that compound **61** undergoes classical desilylation in the presence of F⁻ ion with the formation of compound **62** (Figure 1.15). These chromogenic and fluorescent changes led to the development of a test-strip kit for the detection of F⁻ ions⁷⁵.

Scheme 1.15: Synthetic route of chemosensor 61

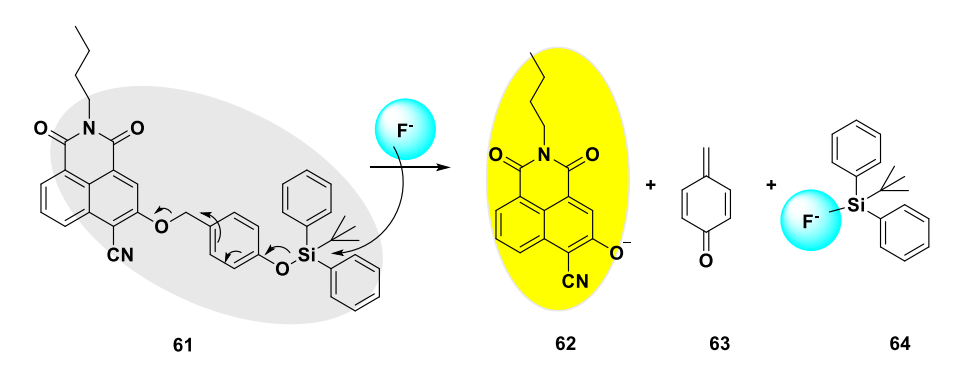


Figure 1.15: Sensing mechanism of 61 towards F-ions.

Xiao *et al* (2020) developed a 1,8-Naphthalimide appended with antharcarbaldehyde exhibiting a naked-eye chemosensor for the detection of F⁻ ion. The sensor was synthesized in one step using (*N*-butyl-1,8-naphthalimide)hydrazine (65) and 9-anthracenecarboxaldehyde (66) in acetic acid at reflux conditions for 6 hours to obtain the desired chemosensor (67) in good yield as red precipitates (Scheme 1.16). The UV-visible absorption study of the chemosensor revealed an absorption band centered at 490 nm in DMSO: H₂O (v/v, 7:1). The introduction of F⁻ ion into the free chemosensor solution led to the gradual decrease of the band at 490 nm with the emergence of the new band at 364 and 690 nm with naked-eye color change from yellow to blue (Figure 1.16). Further, the formation of an isosbestic point at 511 nm depicts the formation of new species, while other ions F⁻, Cl⁻, Br⁻, I⁻, H₂PO₄⁻, AcO⁻, HSO₄⁻, and ClO₄⁻ reveal no significant changes.

In addition, the emission peak of the chemosensor was found at 556 nm, which decreases in the presence of F⁻ ions. To investigate the binding mode, Job's plot analysis and ¹H-NMR titration exhibited a 1:1 stoichiometric ratio⁷⁶.

Scheme 1.16: Synthetic route of chemosensor 67

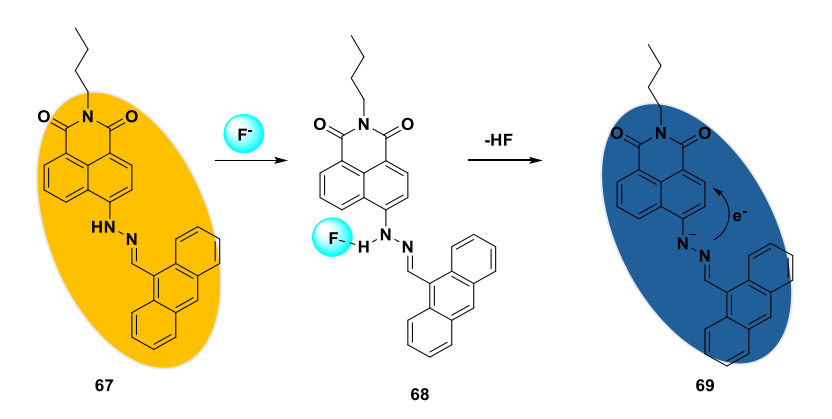


Figure 1.16: Sensing mechanism of 69 towards F-ions.

Pati *et al* (2020) designed compounds by varying the substituents at 4-position of the naphthalimide ring for the detection of F⁻ ions through the deprotonation mechanism of NH protons. These adenine-linked naphthalimide motifs were synthesized in a one-step reaction under harsh conditions. Compound **1** was treated with different aromatic compounds (**70**, **73**, **76**) in the presence of CS₂CO₃ and PdCl₂(PPh)₃ in dry toluene. The reaction mixture was allowed to reflux at 140 °C under an N₂ gas atmosphere. The reaction mixture was quenched with water, followed by its sequential extraction with the organic solvent. The organic layer was collected, and the solvent evaporated till dryness, yielding the crude product, which was further purified using column chromatography. This led to the formation of the desired chemosensors **71**, **74** and **77**. The chemosensors were treated with different anions to know their behavior, particularly towards

the F-ions. The selectivity studies were one in CH₃CN 1% DMSO solution. Compound 71 exhibits an absorption band at 395 nm which decreases with the emergence of a new band at 546 and 362 nm. This could be attributed to the deprotonation of the NH proton which led to the accumulation of charge on the N atom of the amino group thereby creating a push-pull effect between the electron-rich and electron-withdrawing naphthalimide ring, leading to ICT. This deprotonation was confirmed by the addition of protic solvents like MeOH, which led to the regain of the original peak and confirmed the re-protonation of the chemosensor. While the fluorescence studies revealed quenching of the fluorescence band at 470 nm. Similarly, chemosensor 73 exhibits an absorption band at 410 nm, which concomitantly decreases with the appearance of a new band at 546 nm, leading to the ratiometric response. The color of the free chemosensor transforms from light yellow to pink with the addition of F- ions. Also, the emission intensity of the free chemosensor exhibits a peak at 516 nm, which is significantly quenched on the introduction of F- ions. This quenching in emission intensity could be attributed to the PET process from the electron-rich nitrogen center to the electron-deficient naphthalimide ring. On the other hand, chemosensor 77 revealed no significant perturbations in the presence of anions. It was observed that the substitution of the adenine ring with benzothiazole in chemosensor 75 influenced the acidic character of the amine proton, which was responsible for the selectivity of F ions. This highlighted the role of acidic proton amine, which was absent in chemosensor 77, thereby exhibiting no alterations (Scheme **1.17**)⁷⁷.

Scheme 1.17: Synthetic route and sensing mechanism of chemosensor 71, 74, and 77 towards F-ions.

Yang *et al* (2021) developed a dual-platform colorimetric and ratiometric chemosensor **82** to detect F- ions. The chemosensor was synthesized from n-butyl-4-amino-1,8-naphthalimide (**80**) and 2-hydroxy-1-naphthaldehyde (**81**) in ethanol yielding a Schiff base (**82**) (Scheme 1.18). The absorption study revealed a band at 422 nm which showed a red shift to 583 nm with the addition of F- ions while other ions s (Cl⁻, Br⁻, I⁻, NO₃⁻, HSO₄⁻, SCN⁻, ClO₄⁻, AcO⁻, OH⁻ and CN⁻) exhibits no response in DMSO. Also, the chemosensor solution's color turned yellow to purple (**Figure 1.17**) with the formation of the isosbestic point at 500 nm, revealing the formation of a new species. The detection limit was found to be 0.61 μM with a stoichiometric ratio of 3:2 between the chemosensor and F- ions. The changes could be attributed to the deprotonation of the OH proton, which was also validated by theoretical studies. The chemosensor possesses practical application in real water samples⁷⁸.

Scheme 1.18: Synthetic route of chemosensor 82

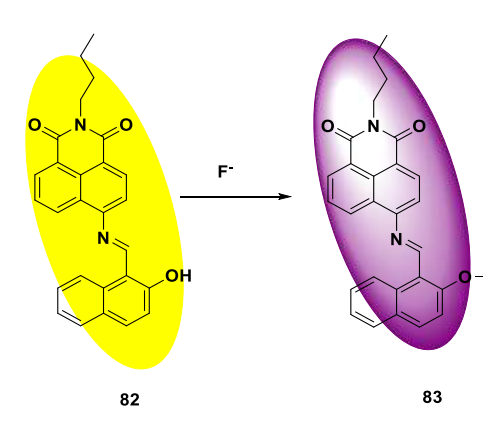


Figure 1.17: Sensing mechanism of 83 towards F-ions.

Pati *et al.* constructed three colorimetric and ratiometric chemosensors for the detection of F^- ions. The chemosensors were synthesized by displacement reaction of 4-bromo-1,8-naphthalic anhydride (1) with butylamine (84), aniline (85), and 2-aminopyridine (86). Then the 4-position of the naphthalimide ring was substituted with diethyl malonate (90), yielding three chemosensors. The absorption studies of the chemosensor revealed the appearance of the chemosensor band in a non-visible region at 265 nm. However, the addition of F^- ions to chemosensors 91, 94, and 97 exhibits a red shift at 560 nm with a decrease in the peak at 265 nm. This remarkable shift exhibits a visible change from colorless to violet, revealing remarkable colorimetric properties. Despite a similar change in the presence of F^- ion, the detection limit was determined to be 7.6 × 10⁻⁸ M, 9.4 × 10⁻⁸ M, and 1.1 × 10⁻⁷ M for 91, 94, and 97, respectively. The Job's plot was investigated for determining the binding ratio, revealing 1: 1 stoichiometry. Although there is no acidic proton like OH, NH; still the chemosensors detected F^- ion due to the activation of methylene proton due to keto-enol tautomerism, which led to significant spectral changes with F^- ion (Scheme 1.19)⁷⁹.

Scheme 1.19: Synthetic route and sensing mechanism of chemosensors 91, 94, and 97 towards F-ions.

1.2.2.2. Detection of hyphochlorite (ClO-) ions

Bi *et al.* synthesized a fluorescent chemosensor with AIE characteristics for the ratiometric detection of F⁻ ion. The synthesis of chemosensor **103** involved a two-step reaction. Initially, compound **1** was treated with 2-dimethylaminoethylamine (**100**) in ethanol, yielding compound **101** at reflux conditions. Further, compound **101** was reacted with coupled with 4-(methylthio) phenyl (**102**) in ethanol under a N₂ environment to get the desired chemosensor **103** in good yield (**Scheme 1.20**). The optical studies of the chemosensor **103** revealed an absorption band at 378 nm, which shifts to a lower wavelength on gradual addition of ClO⁻ ions using DMF: H₂O (1:9, v/v). On the other hand, the free chemosensor reveals no fluorescence, while the addition of ClO⁻ ions leads to significant enhancement in the fluorescence at 425 nm accompanied by a blue shift to 427 nm. Also, the fluorescence color of the chemosensor shifted from yellow to blue on increasing the concentration of ClO⁻ ions, which could be attributed to the transformation of thioether to thiosuphoxide thereby generating a push-pull effect (**Figure 1.18**). In addition, the presence of other ions, Ag⁺, Cu²⁺, Ni²⁺, Fe²⁺, Fe³⁺, Mg²⁺, H₂O₂, NO₂⁻, NO₃⁻, HCO₃⁻, CO₃²⁻, SO₃²⁻, and SO₄²⁻ has no effect on the chemosensor **103**. The detection limit was found to be 1.22 μM for

ClO⁻ ions. Further, the visual detection led to the development of test strips, and the fluorescent behavior was exploited for the confocal fluorescent imaging of endogenous ClO⁻ ions in HeLa cells⁸⁰.

Scheme 1.20: Synthetic route of chemosensor 103

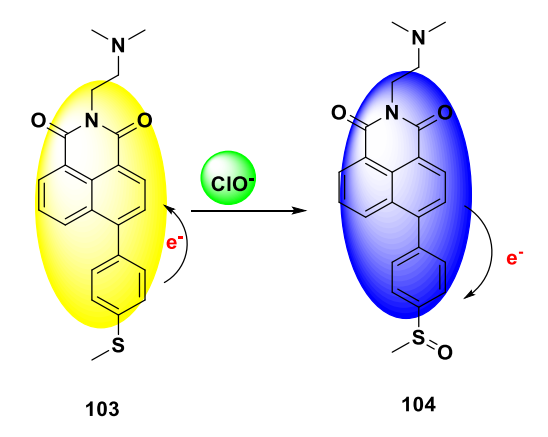


Figure 1.18: Sensing mechanism of 104 towards ClO⁻ions.

Zhang *et al* (2023) developed a phenothiazine appended naphthalimide-based chemosensor for the detection of ClO⁻ ions with naked eye color changes. The chemosensor was synthesized in a single-step process in ethanol. Compound **107** and compound **110** were synthesized as reported in the literature and were allowed to be stirred at reflux temperature of 12 h in ethanol with a few drops of acetic acid (**Scheme 1.21**). This led to the formation of yellow precipitates which were filtered and recrystallized in ethanol to obtain the desired chemosensor in good amounts. The chemosensor was further analyzed for the detection of ClO⁻ ion using spectroscopic studies in DMSO: PBS buffer (1:1, v/v). The free chemosensor solution reveals an absorption band at 433 nm which gradually disappeared on the introduction of ClO⁻ ions with the emergence of a new

peak in the range of 556-600 nm, along with the formation of isosbestic point at 480 nm. No other ions reveal any significant changes (K⁺, Na⁺, Ca²⁺, Mg²⁺, Al³⁺, Zn²⁺, Fe³⁺, Fe²⁺, Sn²⁺, Pb²⁺, Cu²⁺, Hg²⁺, Ag⁺, F⁻, Cl⁻, Br⁻, I⁻, HSO₃⁻, SO₄²⁻, SO₃²⁻, NO₃²⁻, NO₂⁻, PO₄³⁻, HPO₄²⁻, H₂PO₄²⁻, H₂S, H₂O₂, HClO₄, ONOO⁻, O₂⁻).Also, a naked eye color change was observed from green to brown (**Figure 1.19**). In addition, the fluorescence studies revealed a "turn-off" effect on the addition of ClO⁻ ions at 211 nm on excitation at 370 nm. This could be ascribed to the oxidation of sulphur into sulphoxide group, leading to the inhibition of ICT process. This reveals the selectivity of the chemosensor for ClO⁻ ion with a detection limit of 9.5 nM. Moreover, the chemosensor was found to be suitable under physiological pH, revealing its practical application in the endogenous detection of ClO⁻ ion in MCF-7 cells. Also, the naked eye changes led to the development of test strips and efficient tools for detecting ClO⁻ ion in tap water analysis⁸¹.

Scheme 1.21: Synthetic route of chemosensor 111

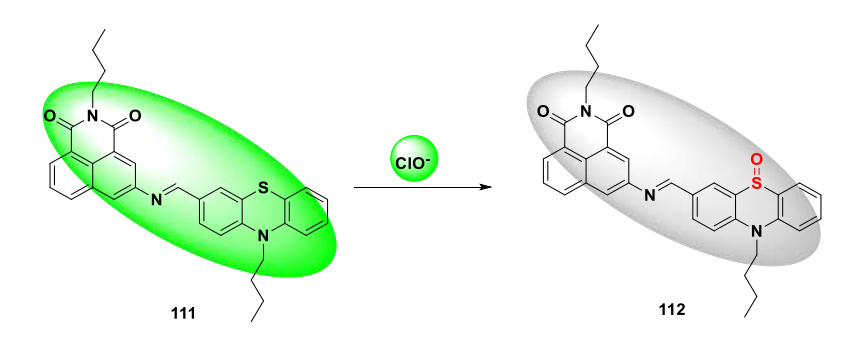


Figure 1.19: Sensing mechanism of 112 towards ClO-ions

Shirashi *et al* (2020) fabricated a naphthalimide-sulphonylhyrazine conjugate for the fluorescent detection of ClO⁻ ion. The chemosensor was synthesized in a single-step condensation reaction between 3-formyl-4-hydroxy-*N*-butyl-1,8-naphthalimide (46) and *p*-toluenesulfonyl hydrazide (113) in ethanol at reflux conditions for 21 hours. This led to the formation of yellow color precipitates affording the desired chemosensor 114 (Scheme 1.22). The optical analysis of chemosensor 114 towards different ions was investigated using the emission spectroscopic technique in H₂O: CH₃CN (8:2, v/v) as the solvent medium. The free solution exhibits a weak fluorescence intensity on excitation at 370 nm, whereas a strong fluorescence response was triggered in the presence of ClO⁻ ions at 519 nm (Figure 1.20). While the presence of other ions barely exhibits any effect on the spectrum. Further, the yellow color of the chemosensor solution turns green with the addition of ClO⁻ ions. A linear relationship between the fluorescence emission and the concentration of ClO⁻ ions was found revealing the detection limit to be 1.6 μM. The results were found to be useful in the detection of ClO⁻ ions in living cells⁸².

Scheme 1.22: Synthetic route of chemosensor 114

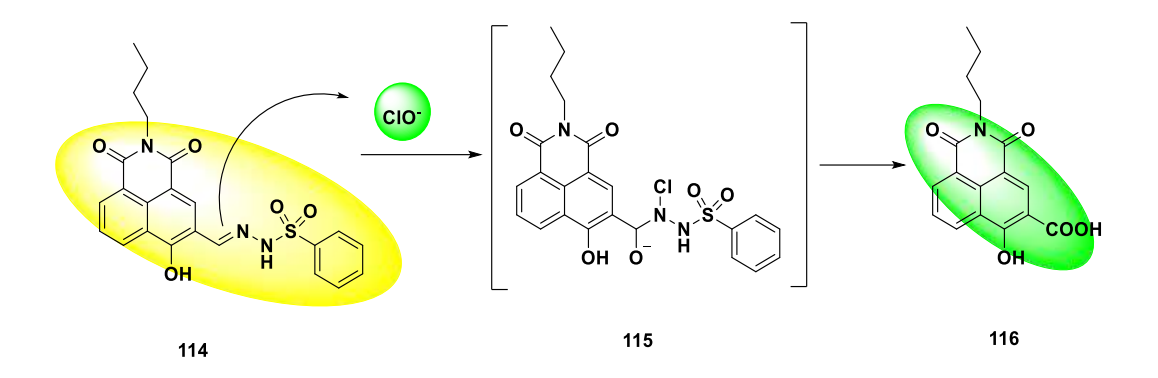


Figure 1.20: Sensing mechanism of 116 towards ClO-ions.

1.2.2.3. Detection of cyanide (CN-) Ions

She et al (2025) developed a FRET-based ratiometric chemosensor to detect CN⁻ ion in DMF: H₂O (9:1, v/v). The chemosensor comprises of coumarin and naphthalimide ring which was synthesized initially by classical Boc-deprotonation reaction using trifluoroacetic acid (TFA), followed by the subsequent displacement of the O atom at reflux in ethanol yielding the targeted chemosensor 119 (Scheme 1.23). The free chemosensor solution, green in color revealed a band at 425 nm in DMF/H₂O solution. The presence of CN⁻ ion revealed a colorimetric and ratiometric response with the formation of a new peak at 211 nm accompanied by a color change from green to pink. While the addition of other metal ions (Br⁻, Cl⁻, AcO⁻, DTT, F⁻, Gly, GSH, H₂O₂, HSO₃⁻, HSO₄⁻, I⁻, Leu, NO₃-, S₂-) didn't induce any change. Further, the fluorescent study revealed a blue emission band at 468 nm which gradually decreased with the formation of a new emission band at 582 nm (orange in color). These changes could be attributed to the FRET mechanism and cyanide-induced SNArH reaction followed by denitration and hydroxylation (Figure 1.21) which was confirmed through NMR titrations and LC-MS spectra, Further, the pH studies revealed its physiological activity to detect CN⁻ in the pH range of 4-12 with a detection limit of 5.3 μM. In addition, the paper strips loaded with chemosensors serve as a portable device for on-site monitoring of CN ions due to visible color changes. Also, it was used in the real-time detection of food and water samples⁸³.

Scheme 1.23: Synthetic route of chemosensor 119

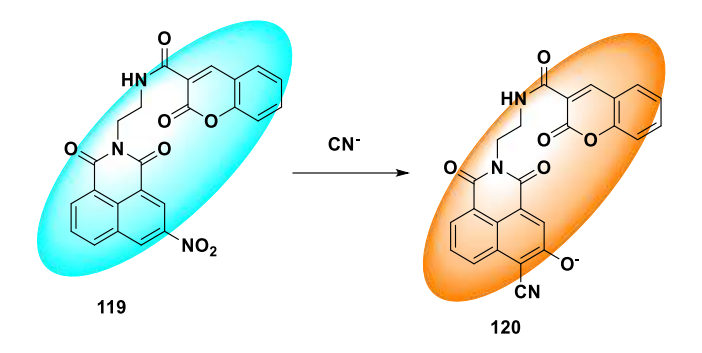


Figure 1.21: Synthetic route and sensing mechanism of **119** towards CN⁻ions.

Zhang *et al* (2024) fabricated a fluorescent chemosensor (122) for the detection of CNions. The chemosensor comprising of compound 46 and 8- Hydroxyquinaldine (121) was
synthesized in acetic anhydride at reflux conditions yielding a brown color targeted chemosensor
122 (Scheme 1.24). The optical studies of the free chemosensor revealed the absorption band at
455 nm in DMF: PBS (1: 1, v/v). While excitement at 380 nm, an emission peak at 479 nm was
observed. In addition to different anions, a significant decrease was observed in the addition of
CN⁻ ion in the absorption spectra. Also, the quenching in fluorescent spectra was observed with
the introduction of CN⁻ ions, revealing its selectivity. These changes could be ascribed to the
inhibition of the ICT phenomenon on the addition of CN⁻ ions, which hinders the conjugated
system hence, weakening the fluorescence intensity (Figure 1.22). The stoichiometric ratio was
calculated to be 1: 1. Further, the practical applicability of the chemosensor was determined in seawater, river water, and tap water⁸⁴.

Scheme 1.24: Synthetic route of chemosensor 122

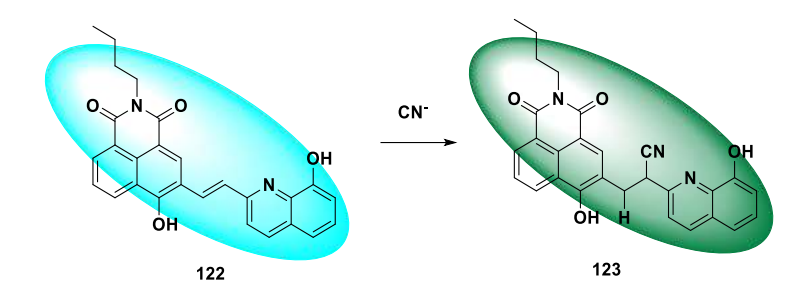


Figure 1.22: Sensing mechanism of 122 towards CN⁻ ions.

CHAPTER – 2

Materials and Methodology

This chapter outlines the detailed protocols employed in this research, covering the methodologies and procedures used to achieve the objectives of the study. Each protocol is systematically described to ensure reproducibility and provide a comprehensive understanding of the experimental approaches undertaken.



2.1. Materials and Instrumentation

Acenaphthene, ethylenediamine, hydrazine hydrate, Morpholine, 2-morpholinoethan-1-amine, 6methoxybenzo[d]thiazol-2-amine, salicylaldehyde, triethylamine (TEA), sodium dichromate, Nbromosuccinimide (NBS), hexane, and ethyl acetate were purchased from SD Fine-Chem Limited. We bought solvents like 2-methoxyethanol, dimethyl sulphoxide (DMSO), chloroform (CHCl₃), acetonitrile (CH₃CN), dimethylformamide (DMF), methanol (CH₃OH), ethanol (C₂H₅OH) from Loba Chemie. The acetate and chloride salts of cations, and tetrabutylammonium salts of anions and other reagents were from the Sigma Aldrich company. Also, thiophene-2-carbaldehyde, 6methoxybenzo[d]thiazol-2-amine, morpholine, 2-morpholinoethan-1-amine, and salicylaldehyde were purchased from Sigma Aldrich. Silica gel F₂₆₅ plates were used to monitor the reaction, while silica gel (60-120 mesh) was used for column chromatography. Tetramethylsilane (TMS) was used as an internal standard in ${}^{1}H$ and ${}^{13}C$ -NMR spectra using CDCl₃ or DMSO- d_6 as solvent. The Nuclear Magnetic Resonance (NMR) spectra were recorded on a JOEL-500 NMR spectrometer. On the Brucker MicroToff/QII, high-resolution mass spectra (HRMS) were recorded. In addition, the absorption spectra were recorded on SHIMADZU-1900i using a quartz cell of 1 cm path length in the range of 200-800 nm. On a PerkinElmier 5600, fluorescence spectra were captured in a 1cm quartz cuvette. All the spectroscopic experiments were performed in HPLC-grade solvents. The time-resolved studies were carried out on a DeltaFlex Modular Fluorescence Lifetime Spectrofluorimeter (HORIBA Scientific).

2.2. Preparation of Stock Solutions

To carry out the spectroscopic studies *i.e.*, absorption and emission studies, the stock solution of probe (1-5) of concentration 10⁻³ M was prepared in DMSO, which was subsequently diluted as per the requirement for photophysical studies. For cations, the stock solution of the acetate salts of various cations, *viz*. Mn²⁺, Fe²⁺, Co²⁺, Ni²⁺, Cu²⁺, Cd²⁺, Cs²⁺, Zn²⁺, Hg²⁺, and Pb²⁺ whereas chloride salts of Al³⁺ and Mn²⁺ were prepared at a concentration of 1×10⁻¹ M in deionized water. Further, the stock solutions of tetrabutyl ammonium (TBA) salts of various anions, *viz*. CN⁻, I⁻, AcO⁻, Br⁻, SO₄²⁻, Cl⁻, NO₃²⁻, F⁻, PO₄²⁻, P₂O₅⁻ of concentration 1×10⁻³ M were prepared in acetonitrile. The solutions were further diluted as per the suitable solvent system to the desired concentrations.

2.3. Spectroscopic Measurements

Spectroscopic studies of probes (1-5) were conducted at concentrations ranging from 20 to 40 µM, using the appropriate solvent system as the medium. For the UV-Vis absorption study, a baseline was recorded using the reference cell, followed by the measurement of the desired solution (2 ml) in the sample cell over a wavelength range of 200-800 nm. Initially, various solvent systems were tested to determine the solubility of the probes and identify their maximum absorption wavelength (λ_{max}) . Subsequently, screening was performed in the presence of different ions in various solvents to assess the probes' selectivity toward a specific ion. Any alterations in the spectrum, such as bathochromic (redshift), hypsochromic (blueshift), hypochromic, or hyperchromic shifts, indicate the detection of a particular ion in the selected solvent system. Similarly, fluorescence spectroscopy was conducted using a quartz cuvette with a path length of 1 cm. Different solvents were tested in fluorescence spectroscopy, and the selectivity of ions was observed in the specific solvent system at a particular excitation wavelength (λ_{ex}). The perturbations in fluorescence intensity, whether an increase or decrease, or shifts in wavelength (toward longer or shorter wavelengths) indicated the detection of a specific ion. The screening of selected ion(s) in a particular solvent medium was followed by their titration study with the detected ion of concentration 1×10^{-3} M, with subsequent addition of aliquots till saturation was attained. Further, the titration data obtained were used for quantitative analysis. All the parameters were kept the same to get precise and accurate results.

2.4. Quantitative Analysis

The limit of detection (LOD) was determined from the following equation 1:

$$LOD = \frac{3\sigma}{K} \tag{1}$$

The limit of quantification (LOQ) is calculated from the following equation 2:

$$LOQ = \frac{10 \sigma}{K}$$
 (2)

Where σ is the standard deviation of the ten blank samples and K is the slope of the graph.

Further, the association constant was calculated by using the Benesi-Hildebrand method using equation (3) as follows:

$$\frac{1}{I-I_0} = \frac{1}{K_a(I_{\text{max}}-I_0)[C]^n} + \frac{1}{I_{\text{max}}-I_0}$$
 (3)

where I_0 is the absorption intensity of the probe (1-5) in the absence of the ion, I is the intensity at an intermediate level of interaction with the ion, and I_{max} is the intensity when there is complete interaction (saturation) with the ion, K_a is the binding constant, which determines the affinity between the probe and ion, C is the concentration of analyte and n is the number of analytes bound per compound molecule.

The Stern-Volmer equation was employed to calculate the quenching constant (K_{SV}) as follows:

$$F_o/F = 1 + K_{SV}[M] = 1 + \tau_o k_q$$
 (4)

Where F_0 is the emission intensity of probe (1-5) without ions while F is the emission intensity of probe (1-5) with ions, K_{SV} is the Stern-Volmer quenching constant, and M is the concentration of ions, τ_0 is is the average fluorescence decay free from quencher, and k_q is linear quenching constant.

In addition, to calculate the fluorescence quenching efficiency (η), the following equation was employed:

$$\eta = [(I_0 - I)/I_0] \times 100 \% \tag{5}$$

Where I₀ is the fluorescent intensity before the addition of ions, and I is the fluorescent intensity after the addition of ions.

2.5. Quantum Yield

The fluorescence quantum yield of probe 1 and its complex with the Fe³⁺ ion was determined by Williams' method using the gradients methodology⁸⁵. The quantum yield of the sample was calculated in methanol, and quinine sulfate was used as the standard ($\phi_r = 0.55$ in 0.1 M H₂SO₄). The determination of fluorescence quantum yield for probe 1 (ϕ_s) and its complex (ϕ_c) was calculated by using the following formula:

$$\Phi_{s,c} = \Phi_r \left(\frac{Grad_{s,c}}{Grad_r} \right) \left(\frac{\eta_{s,c}^2}{\eta_r^2} \right)$$
 (6)

Where " Φ " represents quantum yield; "Grad" is the slope of the plot from integrated fluorescence v/s absorbance; " η " is the refractive index of the solvent used; and s, c, and r denote probe 1, complex, and standard, respectively.

2.6. Time-Resolved Emission Spectroscopy

To investigate the excited-state fluorescence lifetime analysis, time-resolved emission spectroscopy of probe 1 (20 μ M) was performed in the absence and presence of Fe³⁺ ions. The value of the average decay time was calculated with the help of the following equation⁸⁶:

$$\tau = \sum \tau_i \alpha_i \tag{7}$$

where τ is the average lifetime decay and α_i is the relative amplitude along the value of decay time, τ_i .

To understand the radiative and non-radiative decay, the radiative decay (k_r) constant and non-radiative decay constant (k_{nr}) of probe 1 and its complex were calculated using the equation mentioned below:

$$\mathbf{k}_r = \frac{\mathbf{\Phi}}{\mathbf{T}} \tag{8}$$

$$k_{nr} = \frac{\Phi}{(1/\tau) - kr} \tag{9}$$

Where ϕ and τ are the quantum yield and average lifetime of probe 1 and its complex with Fe³⁺ ions, respectively.

2.7. Job's Plot

The Job's plot experiment has been carried out to determine the stoichiometric ratio between the probe (1-5) and the detected ions. A series of solutions containing probe (1-5) (20 μ M) and ions (20 μ M) were prepared in the chosen solvent system. The experiment has been carried out by keeping the total volume (3 ml) and total concentration (20 μ M) constant of probe 1 and selected ion(s). The study was performed at different mole fractions, and the highest absorbance to the concentration of ions reveals the stoichiometric ratio of the complex.

2.8. Interference Studies

To gain further insights into the selectivity of the probe (1-5), the interference of other ions present in the environment was evaluated. To examine this, various ions were added to the mixture of probe (1-5) and detected ions individually, and the absorption/emission was recorded, respectively.

Any deviation from the peaks exhibits its interference, while no deviation exhibits the unaltered nature of the chemosensor, revealing no effect of other ions in the environment.

2.9. pH Study

In a pH titration experiment, solutions of different pH were prepared, and the variations were done by adding small aliquots of 0.1 M hydrochloric acid (HCl) or 0.1 M sodium hydroxide (NaOH). The change in the pH was continuously monitored by a digital pH meter. The solutions were allowed to equilibrate with each addition for 1 min. and were then transferred into a dry quartz cuvette of path length 1.0 cm each time, and spectral data were recorded. Notably, the digital pH was calibrated with standard solutions each time before conducting the measurements. All the spectroscopic measurements were carried out at room temperature.

2.10. ¹H-NMR titrations, ATR-FTIR analysis, and HR-MS

The binding of the ion was determined with various spectroscopic analyses. To investigate the plausible binding mechanism, the 1 H-NMR of the free probe was recorded using d_{6} -DMSO. Then the addition probe equivalent of the detected ion (in d_{6} -DMSO) solution was added, and the spectrum was recorded. The disappearance or any noticeable shift in the spectra revealed the coordination of a particular ion and was interpreted. Additionally, the ATR-FTIR analysis of the free probe and after the addition of a selected ion was performed to determine the binding site of the guest with the probe. To further validate the stoichiometric ratio, the HR-MS analysis of the probe was performed in the presence of ions, which was complementary to the Job's plot analysis.

2.11. Reversibility Study

To investigate the reversibility of the probe-ion complex, spectroscopic studies including absorption/fluorescence were performed. The complex containing a metal ion was checked in the presence of ethylenediaminetetraacetic acid (EDTA) to determine the reversibility due to its greater chelation capability. While the cationic complex was checked in the presence of methanol or TFA, in case of deprotonation in the probe. This further led to the development of different types of molecular logic gates. In addition, the number of cycles was performed with subsequent addition of ions, followed by a chelating agent, and again an ion, followed by an agent, and so on, to determine the recyclability of the designed probe.

2.10. Test-Strip Development

To develop test strips, Whatman filter paper was cut into thin strips of equal dimensions of 0.5×2 cm. Then the paper strips were soaked for 1 h in the probe solution, followed by drying at room temperature. The developed test strips were observed in visible light, short UV rays, and long UV rays. This was followed by application of the detected ion(s) of various concentrations onto the test strip with a narrow mouth capillary tube to avoid spreading. The test strips were then studied under visible light, short UV rays, and long UV rays. The pictures of the same were recorded with high resolution camera. This further led to the development of concentration-dependent test strips for on-site monitoring of the ion(s) in real-time applications.

2.11. Smartphone Analysis

The smartphone analysis was performed by the free mobile app (Color Picker), which was downloaded on Android (RedmiNote 10T 5G). This app provides red, green, and blue (RGB) values against a particular color. The color of the free probe solution was clicked, followed by the gradual addition of the ions. The color changes observed with each addition of an aliquot were noted, and the variation in the RGB ratio was studied. The linear plot between the R/G ratio and concentration of the ion revealed its detection limit, guaranteeing inexpensive and real-time application.

2.12. Computational Studies

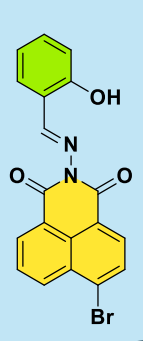
The electronic structural calculation was performed using Gaussian 09W package⁸⁷ for the target probe (1-5) and its complexes. The molecules were viewed using Gauss View 6. The frequency optimization of the probe and its complexes were carried out using the DFT and Becke 3-parameter Lee–Yang–Parr (B3LYP) function method with 6-31G (d,p) as a basis set. Usually, B3LYP along with DFT calculation is widely used and shows better results with experimental values. The 6-31G (d,p) basis set was used for all the non-metal (H, C, O, and N) while the lanL2DZ basis set was used for the metal ion. The Integral Equation Formalism PCM (IEFPCM) solvent model was applied to determine the effect of the solvent. Furthermore, to confirm that the optimized structures represent a true minimum, stability checks and frequency calculations were conducted. The Time Dependent- Density Functional Theory (TD-DFT) calculations were performed to calculate the various electronic transitions and UV-visible absorption spectrum. HOMO and LUMO images were generated from the corresponding checkpoint files of the optimization process and global

chemical descriptors were studied. Also, the electrostatic potential (ESP) maps were analyzed using the same basis set. Multiwfn 3.8 tool is used to calculate various parameters electron localization function (ELF) and localized orbital locator (LOL) for topological analysis.

CHAPTER - 3

Synthesis and photophysical study of Naphthalimide appended Salicylaldehyde (Probe 1)

In this chapter, a Schiff base derived from naphthalimide and salicylaldehyde was designed and prepared for the detection of Cu^{2+} , F, and CN ions in CH₃CN as the medium. The designed probe exhibits ratiometric behaviour in the presence of ions, accompanied by a naked eye color change. While a "turn-off" behaviour was noticed in the fluorescent spectrum.



Journal of Molecular Structure 1319 (2025) 139252



Contents lists available at ScienceDirect

Journal of Molecular Structure

journal homepage: www.elsevier.com/locate/moistr





A novel naphthalimide-derived "turn-off" chemosensor for the detection of Cu2+, F and CN ions

Gurdeep Kaur a, Gulshan Kumar b, Iqubal Singh 5.

- Department of Chemistry, School of Chemical Engineering & Physical Sciences, Lovely Professional University, Phagwara, 144411, India
- b Department of Chemistry, Banasthali University, Banasthali Newai, Rajasthan, 304022, India
 5 School of Pharmaceutical Sciences, Lovely Professional University, Phagwara, 144411, India

ARTICLE INFO

Keywords: Napthalimide Absorbance Chemosensor Limit of detection TD- DFT

ABSTRACT

The development of selective chemosensor for the detection of detrimental analytes in the environment is crucial due to their catastrophic effects. In this study, a novel Schiff base derived from naphthalimide and salicylaldehyde was designed and prepared for the detection of Cu2+, F, and CN ions in CH3CN as medium. The chemosensor exhibits a red shift in the presence of Cu²⁺, F', and CN' ions accompanied by naked eye color change in the presence of F and CN ions. On the other hand, a "turn-off" response was observed in the presence of ion Cu2+, F', and CN' ions in the fluorescent spectrum. The good anti-interference characteristics, strong binding, and low limit of detection (LOD) of the chemosensor revealed its sensitivity against Cu2+, F, and CN ions i.e. 1.25 × 10^{-5} M, 1.07×10^{-6} M, and 0.98×10^{-6} M, respectively. The binding ratio (1:1) was determined by Job's plot between the chemosensor and ions. In addition, the binding of ions with the chemosensor was proposed which was further supported by time-dependent density functional theory (TD-DFT) and IR spectrum data.

3.1. Introduction

The field of Supramolecular Chemistry has witnessed a tremendous revolution in recent years. The advanced properties of low cost, facile synthesis, excellent sensitivity, and good operability that are capable of detecting harmful analytes in biological as well as environmental systems have gained significant attention in the research field. Ions play a crucial role in governing biological processes and affect human health⁸⁸. Copper (Cu²⁺) is one of the third most copious metals found in the human body, responsible for various biological functions⁸⁹. Cu²⁺ is the most common ionic form of copper that is present in the environment and is responsible for various biological activities. Various physiological processes, including enzyme-catalyzed procedures and redox reactions depend severely on Cu²⁺ ions⁹⁰. It possesses wide application in different areas such as electrical wires, fertilizers, pesticides, water pipes, machinery parts, used in valves, feeds used for animals or birds, and the release of industrial effluents is the major cause of water contamination⁹¹. The augmented level of Cu²⁺ ions can be the cause of severe diseases like Wilson's disease⁹², Alzheimer's disease, Menkes syndrome⁹³, Parkinson's disease⁹⁴, etc. The wide-ranging application of this metal in different spheres, including agriculture, domestic, construction, and industry, is the primary cause of metal pollutants globally⁹⁵. The permissible amount of copper ions in the human body usually ranges from 1-5 mg/day. Amongst anions, fluoride (F⁻) and cyanide (CN⁻) have been widely studied due to their wide use in chemical and industrial fields. F is one of the imperative anions possessing a significant role in numerous activities like water fluoridation, dental care, and chemical components in medical systems⁹⁶. It is also used in various materials like toothpaste, medicine, tea, and food⁹⁷. Its ingestion in minute amounts can avert bone deformity and various other dental problems⁹⁸. However, as per the WHO, the level of fluoride should be less than 1.5 ppm in drinking water⁹⁹. Also, the presence of a high level of CN⁻ in the biological systems can lead to disruption of various processes due to its ability to bind with Fe³⁺ ions¹⁰⁰. It can cause severe damage and in certain cases death if ingested more than 0.05mg/kg body weight. As per the WHO guidelines, the acceptable amount of CN in drinking water is 1.6 µM due to its acute toxicity¹⁰¹. Therefore, it has become essential to monitor the level of anions by developing such effective methods.

In this study, a novel "turn-off" schiff base (*E*)-6-bromo-2-((2-hydroxybenzylidene) amino)-1*H*-benzo[de]isoquinoline-1,3(2*H*)-dione (probe 1) has been prepared for the selective detection of Cu^{2+} , F^{-} , and CN^{-} ions. The probe (1) was synthesized through a condensation reaction

between 2-hydroxybenzaldehyde and 2-amino-6-bromo-1*H*-benzo[*de*]isoquinoline-1,3(2*H*)-dione. The absorption studies revealed a hypochromic shift accompanied by a red shift on the addition of Cu²⁺, while a significant red shift was observed on the addition of F⁻ and CN⁻ ion. A visible color change from colorless to faint yellow was observed with the addition of F⁻ and CN⁻ ions. Further, TD-DFT was performed to get a deeper insight into the binding mode with respective ions.

3.2. Synthesis of Probe 1

To the solution of 1, NBS was added with constant stirring at room temperature to yield intermediate 2. The intermediate 2 was further reacted with sodium dichromate at reflux conditions which produced intermediate 3 in moderate yield. The intermediate 3 was then further reacted with hydrazine hydrate in ethanol at reflux temperature to produce 4. The intermediate 4 undergoes a condensation reaction with salicylaldehyde in ethanol at reflux conditions, yielding probe 1. The precipitates formed were allowed to cool down to room temperature, then filtered under vacuum and washed subsequently with ethanol. Hence, probe 1 was obtained as brown-yellow precipitates (Scheme 3.1). The compound was further characterized by ¹H-NMR, ¹³C-NMR, and HRMS.

Scheme 3.1: Synthetic route for the synthesis of probe 1

3.3. Photophysical Properties of Probe 1

The optical performance of probe **1** was examined in the presence of several metal ions (Mn²⁺, Fe²⁺, Al³⁺, Co²⁺, Ni²⁺, Cu²⁺, Cd²⁺, Cs²⁺, Zn²⁺, Hg²⁺, and Pb²⁺) (10 equv.) in CH₃CN as medium. The fluorescence response revealed a feeble emission of **1**, which could be attributed to the C=N isomerization and the prevalence of the ESIPT process (λ_{ex} = 330 nm, λ_{em} = 390 and 509 nm). Notably, a naked eye "turn-off" behavior of the probe was observed in the Cu²⁺ ions under UV light (λ = 365 nm). Whereas no other ion exhibits any significant color change or perturbation in

the fluorescent behavior under UV light. Also, the anionic detection ability of the **1** was determined in the individual presence of different anions (Br⁻, Cl⁻, P₂O₇⁴⁻, CN⁻, H₂PO⁴⁻, HSO⁴⁻, NO³⁻, AcO⁻ and SCN⁻) (10 equv.) using CH₃CN as a medium to study the optical changes. The presence of F⁻ and CN⁻ ions exhibits a visible color change at ambient conditions, whereas a similar "turn-off" response was observed under UV light ($\lambda = 365$ nm) on the addition of F⁻ and CN⁻ ions.

3.3.1. UV-Visible Spectroscopic Study

The UV- Vis absorption spectrum of probe 1 (20 μ M) was recorded in CH₃CN as a medium exhibiting a maximum absorption band at a wavelength of 341 nm, which could be attributed to n- π * transitions. During the addition of up to 10 equivalents of various ions (Mn²⁺, Fe²⁺, Al³⁺, Co²⁺, Ni²⁺, Cd²⁺, Cs²⁺, Zn²⁺, Hg²⁺, and Pb²⁺) to probe 1, the intensity of the band at 341 nm remains unaltered or with slight change except for Cu²⁺ ions (Figure 3.1a). The presence of Cu²⁺ leads to the formation of new bands at 275 nm and 370 nm. After the introduction of Cu²⁺ ions, the presence of equilibrium was assured with the formation of two isosbestic points at 307 nm and 360 nm. Moreover, the incremental introduction of Cu²⁺ ions (0-2 equv.) separately to probe 1 lead to a decrease in the band intensity at 341 nm while the intensity of newly emerged bands at 275 nm and 370 nm increases (Figure 3.1b).

Further, the selectivity of probe 1 (20 μM) was studied amongst different anions (Br⁻, Cl⁻, P₂O₇⁴⁻, CN⁻, H₂PO⁴⁻, HSO⁴⁻, NO³⁻, AcO⁻, and SCN⁻) (10 equv.) using CH₃CN as a medium (**Figure 3.1c**). The presence of other ions didn't display any change except fluoride (F⁻) and cyanide (CN⁻) ions, which exhibited a decrease in intensity of probe 1 at 341 nm, accompanied by redshift at 415 nm and 409 nm. An isosbestic point at 364 nm was observed by adding both CN⁻ and F⁻ ions. In addition, a change in the color of the naked eye from colorless to faint yellow was observed in ambient conditions. These color changes also confirm the red shift of absorption bands. So, it can be concluded that probe 1 enables the visual detection of CN⁻ and F⁻ ions. It is also pertinent that no such red shift was observed with other ions. To better understand the absorption properties, the changes in the absorption spectra were studied with increments in the concentration of both CN⁻ and F⁻ ions (**Figure 3.1d and 3.1e**). The UV-titrations revealed that with the gradual addition of CN⁻ and F⁻ ions, the intensity of the absorption band at 341 nm of the ligand gradually decreases with a concomitant increase in intensity at 409 nm and 415 nm.

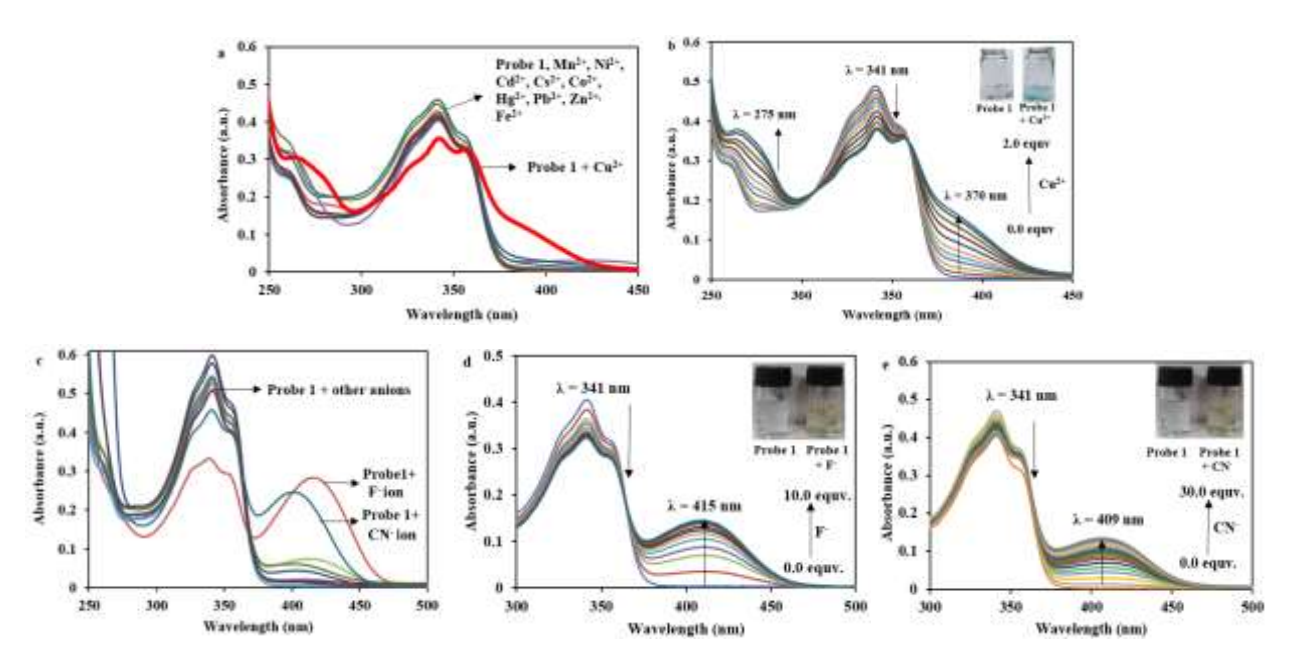


Figure 3.1: UV-spectra of probe **1** (20 μM) in CH₃CN a) in presence and absence of cations (Mn²⁺, Fe²⁺, Al³⁺, Co²⁺, Ni²⁺, Cd²⁺, Cs²⁺, Zn²⁺, Hg²⁺, and Pb²⁺) (10 equv.); b) on incremental addition of Cu²⁺ ions (0-2 equv.); c) in the presence and absence of anions (Br⁻, Cl⁻, P₂O₇⁴⁻, CN⁻, H₂PO⁴⁻, HSO⁴⁻, NO³⁻, OAc⁻ and SCN⁻) (10 equv.); d) on incremental addition of F⁻ ions (0-10 equv.); e) on incremental addition of CN⁻ (0-30 equv.)

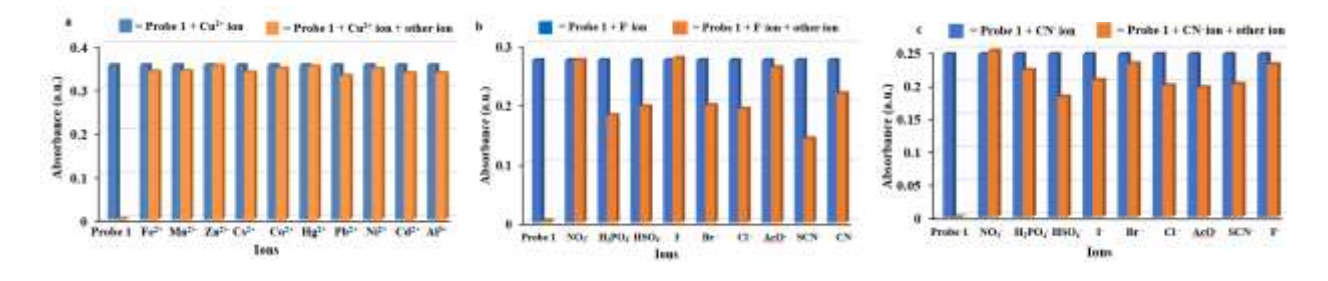


Figure 3.2: Interference study of probe 1 a) with Cu²⁺ ions; b) with F⁻ ions and c) with CN⁻ ions.

Further, the interference study of probe 1 was performed to determine the selectivity of the probe in the presence of other ions. In the typical competition study, probe 1 was treated with the same equivalents of competing ions and then with the Cu²⁺, F⁻, and CN⁻ ions. The results revealed that in the presence of different metal ions, the absorbance didn't exhibit any change, revealing its selectivity. On the other hand, in the case of F⁻ ions, the presence of other competing ions didn't alter the absorbance except for Cl⁻ and SCN⁻ ions. In addition, the presence of competing ions revealed slight interference in the presence of CN⁻ ions (**Figure 3.2**).

3.3.2. Fluorescence Spectroscopic Study

Further investigating the sensing property, the fluorescent studies of probe 1 (20 μM) were conducted using acetonitrile as solvent. On photoexcitation at 330 nm, probe 1 displayed emission at 390 nm and 509 nm. As illustrated in **Figure 3.3a**, the presence of metal ions (Mn²⁺, Fe²⁺, Al³⁺, Co²⁺, Ni²⁺, Cd²⁺, Cs²⁺, Zn²⁺, Hg²⁺, and Pb²⁺) (10 equiv.) displayed no change in the emission properties of probe 1. However, the addition of Cu²⁺ ions results in a significant decrease in emission intensity at 509 nm. Further, for quantitative estimation, titrations were performed with Cu²⁺ ions (0-1.5 equiv.) exhibiting a decrease in intensity at 509 nm on every addition, leading to "turn-off" behavior (**Figure 3.3b**).

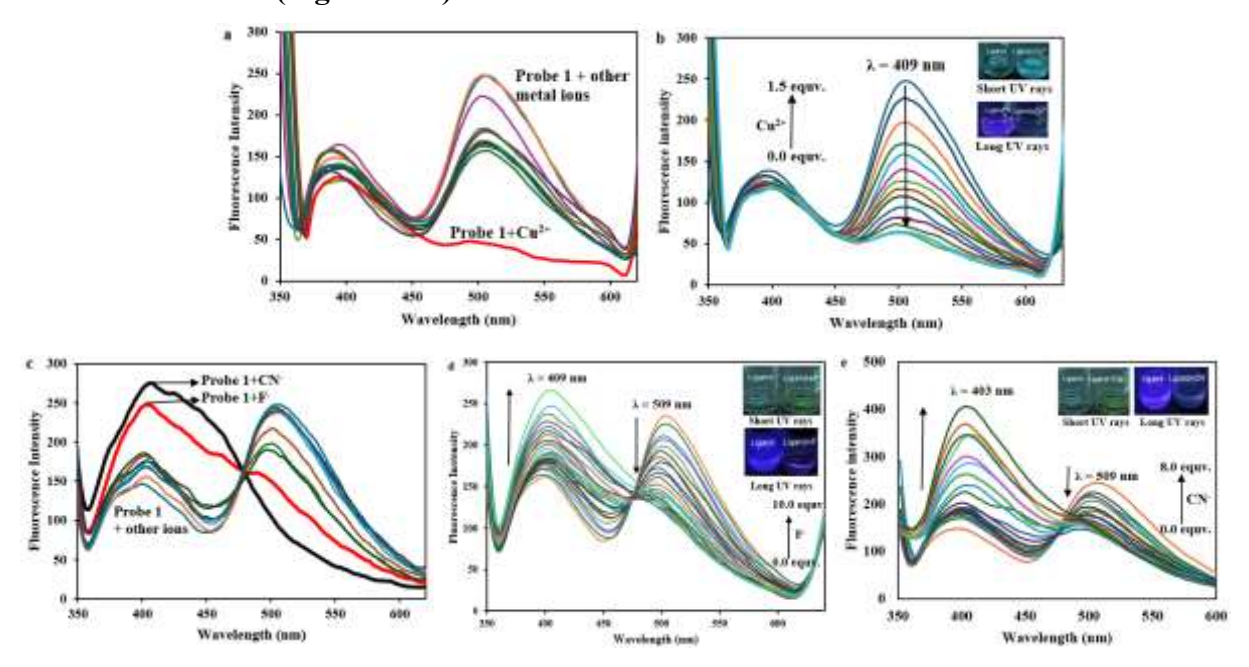


Figure 3.3: Fluorescence spectra of probe **1** (20 μ M) in CH₃CN a) in presence and absence of cations (10 equv.); b) on incremental addition of Cu²⁺ ions (0-1.5 equv.); c) in presence and absence of anions (10 equv.); d) titration with addition of F⁻ ions (0-10 equv.); e) titration with addition of CN⁻ ions (0-8 equv.)

On the other hand, amongst the different anions (Br⁻, Cl⁻, P₂O₇⁴⁻, CN⁻, H₂PO⁴⁻, HSO⁴⁻, NO³⁻, OAc⁻ and SCN⁻) (10 equv.) using CH₃CN as a medium, no change was observed in the fluorescence intensity whereas enhancement in intensity at 409 nm with a simultaneous decrease in intensity at 509 nm was observed with the formation of isosbestic point at 478 nm for F⁻ and CN⁻ ions was observed (**Figure 3.3c**). Further, the subsequent addition of F⁻ ions (0-10 equv.) revealed enhancement in intensity at 309 nm with a concomitant decrease in intensity at 509 nm

(Figure 3.3d). A similar behavior was noticed on incremental addition of CN⁻ ions (0-8 equv.) (Figure 3.3e)

3.4. Limit of Detection (LOD) and Limit of Quantification (LOQ)

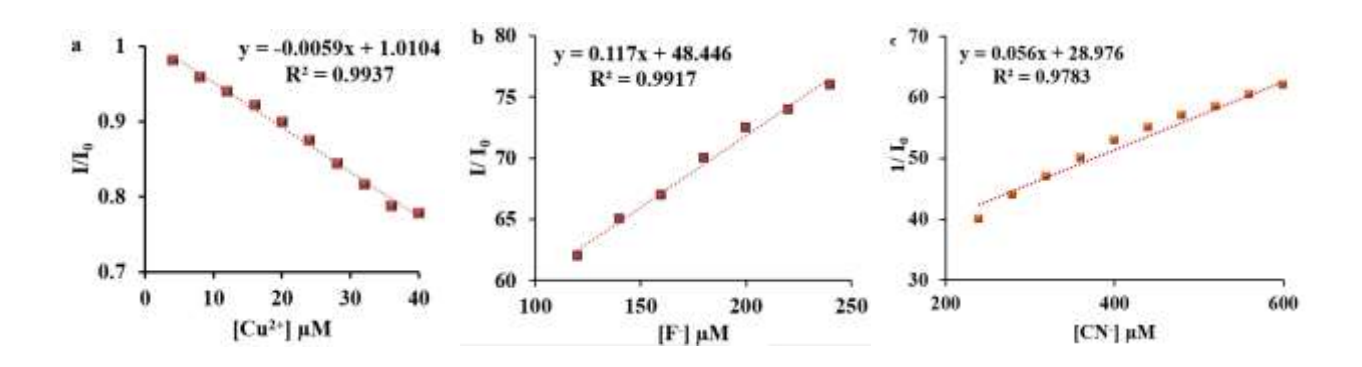
The LOD of probe 1 was calculated from the calibration graph based on the linearity range from equation 1 *i.e.* $3\sigma/k$ (Figure 3.4). Further, the linearity range values were computed to $10\sigma/k$ (equation 2) for the calculation of the LOQ through absorption and fluorescent studies, as given in Table 3.1.

Table 3.1: Values of LOD and LOQ of probe 1 for Cu²⁺, F-, and CN- ions through spectroscopic techniques.

Ions	LOD (M)		LOQ (M)	
	UV-Vis	Fluorescence	UV-Vis	Fluorescence
Cu ²⁺	5.08×10 ⁻⁵	1.25×10 ⁻⁵	1.69×10 ⁻⁴	4.16×10 ⁻⁵
F-	2.56×10 ⁻⁶	1.07×10^{-6}	8.54×10 ⁻⁶	3.57×10 ⁻⁶
CN-	5.08×10 ⁻⁶	0.98×10^{-6}	1.78×10 ⁻⁵	3.31×10 ⁻⁶

3.5. Association constant (K_a) and Quenching Constant (K_{sv})

The association constant (K_a) was calculated using a Benesi-Hildebrand plot (**equation 3**) exhibiting a linear relationship between $1/(A-A_0)$ v/s 1/[M], revealing the association constant (K_a). The association constant was found to be 5.83×10^4 M⁻¹, 1.24×10^4 M⁻¹, and 2.43×10^5 M⁻¹ for Cu^{2+} , F⁻, and CN^- ions, respectively. (**Figure 3.5**). Also, in the presence of Cu^{2+} , F⁻, and CN^- ions, the quenching of fluorescence was observed, revealing quenching constants (K_{SV}) of 9.24×10^4 M⁻¹, 4.16×10^3 M⁻¹, and 1.03×10^3 M⁻¹ for Cu^{2+} , F⁻, and CN^- ions, respectively calculated from Stern-Volmer **equation 4** (**Figure 3.6**)



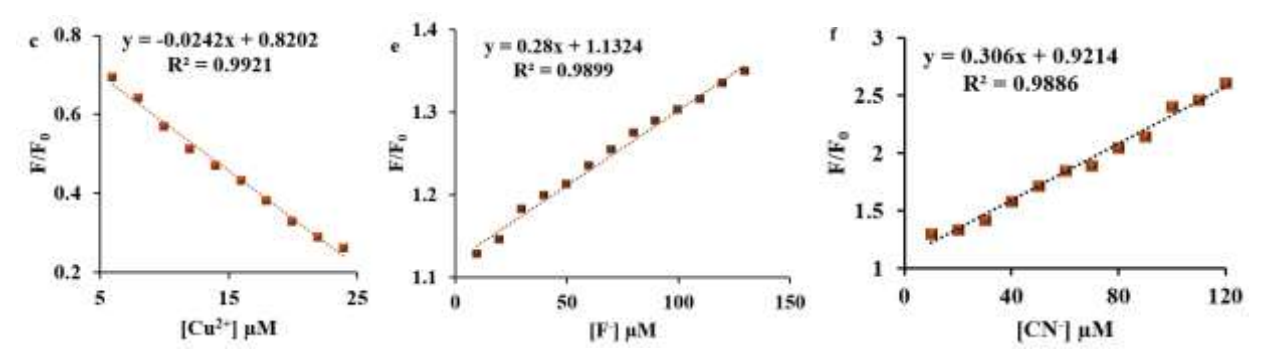


Figure 3.4: Plot of $I/I_0 \text{ v/s a}$) $[Cu^{2+}]$, b) $[F^-]$, and c) $[CN^-]$; Plot of $F/F_0 \text{ v/s d}$) $[Cu^{2+}]$, e) $[F^-]$, and f) $[CN^-]$

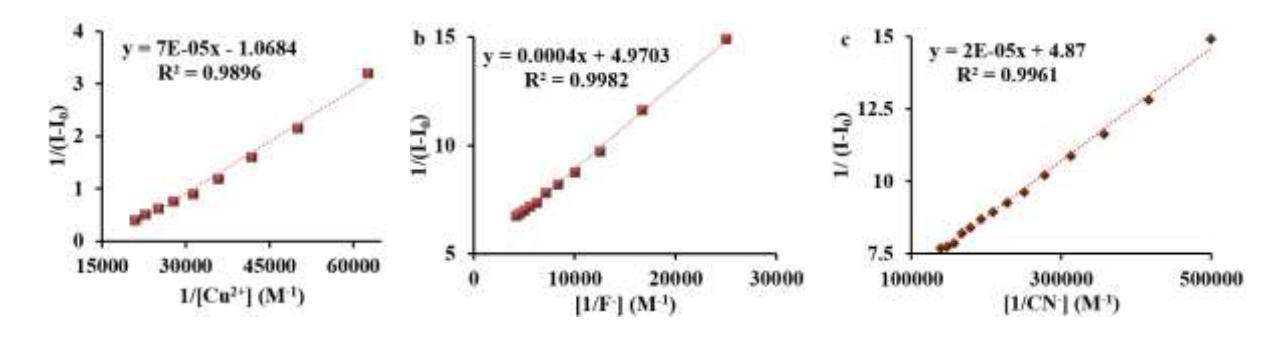


Figure 3.5: Benesi-Hilderbrand plot for determining association constant of probe 1 for a) Cu²⁺ ion, b) F⁻ ion, and c) CN⁻ ion

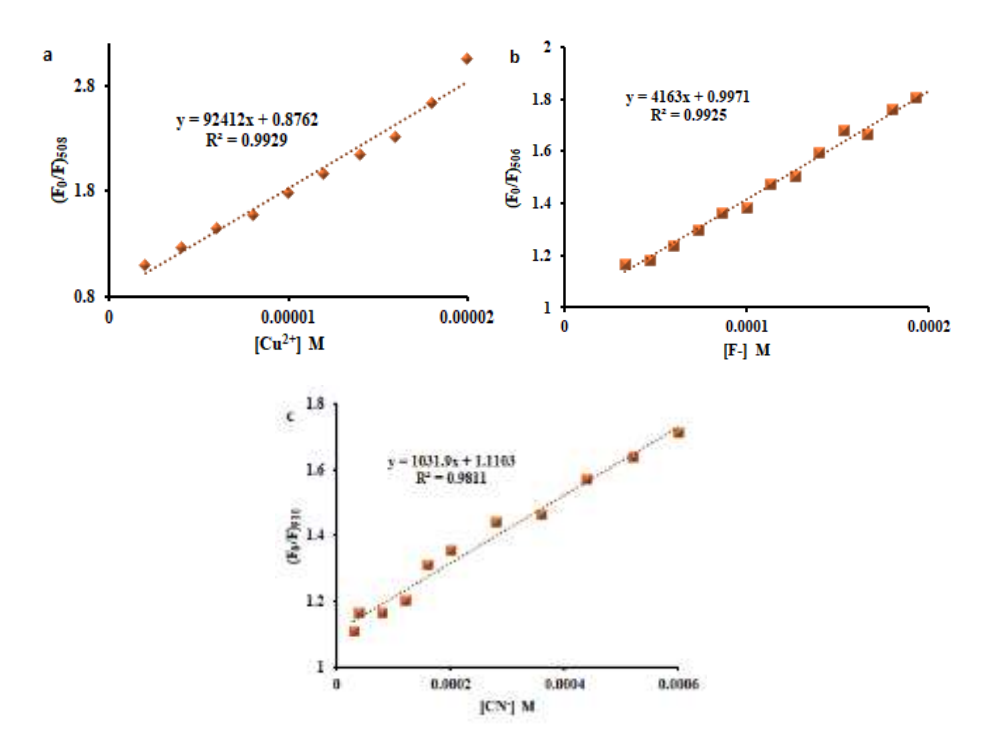


Figure 3.6: Stern-Volmer plot of plot 1 between a) $(F_0/F)_{508}$ v/s Cu^{2+} ions; b) $(F_0/F)_{506}$ v/s F^- ions and c) $(F_0/F)_{510}$ v/s CN^- ions

3.6. Time-Dependent Study

Further, the potential of probe 1 with ions at varying times has been recorded for investigating their role in sensing. The time dependence study of the free probe 1 as well as ion bound was analyzed using the absorption spectra, which remain unaffected after prolonged standing. This implies the strong and stable interactions between the ligands and their ion complexes (Figure 3.7).

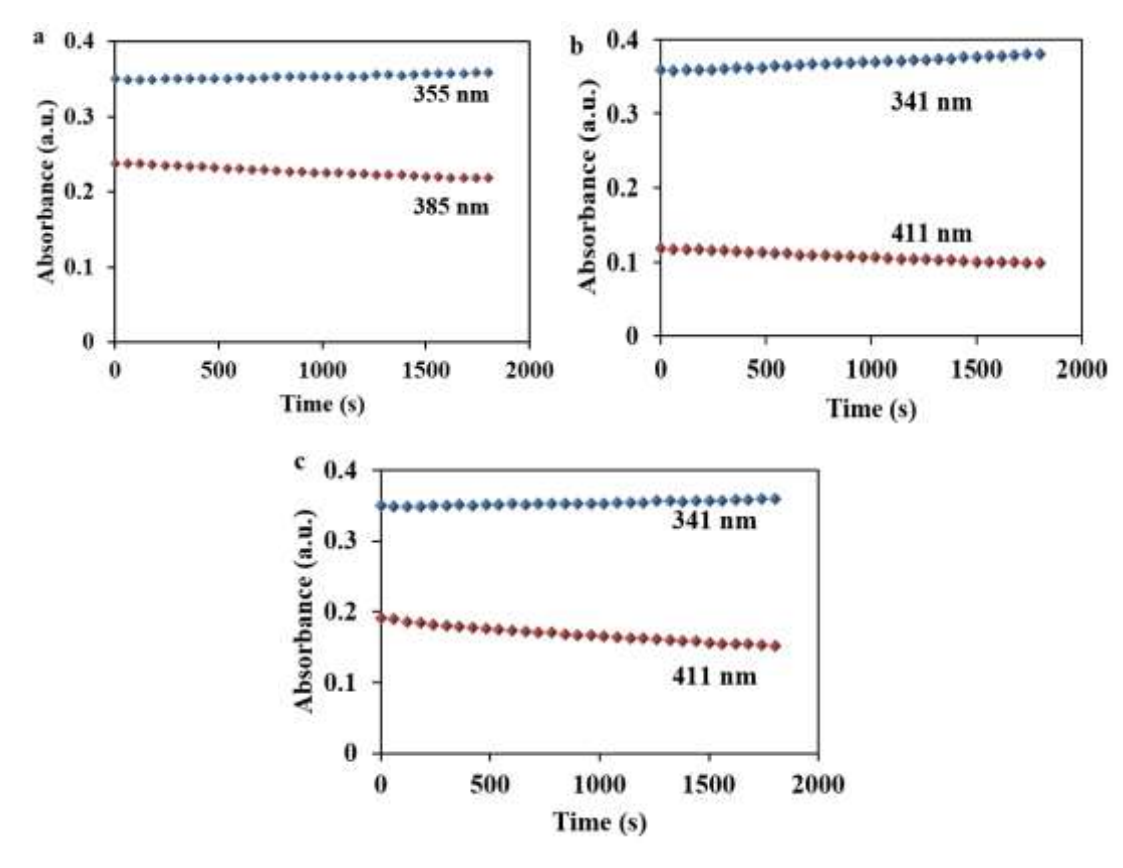


Figure 3.7: Time course study of complexes a) probe 1 + Cu²⁺; b) probe 1 + F⁻ and c) probe 1 + CN⁻

3.7. Binding Mechanism of Probe 1 with Ions

3.7.1. Job's plot and ATR-FTIR analysis

The stoichiometric ratio was calculated by Job's plot between probe 1 and Cu^{2+} , F, and CN^{-} ions. Probe 1 and the ions were taken in equimolar concentration (20 μ M), and the stochiometric calculations were performed. **Figure 3.8** shows that the absorbance value reached a maximum as the concentration ([C]/[C+M]) was 0.5. It was found that the stochiometric ratio was 1:1

between probe 1 and Cu²⁺, F⁻, and CN⁻ ions, respectively. In addition, the plausible mechanism of

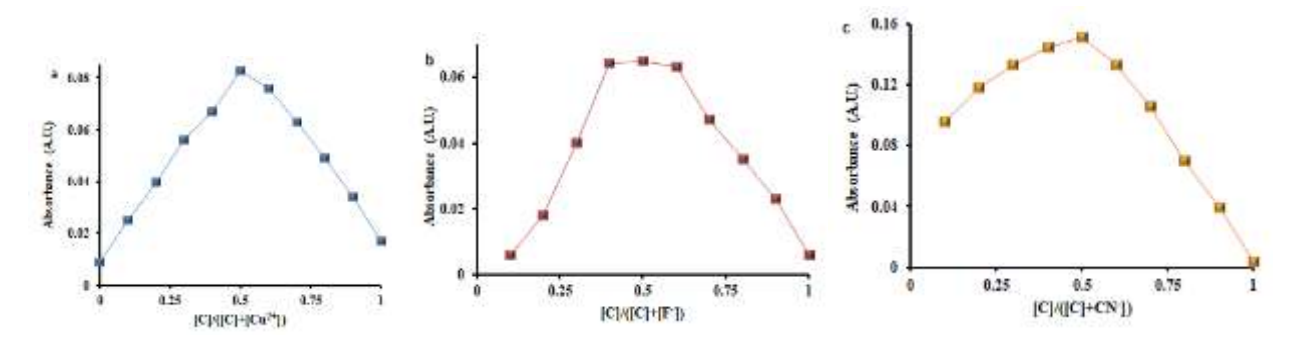


Figure 3.8: Job's plot analysis of probe 1 with a) Cu²⁺ ions; b) F⁻ ions, and c) CN⁻ ions.

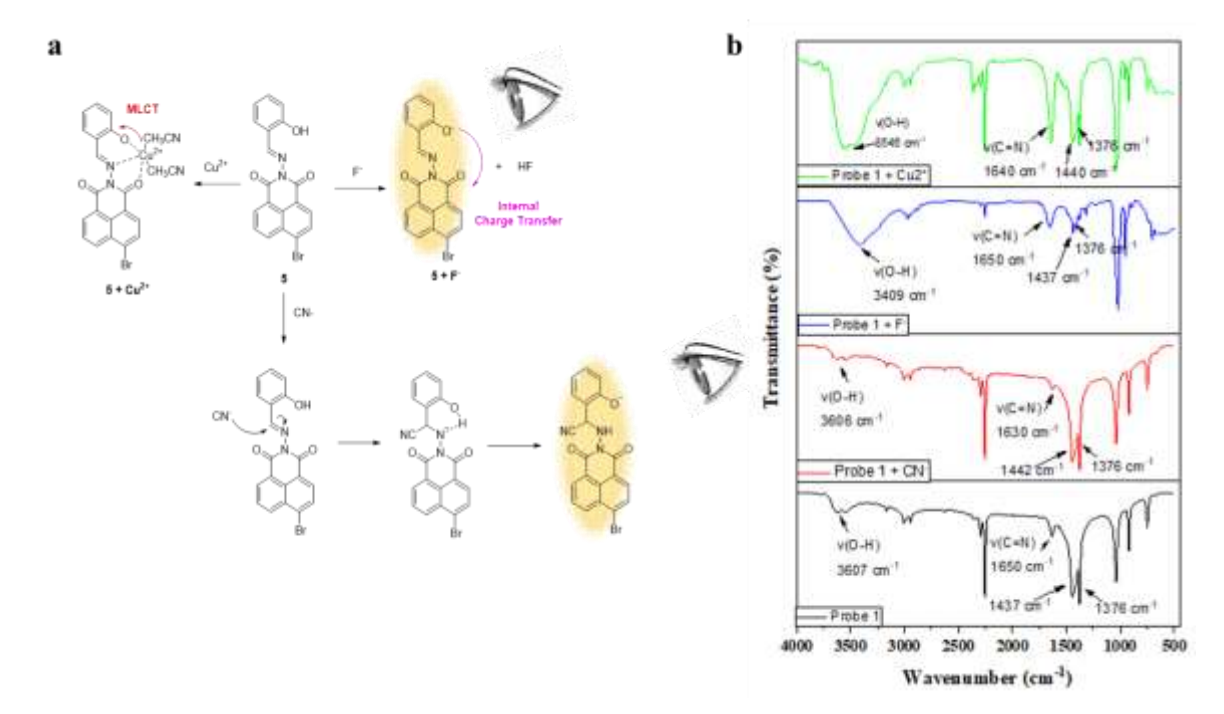


Figure 3.9: a) Proposed binding mechanism of Cu^{2+} , CN^- and F^- ions with ligand **5;** b) ATR-FTIR spectrum of probe **1**, probe **1** + Cu^{2+} , probe **1** + F^- , and probe **1** + CN^- ions

binding is explained in **Figure 3.9a**, which unfolds the binding mechanism of Cu^{2+} ions with the N atom of the C=N group, the O atom of the OH group, and the O atom of the -N=O group of the probe **1**. Further, we speculated that in the addition of F^- , the F^- binds with the probe **1** *via*. H-bonding while deprotonation of OH group takes place in the presence of CN^- ions. Further to support the binding mechanism, the IR spectra of probe **1**, probe **1**- Cu^{2+} , probe **1**-CN, and probe **1**-F complexes were studied. The peak at 1632 cm⁻¹ exhibits the v(C=N) group in the free ligand, and the peaks in the region of 3200-3500 cm⁻¹ exhibit v(-OH) group. In the presence of Cu^{2+} ions, the shift in the frequency of C=N was observed along with a decrease in the stretching and bending

frequency of the OH group at 3607 cm⁻¹ and 1440 cm⁻¹, which shows a slight shift to lower wavenumber. This could be attributed to decrease in the strength of the OH bond on binding with Cu²⁺ ions. Further, on the addition of CN⁻ ions, a decrease in the intensity of the OH band at 3606 cm⁻¹ with a slight shift in the bending frequency. Also, the wavenumber of the C=N group decreases and exhibits a slight shift to 1630 cm⁻¹. However, in the presence of F⁻ ions, a prominent broad peak at 3049 cm⁻¹ indicates coordination of F⁻ ions with the OH group of the ligand *via*. H-bonding is accompanied by a shift to a lower frequency in comparison to the free ligand. This could be attributed to the weakening of the OH bond, which shifts it to a lower wavelength. In addition, the peaks near the region at 2900-3000 cm⁻¹ represent the C-H stretch (**Figure 3.9b**). Further, the binding was validated by the TD-DFT studies.

3.7.2. ¹H-NMR titrations and HR-MS analysis

Further, the ¹H-NMR titrations were performed to study the interaction of probe **1** with CN⁻ and F⁻ ions. The ¹H-NMR study revealed a clear peak of O-H proton at 10.90 δ in the ligand, while **H**-C=N peak was observed at 9.00 δ . On addition of F⁻ (1 equv.), the O-H peak (10.90 δ) completely disappeared, confirming the abstraction of a proton from the O-H group. In addition, most of the aromatic protons of the benzene ring also shifted upfield, which suggests that the negative charge originating from the deprotonation of the O-H group might be delocalized on the whole moiety. Further, an additional peak at 16.00 δ appeared, indicating the formation of [HF₂-] species ¹⁰². On the other hand, the addition of CN⁻ ions revealed the shift in the **H**-C=N peak from 9.00 δ to 8.82 δ , revealing the nucleophilic addition of CN⁻ across the C=N bond. In addition, intramolecular proton transfer occurs from the OH group to the N atom of the C=N group, resulting in the disappearance of the O-H peak at 10.90 δ as depicted in **Figure 3.10**. The upfield shift of aromatic protons (h-k) could be due to the delocalization of the electron on the benzene ring resulting from the intramolecular proton transfer.

3.8. Theoretical Studies

The geometry of probe 1, probe $1 + Cu^{2+}$, probe $1 + F^-$, and probe $1 + CN^-$ were optimized and vertical excitations were calculated using the TD-DFT method (**Figure 3.11**). Due to the presence of single bond rotation at the C-N bond, **5** was optimized in two configurations and each configuration has similar energies. Further, three low-lying vertical excitations were calculated at 396 nm (f = 0.0035), 353 nm (f = 0.4424), and 339 nm (f = 0.0039) for $S_0 \rightarrow S_1$, $S_0 \rightarrow S_2$, and $S_0 \rightarrow S_3$,

respectively. Among these transitions, only the $S_0 \rightarrow S_2$ transition has significant oscillation strength and is therefore discussed further, and this consideration was also incorporated with excitation of probe $1 + Cu^{2+}$, probe $1 + F^-$, and probe $1 + CN^-$. $S_0 \rightarrow S_2$ transition involved the transition from HOMO-1 \rightarrow LUMO with a contribution of 96 %. The electron density distribution showed that the electron density shift from the bromine atom to the naphthalimide unit infers $n-\pi^*$ electronic transition (Figure 3.11a). Further, the vertical excitation corresponds to S_0 state geometry probe $1 + Cu^{2+}$ displayed an excitation peak at 391 nm corresponding to $S_0 \rightarrow S_{14}$ transition from single occupied molecular orbital (SOMO) to single unoccupied molecular orbital (SUMO) +1 and SUMO + 2. The electronic distribution demonstrated the electron density shift from the metal center to the Schiff base unit and therefore demonstrated metal-to-ligand charge

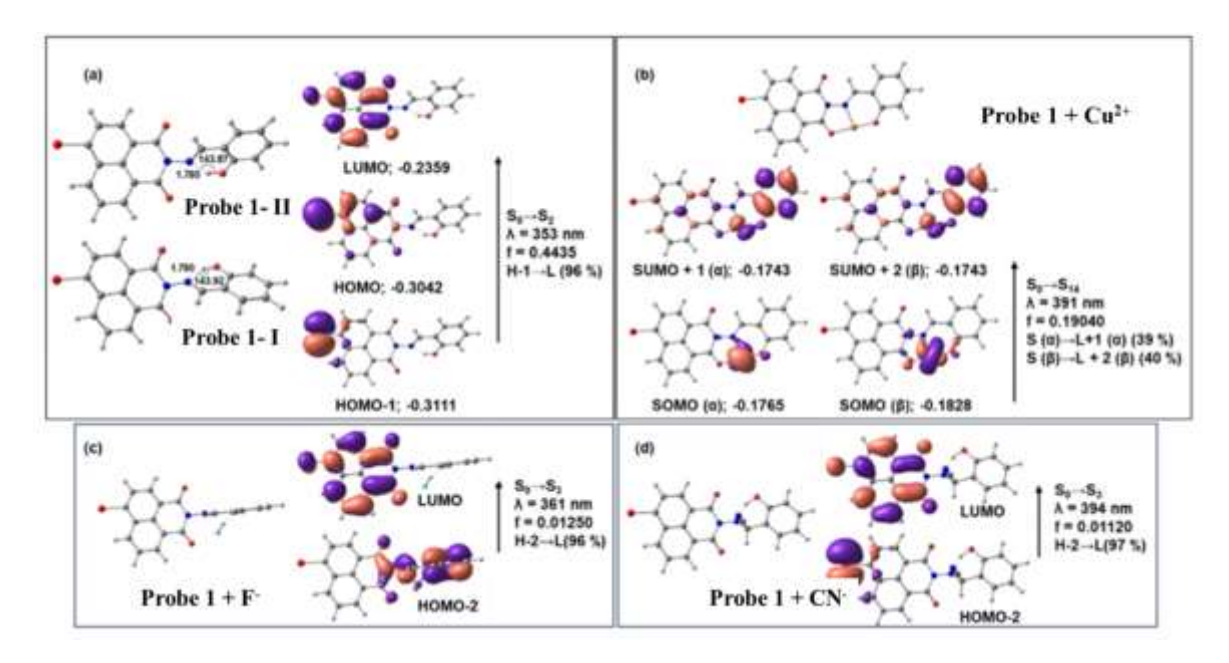


Figure 3.11: Optimized structure of probe 1, probe $1 + Cu^{2+}$, probe $1 + F^-$ and probe $1 + CN^-$ along frontier molecular orbitals

transfer (**Figure 3.11b**). Similarly, the three low-lying vertical excitations were calculated corresponding to the S0 optimized structure of probe $1 + F^-$ and probe $1 + CN^-$. For probe $1 + F^-$, $S_0 \rightarrow S_1$, $S_0 \rightarrow S_2$ and $S_0 \rightarrow S_3$ were calculated at 612 nm (f = 0.00040), 418 nm (f = 0.00570) and 361 nm (f = 0.01250), respectively. The molecular orbital involved in $S_0 \rightarrow S_3$ showed an electron density shift from Schiff base unit to the naphthalimide unit, inferring the ICT (Error! Reference source not found.**3.11c**). For $5.CN^-$, $S_0 \rightarrow S_1$, $S_0 \rightarrow S_2$, and $S_0 \rightarrow S_3$ were calculated at 692 nm (f = 0.00640), 456 nm (f = 0.00060) and 394 nm (f = 0.01120), respectively The molecular orbital

involved in $S_0 \rightarrow S_3$ showed electron density shift from bromine atom to naphthalimide unit inferring the $n-\pi^*$ transition (Figure 3.11d).

3.9. Test Strips Application

The practical applicability of probe **1** was evaluated by a test strip experiment. Initially, the test strips were allowed to be immersed in the solution of probe **1** and then kept for some time to evaporate the excess solvent. Further, the coated test strips were treated with the standard solution of Cu²⁺, CN⁻, and F⁻ ions (0.5 equv.) for an additional twenty minutes and then dried naturally. Subsequently, the test strips were observed under long UV rays, short UV rays, and visible light. The results revealed a "turn-off" response under long UV rays, while the short UV rays showed a yellow color (CN⁻ and F⁻) of strips. In addition, naked eye color change was vividly observed on treating the coated strips with CN⁻ and F⁻ ions, changing their color from colorless to light yellowish-brown (**Figure 3.12**). This indicated the practical relevance of test strips, which could be employed for the rapid analysis of ions using test strips.

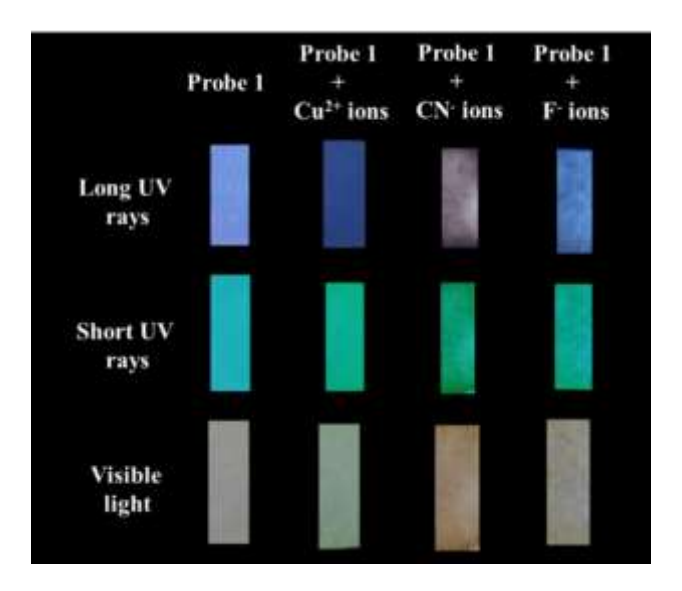


Figure 3.12: Detection of Cu²⁺, CN⁻ and F⁻ (0.5 equv.) on probe 1 coated test strips under UV lamp and visible light

3.10. Conclusion

In summary, a probe 1 with a naphthalimide core appended with a salicylaldehyde unit was synthesized, exhibiting a "turn-off" response towards Cu²⁺, F⁻, and CN⁻ ions in CH₃CN as the medium. The Job's plot studies revealed 1:1 stochiometric binding between the probe 1 and ions

with an association constant (K_a) of 5.83×10^4 , 1.24×10^4 , and 1.24×10^4 for Cu^{2+} , F^{-} , and CN^{-} ions, respectively. Further, the detection limit was found to be as low as 1.46×10^{-5} M, 1.07×10^{-6} M, and 0.99×10^{-6} M in the case of Cu^{2+} , F^{-} , and CN^{-} ions, respectively. In addition, the binding mechanism was proposed and was supported by the FT-IR spectrum and TD-DFT. The theoretical studies reveal metal-to-ligand charge transfer in the case of Cu^{2+} ions, while the ICT process was observed in the case of F^{-} and CN^{-} ions.

3.11. Synthetic Procedure for Probe 1

2.9.1. Synthesis of intermediate 2

To a solution of acenaphthene (1) (2.00 g, 12.9 mmol) and DMF (5 ml), N-bromosuccinimide (2.23 g, 12.5 mmol) was stirred at room temperature for 3 h. After the completion of the reaction, the reaction mixture was poured into cold water to get solid. Then the solid was filtered and washed with water. A light brown crystal of 4-bromoacenaphthene (2) (Yield: 87%) was obtained 103.

2.9.2. Synthesis of intermediate 3

To the solution of **2** (1.50 g, 7.9 mmol) in acetic acid (20 ml), sodium dichromate (11.82 g, 39.6 mmol) was added while stirring at room temperature. The suspension was refluxed at 80°C for 6 h. After the completion of the reaction, the reaction mixture was added to cold water to get solid. Then the solid was filtered and washed with water. A white product of 4-bromo-1,8-naphthalic anhydride (3) (Yield: 77%) was obtained ¹⁰³.

2.9.3. Synthesis of intermediate 4

To the solution of intermediate 3 (1.00 g, 3.6 mmol) in ethanol (10 ml), hydrazine hydrate (0.11 g, 3.8 mmol) was added and refluxed for 3 h. The reaction mixture was cooled and the solid obtained was filtered and recrystallized from ethanol to produce yellow solid precipitates (Yield: 84%)¹⁰⁴.

2.9.4. Synthesis of probe 1

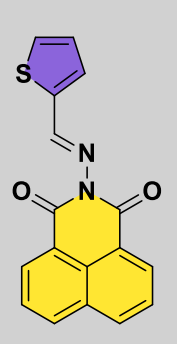
To the solution of intermediate **4** (0.50 g, 1.7 mmol) in absolute ethanol (50 ml), salicylaldehyde (0.18 g, 2.0 mmol) was added with a few drops of acetic acid. The reaction was then allowed to reflux for 10 h. The reaction was monitored with TLC. After the completion of the reaction, the reaction mixture was allowed to cool at room temperature, filtered, and washed with ethanol. The precipitates obtained were then recrystallized in ethanol. The dusty brown precipitates of probe **1** were obtained. Dustry brown solid, 73% yield; R_f 0.45 (20% ethylacetate in hexane); mp 250-265°C; ¹H-NMR (DMSO- d_6 , 500 MHz): δ (ppm) 10.95 (s, 1H, OH), 9.00 (s, 1H, CH), 8.62 (m,

2H, ArH), 8.39 (d, J=10 Hz, 2H, ArH), 8.27 (d, J=10 Hz, 1H, ArH), 8.05 (t, J=10 Hz 1H, ArH), 7.85 (m, 1H, ArH), 7.00 (m, 2H, ArH), 13 C-NMR (DMSO- d_6 , 125 MHz): δ (ppm) 170.45, 160.51, 159.32, 134.76, 133. 29, 132.41, 131.98, 131.76, 130.39, 129.93, 129.42, 128.33, 123.63, 122.89, 120.10, 118.37, 117.26, 115.00; M/z ratio: Calculated- 394.01, Found- 395.00 (Figure A1-A3).

CHAPTER - 4

Synthesis and photophysical study of Naphthalimide appended Thiophene-2-carboxaldehye (Probe 2)

This chapter deals with the synthesis of naphthalimide-based Schiff base to detect Cu^{2+} ions in MeOH: H_2O (9:1, v/v) as a solvent medium. The optical performance of probe **2** was determined by UV-visible and fluorescence spectroscopic techniques. The DFT studies revealed a charge transfer from the thiophene ring towards the naphthalimide moiety, which was significantly inhibited in the presence of Cu^{2+} ions, thereby revealing a "turn-off" response.



Photochemical & Photobiological Sciences https://doi.org/10.1007/s43630-025-00738-3

ORIGINAL PAPERS



A fluorescent "turn-off" naphthalimide-derived Schiff base for sensing Cu²⁺ ions: experimental and computational approach

Gurdeep Kaur¹ - Igubal Singh² - Gulshan Kumar³

Abstract

A naphthalimide-based Schiff base (probe 1) was synthesized for the selective detection of Cu^{2+} ions in a MeOH: H_2O (9:1, v/v) solvent system. The optical properties of the probe were investigated using UV-visible and fluorescence spectroscopy. In the UV-visible spectrum, probe 1 displayed absorption bands at 260 nm and 330 nm. Fluorescence measurements revealed an emission peak at 445 nm, accompanied by a shoulder at 470 nm. Upon the addition of Cu^{2+} ions, a significant quenching of the fluorescence intensity was observed, whereas other metal ions showed negligible interference. Quantitative analysis revealed a limit of detection (LOD) of 1.22×10^{-5} M and a limit of quantification (LOQ) of 4.08×10^{-5} M for Cu^{2+} . The association constant was calculated from the B-H plot which was determined to be 1.43×10^{2} M $^{-1}$ with the quenching constant of 1.99×10^{2} M calculated from the Stern–Volmer plot. Also, the binding stoichiometry of 2:1 was determined by Job's plot between the probe 1 and Cu^{2+} ions, respectively. Further, the results were validated by HR-MS, DLS, and computational studies. The DFT studies revealed a charge transfer from the thiophene ring towards the naphthalimide moiety which was significantly inhibited in the presence of Cu^{2+} ions.

4.1. Introduction

A chemosensor typically includes a receptor unit that modifies chemical signals from the target analyte and converts them into electrical signals ¹⁰⁵. These devices are cost-effective, user-friendly, and designed to provide accurate electrical responses at specific analyte concentrations. Recent advancements in the synthesis of 1,8-naphthalimide have further enhanced its application in developing fluorescent probes for ion detection across diverse environments, including biological systems. Its structural versatility and effective fluorescence make it a valuable tool for sensitive and selective detection of metal ions¹⁰⁶. Copper is a vital metal ion, that plays essential roles in various biological processes across living organisms, including bacteria, fungi, plants, and animals¹⁰⁷. In humans, copper is crucial for blood clotting, hormone maturation, cellular energy processing, red blood cell formation, and bone health 108-110. It also functions as an oxidant, protecting cells from oxidative damage caused by free radicals. Moreover, copper contributes to brain energy production and neurotransmitter regulation, influencing cognitive function and neurological health¹¹¹⁻¹¹³. In agriculture, copper is utilized as a fungicide and for microbial control; however, its excessive application can lead to environmental toxicity¹¹⁴, impacting aquatic life¹¹⁵ and causing soil contamination. While Cu²⁺ ions are necessary for human health, excessive exposure can result in toxicity and worsening genetic disorders like Wilson's disease^{112, 116}. The WHO sets the limit for copper in drinking water at 2 mg/L. Unfortunately, actual human exposure often exceeds these levels. Therefore, the development of sensors to detect harmful metal ions and other biologically significant molecules is essential for ensuring safety and health. So, sensors must identify these harmful metal ions and other biologically significant molecules.

Herein, we report the naphthalimide-derived Schiff base for the selective detection of Cu²⁺ ions. Probe **2** displays fluorescence quenching in the presence of Cu²⁺ ions, while other ions do not display any significant effect. The binding ratio was found to be 2:1 between probe **2** and Cu²⁺ ions as determined by the Job's plot, which was further supported by the HR-MS and DLS studies. Also, theoretical DFT studies were done to determine the ICT process and the overlap integral for the hole electron distribution. Further, the natural transition orbitals analysis revealed that there is an electron density shift from the thiophene to the naphthalimide unit, therefore inferring ICT.

4.2. Synthesis of Probe 2

The synthesis of (*E*)-2-((thiophen-2-ylmethylene)amino)-1*H*-benzo[*de*]isoquinoline-1,3(2*H*)-dione (probe **2**) proceeds through the following steps. Initially, compound **1** was treated with sodium dichromate in acetic acid under reflux conditions for 7 hours, yielding compound **2**. This intermediate was then reacted with hydrazine hydrate in ethanol at reflux temperature for 7 hours to produce compound **3**. Subsequently, compound **3** was condensed with 2-thiophene carboxaldehyde in ethanol, with a few drops of acetic acid as a catalyst, under reflux conditions to yield probe **2** (**Scheme 4.1**). The reaction mixture was then allowed to cool to room temperature, followed by recrystallization in ethanol. The resulting product was filtered and dried, affording shiny brown crystals of probe **2**. The structure was confirmed by ¹H-NMR, ¹³C-NMR, and mass spectrometry, supporting the successful formation of the expected probe **2**.

Scheme 4.1: Synthesis pathway of probe 2

4.3. Photophysical Properties of Probe 2

The photophysical analysis of probe **2** was investigated through absorption and emission spectroscopic techniques. The absorption and emission of probe **2** was studied in different mediums with increasing polarity *i.e.* THF (f = 0.207), chloroform (f = 0.259), ethyl acetate (f = 0.228), DMF (f = 0.386), DMSO (f = 0.444) acetonitrile (f = 0.460), methanol (f = 0.762), and distilled water (f = 1.000) (**Figures 4.1a and 4.1b**). The absorption bands of **2** revealed a bathochromic shift of 10 nm with an increase in the polarity of the medium, revealing more polarization of the excited state in comparison to the ground state. It may also be associated with the prevalence of the ICT phenomenon in probe **2** as a donor-acceptor (D-A) system. Also, various water fractions (f_w) from 0-100% in combination with DMSO were explored to study the aggregation-induced emission (AIE). The absorption spectra showed no significant changes with increasing water content, revealing the absence of an AIE effect. However, quenching in the

emission spectrum was observed, which could be attributed to π - π stacking interactions as the water fraction increased, since water is a poor solvent (**Figures 4.1c and 4.1d**). Further, the absorption spectra of probe **2** in MeOH: H₂O (9:1, v/v) revealed bands at 260 nm and 330 nm, which could be attributed to n- π * and π - π * transitions, respectively. On photoexcitation at 330 nm, an emission band at 445 nm was noticed, accompanied by a shoulder peak at 470 nm with a Stokes shift of 115 nm. On further increasing the f_w beyond 20%, probe **2** started precipitating, making it unsuitable for exploring the selectivity study towards various ions.

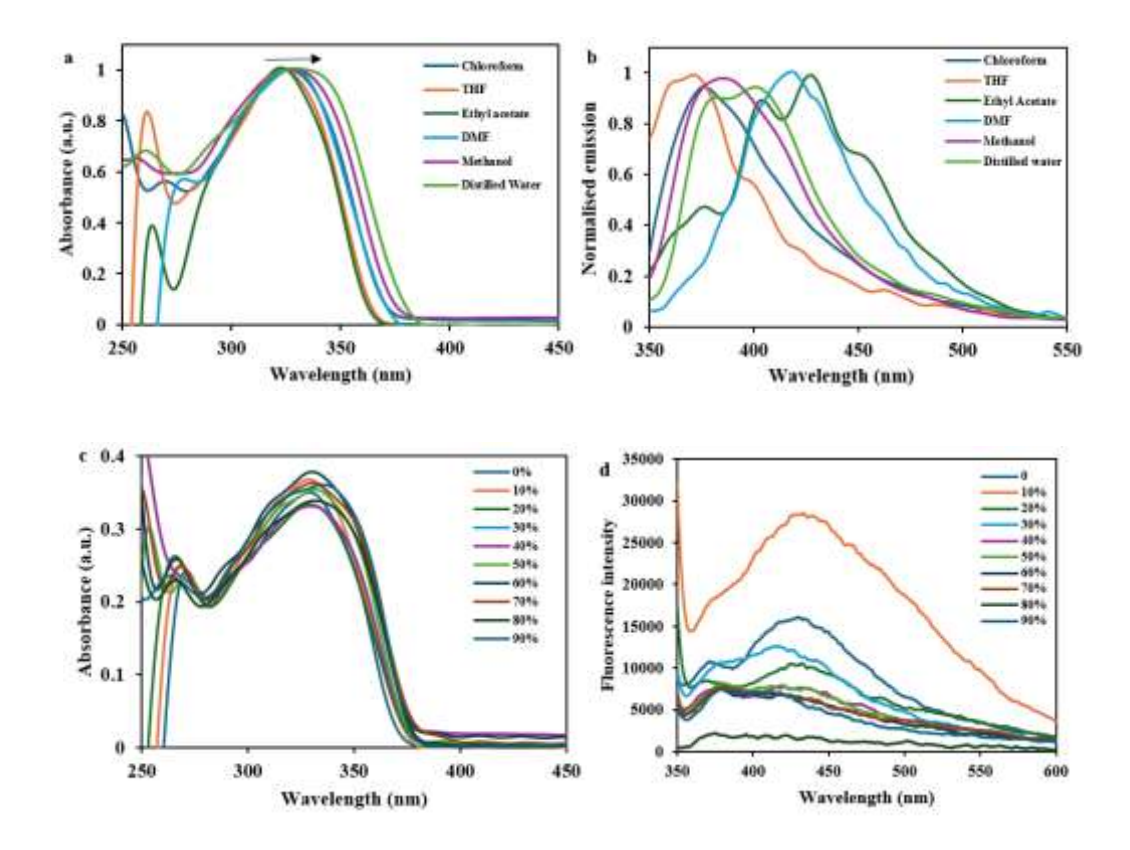


Figure 4.1: Solvatochromic effect of probe 2 in different solvents: a) absorption study and b) fluorescent study; c) UV-Visible study and d) fluorescent study of probe 2 for AIE characteristics

4.4. Spectroscopic Analysis of Probe 2

The spectroscopic analysis of probe **2** (20 μ M) was investigated by UV-visible studies in MeOH: H₂O (9:1, v/v) as the solvent medium. The selectivity of the probe was determined in the presence of different ions *viz*. Al³⁺, Mn²⁺, Pb²⁺, Cu²⁺, Fe³⁺, Hg²⁺, Zn²⁺, Cs²⁺, Ni²⁺, Co²⁺ and Cd²⁺ (10 equv.). It was found that probe **2** revealed perturbations in the region between 250 – 330 nm on the addition of Cu²⁺ ions, while other ions didn't reveal any change (**Figure 4.2a and 4.2b**). Further, for the

quantitative estimation, the titration experiments of probe 2 (20 μ M) were performed with Cu²⁺ ions in UV-visible absorption spectroscopy. On incremental addition of Cu²⁺ ions (0-80 μ M), the absorption intensity increased gradually at 260 nm while a slight increment at 330 nm was observed (Figure 4.2c).

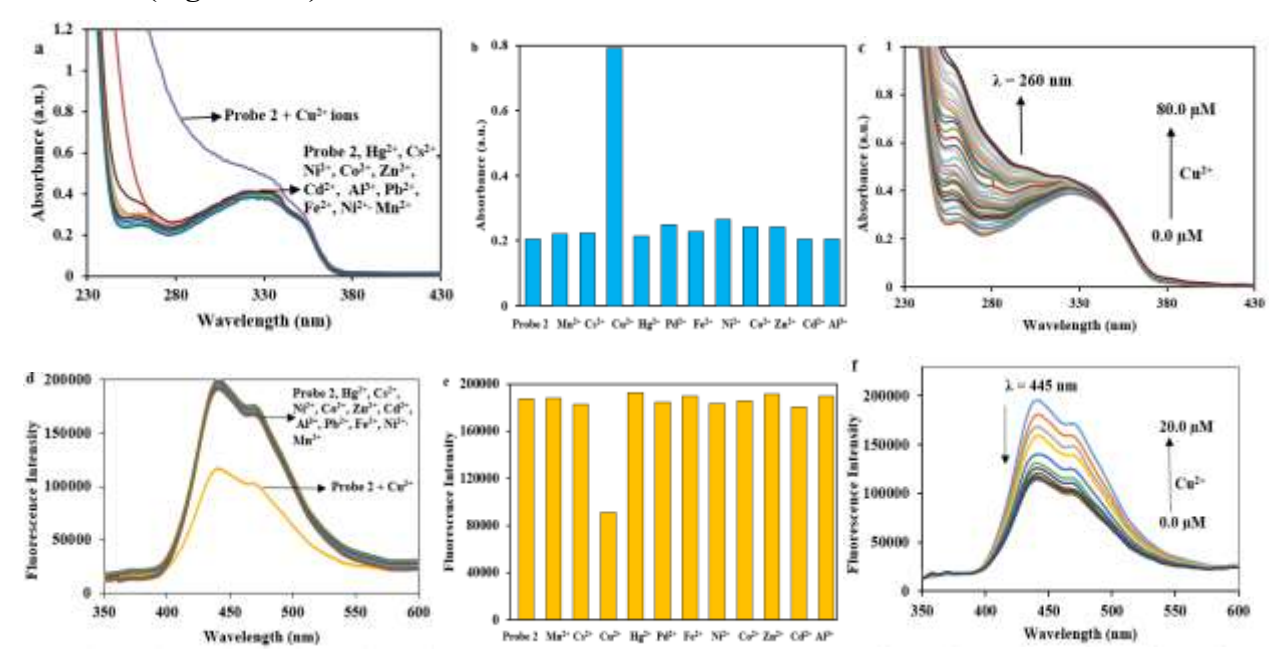


Figure 4.2: a) UV-visible spectrum of probe **2** (20 μ M) in the presence and absence of different metal ions (10 equv.); b) Bar graph representation of absorbance of ions in the presence of probe **2**; c) UV-visible spectra of probe **2** (20 μ M) on incremental additions of Cu²⁺ ions; d) Fluorescence spectra of probe **2** (20 μ M) in the presence and absence of different metal ions (10 equv.); e) Bar graph representation of fluorescence of ions in the presence of probe **2**; d) Fluorescence spectra of probe **2** (20 μ M) on incremental additions of Cu²⁺ ions

In addition, the optical properties of probe 2 were explored with a fluorescence spectrophotometer. Probe 2 on excitation (λ_{ex}) at 330 nm reveals a peak at 445 nm with a shoulder peak at 470 nm with a moderate emission, which could be attributed to C=N isomerization. Furthermore, the addition of various metal ions (Al³⁺, Mn²⁺, Pb²⁺, Cu²⁺, Fe³⁺, Hg²⁺, Zn²⁺, Cs²⁺, Ni²⁺, Co²⁺, and Cd²⁺ (10 equv.)) showed no significant alterations, except in the presence of Cu²⁺ ions. Notably, Cu²⁺ induced fluorescence quenching, whereas other metal ions had no observable effect (**Figure 4.2d and 4.2e**). This quenching effect can be attributed to the paramagnetic nature of Cu²⁺ ions, which possess vacant *d* orbitals and effectively quench the fluorescence intensity of the neighboring fluorophore *via* electron transfer, thereby confirming the "turn-off" behavior of probe 2. The selectivity of probe 2 towards Cu²⁺ is likely due to the soft acidic nature and high

polarizability of copper ions. To gain deeper insight into these changes, titration experiments were conducted using a fluorescence spectrophotometer. With each successive addition of Cu^{2+} ions (0–20 μ M), the fluorescence intensity at 445 nm and 470 nm gradually decreased until saturation was reached (**Figure 4.2f**).

4.5. LOD, Association Constant (K_a), and Quenching Constant (K_{sv})

The quantitative estimations of probe 2 were conducted using the calibration plot shown in **Figure 4.3a** to determine various parameters. The limit of detection (LOD) was calculated using **equation 1**, yielding a value of 1.22×10^{-5} M. Additionally, the limit of quantification (LOQ) was determined from the fluorescence studies using **equation 2** and was found to be 4.08×10^{-5} M. The association constant (K_a) was calculated using a Benesi-Hildebrand plot (**equation 3**) of $1/(I-I_0)$ versus $1/[Cu^{2+}]$, resulting in a value of 1.43×10^2 M⁻¹ (**Figure 4.3b**). Moreover, the fluorescence studies showed quenching in the presence of Cu^{2+} ions, and the quenching constant (K_{SV}) was calculated using the Stern-Volmer **equation 4**, which gave a value of 1.99×10^2 M⁻¹ (**Figure 4.3c**).

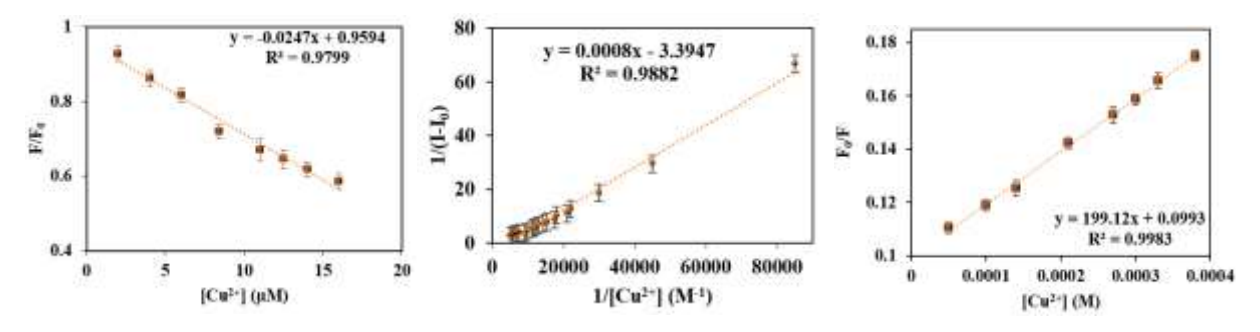


Figure 4.3: a) Linear plot for the determination of limit of detection (LOD) of probe **2** between F/F_o v/s $[Cu^{2+}]$; b) Benesi-Hilderbrand plot of probe **2** for the determination of association constant (K_a) ; c) Stern-Volmer plot of probe **2** for the calculation of quenching constant K_{SV}

4.6. Kinetic Assay and Effect of Environmental Factors on Probe 2

The responsiveness of probe 2 towards Cu^{2+} ions was studied in MeOH: H_2O (9:1, v/v) to explore the coordination ability of the probe towards metal ions. Upon the addition of Cu^{2+} ions (50 μ M) to probe 2 (20 μ M), the absorbance of the system increases as the complexation progresses and becomes stable gradually after some time at 260 nm, whereas no perturbation was observed at 330 nm (**Figure 4.4a**). Notably, the absorbance remains constant thereafter, indicating that the probe is stable enough to reliably detect Cu^{2+} ions. Additionally, the absorbance of probe 2 and its Cu^{2+}

complex was examined across a pH range of 2.0 to 12.0 to assess the probe's potential biological applicability. The pH of the study medium was adjusted with the subsequent addition of 0.1 M NaOH and 0.1 M HCl solutions, followed by the addition of probe 2 (20 µM). As shown in figure 4.4b, the free probe exhibits no change in absorbance spectrum during a wide range of pH from 2.0 to 12.0. Nevertheless, the absorbance of the probe increased in the pH range 3-5 and 9-12 after the addition of Cu²⁺ ions (5 equiv.) Additionally, the effect of other metal ions in the environment was investigated concerning the Cu²⁺ complex of probe 2. The presence of competing ions showed no significant interference with the Cu²⁺ ion complex, demonstrating the probe's sensitivity and selectivity towards Cu²⁺ ions (Figure 4.4c). Furthermore, Job's plot analysis was performed to determine the stoichiometric ratio of the complex, which was found to be 2:1 between probe 2 and Cu²⁺ ions, respectively (Figure 4.4d).

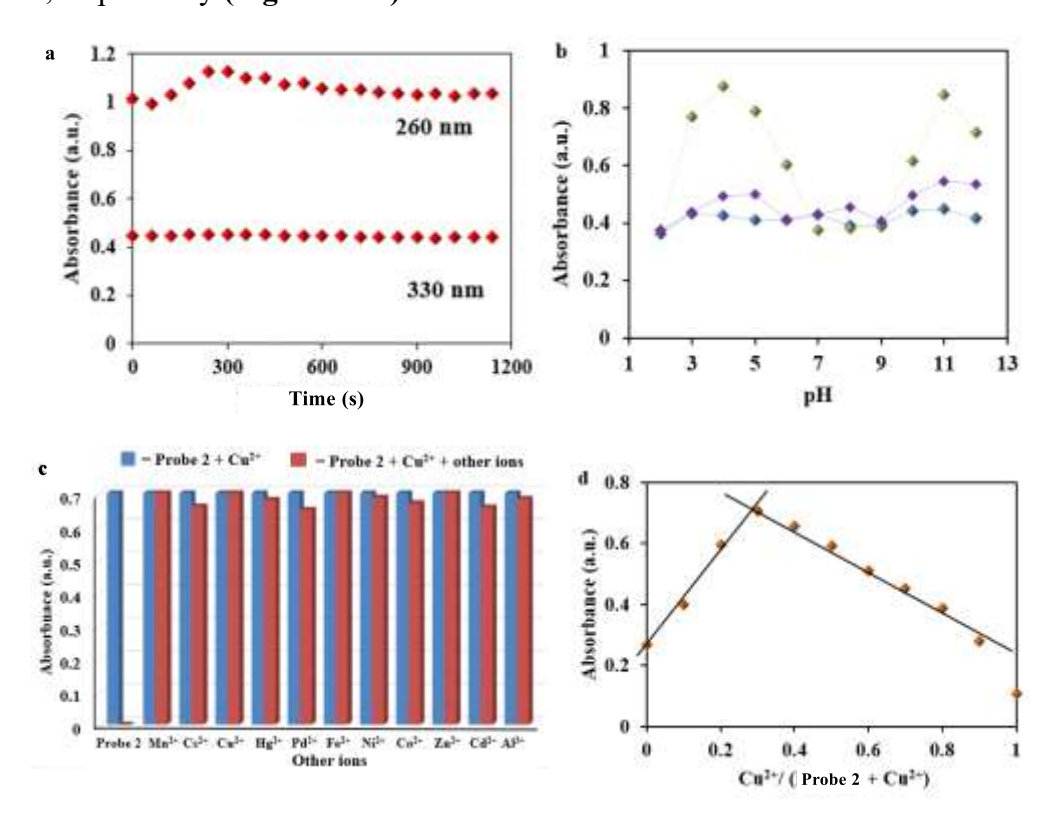


Figure 4.4: a) Time-dependent study of complex probe $2 + Cu^{2+}$ at 260 nm and 330 nm; b) pH study of ligand (blue line at 330 nm), complex probe $2 + Cu^{2+}$ [at 330 nm (green line) and at 260 nm (red line)]; c) Interference study of probe 2 (20µM) at 260 nm upon addition of Cu^{2+} ions (10 equv.) represented by blue bars and on the addition of other metal ions (50 equv.) represented by red bars in MeOH: H₂O (9:1, v/v); d) Job's plot for the determination of stochiometric ration between probe 2 and Cu^{2+}

4.7. Proposed Binding Mechanism of Probe 2

Job's plot analysis was performed to determine the stoichiometric ratio between Cu^{2+} ions and probe **2**, revealing a 1:2 binding ratio based on the absorption spectrum as shown in **Figure 4.5a**. To further confirm this interaction, mass spectrometry analysis was conducted. The mass spectrum exhibited a prominent peak at m/z 675.0240, corresponding to [Cu(probe **2**)₂ + H]⁺, indicating the formation of a 2:1 complex. Additionally, a peak at m/z 307.0561 was observed, corresponding to [probe **2** + H]⁺ for probe **2**, further supporting the complexation of Cu^{2+} with probe **2** (**Figure A4**). The complexation of probe **2** with Cu^{2+} ions was further supported by dynamic light scattering (DLS) measurements. The initial particle size of probe **2** was found to be in the range of 200-400 nm, with a polydispersity index (PDI) of 0.446. Upon the addition of Cu^{2+} ions, the particle size distribution shifted to 450-650 nm, with an increased PDI of 0.550, indicating aggregation or structural changes upon complexation. Additionally, zeta potential measures revealed values of -11.5 mV for probe **2** and -9.5 mV for the probe **2** + Cu^{2+} complex, suggesting a reduction in surface charge upon binding (**Figure 4.5b**).

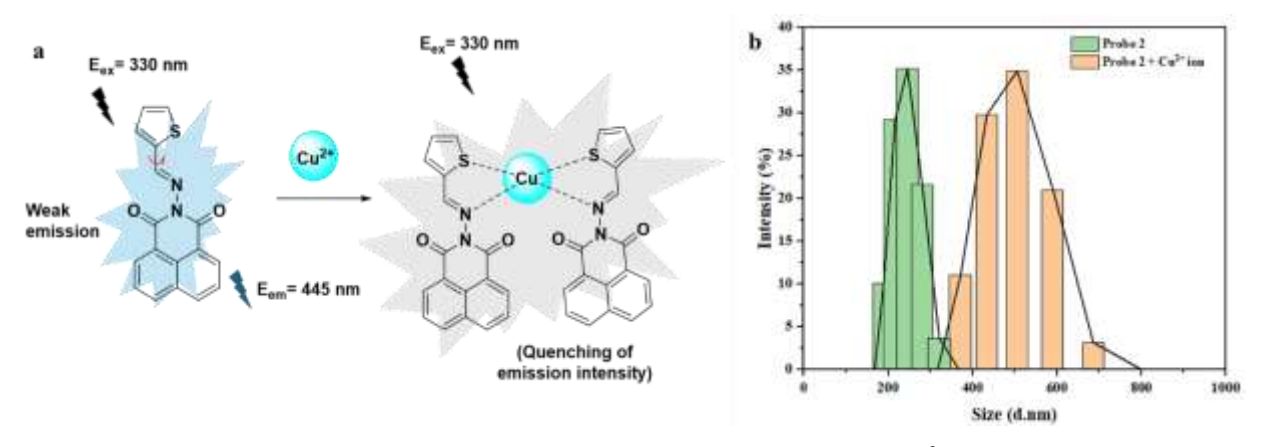


Figure 4.5: a) Plausible binding mechanism between probe **2** and probe **2**-Cu²⁺ complex; b) DLS study of probe **2** and probe **2**-Cu²⁺ complex

4.8. Reversibility Study

The reversibility of probe 2 was evaluated using EDTA. In the absence of Cu^{2+} ions, probe 2 exhibited a fluorescence emission band at 445 nm. Upon the addition of Cu^{2+} , a significant decrease in fluorescence intensity was observed, indicating fluorescence quenching. However, the addition of 20 μ L of 0.1 M EDTA to the probe 2- Cu^{2+} complex resulted in the recovery of fluorescence intensity, confirming the reversibility of the interaction between probe 2 and Cu^{2+}

ions. (**Figure 4.6**). The fluorescence quenching in the presence of Cu²⁺ ions and the subsequent restoration of the original emission intensity at 445 nm upon the addition of EDTA suggest that EDTA effectively reverses the interaction. To further validate this reversibility, multiple cycles of sequential Cu²⁺ and EDTA additions were performed. Each cycle exhibited consistent fluorescence intensity changes, confirming that EDTA serves as an effective chelating agent capable of reversing the interaction between probe **2** and Cu²⁺ ions.

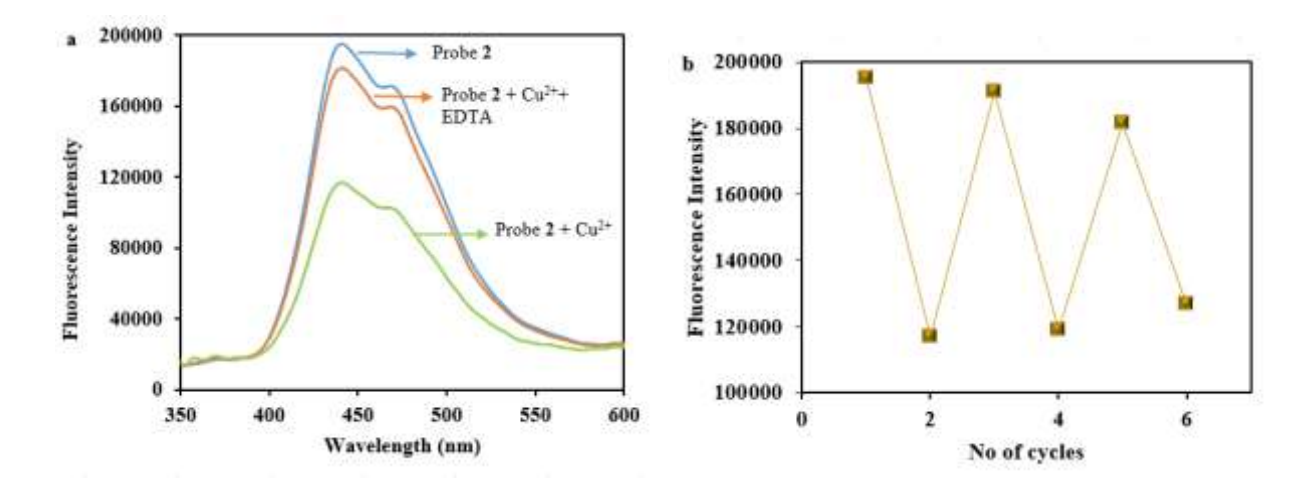


Figure 4.6: a) Reverse reaction of probe **2** (20 μ M) in MeOH: H₂O (9:1, v/v) in the presence of Cu²⁺ ion (20 μ l) and EDTA (20 μ l); b) reversible emission signal at 445 nm of on repetitive addition of Cu²⁺ ion and EDTA.

4.9. Computational Study

The geometry of probe 2 was optimized, and vertical excitations were calculated corresponding to the ground state geometry using the TD-DFT method (**Figure 4.7a**). Further, a similar observation was made. $S_0 \rightarrow S_1$, $S_0 \rightarrow S_2$, and $S_0 \rightarrow S_3$ were calculated at 336 nm (f = 0.3367), 336 nm (f = 0.0014), and 326 nm (f = 0.0003), respectively, for probe 2, in that order. The HOMO \rightarrow LUMO transition contributed 97 % to $S_0 \rightarrow S_1$ excitation, which demonstrated an electron density shift from the thiophene unit to the naphthalimide unit. Additionally, a low overlap integral ($S_T = 0.18775$) of the hole/electron distribution and a large distance of the electron/hole centroid (D = 7.201 Å) were shown by the quantitative hole-electron analysis, indicating an ICT process for probe 2. It is also noteworthy that probe 2 has a large hole/electron centroid distance and low hole/electron overlap value, therefore probe 2 relatively shows a high value of ICT.

Further, the geometries of probe $2 + Cu^{2+}$ complexes were optimized, and several vertical excitations were calculated (**Figure 4.7b**). However, we discussed only the transitions that have significant oscillation strength. For probe $2 + Cu^{2+}$ complex, the excitation values at 375.88 nm (f = 0.2267), 361.19 nm (f = 0.2056), and 346.83 nm (f = 0.3989) were calculated for $S_0 \rightarrow S_{32}$, $S_0 \rightarrow S_{35}$, and $S_0 \rightarrow S_{40}$, transitions, respectively. All these transitions have contributions from several orbital transition, and therefore, natural transition orbitals were calculated and analyzed. The natural transition orbitals analysis revealed that there is an electron density shift from the thiophene to the naphthalimide unit, thus inferring ICT.

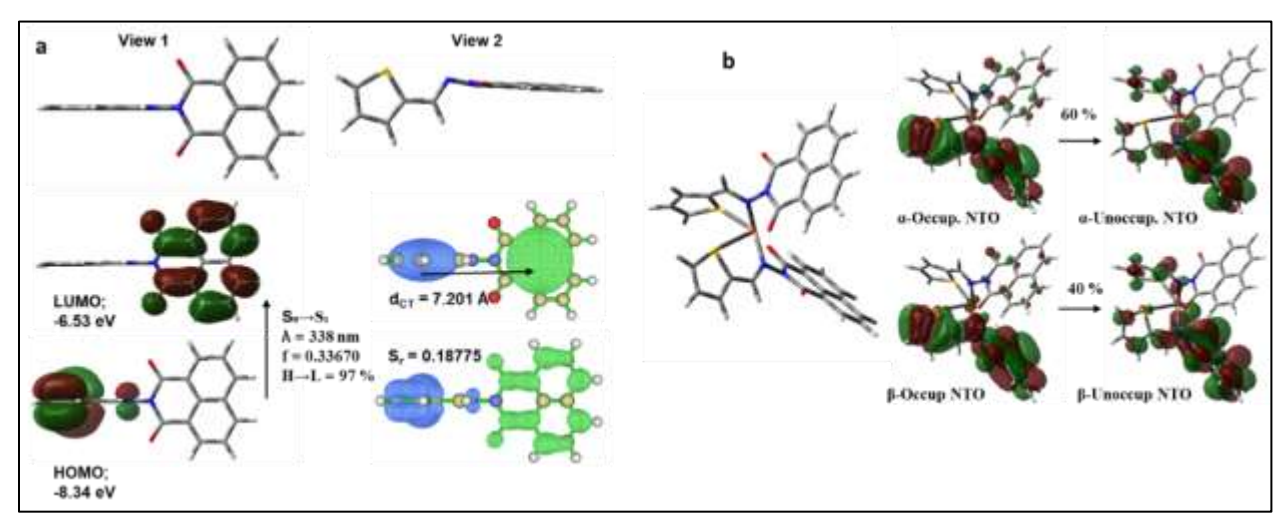


Figure 4.7: Optimized structures and Frontier Molecular Orbitals of a) probe **2** and b) probe **2** + Cu²⁺ complex calculated by DFT study

4.10. Logic Gate

In recent years, logic gates have gained a lot of attention from researchers. Therefore, we also built a combinatorial molecular circuit comprising NOT and NAND logic gates, which could be attributed to the reverse reactions of probe **2** complex in the presence of EDTA. The logic circuit diagram, along with its corresponding truth table, is illustrated in **Figure 4.8**. The addition of Cu²⁺ ions to the system leads to input I, while the addition of EDTA leads to input II. The output signals at 445 nm were obtained through fluorescence signals. The binary codes '0' and '1' illustrate the intensity shift as input or output. For probe **2**, the absorbance threshold was determined to be 12000. The ON-OFF switch correlates to the binary codes. In the non-availability of Cu²⁺ ion and EDTA in the system, *i.e.* no input I and input II, there is emission at 445 nm, which turns "ON" the system. On the other hand, in the presence of Cu²⁺ ion, when input I is 1 and input II is 0, there

is intensity at 445 nm quenched, which switches "OFF" the system, thereby exhibiting interaction between probe **2** and Cu²⁺ ion. An output signal 0 at 445 nm indicates that the system is turned "OFF" while there is no input (0,0) or only one input II there (0,1). The system turns "OFF" in the presence of input I (1,0), while in the presence of both the input (1,1), it further switches "ON". As a result, NOT and NAND logic operations for probe **2** were successfully demonstrated, highlighting its potential application in molecular devices. These operations showcase the ability of probe **2** to function as a molecular switch, effectively responding to the presence of the Cu²⁺ ion and enabling the manipulation of the output signals based on input signals. This capability underscores the versatility of the probe in the development of advanced molecular systems, paving the way for innovative applications in sensing and information processing.

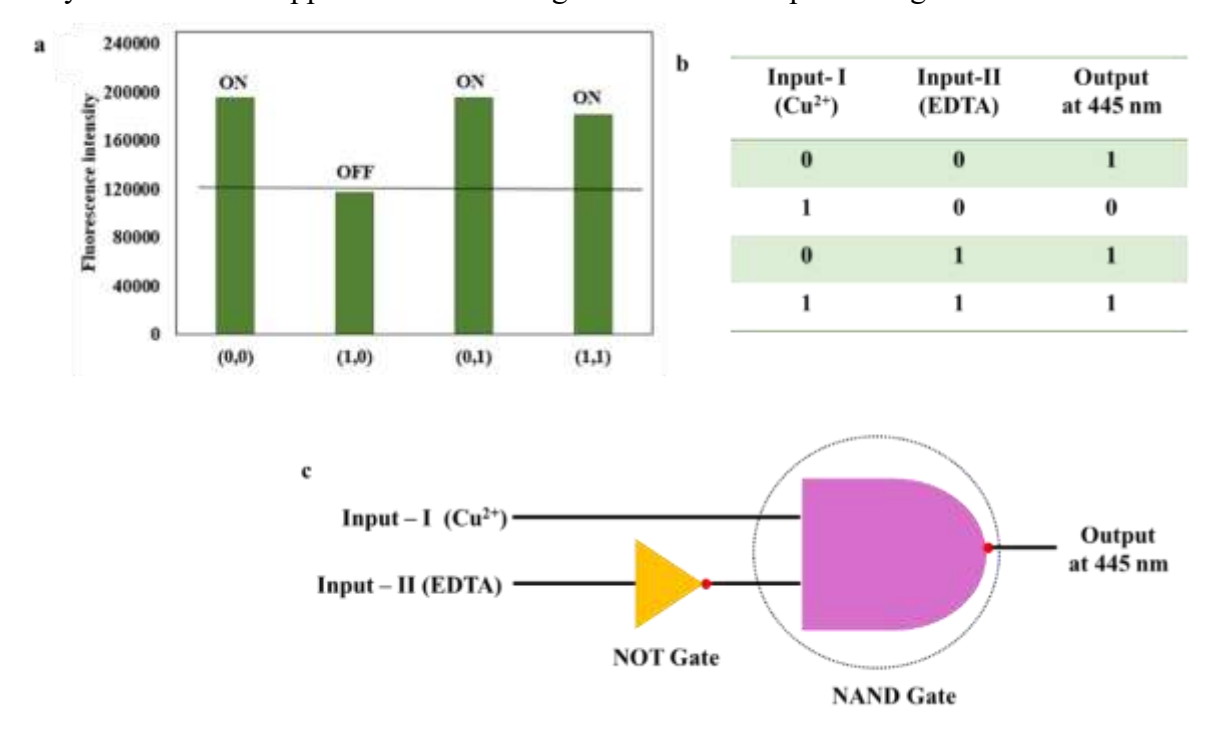


Figure 4.8: Logic gate construction of probe 2 a) absorbance output signals after various chemical inputs; b) truth table; c) logic gate circuit diagram

4.11. Conclusion

A naphthalimide-based Schiff base was synthesized for the selective detection of Cu²⁺ ions. Probe **2** revealed emission at 445 and 470 nm on excitation at 330 nm. The fluorescence quenching was observed in the presence of the Cu²⁺ ions while no perturbations were observed with other ions. Further, the stoichiometric ratio between the probe **2** and Cu²⁺ ions was determined through Job's

plot revealing 2:1 between the probe and metal ion, respectively. The results were further supported by the HR-MS and DLS study. Moreover, the stability of the complex was determined by observing the absorption changes with time. The interference studies were done to examine the selectivity and specificity of the complex. In addition, the LOD was found to be 1.22×10^{-5} M and the stern-volmer quenching constant was determined to be 1.99×10^2 M. To gain deeper insights, DFT studies were performed to optimize the structure and for FMO analysis. Also, a TD-DFT study was done to calculate the vertical excitations and the orbital contributions for various excitations. A significant ICT was observed from the thiophene unit to the naphthalimide which gets inhibited in the presence of Cu^{2+} ions thereby leading to quenching in fluorescence.

4.12. Synthesis of Probe 2

4.12.1. Synthesis of intermediate 2

To the solution of acenaphthene (1) (1 g, 6.4 mmol) in acetic acid (15 mL), sodium dichromate (8.38 g, 32 mmol) was gradually added while stirring at room temperature for 1 hour. After the complete consumption of sodium dichromate, the reaction mixture was stirred at 80 °C for 7 hours, with its progress monitored using thin-layer chromatography (TLC). Upon completion, the reaction was quenched by transferring the mixture into cold water, leading to the formation of precipitates. The precipitates were collected by filtration under reduced pressure and thoroughly washed with distilled water to ensure purity. The lime yellow precipitates formed were oven dried at 40°C yielding 1*H*,3*H*-benzo[*de*]isochromene-1,3-dione (2). Melting point: 230-235°C; Yield: 92%

4.12.2. Synthesis of intermediate 3

To the solution of compound 2 (0.80 g, 4.08 mmol) in ethanol (15 mL), hydrazine hydrate (0.15 g, 4.86 mmol) was added at room temperature. Further, the reaction mixture was stirred at 55°C for 7 hours. A color change from light yellow to bright yellow was observed indicating the progression, which was further monitored by TLC. Upon completion, the reaction mixture was allowed to cool to room temperature. The resulting precipitates were isolated by filtration and subsequently washed with hot ethanol to remove impurities. The yellow precipitates formed were air dried, producing 2-amino-1*H*-benzo[*de*]isoquinoline-1,3(2*H*)-dione (3). Melting point: 263-269 °C; Yield: 87%

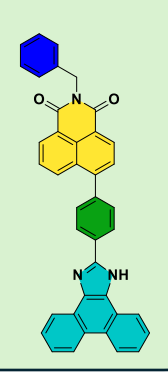
4.12.3. Synthesis of probe 2

Compound **3** (0.50 g, 2.35 mmol) was further reacted with thiophene-2-carbaldehyde (0.31 g, 2.83 mmol) (**4**) in ethanol (10 mL) with a few drops of acetic acid. The reaction was refluxed at 50-55°C for 12 hours, with progress monitored by TLC. Upon completion, the reaction mixture was cooled to room temperature to facilitate crystallization. The precipitates were thoroughly washed with hot ethanol, yielding light brown crystals of the desired probe 2. Shiny light brown crystals, 83% yield; R_f 0.60 (10% ethylacetate in hexane); mp 312-320 °C; ¹H-NMR (CDCl₃, 400 MHz): 8.66 (s, 1H, CH), 8.56 (d, J = 7.28 Hz, 2H, ArH), 8.16 (d, J = 8.28 Hz, 2H, ArH), 7.71 (t, J = 7.92 Hz, 2H, ArH), 7.54 (d, J = 5.00 Hz, 1H, ArH), 7.49 (d, J = 2.88 Hz, 1H, ArH), 7.09 (t, J = 4.92 Hz, 1H, ArH); ¹³C-NMR (CDCl₃, 100 MHz): 164.12, 161.16, 136.98, 134.36, 131.81, 131.63, 127.61, 127.49, 127.10, 122.59, 122.34; HR-MS: m/z ratio (calculated): 307.0463; m/z ratio (experimental): 307.0561(**Figure A5-A7**).

CHAPTER - 5

Synthesis and photophysical study of Naphthalimide appended Phenanthroimidazole (Probe 3)

A naphthalimide-based probe was synthesized via a Suzuki-Miyaura cross-coupling reaction, followed by amination, yielding the desired probe 3. The free probe itself exhibits feeble emission, while in the presence of CN⁻ ion, a "turn-on" response was observed in the fluorescent spectra. Further, the sensor found its practical applicability in detecting CN⁻ ions in real-world water samples.



Microchemical Journal 209 (2025) 112845



Contents lists available at ScienceDirect

Microchemical Journal







Fluorescent "turn-on" naphthalimide conjugate for the detection of CN⁻ ion with potential applications in real water samples and molecular logic gate

Gurdeep Kaura, Aastha Paltab, Gulshan Kumar, Kamaldeep Paulb, Iqubal Singhd,

- * Department of Chemistry, School of Chemical Engineering & Physical Sciences, Lovely Professional University, Phagwara, India
- Department of Chemistry and Biochemistry, Thapar Institute of Engineering and Technology, Patiala, India
- Department of Chemistry, Banasthali University, Banasthali Newal, Rajasthan, India ^d School of Pharmaceutical Sciences, Lovely Professional University, Phagwara, India

ARTICLE INFO

Keywords: Suzuki-Miyaura Fluorescence Detection limit ¹H NMR titration Practical applicability

ABSTRACT

A naphthalimide-based chemosensor was synthesized via a Suzuki-Miyaura cross-coupling reaction followed by amination yielding the desired chemosensor. The free probe itself exhibits feeble emission while in the presence of CN" ion, a "turn-on" response was observed in the fluorescent spectra. Also, the solvatochromic behaviour of the chemosensor was studied with different solvents of increasing polarity revealing the presence of Intramolecular Charge Transfer (ICT) phenomenon specifically between the naphthalimide and phenanthroimidazole units. Further, the chemosensor exhibited remarkable selectivity and sensitivity towards CN- ion with a detection limit as low as 4.2×10^{-8} M. At the same time, the sensor-ion ensemble was found to have a reversible effect in the presence of Fe3+ ions (LOD = 8.9 nM) which led to the construction of molecular logic INHIBIT gate. In addition, the plausible binding mechanism was studied through Job's plot, 1H NMR titrations, and DFT studies revealing a 1:1 binding ratio between the chemosensor and ion. Further, the sensor found its practical applicability in detecting CN ions in real-field water samples.

5.1. Introduction

In past years, there has been a burgeoning attention in the detection of anions because of their significant role in biological, chemical, and environmental processes¹¹⁷. However, the challenge is generally faced in terms of its diffused charges in comparison to cations while the interaction between the receptor and anion is generally weak and electrostatic ^{118, 119}. Amongst various anions, one of the most hazardous ions is cyanide ion (CN⁻). The presence of CN⁻ ion is abundant in nature as well in synthetic materials. It is not just limited to industries but also has entered the normal supplies, for instance, the seed of various fruits, and enters into the environment as by-product of the combustion of various materials. Also, it is widely used by industries in electroplating, resin production, pharmaceuticals, gold mining, and textiles^{120, 121}. Further, accidental leaks, inappropriate discarding of industrial waste containing CN⁻ ion, and the breakdown of cyanide-based chemical warfare agents pose potential threats to the environment ¹²². Immoderate contact with CN⁻ anion can cause various health issues, acting as a poison for the lungs, stomach, and skin. According to the Environmental Protection Agency (EPA), the suggested tolerable level of CN⁻ ion in drinking water is 0.2 ppm¹²³. Therefore, developing a competent, quick-to-respond, and highly selective CN⁻ sensor holds immense significance for the environment.

In this chapter, we reported the synthesis of a naphthalimide derivative for the fluorescence "turn-on" detection of CN ion, which could be attributed to ICT. The phenanthroimidazole moiety appended to naphthalimide provides a coordination site at the C=N group, facilitating the nucleophilic attack of CN $^-$ ions. This moiety undergoes ICT, which imparts notable optical properties. However, the introduction of CN $^-$ ions disrupts the π -conjugation between the naphthalimide and phenanthroimidazole units, resulting in significant changes in spectroscopic characteristics. This disruption suppresses ICT processes, thereby altering the electronic configurations and enhancing fluorescence. Additionally, titration experiments were conducted for quantitative analysis to determine binding constants for complexation and detection limits of the ion using various experimental methods. The results demonstrated that the synthesized probe is highly effective for the selective detection of CN $^-$ ions over other ions. Furthermore, the binding properties of probe 3 with the CN $^-$ ion were analyzed by Job's plot, 1 H NMR titration method, and DFT studies.

5.2. Synthesis of Probe 3

Probe 3 was synthesized in a multistep process as shown in Scheme 5.1¹²⁴. In the first step, to the solution of compound 1 in DMF, the solution of N-bromosuccinimide was added at room temperature with continuous stirring at room temperature, affording intermediate 2 in good yield. Then intermediate 2 was treated with Na₂Cr₂O₇ in acetic acid and was heated to reflux temperature, yielding intermediate (3). On the other hand, the condensation of compound 4 with 5 and ammonium acetate in the presence of glacial acetic acid leads to the formation of boronates (6). Further, the Suzuki-Miyaura cross-coupling reaction of 6 with 3 in the presence of K₂CO₃ and Pd(PPh₃)₄ in CH₃CN: H₂O mixture (9:1), the intermediate 7 was produced, which subsequently was treated with butylamine in ethanol at reflux conditions, yielding probe 3 as light-yellow colored precipitates. The precipitates were filtered and washed thoroughly with ethanol. Further, for the purification of the crude product, column chromatography was performed using ethyl acetate and methanol as eluents to get the desired product as probe 3. Furthermore, the desired probe 3 was characterized by spectroscopic techniques including ¹H-NMR, ¹³C-NMR, and HRMS (Figure S1-S3).

Scheme 5.1: Synthetic procedure for the synthesis of probe 3

5.3. Photophysical Properties of Probe 3

The photophysical properties of probe 3 were examined using absorption and emission spectroscopic techniques. The UV-visible absorption spectra of probe 3 (20 μ M) were recorded using CH₃CN: H₂O (9:1, v/v) as the solvent system. The absorption spectra of probe 3 revealed dual absorption bands at 320 nm and 370 nm, respectively, which could be attributed to the n- π * transition. Further upon photoexcitation at 370 nm, probe 3 (20 μ M) exhibits a dual emission band at 460 nm and 615 nm, resulting in a notable stokes shift of 90 and 245 nm, respectively, as illustrated in **Figure 5.1a and b**. Consequently, with the change in the polarity of the solvent, the absorption peak of probe 3 exhibits a bathochromic shift of 15 nm *i.e.* from 365 nm to 380 nm. Also, the emission spectra exhibit significant changes with the perturbation in the environment. In addition, the emission spectra recorded a red shift on increasing the polarity of the environment from 450 nm to 590 nm (**Table 5.1**).

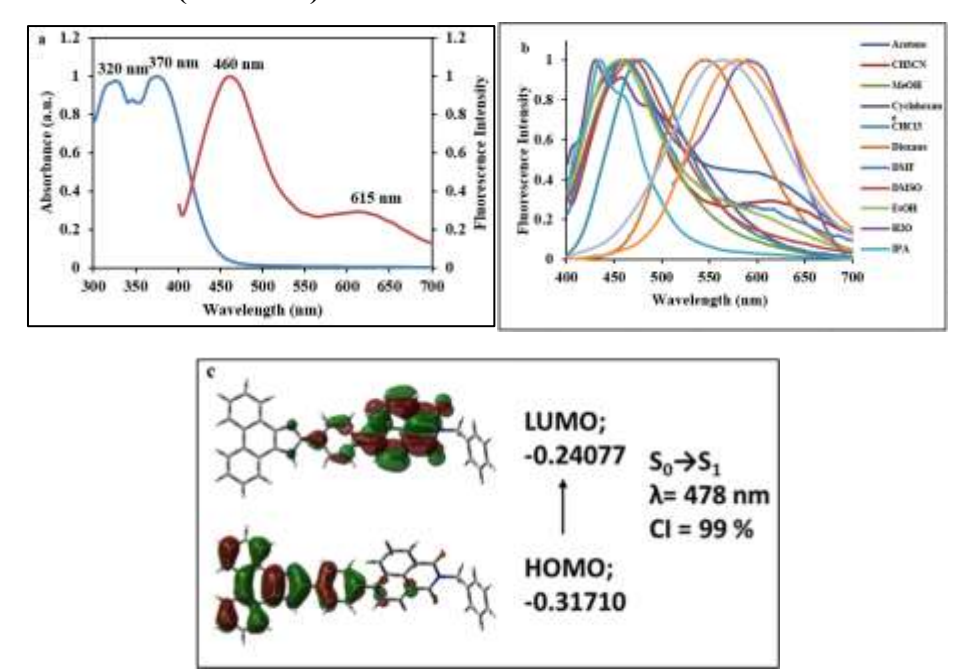


Figure 5.1: a) Normalized absorption and emission spectra of probe **3** (20 μ M, CH₃CN: H₂O, 9:1, v/v; λ_{ex} = 370 nm); b) emission spectra of probe **3** in different solvents; c) HOMO-LUMO orbitals of the optimized structure of probe **3**

In addition, the aforementioned changes in the absorption and emission spectra with the change in polarity of the solvent signify the interplay of the ICT process. The observed dual emission with varying solvent polarity is attributed to the ICT phenomenon occurring within the molecule, specifically between the naphthalimide and phenanthroimidazole units. In addition,

theoretical calculations further advocated the presence of the ICT phenomenon (Figure 5.1c). The first three vertical excitations were calculated corresponding to the ground state optimized structure. The calculations showed that the $S_0 \rightarrow S_1$ excitation was dominated by the highest oscillation strength of 1.4102 with a transition contribution of 99 % from the highest occupied molecular orbital to the lowest unoccupied molecular orbital. Subsequently, **Table 5.1** presents data about the quantum yield (Φ) and average decay time (τ avg) of probe 3 across different solvent media.

Table 5.1: Photophysical properties of probe **3** in different polarity solvents

S. No.	Solvent	Dielectric constant	λ _{max} (nm)	Molar absorptivity constant $\epsilon = M^{-1}cm^{-1}$	λ _{em} (nm)	Stokes shift Δv (cm ⁻¹)	Quantum yield (Φ)	Average decay time (t_{avg}) (ns)
1	Cyclohexane	2.02	380	3550	450	4000	17.55%	1.03
2	Toluene	2.38	365	17600	555	9000	14.58%	1.01
3	IPA	17.9	375	21700	430	3000	19.73%	0.86
4	Chloroform	4.81	370	31950	470	6000	19.66%	0.98
5	THF	7.58	380	19750	450	4000	16.84%	1.02
6	Acetone	20.7	365	21450	455	5000	22.37%	1.01
7	Dioxane	2.25	375	21600	465	5000	12.21%	1.10
8	DMSO	46.7	380	16550	465	5000	13.37%	0.90
9	Acetonitrile	37.5	370	23200	460	6000	26.50%	1.03
10	Ethanol	24.5	380	21200	575	9000	23.78%	0.88
11	Methanol	32.7	375	20100	460	5000	24.69%	0.95
12	Water	80.1	400	14150	590	8000	11.52%	0.97

5.4. Spectroscopic Analysis of Probe 3

The most vital feature of a probe is its selectivity towards target ions which adds to the precision of analytical results. We selected common anions including CN⁻, SCN⁻, P₂O₇⁴⁻, NO₃⁻, CH₃COO⁻, H₂PO₄⁻, HSO₄⁻, F⁻, Cl⁻, Br⁻, ClO⁻, BF₄⁻, SO₄²⁻, PO₄⁻, PF₆, and OH⁻ to determine the selectivity of probe **3** (20 μM) amongst the different ions in CH₃CN: H₂O (9:1, v/v) solution. In addition to being studied in a mixture of CH₃CN: H₂O (9:1, v/v). Probe **3**'s photophysical characteristics were also explored in various other solvents, including pure CH₃OH, CH₃CN, and pure H₂O. It was

observed that probe 3 displayed high selectivity and sensitivity only in the CH₃CN: H₂O (9:1, v/v) mixture. The absorption spectra were recorded, and no obvious changes were observed. Further, the sensing property of probe 3 (20 μ M) was evaluated by observing the perturbations in emission spectra in the presence of several anions such as CN⁻, SCN⁻, P₂O₇⁴⁻, NO₃⁻, CH₃COO⁻, H₂PO₄⁻, HSO₄⁻, F⁻, Cl⁻, Br⁻, ClO⁻, BF₄⁻, SO₄²⁻, PO₄⁻, PF₆, and OH⁻ in CH₃CN: H₂O (9:1, v/v) as medium. The free receptor exhibits a weak emission band (λ_{em}) at 450 nm upon excitation (λ_{ex}) at 375 nm. The emission spectra revealed no change in the presence of different ions except CN⁻ ions. It was observed that the fluorescent intensity was significantly enhanced after the addition of CN⁻ ions. (Figure 5.2) . To further examine the binding of probe 3 with CN⁻, the association constant was determined by linear fitting of 1/ (I-I₀) to 1/ [CN⁻] according to the B-H equation (where, n = 1). The binding constant for probe 3 + CN⁻ was found to be 2.0 × 10³ M⁻¹. With increasing CN⁻ concentration, a linear increase in the fluorescence intensity was observed up to 160 μ M, and the detection limit was 4.2 × 10⁻⁸ M (Figure 5.3).

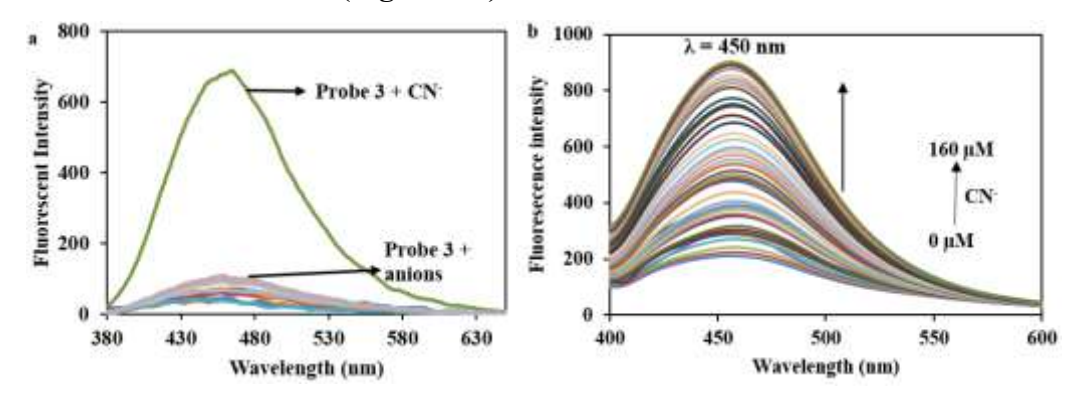


Figure 5.2: Fluorescence spectra of probe 3 (20 μ M) in CH₃CN: H₂O (9:1, v/v) a) with various anions and (b) upon continuous addition of 0-160 μ M of CN⁻

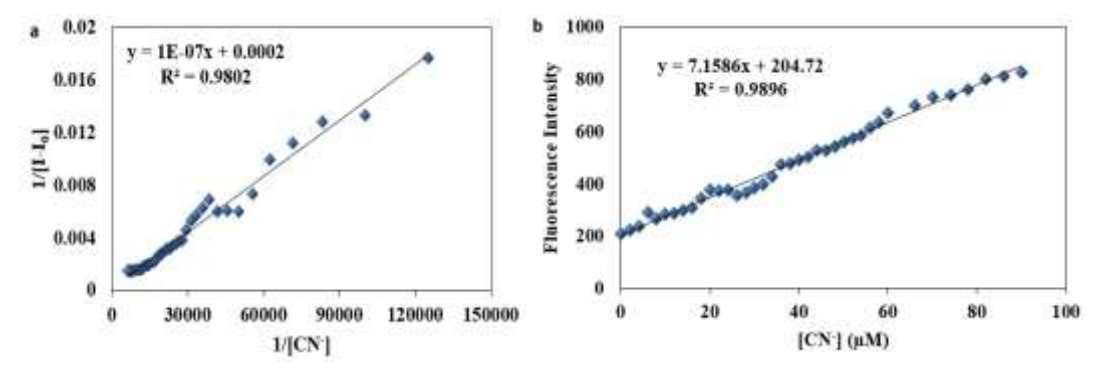


Figure 5.3: a) Benesi-Hildebrand plot for determination of binding constant; b) Plot for the determination of the lowest detection limit of probe **3** (20 μM) in CH₃CN: H₂O (9:1, v/v) with CN⁻ ions

5.5. Time-Correlated Single Photon Counting (TCSPC) Study

The enhancement in the fluorescence on binding with the anions has been supported by the results obtained from fluorescence decay measurement, using the TCSPC study. The decay behavior of probe **3** and its complexes is best fitted in with a bi-exponential function. Probe **3** showed two components having lifetimes of 0.57 ns (50.83 %) and 1.83 ns (49.17 %). The average lifetime for probe **3** comes out to be 1.02 ns. Upon the addition of CN⁻ ion to the solution of probe **3**, again two components were obtained with a lifetime of 1.97 ns (38.87 %) and 3.01 ns (61.13 %). The average lifetime was calculated to be 2.50 ns. The average lifetime of probe **3** on interaction with CN⁻ ion was increased. Similarly, with the addition of Fe³⁺ ions to the complex of probe **3**.CN⁻ the average lifetime again decreased to 1.06 ns (**Table 5.2**). Hence, we can say that probe **3** binds with anions in a purely dynamic manner.

Table 5.2: Fluorescence lifetime measurements for probe 3 and its complex in CH₃CN: H₂O (9:1, v/v)

CH ₃ CN: H ₂ O (9:1, v/v)	$\tau_1(ns)$	τ_2 (ns)	α_2	α_2	χ^2	τ _{av} (ns)
Probe 3	0.57	1.83	51.83	49.17	1.45	1.02
Probe $3 + CN^{-}$	1.97	3.01	38.87	61.13	1.09	2.50
Probe $3 + CN^- + Fe^{3+}$	1.27	1.06	2.27	97.73	1.03	1.06

5.6. Job's Plot, pH, and Interference study

To gain insights into the binding ratio of probe 3 with CN⁻ ion Job's plot experiment was carried out. It is a well-established approach for determining the stoichiometry of interactions between ligands and target analytes in liquid-phase systems. Fluorescence spectroscopy was employed to elucidate the coordination ratio between probe 3 and CN⁻ ion. The findings revealed a 1:1 stoichiometry ratio between probe 3 and CN⁻ ion (Figure 5.4a). Given the sensor's remarkable sensitivity and selectivity towards CN⁻ ions, the preferential selectivity of probe 3 was investigated in the presence of various competing anions. To assess this, a solution of probe 3 (20 μM) in CH₃CN: H₂O (9:1, v/v) was exposed to CN⁻ ion in the presence of other potentially interfering anions. Notably, our results indicated that the presence of these additional anions did not alter the spectra exhibiting negligible interference in the presence of competing ions (Figure 5.4b). Consequently, probe 3 demonstrated a practical capability to effectively detect CN⁻ ions in the presence of other anionic species. In addition, the pH level of a solution plays a critical role in

modulating charge distribution, thereby influencing the optical properties of the compound under investigation. In this context, we conducted a systematic examination of the pH-dependent variations in fluorescence intensity for probe 3 and its complexation with CN⁻ in a solvent system composed of CH₃CN: H₂O (9:1, v/v). Within the pH range of 6.9 to 10.3, we ascertained that probe 3 remained chemically stable (Figure 5.4c).

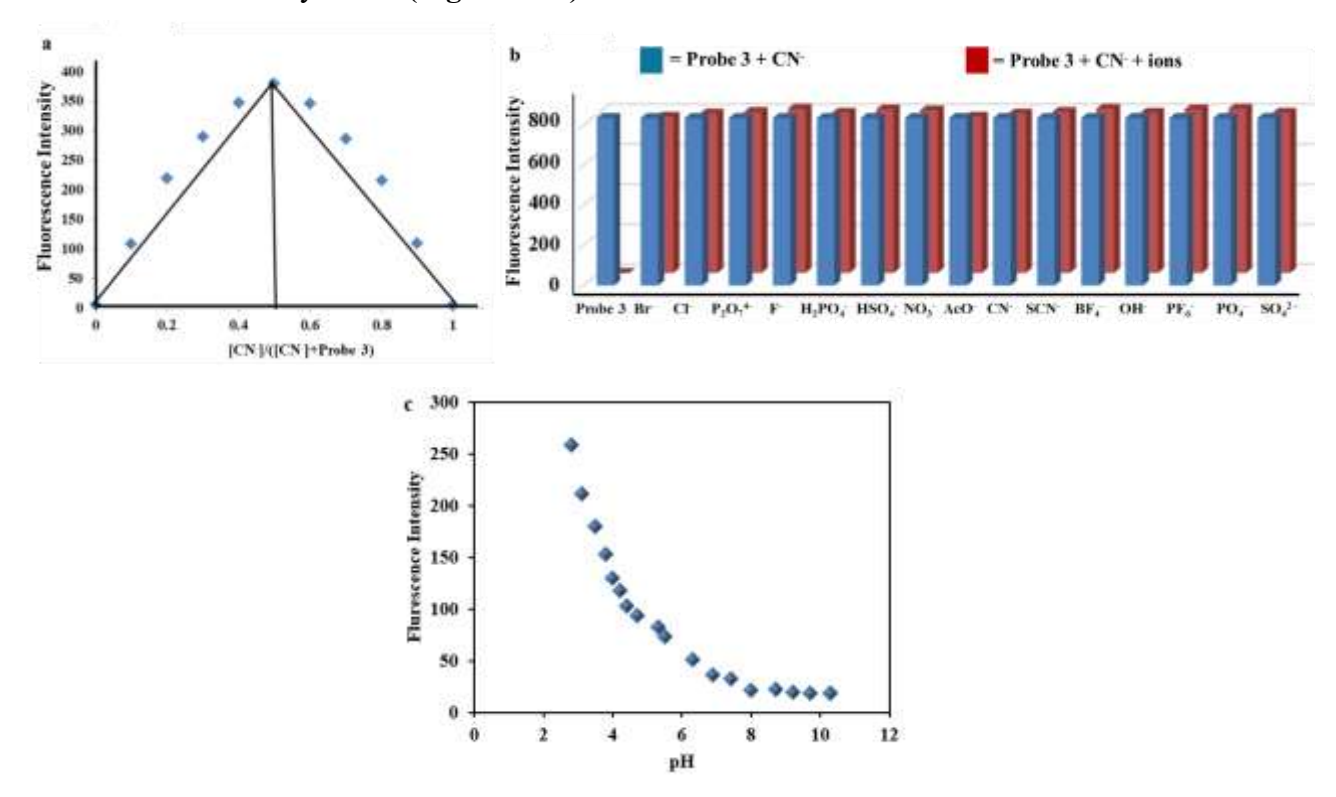


Figure 5.4: a) Job's plot for probe **3** for CN⁻ ions; (b) Relative emission intensity of probe **3** (20 μM) in CH₃CN: H₂O (9:1, v/v) (λ_{ex} = 375 nm) with different competing analytes in the absence and presence of CN⁻ at λ_{em} = 450 nm, where blue bars represent the emission intensity change of probe **3** on addition of different analytes (20 μM) and red bars represents the emission intensity changes of probe **3**+CN⁻ complex in the presence of different competing analytes (20 μM); c)Effect of pH on probe **3** (20 μM) in CH₃CN: H₂O (9:1, v/v)

5.7. Counter Ion Effect of the Ensemble

In addition, the presence of counter ions plays a pivotal role in shaping the responses of chemosensors, making it essential to investigate their impact. To this end, we conducted an extensive examination of the influence of biologically relevant metal ions, including Ca²⁺, Al³⁺, Pb²⁺, Co²⁺, Ni²⁺, Cu²⁺, Cr³⁺, Hg²⁺, Mn²⁺, Fe³⁺, and Zn²⁺, on the complexation between probe **3** and CN⁻ ions. Our observations revealed that the majority of these metal ions had either no discernible

effect or produced negligible alterations in the emission intensity (**Figure 5.5a**). However, a notable exception was found with Fe³⁺, which exhibited a substantial quenching effect on the emission band at 450 nm. This quenching phenomenon was particularly evident as we successively introduced Fe³⁺ ions. Further, the titration of the ensemble, probe $3 \cdot \text{CN}^-$ was done with Fe³⁺ ions ranging from 0 μ M to 100 μ M, into the solution exhibiting "turn-off" behavior (**Figure 5.5b**). Furthermore, we quantified the limit of detection (LOD) for Fe³⁺ ions, which was determined to be 8.9×10^{-9} M, employing a linear relationship between fluorescence intensity and concentration (**Figure 5.5c**). The synthesis of reversible probe holds prime significance with high selectivity and sensitivity for sensing harmful ions. As probe 3 exhibits reversibility with Fe³⁺ ions, the emission intensity at 450 nm was decreased (**Figure 5.5d**). The reversible nature of probe 3 and CN-complex with Fe³⁺ ions can be used for the construction of the molecular logic gate

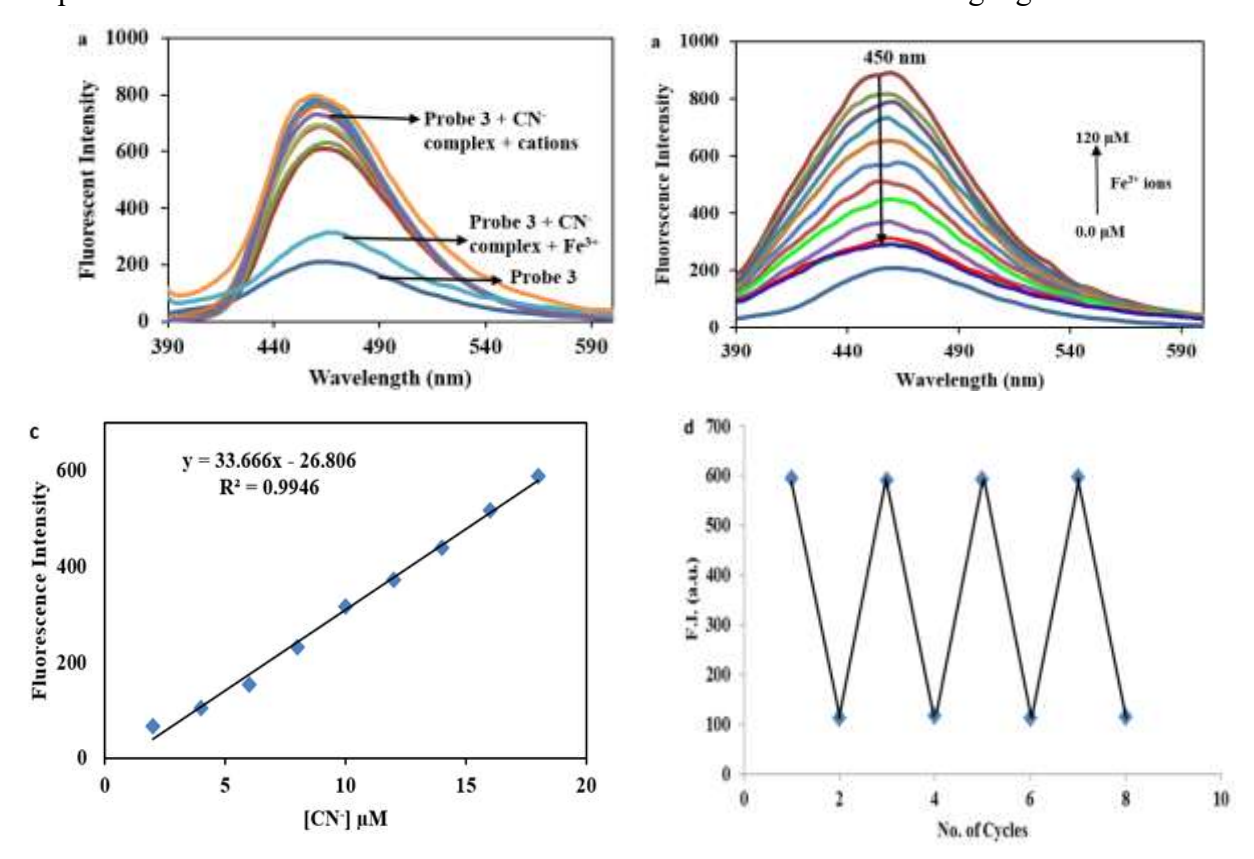


Figure 5.5: Fluorescence spectra of probe 3.CN⁻ complex (20 μ M) in CH₃CN: H₂O (9:1, v/v) (a) with various cations; b) upon continuous addition of 0-120 μ M of Fe³⁺ ions; c) plot for calculating LOD; d) reversible emission signal at 450 nm on repetitive addition of CN⁻ ion and Fe³⁺ ions.

5.8. Possible Mechanism

5.8.1. ¹H NMR titrations and HR-MS analysis

To elucidate the binding mechanism between probe 3 and CN⁻ ions, 1 H NMR titrations were carried out using DMSO- d_6 as the solvent. Notably, on the addition of CN⁻ ions, the triplet observed as a doublet of triplet at 8.86 ppm, exhibited a discernible shift to a double of a doublet at 8.78 ppm. Also, the doublet peak at 8.4 ppm corresponding to **b** protons of the phenanthroimidazole moiety shifted upfield. This could be attributed to the shift of electron density from the phenanthroimidazole moiety to the naphthalimide moiety on addition of CN⁻ ions. Moreover, the protons corresponding to the naphthalimide ring (c-f and k) displayed an up-field shift accompanied by the merging of peaks at 8.31 ppm and 8.21 ppm with the shift to 8.08 ppm. Furthermore, a collective up-field shift was observed in all other signals, which can be attributed to alterations in electron density resulting from the addition of CN⁻ ions to probe 3 (Figure 5.6a). In addition, the plausible binding mechanism is explained as shown in Figure 5.6b. In addition, HR-MS analysis of probe 3 + CN⁻ ion ensemble was done, revealing m/z ratio [M+H]⁺ value at 607.8184 (Figure A8), thereby confirming the 1:1 stoichiometric ratio.

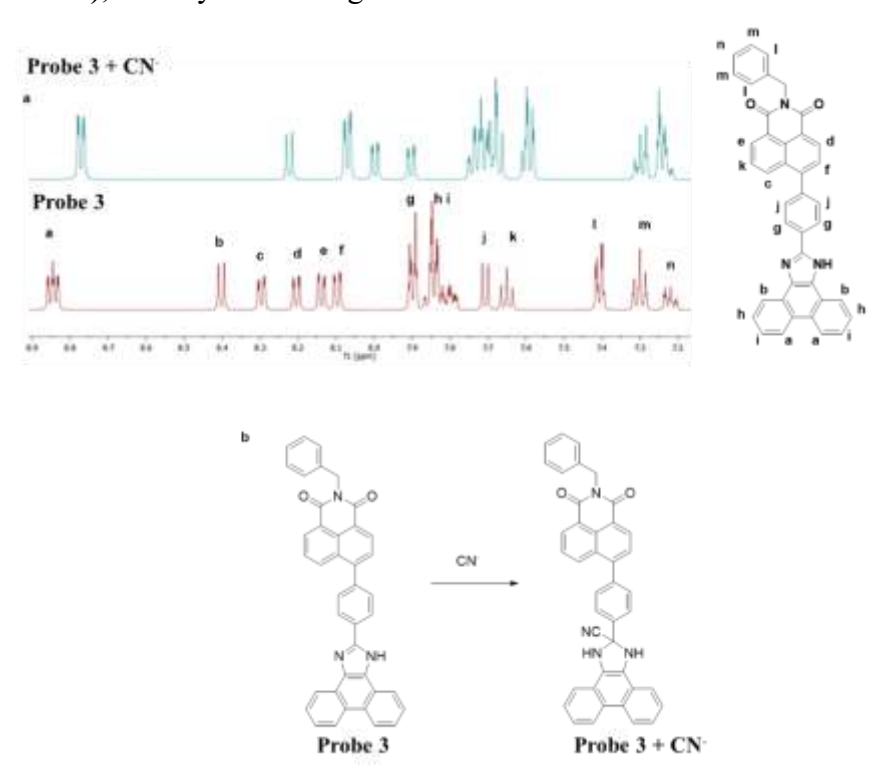


Figure 5.6: a) ¹H NMR titration of probe 3 with CN⁻ ions; b) Plausible binding mechanism of probe 3 with CN⁻ ion

5.8.2. Computational Studies

For the first three low-lying excited states, the probe $3 + CN^-$ complex was further refined, and its frontier molecular orbitals were examined (**Figure 5.7**). Notably, the oscillation strengths of the S_0 - S_1 , S_0 - S_2 , and S_0 - S_3 were computed at 319 nm, 317 nm, and 316 nm, respectively, with values of 0.2812, 0.1942, and 0.4744. Additionally, it was revealed that the electronic distribution mostly resides on the phenanthroimidazole moiety, indicating that emission enhancement may be the result of intramolecular motion restriction at the phenanthroimidazole and phenyl linkage, which can limit intramolecular charge.

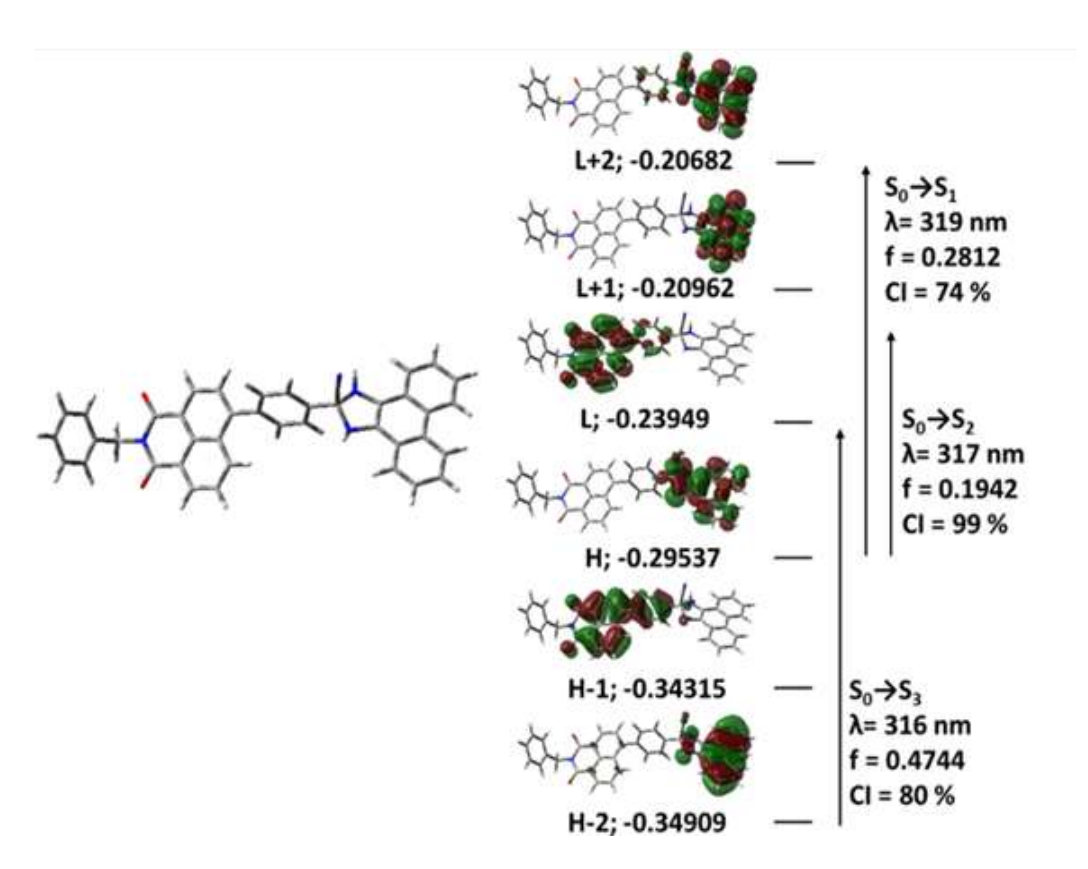


Figure 5.7: Optimized structures and frontier molecular orbitals of probe $3 + CN^{-1}$ ion complex.

5.9. Practical Applicability

5.9.1. Logic gate construction of probe 3

The reversible nature of probe 3 and CN⁻ complex with Fe³⁺ ions was used to construct a molecular logic gate. Further, the INHIBIT molecule logic gate is designed to demonstrate its use in biosensors and bioimaging. The two inputs In1= CN⁻, In2 = Fe³⁺, and output at λ_{em} = 450 nm (OUT1) were taken into consideration. The fundamental principles of Boolean algebra apply to

the absence and presence of input, where "1' denotes the YES/ON state and "0" the NO/OFF state. In variation 1, the output was 0 and indicated an OFF state when neither of the inputs was present. In variation 2, the highest emission intensity was seen at 450 nm, pointing to 1 or ON state when only CN⁻ was present. Similar to the second variation, the third variation's output was 0 (OFF state) when CN⁻ was absent and only Fe³⁺ was present. For variation 4, when both the inputs were present again the output was 0 *i.e.* OFF state. Input 1 thus meets the prerequisites for an OR gate, and input 2 meets those for a NOT gate. Our truth table, when all the results were taken into account matches the truth table of the INHIBIT logic gate. As a result, the emission peak at 450 nm with CN⁻ and Fe³⁺ as inputs can be accounted for an INHIBIT logic function (**Figure 5.8**)

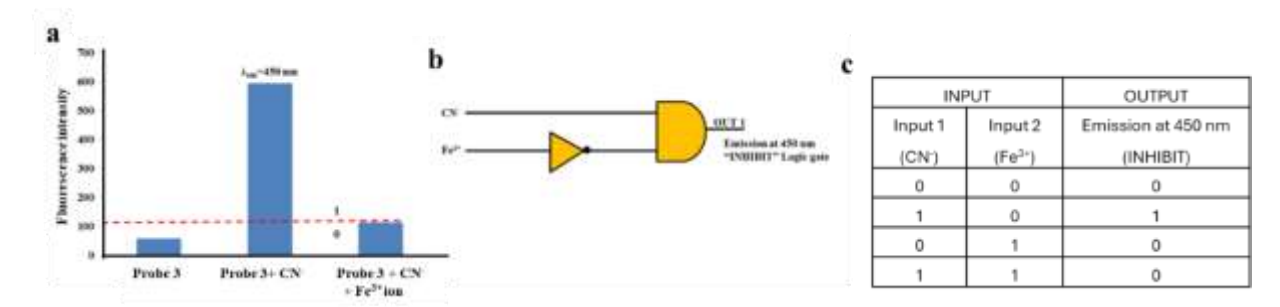


Figure 5.8: a) Emission profile of probe **3** at 450 nm with different outputs; b) circuit diagram for INHIBIT logic gate; c) Truth table for logic gate

5.9.2. Detection of CN⁻ in industrial effluent

Industrial effluent from industry was collected to exhibit the applicability of probe **3** as a CN-sensor in real samples. To test for the presence of free CN- in industrial waste, we spiked it with different concentrations of CN- (10, 20, and 30 μM). This spiked solution was added to probe **3**'s (20 μM, CH₃CN: H₂O (9:1, v/v) solution, and its emission spectrum was recorded. The emission spectrum revealed an enhancement at 450 nm in the emission band (**Figure 5.9**). The actual concentration and percent recovery were calculated from spectral changes as shown in **Table 5.3**. As a result, probe **3** could be used to detect CN- in real-time samples.

Table 5.3: Recovery of CN⁻ ions spiked in industrial water by probe 3

S. No.	Spiked amount (µM)	Recovered amount (µM)	Recovery (%)
1	10	10.9	109
2	20	21.2	106
3	30	40.5	101.3

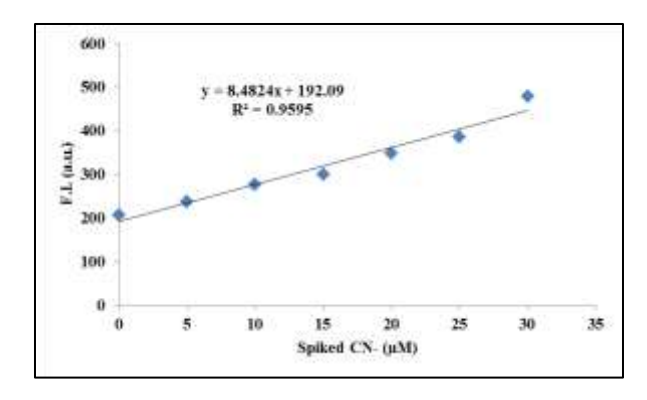


Figure 5.9: Calibration curve of probe 3 for CN⁻ ion detection in industrial water samples

5.10. Conclusion

In conclusion, herein a "turn-on" 1,8-naphthalimide-based fluorescent probe was synthesized that selectively recognizes CN⁻ ions detection in CH₃CN: H₂O (9:1, v/v). Probe **3** exhibited the Internal Charge Transfer (ICT) phenomenon by treating it with a solvent to increase the polarity. Moreover, the compound exhibited weak emission at 450 nm, which was significantly enhanced on the addition of CN⁻ ions. The binding stoichiometry of the complex of CN⁻ and probe **3** was determined by fluorescence spectroscopy, and it was calculated to be 1:1 with a detection limit as low as 4.2 × 10⁻⁸ M. Further, the DFT studies and ¹H-NMR studies were performed in support of the binding mechanism. In CH₃CN: H₂O (9:1, v/v), probe **3** + CN⁻ ensemble was studied with different cations, among which Fe³⁺ ions showed high selectivity with a lowest detection of 8.9 nM. Furthermore, the sensor finds its practical application in the designing of molecular logic INHIBIT gates and also in the detection of CN⁻ ions in industrial effluents.

5.11. Synthesis of Probe 3

5.11.1. Synthesis of intermediate 2

To the solution of N-bromosuccinimide (2.54 g, 14.28 mmol) in dimethylformamide (20 ml), acenaphthene (1) (2 g, 12.98 mmol) was added at room temperature. The reaction mixture was allowed to stir at room temperature for 3 h. The progress of the reaction was monitored by TLC. After completion of the reaction, the reaction mixture was poured into ice-cold water. The precipitates were subsequently filtered and thoroughly washed with distilled water, followed by air drying to obtain light brown crystals as product (2) in 2.92 g, 94% yield; mp 52-55 °C.

5.11.2. Synthesis of intermediate 3

To the solution of intermediate 2 (2 g, 5.58 mmol) in acetic acid (50 ml) at 0 °C, sodium dichromate (10 g) was added. The reaction was heated and transferred to a reflux condition after its completion for 2.5 h. Further, the reaction was quenched by transferring it to ice, and the white solid precipitate formed was filtered and thoroughly washed with hot water. The product (3) was obtained in 1.75 g, 72% yield; mp 222-225 °C.

5.11.3. Synthesis of intermediate 6

Further, the compound **4** (1 g, 6.67 mmol), **5** (1.52 g, 7.33 mmol), and ammonium acetate (10.26 g, 133.34 mmol) were allowed to heat till reflux temperature in glacial acetic acid (40 ml) for 10 h. After the completion of the reaction, the reaction mixture was poured into ice-cold water yielding light yellow precipitates as product (**6**) in 1.12 g, 58% yield; mp 278-281 °C.

5.11.4. Synthesis of intermediate 7

The Suzuki-Miyaura coupling reaction was carried out between compound **3** (1 g, 3.61 mmol) and **6** (1.22 g, 3.61 mmol) was carried out using potassium carbonate (0.5 g, 3.61 mmol) and Pd(PPh₃)₄ (5 mol%) in CH₃CN and H₂O (9:1). The reaction was heated till reflux temperature for 12 h under N₂ environment. The progress of the reaction was monitored with TLC and after its completion, CH₃CN was evaporated under reduced pressure.100 ml of H₂O was added to the crude mixture followed by its extraction using CHCl₃. The CHCl₃ layer was dried over Na₂SO₄ to obtain the crude product. The crude was purified by column chromatography using ethyl acetate: methanol (9.5:0.5) as eluents yielding product **7** in 0.765 g, 72% yield; mp 280-287 °C.

5.11.5. Synthesis of probe 3

To the solution of 7 (100 mg, 0.20 mmol) in ethanol (5 ml), benzylamine (0.24 mmol) was added and heated till reflux temperature for 7-9 h. The reaction was allowed to cool to room temperature to form precipitates. The precipitate formed was then filtered and thoroughly washed with ethanol. For the purification of the compound, the crude product was subjected to column chromatography using ethyl acetate and methanol as eluents to get the desired products. Light yellow solid; 88% yield; R_f 0.6 (5% methanol in ethylacetate); mp 292-295 °C; 1 H-NMR (DMSO- d_6 + CDCl₃, 400 MHz): δ (ppm) 8.76-8.71 (m, 2H, ArH), 8.67 (d, J = 7.76 Hz, 1H, ArH), 8.60 (d, J = 7.56 Hz, 1H, ArH), 8.56 (d, J = 8.20 Hz, 4H, ArH), 8.37 (d, J = 8.52 Hz, 1H, ArH), 7.84 (d, J = 7.52 Hz, 1H, ArH), 7.80 (t, J = 8.04 Hz, 1H, ArH), 7.73-7.68 (m, 4H, ArH), 7.64-7.59 (m, 2H, ArH), 7.46 (d, J = 7.36 Hz, 2H, ArH), 7.33 (t, J = 7.68 Hz, 2H, ArH), 7.26 (t, J = 7.68 Hz, 1H, ArH), 5.34 (s, 2H, ArH), 7.36 (t, J = 7.68 Hz, 2H, ArH), 5.34 (s, 2H, ArH), 7.26 (t, J = 7.68 Hz, 1H, ArH), 5.34 (s, 2H, ArH), 7.36 (t, J = 7.68 Hz, 2H, ArH), 7.37 (t, J = 7.68 Hz, 2H, ArH), 7.26 (t, J = 7.68 Hz, 1H, ArH), 5.34 (s, 2H, ArH), 7.38 (t, J = 7.68 Hz, 2H, ArH), 7.26 (t, J = 7.68 Hz, 1H, ArH), 5.34 (s, 2H, ArH), 7.39 (t, J = 7.68 Hz, 2H, ArH), 7.39 (t, J = 7.68 Hz, 2H, ArH), 7.26 (t, J = 7.68 Hz, 1H, ArH), 5.34 (s, 2H, ArH), 7.39 (t, J = 7.68 Hz, 2H, ArH), 7.26 (t, J = 7.68 Hz, 1H, ArH), 5.34 (s, 2H, ArH), 7.39 (t, J = 7.68 Hz, 2H, ArH), 7.26 (t, J = 7.68 Hz, 1H, ArH), 5.34 (s, 2H, ArH), 7.39 (t, J = 7.68 Hz, 2H, ArH), 7.26 (t, J = 7.68 Hz, 1H, ArH), 5.34 (s, 2H, ArH), 7.39 (t, J = 7.68 Hz, 2H, ArH), 7.26 (t, J = 7.68 Hz, 1H, ArH), 5.34 (s, 2H, ArH), 7.26 (t, J = 7.68 Hz, 2H, ArH), 7.39 (t, J = 7.68 Hz, 2H, ArH), 7.26 (t, J = 7.68 Hz, 2H, ArH),

benzyl-CH₂); 13 C-NMR (DMSO- d_6 + CDCl₃, 100 MHz): δ (ppm) 163.9, 163.7, 148.8, 146.3, 139.1, 137.6, 132.7, 131.4, 131.0, 130.5, 129.8, 128.6, 128.3, 128.1, 128.0, 127.4, 127.2, 127.1, 126.8, 125.6, 125.4, 124.0, 123.6, 122.9, 122.7, 122.4, 121.6 (ArC), 43.4 (benzyl-CH₂); MS (ESI): m/z 580.2033 (M⁺+1); Anal Calcd for: $C_{40}H_{25}N_3O_2$: C, 82.88; H, 4.35; N, 7.25; found C, 82.80; H, 4.30; N, 7.32. (Figure A8-A11)

CHAPTER - 6

Synthesis and photophysical study of Naphthalimide appended Chromone

(Probe 4)

This chapter deals with the detection of unanimously toxic cyanide (CN⁻) ion. Probe 4 displayed high selectivity and specificity against cyanide (CN⁻) ion and exhibited naked eye changes accompanied by "turn-off" fluorescence behavior. Job's plot analysis revealed 1:1 stoichiometric binding between probe 4 and CN⁻ ion, which was further supported by FT-IR analysis, mass analysis, ¹H-NMR titrations, and TD-DFT study.



Inorganica Chimica Acta 581 (2025) 122615



Contents lists available at ScienceDirect

Inorganica Chimica Acta





Research paper

A "naked-eye" Naphthalimide based Chemosensor for CN¯ ion detection: Investigating its application as test-strips, Smartphone Analysis & Molecular Logic gate and its TD-DFT study



Gurdeep Kaur a, Iqubal Singh b, Gurpinder Singh a, Deepak Kumar a

- Department of Chemistry, School of Chemical Engineering and Physical Sciences, Lovely Professional University, Phagwara 144411, India
- School of Pharmaccutical Sciences, Lovely Professional University, Phagwara 144411, India

ARTICLEINFO

Keywords: Naphthalimide Cyanide sensing Naked eye detection Limit of detection TD-DFT Logic gate

ABSTRACT

It is unanimously known that cyanide (CN $^-$) is one of the most toxic ions because it can interfere with the body's physiological phenomenon causing endocrine disorders, respiratory failure, hypoxia, vascular necrosis, and even death. Therefore, it is essential to develop cost-effective, sensitive, rapid, and efficient methods for sensing CN-ions. The naphthalimide-based highly selective probe 1 was successfully synthesized in a multi-step process. Probe 1 displayed high selectivity and specificity against cyanide (CN $^-$) ion and exhibited naked eye changes accompanied by "turn-off" fluorescence behavior. The introduction of CN $^-$ ion into the probe solution shows a visible color change from yellow to blue. Further, the optical methods were employed to determine the sensing performance of probe 1 towards CN $^-$ ion. The CN $^-$ ion detection limit was 5.47 μ M with a binding constant of 1.52 \times 10 5 M $^{-1}$. The fluorescence quenching efficiency towards cyanide ion was found to be 73.21 %, with the Stern-Volmer quenching constant to be 1.22 \times 10 5 M $^{-1}$. Job's plot analysis revealed 1:1 stoichiometric binding between probe 1 and CN $^-$ ion, further supported by FT-IR analysis, mass analysis, 1 H NMR titrations, and TD-DFT study. Probe 1 finds its practical application for detecting CN $^-$ ion using the test strip method. In addition, chemically switchable fluorescent dyes provide helpful building blocks for developing intricate molecular devices that communicate via adjustments in their emission characteristics; therefore, probe 1 was also used to establish molecular logic gates.

6.1. Introduction

Amongst various anions, one of the most hazardous ions is cyanide ion (CN⁻). The presence of CN⁻ ion is abundant in nature as well as in synthetic materials. It is not just limited to the industries but also has entered the ordinary sources, for instance, the seed of various fruits, and enters into the environment as a by-product of the combustion of various materials. Therefore, developing a highly selective, rapidly responsive, and efficient CN sensor is of immense significance for the environment. The strategy for CN⁻ ion sensing is usually based on coordination bonding and nucleophilic addition¹²¹. The hydrogen bonding method involves CN⁻ association with the binding unit, resulting in the formation of hydrogen bonds, thereby causing significant alterations in color or fluorescence signals^{125, 126}. However, this approach suffers from poor selectivity and inhibition in protic solvents. In addition, the chromogenic approach involves a chemical reaction where reactive sites are selectively attacked by CN⁻ nucleophiles, showing better sensitivity and selectivity towards CN⁻ ion. Photophysical properties of organic fluorophores are commonly affected in the presence of external stimuli, altering the fluorophore's electronic structure and fluorescence signals^{26, 127-129}.

Herein, we synthesized a Schiff Base utilizing naphthalimide and chromone moiety. As per our expectations, the cyanide ion explicitly exhibits nucleophilic attack across the C=N group altering the electronic configuration of the probe and hence leading to spectral changes. Also, a "naked-eye" color change was observed from yellow to blue with the addition of CN⁻ ion, which could be attributed to ICT. Furthermore, Job's plot and HR-MS studies were employed to determine the stoichiometric ratio. The binding constants and detection limits for the ion were determined utilizing titration experiments. The experimental results were further validated by using computational approaches, including DFT and TD-DFT, which reveal the theoretical λ_{max} value at 600 nm of the probe and CN⁻ complex, which is quite close to the experimental value *i.e.* 595 nm. In addition, the development of a test strip, smartphone analysis, and design of a molecular logic gate and molecular keypad exhibit the probe's practical applicability.

6.2. Synthetic route to the synthesis of probe 4

Probe 4 was synthesized through a multistep reaction sequence, as illustrated in Scheme 1. Initially, acenaphthene (1) was treated with NBS in DMF and stirred at room temperature for 3 hours, yielding intermediate 2. This intermediate was then oxidized using Na₂Cr₂O₇ in acetic acid under

reflux conditions for 6 hours to afford 5-bromo-1,2-dihydroacenaphthylene (3). Subsequent reaction with 2-morpholinoethanamine produced compound 4 which was then treated with hydrazine hydrate in ethanol, leading to an aromatic substitution at the bromo position of the naphthalimide ring, forming compound 5. Finally, compound 5 underwent a condensation reaction with 4-oxo-4*H*-chromene-3-carbaldehyde (6) under reflux in ethanol for 8 hours, yielding the desired molecular probe 4 (Scheme 6.1). The structure and purity of the synthesized probe were confirmed through spectroscopic characterization techniques including ¹H-NMR, ¹³C-NMR, and HR-MS.

Scheme 6.1: Synthetic route to the synthesis of probe 4

6.3. Photophysical Properties of Probe 4

The photophysical properties of probe 4 were explored in different solvents, including water, dimethyl sulphoxide (DMSO), dimethylformamide (DMF), methanol (MeOH), acetonitrile (ACN), chloroform, ethyl acetate, and hexane using UV-visible spectroscopic technique (**Figure 6.1**). The absorption spectra of the probe in various solvents at a concentration of 20 µM were recorded. It was found that probe 4 was insoluble in water, exhibiting no characteristic peak on the other hand, the peaks at 465 nm and 333 nm were observed using DMSO as solvent. Remarkably,

the absorption of probe 4 showed a redshift, and the absorption profile became broader with increasing solvent polarity upon changing from hexane to DMSO, which could be attributed to π - π * and intra-molecular charge transfer (ICT) transitions from the donor moiety to the electron-deficient acceptor moiety. From the observed results, the polar protic solvents such as MeOH is strongly bonding with the acceptor part, which may induce the strong acceptor character and hence influence the π - π * and ICT process in comparison to the polar aprotic solvents. Further, the absorbance at different wavelengths and molar absorptivity value of probe 4 in different solvents have been tabulated in **Table 6.1.**

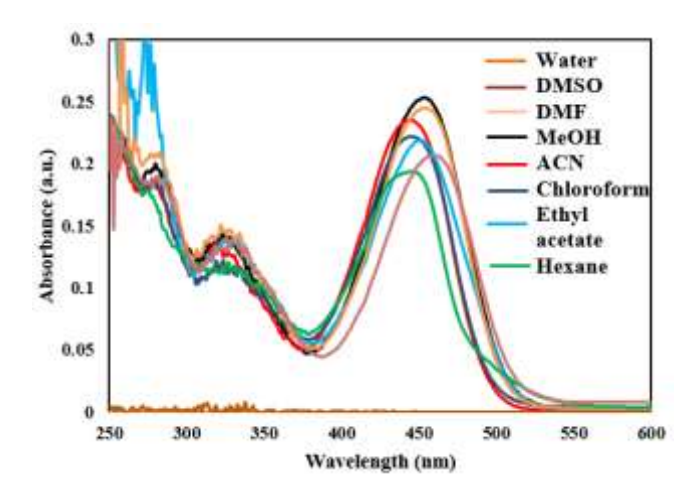


Figure 6.1: Absorption spectra of probe 4 in different solvents

6.4. Optical Performance of Probe 4

The optical performance of probe 4 towards different ions was characterized by naked-eye detection, absorption, and emission spectroscopy. The screening of the probe towards different anions was done at a concentration of 30 µM of probe 4 in DMSO: H₂O (4:1, v/v) as the solvent medium. Besides choosing the studied solvent medium, other solvents like H₂O, EtOH, MeOH, CH₃CN, and their different water fractions were explored, but the DMSO: H₂O (4:1, v/v) displayed high selectivity, sensitivity, and naked-eye response. Also, the probe exhibits poor solubility in an aqueous medium, and on further increasing the water fractions, probe 4 started precipitating. Further, probe 4 shows an absorption band at 460 nm while the emission band is formed at 560 nm on photoexcitation at 465 nm. The Stokes shift was found to be 100 nm (Figure 6.2)

Table 6.1: Photophysical properties of probe 4 in different polarity solvents

Solvent	Dielectric constant	Wavelength	Absorbance	Molar extinction coefficient (M ⁻¹ cm ⁻¹)	
Solvent	(F/m)	(λ_{max}) (nm)	(a.u.)		
Water	80.1	-	-	-	
DMSO	46.7	465	0.206	10,300	
Acetonitrile	37.5	442	0.236	11,800	
DMF	36.7	457	0.244	12,200	
Methanol	32.7	457	0.253	12,650	
Ethyl acetate	6.02	455	0.219	10,950	
Chloroform	4.81	449	0.217	10,850	
Hexane	1.88	445	0.191	9,550	

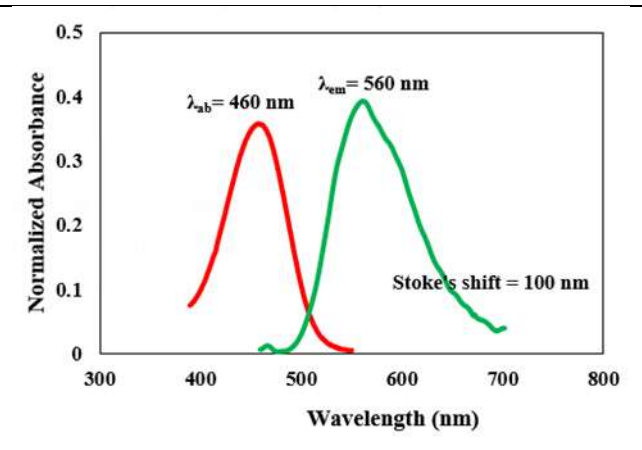


Figure 6.2: A depiction of Stokes shift between absorption (red) and emission (green) spectra

6.4.1. Visual detection

In a solution of probe **4** (30 μM) in DMSO: H₂O (4:1, v/v) as medium, different anions including I⁻, Br⁻, F⁻, AcO⁻, H₂PO₄⁻, HSO₄⁻, SCN⁻, NO₃⁻, Cl⁻, PO₄³⁻, S²⁻, oxalate, lactate, and CN⁻ were added for visual detection. The ability of probe 4 was assessed by observing color changes both with the naked eye and under 365 nm UV rays. At ambient conditions, it was observed that when CN⁻ ions were added, the probe solution transformed from yellow to violet-blue, whereas other ions did not cause any significant change (**Figure 6.3a**). Under 365 nm UV light, the probe's bright yellow color was quenched in the presence of CN⁻ ions while other ions exhibited no noticeable effect (**Figure 6.3b**). These visual alterations indicate that probe **4** can be utilized as a chemosensor for the subtle detection of CN⁻ ion. Furthermore, the sensing performance of the probe was studied through UV-visible and fluorescence spectroscopic techniques.

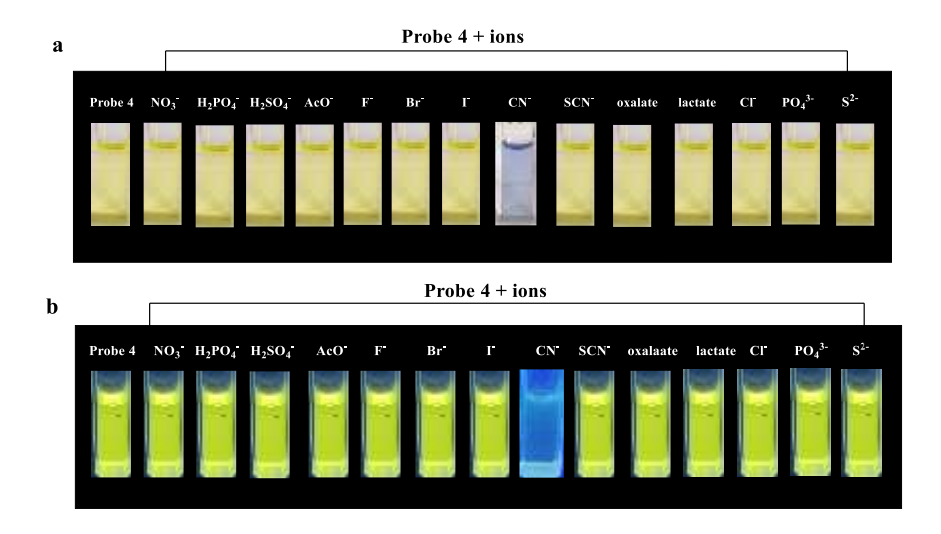


Figure 6.3: Visible changes of probe **4** in DMSO: H2O (4:1, v/v) in the presence of different anions a) with naked-eye and b) under UV light (365 nm)

6.4.2. UV-Visible absorption study of probe 4

The UV-visible spectroscopy was utilized to explore the sensing ability of probe 4 (30 µM) in DMSO: H₂O (4:1, v/v) towards various ions including I⁻, Br⁻, F⁻, AcO⁻, H₂PO₄⁻, H₂SO₄⁻, SCN⁻, NO₃-, Cl⁻, PO₄³-, S²-, oxalate, lactate, and CN⁻ (10 equiv.). The UV spectra were noted in aqueous DMSO before and after the introduction of different ions. The absorption spectra of probe 4 showed an absorption band at 460 nm ($\varepsilon = 13,333.33 \text{ M}^{-1} \text{ cm}^{-1}$) attributed to $n-\pi^*$ transitions (Figure 6.4a). After adding the aforementioned ions, the absorption spectra revealed significant perturbations only in the presence of CN⁻ ions. The introduction of CN⁻ ions decreases the band's intensity at 460 nm with the gradual development of a new band at 595 nm, indicating the alterations in the electronic environment of the probe. A redshift of 135 nm was noticed accompanied by the generation of isosbestic points at 405 nm and 502 nm revealing the complex formation (Figure 6.4b). This behavior suggests that CN⁻ ions are effectively interacting with the probe, forming a new complex that alters its optical properties. The other ions show no significant alterations in the intensity of the probe. These results show that probe 4 is highly selective towards CN⁻ ions. Further, the probe was titrated with CN⁻ ions in DMSO: H₂O (4:1, v/v) solution for detailed understanding. The titration experiments vividly exhibit that upon incremental addition of CN⁻ ions (0-3 equiv.), the intensity of the band at 460 nm gradually decreases with the simultaneous emergence of a new band at 595 nm. Hence, the UV-visible spectra display probe 4 as a promising tool for the selective detection of CN⁻ions.

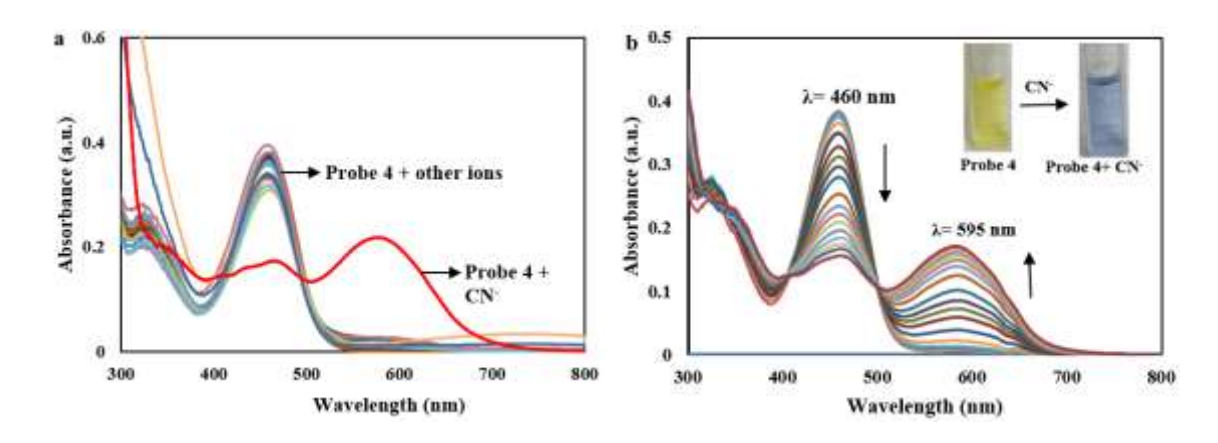


Figure 6.4: UV-vis spectra of a) probe 4 (30 μ M) in DMSO: H₂O (4:1, v/v) in the presence of different anions (10 equiv.); b) titration of probe 4 (30 μ M) in DMSO: H₂O (4:1, v/v) with CN⁻ ion (0-3 equv.)

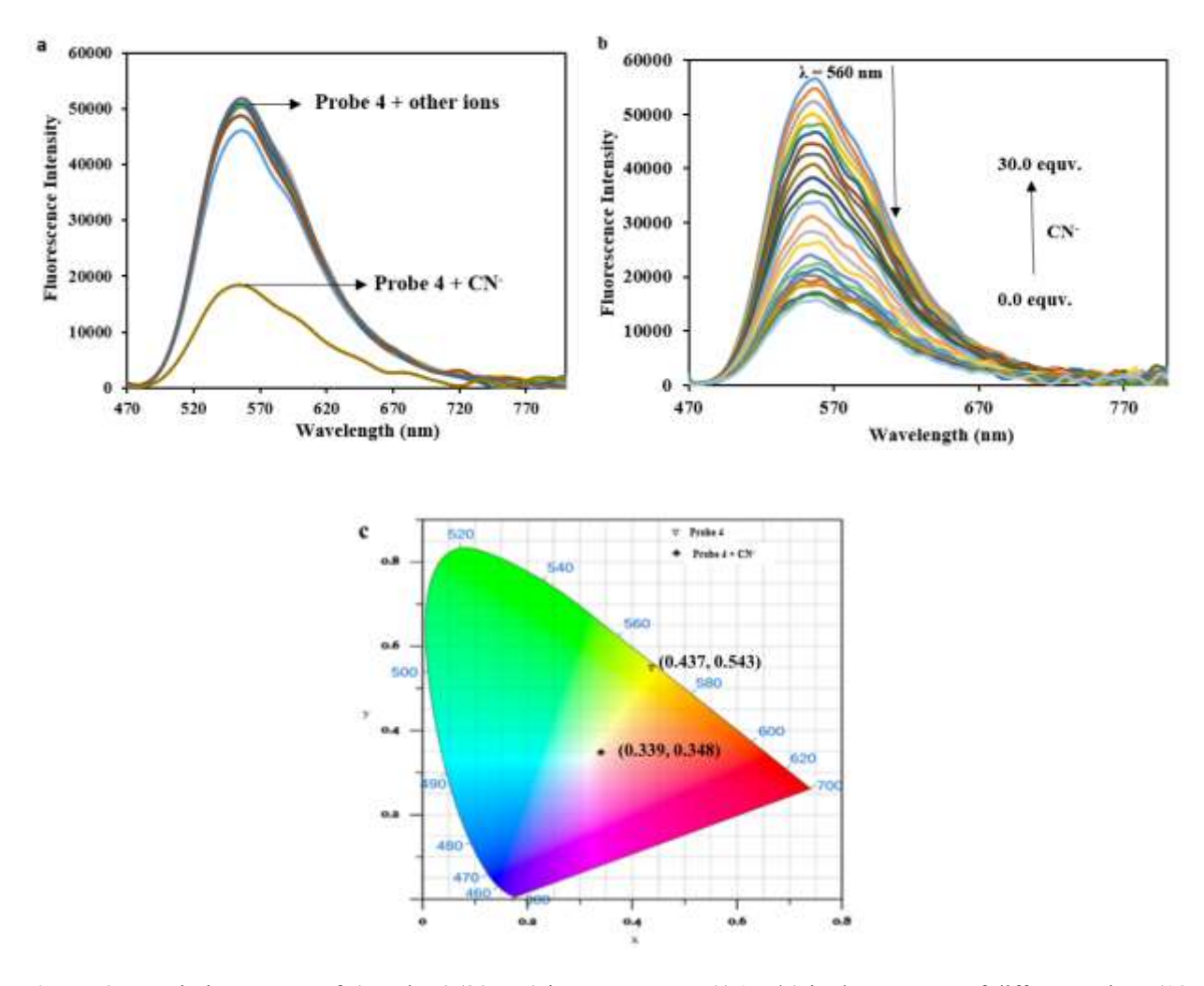


Figure 6.5: Emission spectra of a) probe **4** (30 μ M) in DMSO: H₂O (4:1, v/v) in the presence of different anions (10 equiv.); b) titration of probe **4** (30 μ M) in DMSO: H₂O (4:1, v/v) with CN⁻ ion (0-30 equv.); c) Chromaticity CIE 1931 diagram of probe **4** and its complex with CN⁻ ion

6.4.3. Emission characteristics of probe 4

Furthermore, fluorescence spectroscopy was implemented to scrutinize the sensing competence of probe 4 (30 µM) in DMSO: H₂O (4:1, v/v) towards various ions including I⁻, Br⁻, F⁻, AcO⁻, H₂PO₄⁻ , H₂SO₄-, SCN-, NO₃-, Cl⁻, PO₄³⁻, S²⁻, oxalate, lactate, and CN⁻ (10 equiv.) at room temperature. On excitation at wavelength (λ_{exc}) 465 nm, the probe exhibits an emission band (λ_{em}) at 560 nm, which was utilized to examine the optical performance of the probe. A significant quenching of the emission band was noticed at 560 nm in the presence of CN ions, while other ions revealed no significant perturbation in the emission band (Figure 6.5a). A dramatic decline in the emission intensity was observed, which supports its high selectivity for CN⁻ion. Furthermore, the titration experiments of probe 4 were performed with CN⁻ ion, revealing deeper insights and for quantitative analysis. The incremental additions of CN⁻ ions to the probe solution revealed quenching in the fluorescence intensity till saturation was achieved (Figure 6.5b). The exact color perception was best visualized by the Chromaticity Commission Internationale de l'Eclairage (CIE) 1931 diagram, utilizing CIE-X and CIE-Y coordinates whose values were found to be 0.437 and 0.543, respectively. However, in addition to CN ions, the coordinates shift to 0.339 and 0.348, respectively (Figure 6.5c), which complements the fluorescence spectroscopic results and under UV lamp.

6.5. Quantitative Analysis

The LOD was calculated from the graph depicting absorbance/emission intensity as a function of CN⁻ ions and was plotted as shown in **Figure 6.6a**. The LOD and LOQ were calculated to be 5.47 μ M and 1.82 μ M, respectively, from equations 1 and 2. In addition, the binding constant (K_a) was estimated using a B-H plot from equation 3, revealing a direct relationship between 1/(I-I₀) v/s 1/[M] and was determined to be $1.52 \times 10^5 \,\mathrm{M}^{-1}$ (**Figure 6.6b**). Also, the Stern-Volmer plot reveals a quenching constant (K_{SV}) of $1.22 \times 10^5 \,\mathrm{M}^{-1}$ (**Figure 6.6c**) calculated from equation 4. In addition, the quenching of emission intensity leads to the calculation of fluorescence quenching efficiency (η) using equation 5, which was determined to be. 73.21%.

6.6. Interference and Reversibility Study

To further investigate the selectivity of probe 4 towards CN⁻ ion, the competitive analysis of the probe was carried out in the presence of various anions I⁻, Br⁻, F⁻, AcO⁻, H₂PO₄²⁻, HSO₄²⁻, SCN⁻,

NO₃²⁻, Cl⁻, PO₄³⁻, S²⁻, oxalate, lactate, and CN⁻ (10 equiv.). As depicted in **Figure 6.7**, the yellow bars correspond to probe 4 with tested anions and the blue bars correspond to probe 4 + CN⁻ complex with competing anions. It was noticed that the CN⁻ ions decrease the absorption intensity of probe 4 in the presence of tested ions, thereby revealing the high selectivity and specificity of the probe towards CN⁻ ions and exhibiting negligible interference in the presence of other ions.

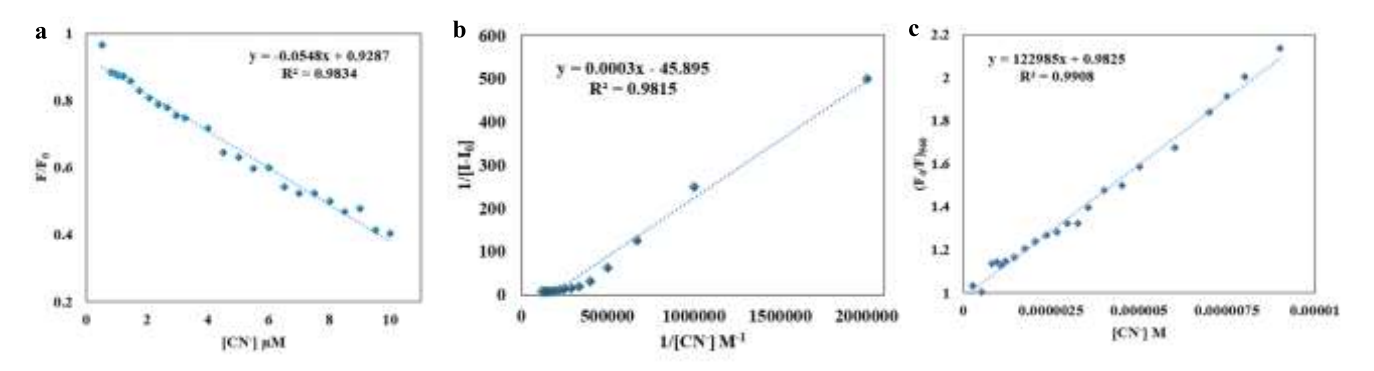


Figure 6.6: a) Emission plot of F/F_0 v/s $[CN^-]$ for the determination of the limit of detection; b) Benesi-Hilderbrand plot for determining the binding constant of probe 4 for CN^- ion; c) Stern-Volmer plot for the determination of the quenching constant

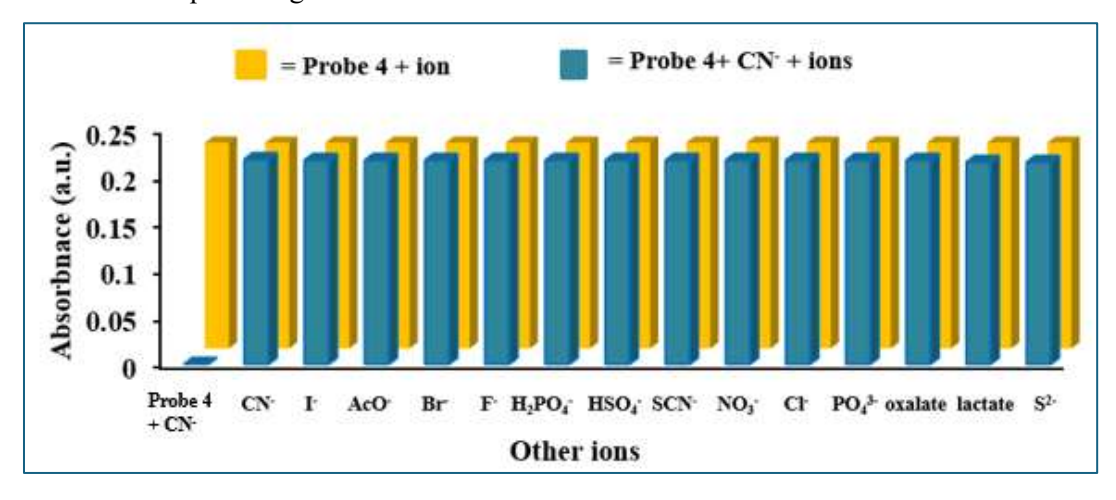


Figure 6.7: Interference study of a) probe 4 (30 μ M) (yellow bars) and b) probe 4 + CN⁻ complex (blue bars) in DMSO: H₂O (4:1, v/v) in the presence and absence of various ions (in excess)

Further, the reversibility of the probe was examined with TFA as reported earlier¹²¹. It was observed that in the absence of CN⁻ ion, probe 4 exhibits an absorbance band at 460 nm. The intensity of the absorbance band of the probe decreases upon the addition of CN⁻ ion, leading to the band's emergence at 595 nm. The transition is accompanied by a noticeable color change from yellow to blue. By adding 0.12 ml of 1% TFA to the complex, the yellow color was regained,

indicating the reversal of the reaction between probe 4 and CN⁻ ion (**Figure 6.8**). The observation of the newly emerged band at 595 nm disappears, and the reappearance of the original band at 460 nm suggests that TFA effectively reverses the reaction. To further confirm this reversibility, several cycles were conducted with repeated additions of TFA. Each cycle demonstrated consistent changes in the absorption spectrum, reinforcing the idea that TFA acts as a reliable agent for reversing the reaction dynamics.

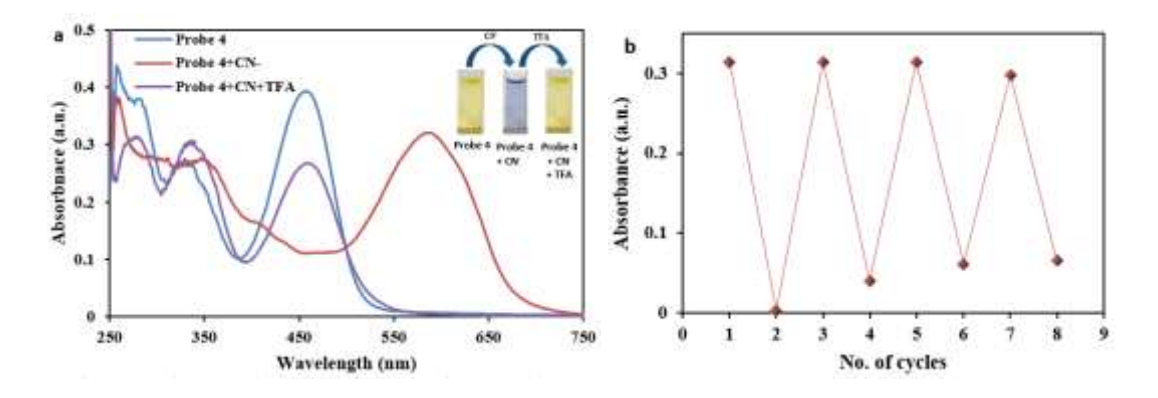


Figure 6.8: a) Reverse reaction of probe **4** (30 μ M) in DMSO: H₂O (4:1, v/v) in the presence of CN⁻ ion (20 μ l) and TFA (0.12 ml); b) reversible emission signal at 595 nm on repetitive addition of CN⁻ and TFA.

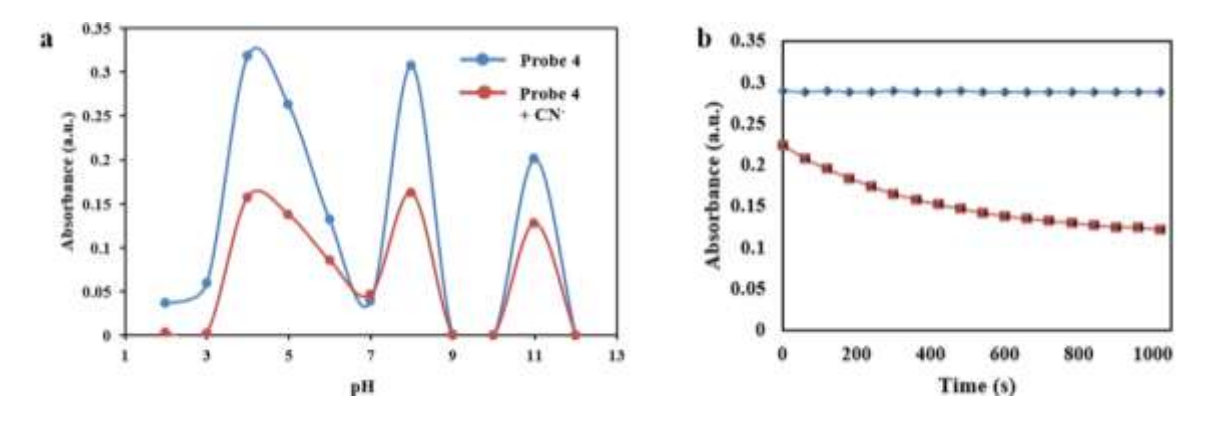


Figure 6.9: a) Effect of pH on probe **4** and probe **4** + CN⁻ complex; b) Time course study of probe **4** (blue) and probe **4** + CN⁻ complex (red)

6.7. Effect of pH and Response Time

The applicability of probe 4 and its complex with CN⁻ ions was evaluated by measuring absorption intensities at varying pH values (2.0-12.0) in a DMSO: H₂O (4:1, v/v) solution. A distinct pH-dependent change in absorption intensity was observed, highlighting the probe's environmental sensitivity. The probe exhibited insolubility and negligible absorption intensity at pH 2, 3, 7, 9,

10, and 12. The highest absorption intensity was recorded at pH 4, followed by pH 8 and 11. A similar pH-dependent trend was observed for the probe's complex with CN⁻ ions (Figure 6.9a). Additionally, a time-course UV-visible absorption study was conducted to assess the stability of probe 4 and its complex with CN⁻ ions. Probe 4 exhibited no significant changes in absorption over time, demonstrating its stability under ambient conditions. In contrast, its complex with CN⁻ ions showed an initial decrease in absorption intensity, which stabilized after approximately 600 seconds. Further, this study demonstrates good stability and a quick response time exhibiting the robust nature of the chemosensor (Figure 6.9b).

6.8. Binding Mechanism

6.8.1. Job's plot and ATR-FTIR analysis

To explore the binding between probe 4 and CN⁻ ion, the Job plot experiment was conducted. The change in the absorbance was plotted against the molecular fraction [Probe 4/(Probe 4 + CN⁻)] shown in Figure **6.10a**. The results from this plot indicated a 1:1 stoichiometric binding between probe 4 and CN⁻ ion. The peak at 0.5 validates the stoichiometry, providing a clear understanding of the binding dynamics with probe 4. The CN⁻ ion being nucleophilic leads to addition across the double bond (C=N) in probe 4. This nucleophilic addition across the imine bond leads to spectral changes, thereby perturbing the electron density (**Figure 6.10b**).

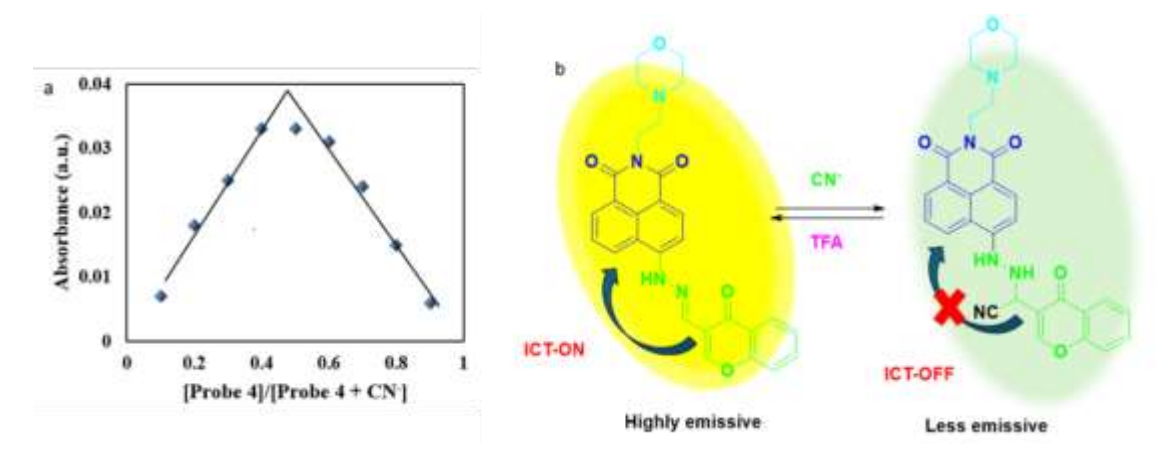


Figure 6.10: a) Job's plot for the determination of stoichiometric ratio between probe 4 and CN⁻, b) plausible mechanism of binding of CN⁻ ions with probe 4

The study revealed significant perturbations between the region 1300-4000 cm⁻¹ on the addition of CN⁻ ions. In the presence of CN⁻ ions, the N-H peak at 3698 cm⁻¹ shifted to 3678 cm⁻¹ with the emergence of a new broad peak at 3534 cm⁻¹. Also, a change in intensity at 3022 cm⁻¹ was

observed, which could be attributed to =C-H stretching. Further, the emergence of a new peak at 2255 cm⁻¹ signifies the stretching of the nitriles (-CN) group in probe 4, leading to the formation of the complex. The strong peaks between 1440 - 1350 cm⁻¹ correspond to the C-H bending of methylene and methyl groups. The peak at 1215 cm⁻¹ corresponds to the C-N stretching of the amine, which exhibits significant changes in addition to the CN⁻ ion (**Figure 6.11a**). In addition, the peaks in the region near 2800 - 3000 cm⁻¹ correspond to the -C-H stretching of alkanes. Furthermore, the DFT and TD-DFT studies were employed to investigate the possible complex formation.

6.8.2. ¹H-NMR titration experiment

In addition, 1 H-NMR titration experiments (in d_{6} -DMSO) were performed to acquire more information about the plausible binding mechanism. The 1 H-NMR spectra of the probe revealed a doublet peak at 11.59 and 9.02 δ corresponding to the long-range coupling between NH and imine protons, respectively. While the peaks of the aromatic region were found between 8.90 to 7.50 δ . On the other hand, the addition of CN^{-} ion led to the downfield shift of the NH proton from a doublet peak observed at 11.59 to a singlet peak at 9.07 δ , which could be attributed to the nucleophilic attack of the CN^{-} . Moreover, the protons of the imine group (CH*-N) at 9.02 δ exhibit up-field shift to 5.74 δ on addition of the CN^{-} ion (Figure 6.11b). Furthermore, a collective downfield shift of the aromatic region reveals the alterations in the electron density of the probe in the presence of CN^{-} ion. In addition, the mass spectra of the complex were found with m/z ratio at 524.1917, revealing the formation of the complex (Figure A12).

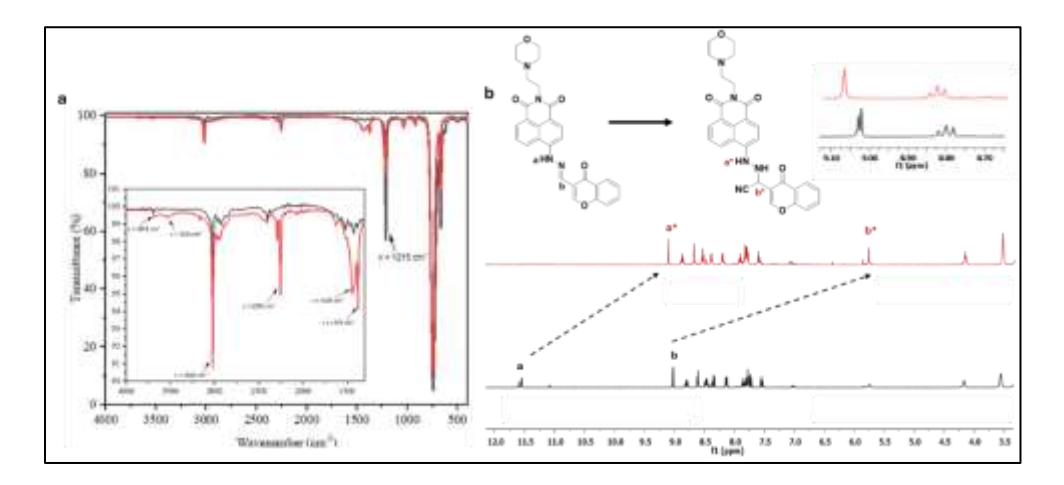


Figure 6.11: a) ATR-FTIR analysis and b) ¹H-NMR titrations of probe **4** (black) and the addition of 1 equv. of CN⁻ions (red)

6.9. Density Functional Theory (DFT) Study

Figure **6.12** shows the optimized structure of probe **4** and probe **4**+CN⁻ complex through B3LYP/6-31G(d,p) basis set. Probe 4 exhibits an angle of 119.25° across the C atom of the imine bond, leading to planarity across the naphthalimide and chromone moiety as shown in View I and II. On the other hand, the addition of CN⁻ across the imine bond distorts the planarity, and the angles change to 122.11°, thereby perturbing the electron system and inhibiting the ICT phenomenon. This inhibition of ICT leads to spectral changes and fluorescence quenching. Also, the polarity of the compound was examined from the molecular electrostatic potential maps which aids in knowing the reactive component within the molecule against a charge species. The red color in the map represents the concentration of the negative charge due to proton attraction, while the blue region is due to the concentration of the positive charge caused by the electron repulsion (**Figure 6.13**). The red region is mainly localized on the O atom of the naphthalimide and morpholine unit, while the blue region is localized on the C atom of the imine group, making it electrophilic in nature thereby facilitating the attack of the CN⁻ group.

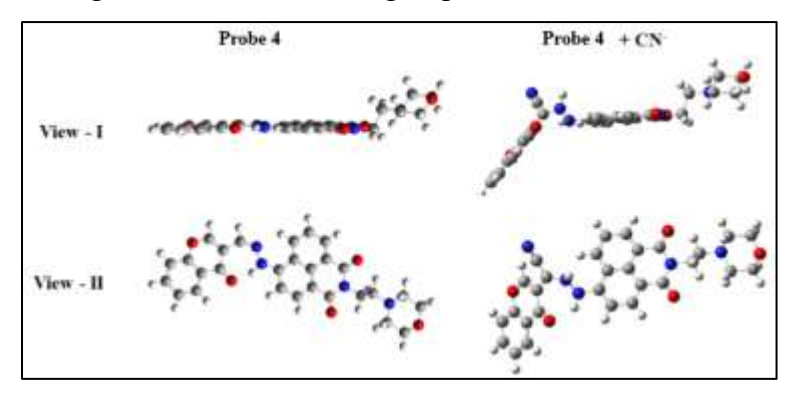


Figure 6.12: Optimized structure of probe **4** and probe **4**+ CN⁻ ions using B3LYP/6-31G(d,p) basis set through DFT study.

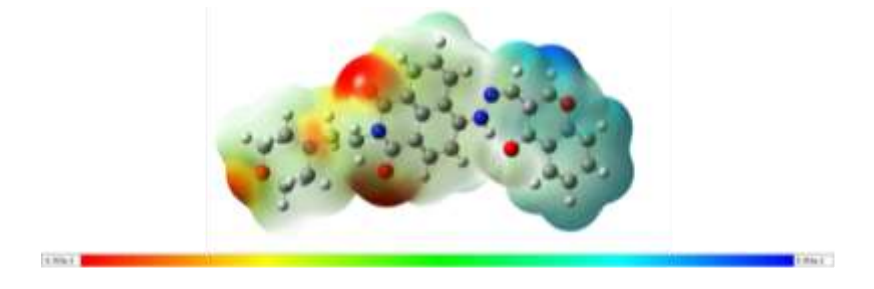


Figure 6.13: Electrostatic potential map (ESP) of probe **4** (blue regions represent positive sites and red regions as negative sites)

Furthermore, TD-DFT was done to study the vertical excitations calculated at 513.86 nm (f = 0.0045), 436.71 nm (f = 0.8446), and 419.91 nm (f = 0.0000) corresponding to transitions from S_0 to S_1 , S_2 , and S_3 excited states, respectively. Amongst this, the transition from $S_0 \rightarrow S_2$ exhibits significant oscillation strength and also the theoretical absorption wavelength of probe 4 is 436.71 nm (**Figure 6.14b**), which almost corresponds to the experimental results ($\lambda_{max} = 460$ nm).

Table 6.2: The experimental and theoretical absorption values of probe 4 and its complex.

Analyte	Experimental value	Theoretical value
Probe 4	460 nm	436.71 nm
Probe 4 + CN	595 nm	600.49 nm

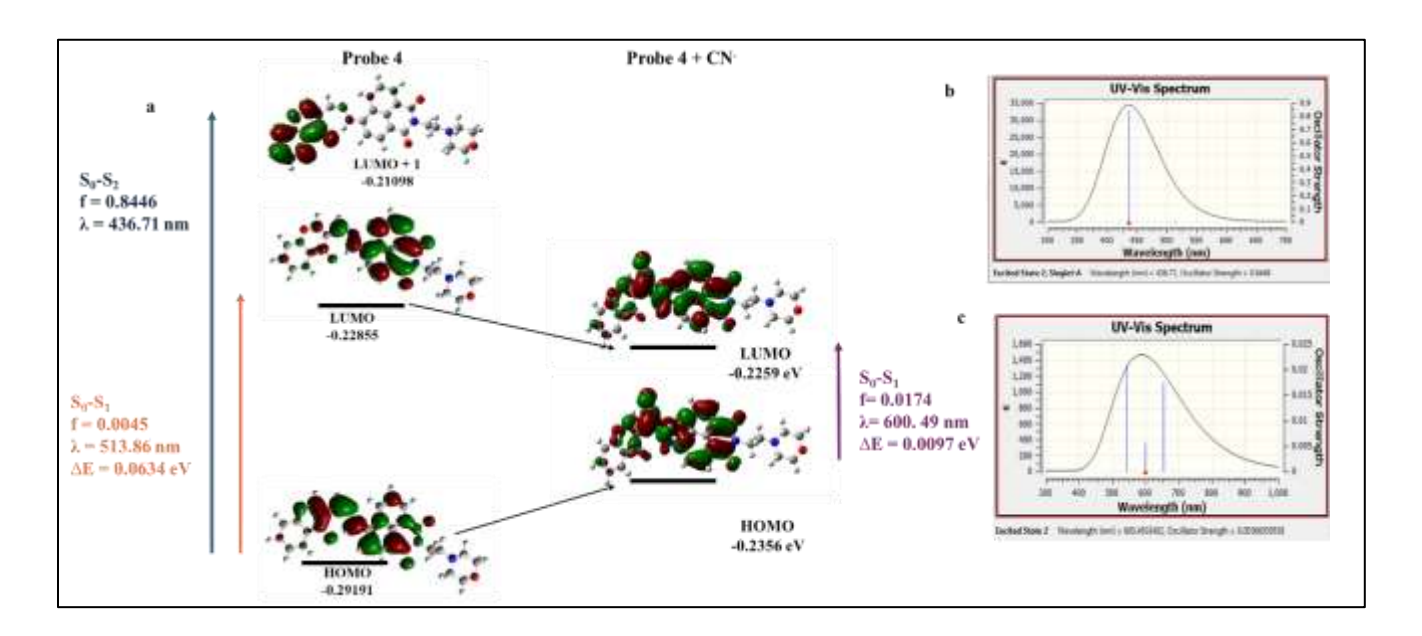


Figure 6.14: a) Frontier Molecular Orbitals (FMOs) of probe **4** and probe **4** + CN⁻ complex; simulated UV-Vis spectrum of b) probe **4** and c) probe **4** + CN⁻ complex

The above transition involves the transition from HOMO \rightarrow LUMO+1 with a shift in electron density from the chromone unit to the naphthalimide ring exhibiting π - π * electronic transition. It was noticed that the electron density in HOMO is mainly localized on the naphthalimide ring while in the case of LUMO+1 the electron density shifted towards the chromone moiety. This significant shift in the HOMO and LUMO+1 energy level confers the prevalence of ICT which is also accountable for fluorescence. Similarly, the vertical excitations

were calculated for the CN⁻ complex. For the complex, the vertical excitations of transitions $S_0 \rightarrow S_1$, $S_0 \rightarrow S_2$, and $S_0 \rightarrow S_3$ were calculated at 600.49 nm (f = 0.0174), 543.37 nm (0.0057), and 419.91 nm (f = 0.0209), respectively. The transition $S_0 \rightarrow S_1$ for the complex exhibits a theoretical absorption wavelength of 600.49 nm (**Figure 6.14c**), which is very close to the experimental results i.e., 595 nm (**Table 6.2**). The addition of CN⁻ distorts the planarity of the molecule, thereby localizing the electron density mainly on the naphthalimide moiety. This further suppresses the charge transfer process, leading to weak fluorescence. Further, the HOMO-LUMO energy gap decreased from 0.0634 eV to 0.0097 eV in the case of probe 4 and its complex with CN⁻ ions, respectively, resulting in the redshift, which corroborates the experimental results (**Figure 11**).

6.10. Multiwave Function Analysis of Probe 4 and its Complex

ELF and LOL study can be utilized to investigate the molecular orbital and its localization in the probe and its complex¹³⁰. This topological analysis explicit electrical characteristics, specifically the localization and delocalization of molecular structure, accompanied by its stability¹³¹. In **Figure 6.15 and 6.16**, the deep blue color in the background represents the absence of electrons, the red color indicates the localization of electrons, while the bright blue indicates the delocalization of electrons¹³². The delocalized electrons exhibit stability as demonstrated by a greater number of resonance structures. The number ranging from 0.000 to 1.000, along with the color chart from deep blue to red, indicates the probability of electrons occupying specific orbitals. In Figure **6.15a**, the electrons are mainly localized on the H atom indicated by the red color in the probe, while the delocalization between the chromone and naphthalimide is represented by the green color of the heavy elements including carbon, nitrogen, and oxygen atoms.

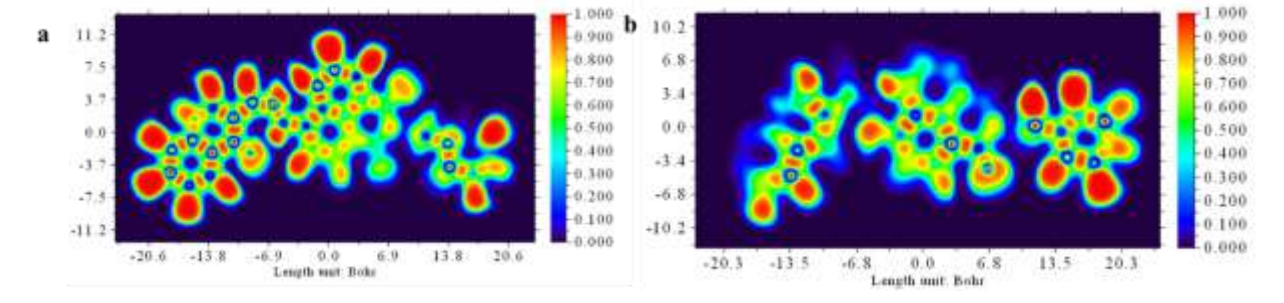


Figure 6.15: ELF diagrams of a) probe 4 and b) probe 4 + CN complex

On the other hand, this delocalization of electrons between the chromone and naphthalimide moiety inhibits its complexation with the CN⁻ ion (Figure 6.15b). This further supports the inhibition of the ICT phenomenon occurring in probe 4. Furthermore, the LOL analysis revealed weak and strong π -delocalized orbitals indicated by blue and red color respectively on the color map of the probe and complex respectively ^{133, 134}. The scale ranging from 0.000 to 0.800 represents the extent of π orbital delocalization with color scale from blue to red depicting weak to strong delocalization (Figure 6.16). In the probe, a strong π -delocalized orbital between the naphthalimide and chromone unit is observed while ranging from 6.9 to -20.6 Bohr. On the other hand, the delocalization between the two units gets disturbed upon complexation as displayed by two separate patches of green-colored units depicting chromone and naphthalimide respectively between 6.8 and -17.5 Bohr approximately.

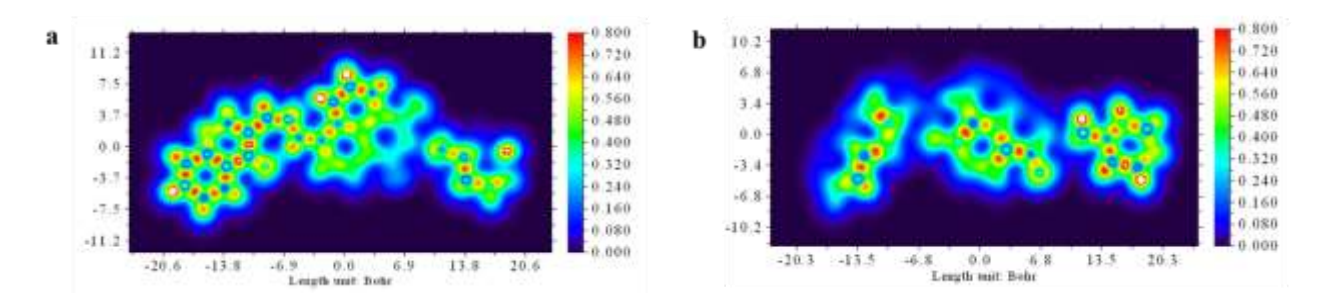


Figure 6.16: LOL diagrams of a) probe 4 and b) probe 4 + CN⁻ complex

6.11. Practical Applicability of Probe 4

6.11.1. Test strips

For practical applications, the test strips method was employed for the detection of CN⁻ ions. The Whatman filter paper was allowed to be soaked in the solution of probe 4 to prepare the test strips ¹³⁵. The test strips were golden brown in visible light, mint green under short UV rays, and lemon yellow under long UV rays. When treated with CN⁻ ion the color changes to iris purple in visible light, turquoise under short UV rays, and indigo under long UV rays. These findings suggest that the probe can serve as a test strip for the detection of CN⁻ ion (**Figure 6.17**).

6.11.2. Smartphone analysis

For this, the free mobile app (Color Picker) was downloaded on Android (RedmiNote 10T 5G) and the photographs were clicked following the procedure as reported in the literature ¹³⁶. The photos were clicked before and after the addition of CN⁻ ions. In addition, the Red/Green (R/G ratio) was

studied with each successive addition of the ion (0-4 equiv.). Good linearity was observed between the R/G value and the concentration of CN^- ions ($R^2 = 0.989$) with a detection limit of 13.27 μM . Therefore, smartphone analysis guarantees inexpensive and real-time application to detect CN^- ions (**Figure 6.18**).

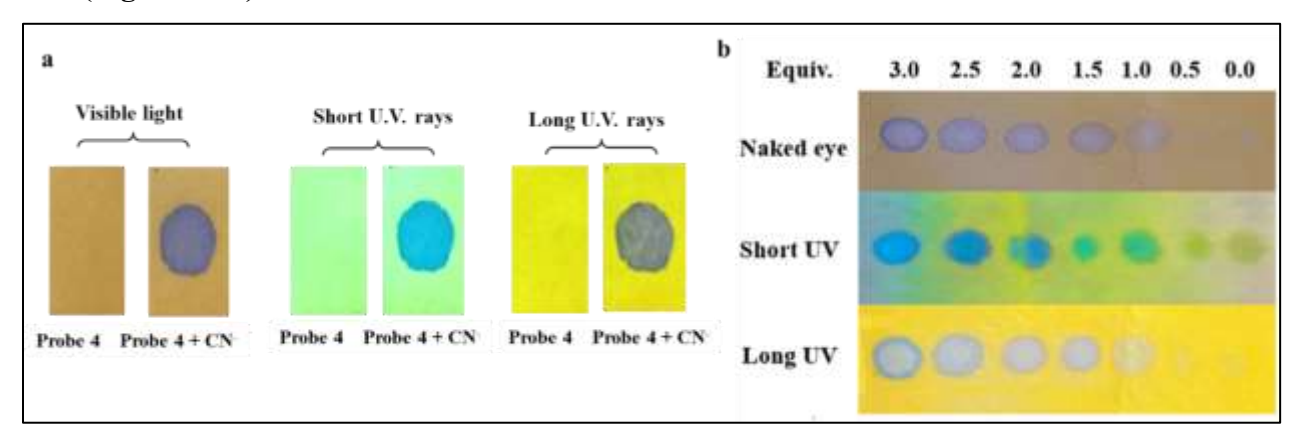


Figure 6.17: a) Test strip of probe 4 and with CN⁻ ions in visible light, under short UV rays, and long UV rays; b) concentration-dependent performance of test strips from 0.5-3.5 equv.

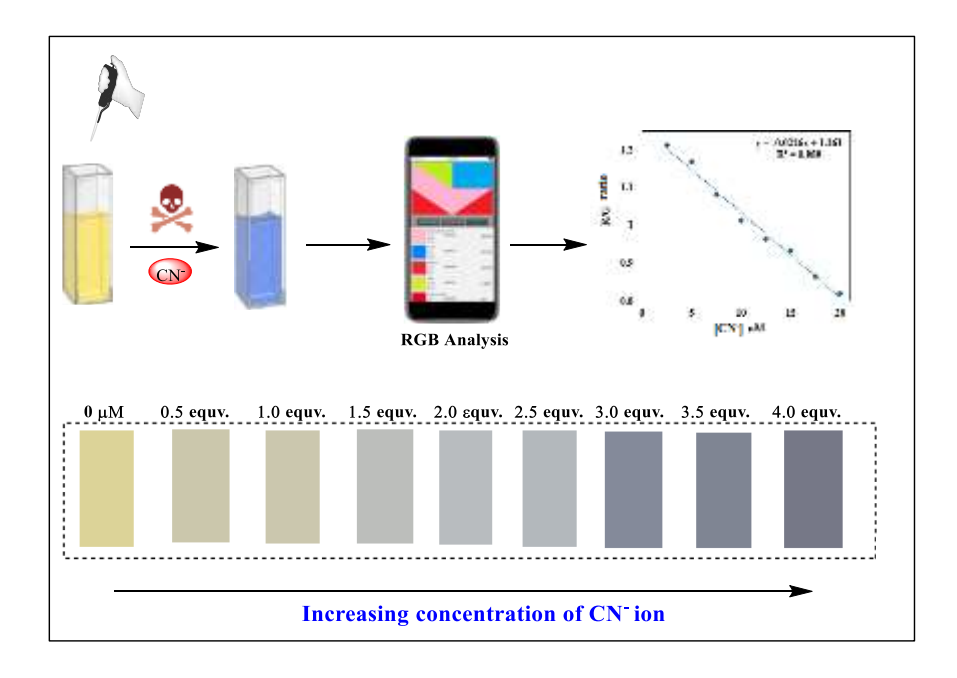


Figure 6.18: Smartphone-based application of probe 4 to detect CN⁻ion.

6.11.3. Designing of logic gate and molecular keypad

In the recent few years, logic gates have gained a lot of attention by researchers. Therefore, we also built a combinatorial molecular circuit for IMPLICATION (IMP) and INHIBIT (INH), which could be attributed to the reverse reactions of the probe 4 complex in the presence of TFA. The

logic circuit diagram along with its corresponding truth table, is illustrated in **Figure 6.19**. The addition of CN⁻ ion to the system leads to input I while the addition of TFA leads to input II. Both the output signals- output I (460 nm) and output II (595 nm) were devised through absorbance signals. The binary codes '0' and '1' illustrate the chemical shift as input or output. For probe 4, the absorbance threshold was determined to be 0.05.

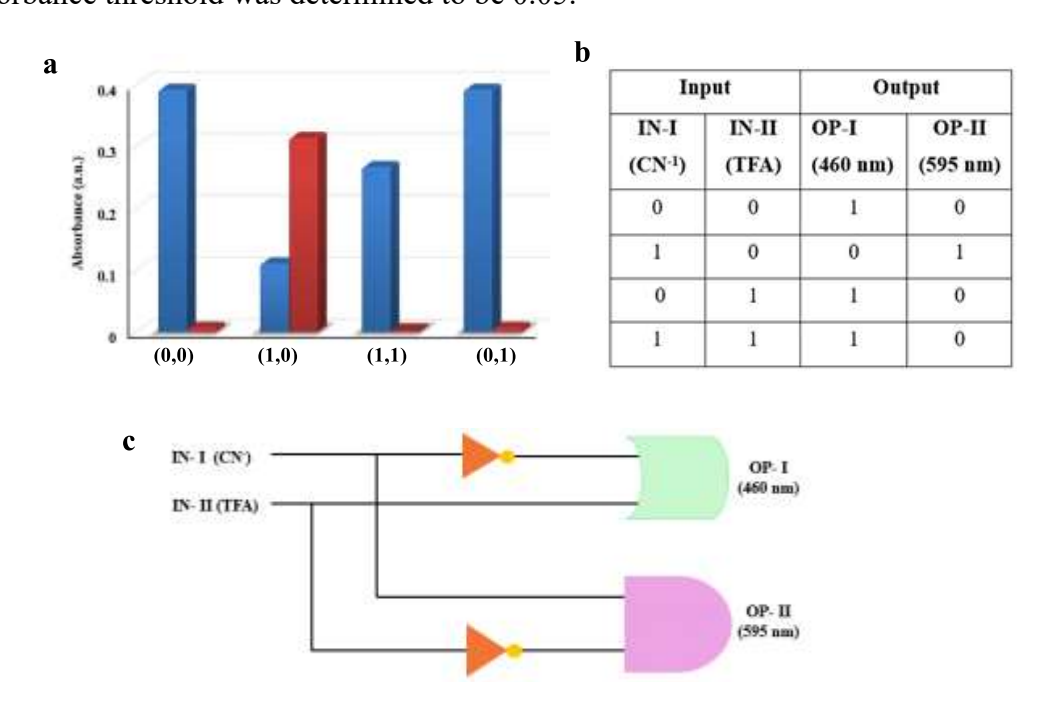


Figure 6.19: Logic gate construction a) absorbance output signals after various chemical inputs; b) truth table; c) logic gate circuit diagram

The ON-OFF switch correlates to the binary codes. In the non-availability of CN⁻ ion and TFA in the system, *i.e.*, no input I and input II, or in the presence of TFA there is no absorbance at 595 nm, which turns "OFF" the system. On the other hand, in the presence of CN⁻ ion, when input I is 1 and input II is 0, there is absorbance at 595 nm, which switches "ON" the system thereby exhibiting interaction between probe 4 and CN⁻ ion. This exhibits that its output II signal turns "ON" the system. These results led to the development of the INH logic gate at 595 nm. To examine the performance of probe 4 with CN⁻ ion and TFA, another logic gate was also *i.e.*, IMP was obtained. An output signal 1 at 460 nm indicates that the system is turned "ON" while there is no input (0,0) or only one input II there (0,1). The system turns "OFF" in the presence of input I (1,0) while in the presence of both the input (1,1), it further switches "ON". As a result, complementary INH/IMP logic operations for probe 4 were successfully demonstrated, highlighting its potential application

in molecular devices. These operations showcase the ability of probe 4 to function as a molecular switch, effectively responding to the presence of the CN⁻ ion and enabling the manipulation of the output signals based on input signals. This capability underscores the versatility of the probe in the development of advanced molecular systems, paving the way for innovative applications in sensing and information processing. Since probe 4 exhibits maximum absorption at 460 nm and at 595 nm on addition of CN⁻ ions, hence sequential input for probe and CN⁻ ion could be used as code for molecular keypad lock for molecular traffic signals for two chemical inputs. These observations inspire us to explore probe 4 to construct molecular keypad lock. To develop this, input 1 and input 2 was assigned 'A' and 'D' and the output signals at 460 nm and 595 nm were assigned 'O' and 'R'. Now, key 'E' is utilized to 'open' the locked state of system. Now the password that would open the lock state of system through chemical inputs will be "ADORE". Also, it was observed that the addition of TFA shifts the absorption wavelength back to original i.e. at 460 nm. Therefore, to lock the molecular keypad the input 1 would be assigned as 'H' with output signal at 460 nm assigned as 'E'. Now, key 'R' is utilize to 'switch-off' or 'lock' the molecular keypad. So, the password to lock the molecular keypad through various chemical inputs will be "HER" (Figure 6.20).

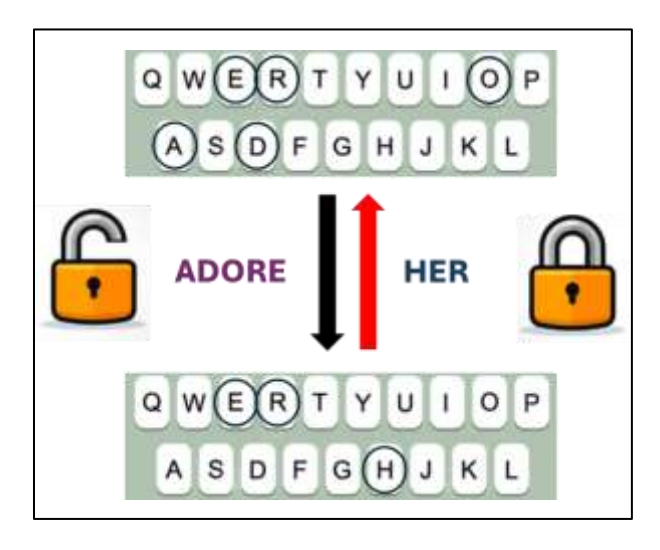


Figure 6.20: Keypad lock for assessing secret password generated by sequential chemical inputs

6.12. Conclusion

A highly selective naphthalimide-derived probe 4 was synthesized to detect CN⁻ ion using DMSO: H₂O (4:1, v/v) as the medium. Probe 4 exhibits "naked-eye" changes on adding CN⁻ ion from

yellow to blue. Also, the addition led to the shift of the band towards a longer wavelength at 595 nm. The fluorescence spectra reveal an emission peak at 560 nm which significantly decreases with the addition of CN⁻ ion which could be attributed to ICT inhibition. In addition, the TD-DFT study reveals the localization of HOMO electrons on the naphthalimide ring which shifts towards the chromone unit in LUMO+1 state exhibiting the prevalence of ICT which significantly got inhibited with the addition of CN⁻ ions leading to fluorescence quenching due to distortion in its planarity. Further, the stoichiometric ratio was calculated by Job's plot analysis revealing a 1:1 ratio. It was additionally supported by FT-IR, mass spectrometry, and ¹H-NMR titrations revealing the nucleophilic addition of CN⁻ ion across the C=N bond. The ELF and LOL studies were done to examine the topological analysis explicating electrical characteristics, specifically the localization and delocalization of molecular structure, accompanied by its stability. Further, the probe finds its practical application in the test strips analysis and its reversibility with TFA leads to the fabrication of a molecular logic gate. The colorimetric effect expands its application to smartphone analysis and molecular keypad lock.

6.13. Synthesis of Probe 4

6.13.1. Synthesis of intermediate 5:

The compound (3) was synthesized following the procedure outlined in the literature (S1)¹⁰³. The compound 3 was then treated with morpholine in ethanol at reflux conditions, yielding compound 4^{62} . It was further treated with hydrazine hydrate in ethanol at reflux for 5 hours, affording compound 5 as reported in the literature¹³⁷. Compound 4 (1 g, 2.5 mmol) was reacted with hydrazine hydrate (0.15 mL) in ethanol at 40–50 °C for 5 hours. After completion, the reaction mixture was cooled to room temperature, and the solvent was evaporated under vacuum. The resulting precipitate was then filtered and dried. A yellow-orange powder was obtained, which was further washed in ethanol and dried, affording compound 6-bromo-2-(2-morpholinoethyl)-1*H*-benzo[*de*]isoquinoline-1,3(2*H*)-dione (5). Color: Orange; Yield: 67%; Melting point: 256 – 259 °C

6.13.2. Synthesis of probe 4

Further, the compound (5) (0.5 g, 1.30 mmol) was allowed to react with aldehyde 4-oxo-4*H*-chromene-3-carbaldehyde (6) (0.30 g, 1.76 mmol) in ethanol (20 ml) at reflux conditions for 8 h

with a few drops of acetic acid. Once the reaction was complete, the mixture was permitted to cool to room temperature. The resulting precipitates were then filtered and washed with hot ethanol. Further purification of the crude product was done by recrystallizing it in ethanol. The desired product was acquired as solid red precipitates, and the supernatant was discarded. Finally, the red precipitates were obtained as the desired probe **4**, (*E*)-2-(2-morpholinoethyl)-6-(2-((4-oxo-4*H*-chromen-3-yl)methylene)hydrazinyl)-1*H*-benzo[*de*]isoquinoline-1,3(2*H*)-dione. Reddish brown solid, 61% yield; R_f 0.5 (5% methanol in chloroform); mp 285-290 °C; 1 H-NMR (DMSO- d_6 , 500 MHz): 11.59 (ds, J = 21.3 Hz, 1H, NH), 9.02 (ds, J = 3.8 Hz, 1H, CH), 8.81 (t, J = 9.45 Hz, 1H, ArH), 8.60 (d, J = 6.1 Hz, 1H, ArH), 8.49 (m, 1H, ArH), 8.36 (t, J = 7.75 Hz, 1H, ArH), 8.14 (d, J = 7.95 Hz, 1H, ArH), 7.86 (t, J = 7.0 Hz, 1H, ArH), 7.81-7.77 (m, 2H, ArH), 7.73 (d, J = 8.45 Hz, 1H, ArH), 7.56 (t, J = 7.85 Hz, 1H, ArH), 4.17 (s, 2H, ethyl-CH₂), 3.55 (s, 4H, morph-CH₂), 2.58 (2H, ethyl-CH₂, merged with solvent), 2.47 (4H, morph-CH₂, merged with solvent); HR-MS m/z ratio: 497.1819 [M+1] (Figure A13 and A14).

CHAPTER - 7

Synthesis and photophysical study of Naphthalimide appended Benzothiazole (Probe 5)

In this chapter, we synthesized a fluorescent probe (5) based on a naphthalimidebenzothiazole skeleton for selective detection of Fe^{3+} ions. The optical performance of the probe reveals ratiometric behavior with absorption spectroscopy, while a "turn-off" response was noticed with fluorescence spectroscopy in the presence of Fe^{3+} ions. These perturbations could be attributed to the formation of a metal-probe complex, thereby altering the electronic configuration.



Track Your Accepted Article

The easiest way to check the publication status of your accepted article

Synthesis of Naphthalimide-based Benzothiazole as Reversible Fluorescent Probe for the Selective Detection of Fe3+ ion: An Experimental and Computational (LOL/ ELF/ NLO/ DFT/ in silico) Approach

Article reference SAA_127044

Journal Spectrochimica Acta Part A: Molecular and Biomolecular

Spectroscopy

 Corresponding author
 Iqubal Singh

 First author
 Gurdeep Kaur

 Received at Editorial Office
 17 Jul 2025

 Article revised
 9 Sep 2025

 Article accepted for publication
 1 Oct 2025

SPECTROCHIMICA ACTA

ISSN 1386-1425 7

Last update: 8 Oct 2025

Share via email

Share via email

7.1. Introduction

Fluorescent probes have become indispensable tools in chemical, biological, and medical research, owing to their sensitivity, selectivity, and versatility ¹³⁸. These probes are particularly valuable in the detection of metal ions, which are critical for a variety of biochemical processes in living organisms ^{139, 140}. Among the various metal ions, the fourth most abundant metal present on earth, Fe³⁺ (iron) plays a crucial role in several biological functions, including oxygen transport, electron transfer, and enzymatic catalysis ¹⁴¹⁻¹⁴³. It is essential for the proper functioning of haemoglobin and myoglobin, which are responsible for oxygen transport and storage in the human body ¹⁴⁴. However, both iron deficiency and iron overload can have detrimental effects on health ¹⁴⁵. A deficiency of iron leads to anaemia, characterized by fatigue, weakness, and impaired cognitive function, as iron is a critical component of haemoglobin in red blood cells 146, 147. On the other hand, excessive iron levels can lead to iron toxicity, where free iron accumulates in tissues, causing oxidative stress and damage to organs such as the liver, heart, and pancreas ¹⁴⁸. This is particularly concerning in conditions like hemochromatosis, where excessive iron accumulation can lead to tissue damage and the development of chronic diseases ¹⁴⁹. Fluorescent probes have emerged as effective tools for detecting iron levels due to their high sensitivity, selectivity, and ease of use ¹⁵⁰. These probes often utilize a "turn-off" fluorescence mechanism, where binding of Fe³⁺ to the probe results in a significant decrease in fluorescence intensity, providing a clear and real-time signal ¹⁴¹, ¹⁵¹. This approach enables accurate, non-invasive monitoring of iron imbalances, aiding in the detection of iron deficiency or overload in biological systems.

This study investigates a naphthalimide-appended benzothiazole-based fluorescent probe (probe 5) with high selectivity for Fe³⁺ ion detection. The optical study of the probe 5 was investigated using absorption and emission spectroscopy. The probe 5 exhibits a "turn-off" fluorescence response upon binding with Fe³⁺ ions, allowing for rapid and sensitive detection of iron. The unique structural features and binding characteristics of probe 5 highlight its potential as a valuable tool for monitoring Fe³⁺ levels in biological systems, providing a platform for future research and applications in metal ion sensing. Additionally, the DFT study was performed to explore the HOMO-LUMO energy levels which further reveal various parameters including, ionization potential (I), electron affinity (A), global hardness (n), softness (s), chemical potential (μ), electrophilicity (Ω), and electronegativity (χ). The findings of this study lay the groundwork

for the development of highly efficient, selective, and multifunctional probes, offering new perspectives in both chemosensing and therapeutic applications.

7.2. Synthesis of Probe 5

The synthesis of 6-bromo-1H,3H-benzo[de]isochromene-1,3-dione (1) was done as reported in the literature¹⁵². Further, compound 1 reacted with 5-methoxybenzo[d]thiazol-2-amine (2) in the presence of triethylamine (TEA) in ethanol, and the reaction mixture was heated to reflux temperature. The precipitates formed were allowed to cool at room temperature, yielding 6-bromo-2-(5-methoxybenzo[d]thiazol-2-yl)-1H-benzo[de]isoquinoline-1,3(2H)-dione (3). Compound 3 was then treated with morpholine in methoxyethanol at reflux conditions for 13 h, yielding probe 5 (Scheme 7.1). The structure of the molecular probe was characterized using spectroanalytical techniques such as ¹H-NMR, ¹³C-NMR, and Mass Spectrometry.

Scheme 7.1: Synthetic scheme for the synthesis of probe 5

7.3 Spectroscopic Analysis of Probe 5

7.3.1. Photophysical properties of probe 5

The photophysical properties of probe **5** were examined using absorption and fluorescence spectroscopy. Probe **5** (20 µM) was studied using solvents of different polarities, including chloroform, THF, acetonitrile, and methanol. It was noticed that with increasing polarity, the band shifts to longer wavelengths in both the absorption and emission spectra. This could be attributed to more stabilization of the excited state in comparison to the ground state on increasing the polarity of the solvent, hence shifting to a longer wavelength ¹⁵³. The absorption spectrum merely revealed a bathochromic shift of 12 nm (**Figure 7.1a**), while a significant shift was observed in

emission spectra (43 nm) on varying the polarity of solvents from non-polar to polar. Also, the emission spectrum reveals the broadening of bands with increasing polarity (**Figure 7.1b**). Remarkably, the non-polar solvents exhibit enhanced fluorescence in comparison to the polar solvents. Furthermore, this implies the prevalence of the ICT phenomenon in the moiety in asymmetric D-A (Donor-Acceptor) systems ¹⁵⁴.

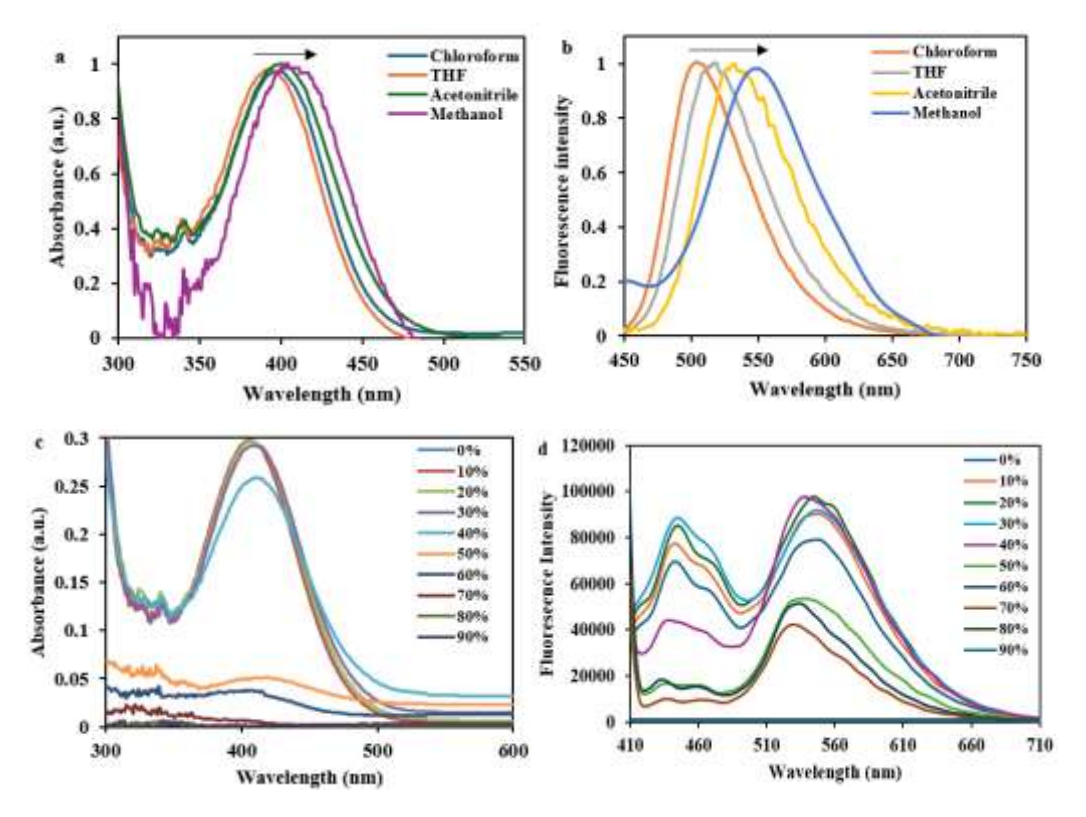


Figure 7.1: a) Absorption spectra and b) emission spectra of probe 5 in different solvent systems; c) absorption spectra and d) emission spectra of probe 5 in DMSO/H₂O mixture with different water fractions

In addition, the aggregation-induced emission spectrum was studied by absorption and emission spectroscopy in a binary mixture of DMSO/H₂O with varying water fractions. In this solvent system, the water serves as a poor solvent, so the aggregation response aggrandizes. The absorption spectrum revealed no significance till the 30% water fraction, while a decrease in intensity at 40% was observed with a prominent level-off tail in the spectrum with a slight shift towards the longer wavelength, while further increasing the water fraction, probe 5 started precipitating, and the absorbance intensity started dwindling and approached zero at 90% (Figure 7.1c). On the other hand, the emission spectra revealed two bands centered at 445 nm and 460 nm. With the increase in water fractions, a concomitant increase in fluorescence intensity was observed

at 445 nm, while the changes in the band at 460 nm initially increased and became stable at 40% water fraction, with the highest emission revealing the AIE response at this water fraction. On further increasing the water fractions, a blue shift was noticed due to its insolubility in water mixtures (Figure 7.1d).

7.3.2. UV-visible absorption studies of probe 5

Spectroscopic studies were performed to scrutinize the sensing of metal ions. For this, the UVvisible absorption study of free probe 5 was carried out, revealing a band at 400 nm attributed to π - π * transitions. Further, the addition of metal ions (Al³⁺, Fe³⁺, Cs²⁺, Cu²⁺, Co²⁺, Ni²⁺, Zn²⁺, Hg²⁺, Pb²⁺, Fe²⁺, Mn²⁺, and Cd²⁺) (5 equiv.) to probe **5** (20 μM) was performed to determine the sensing ability using MeOH as a medium. Amongst the ions, the appearance of a new band at 365 nm was observed for Fe³⁺ ions with a concurrent increase in absorption intensity. In contrast, no other metal ion exhibits any noticeable change (Figure 7.2a). Further, the UV-visible titration studies were performed with Fe³⁺ ions to determine the plausible binding mechanism. With each successive addition of Fe³⁺ ion (0-2.5 equiv.) into the free probe solution, the absorbance at (λ_{abs}) 400 nm of the probe exhibits a blue shift to 365 nm ($\Delta\lambda = 35$ nm) with a concomitant increase in intensity. A plateau in absorption was observed after the addition of 2.5 equivalents of ion, suggesting its saturation (Figure 7.2b and c). However, it was observed that the competitive ions exhibit negligible interference from other ions, revealing the selectivity and specificity of probe 5 towards Fe³⁺ ions (Figure 7.2d). In addition, the complexation mechanism was determined by utilizing the continuous variation method, revealing a 1:1 stoichiometric ratio between the probe 5 and Fe³⁺ ions (Figure 7.22e), which was further supported by the straight line of the Benesi-Hildebrand plot between $1/I-I_0$ and $1/[Fe^{3+}]$ ions reveals the binding constant of $1.62 \times 10^5 \,\mathrm{M}^{-1}$ (Figure 7.22f).

7.3.3. Fluorescent spectroscopic studies of probe 5

The fluorescent behavior of probe **5** (20 μ M) in MeOH was subsequently explored. The free probe **5** solution revealed an emission band at (λ_{em}) 550 nm on excitation at (λ_{ex}) 400 nm with a slit width of 5 mm. Upon addition of 5 equiv. of metal ions (Al³⁺, Fe³⁺, Cs²⁺, Cu²⁺, Co²⁺, Ni²⁺, Zn²⁺, Hg²⁺, Pb²⁺, Fe²⁺, Mn²⁺, and Cd²⁺) to probe **5**, a significant quenching was observed with the addition of Fe³⁺ ions (**Figure 7.3a**), whereas no other metal ion displayed any observable change. The fluorescence intensity decreased by 3-fold on the addition of Fe³⁺ ions. The quenching could be attributed to probe-metal charge transfer (LMCT) between probe **5** and the Fe³⁺ ion. Also, a

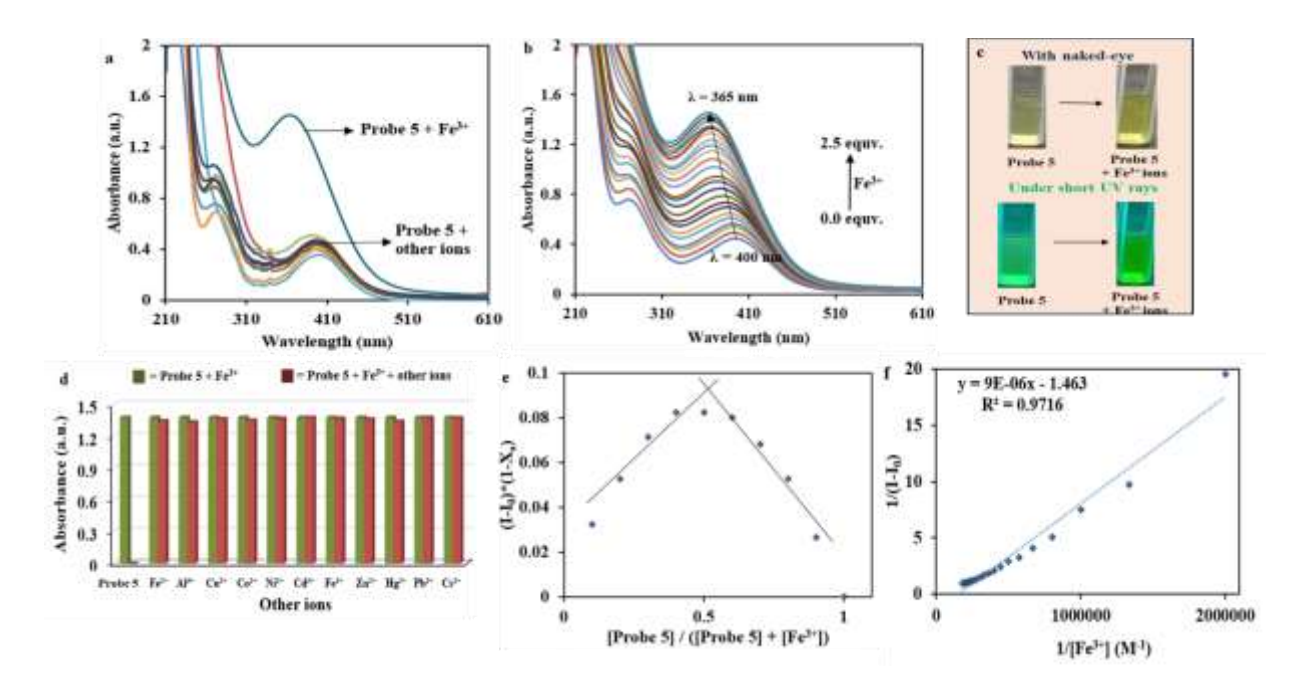


Figure 7.2: The UV-vis spectral analysis of a) probe **5** (20 μM) in response to 5 equiv. of different metal ions (Al³⁺, Fe²⁺, Cs²⁺, Cu²⁺, Co²⁺, Ni²⁺, Zn²⁺, Hg²⁺, Pb²⁺, Fe²⁺, Mn²⁺, and Cd²⁺) in MeOH as a medium; b) titration of probe **5** (20 μM) with incremental addition of Fe³⁺ ions form 0–2.5 equiv. was investigated using MeOH as a medium: c) changes in probe **5** on addition of Fe³⁺ ions with naked eye and under short UV-rays; d) Interference study of the probe **5** and its Fe³⁺ complex in the presence of other ions (in excess); e) Job's plot for the determination of stochiometric ratio between the probe **5** and its metal complex; f) Benesi-Hilderbrand plot for the determination of association constant.

noticeable change from fluorescent neon to colorless was observed with each addition of Fe³⁺ ions under a UV light, while no perturbations were observed when other metal ions were added. Furthermore, fluorescence titration involving quenching by Fe³⁺ ions was performed as depicted in **Figure 7.3b**, and when its concentration reached a maximum (2.0 equiv.), saturation was attained with minimum fluorescence. Further, the CIE 1931 chromaticity diagram reveals coordinates for probe **5** in the neon green region (0.38, 0.52), while on complexation with Fe³⁺ ions, the coordinates shift in the lime green region (0.37, 0.47) (**Figure 7.3c**). In addition, the fluorescence response of probe **5** on the addition of Fe³⁺ ions was noticed under long UV-rays, which reveals a significant decrease in fluorescence (**Figure 7.3d and e**). Also, the varying concentrations of Fe³⁺ ions reveal a strong linear relationship between the metal ion concentration and emission intensity. The limit of detection (LOD) was determined to be 1.05 μM, while the limit of quantification (LOQ) was found to be 3.52 μM (**Figure 7.3f**). The quenching in the

emission intensity leads to the determination of the Stern-Volmer quenching constant (K_{SV}), which was found to be 6.87×10^5 M. The linear S-V plot indicates static quenching, which could be attributed to the formation of the ground-state charge-transfer complex. Moreover, the correlation coefficient (R²) was calculated to be 0.9548, as determined *via* regression analysis (**Figure 7.3g**). In addition, the value of the linear quenching rate constant (k_q) of probe 1 was found to be 4.29 × 10^{14} M⁻¹s⁻¹ much higher than the dynamic collision ($\approx 10^{10}$ M⁻¹s⁻¹). This indicates that the quenching process was not regulated by the collision process; rather, it is derived from the complex formation between probe 1 and Fe³⁺ ions, revealing the possibility of static interaction ⁸⁶. The fluorescence quenching efficiency (η) was calculated to be 60% (**equation 5**). Also, the quantum yield (ϕ) of probe 1 and its complex was determined to be 0.0069 and 0.0008, respectively (**equation 6**) (**Figure 7.4**). This demonstrates further quenching of the probe on the addition of Fe³⁺ ions.

In addition, the fluorescence quenching efficiency (η) was found to be 60%.

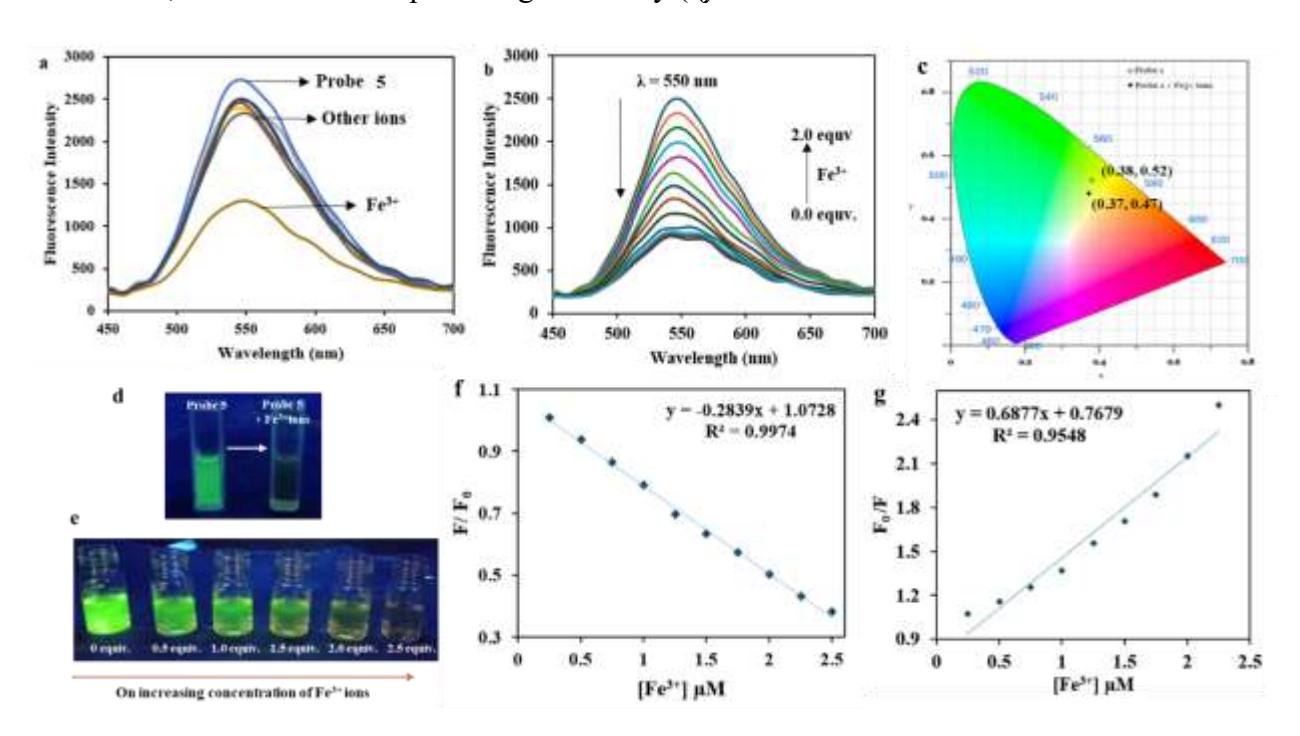


Figure 7.3: The fluorescence spectral analysis of a) probe **5** (20 μ M) in response to 5 equiv. of different metal ions (Al³⁺, Fe³⁺, Cs²⁺, Cu²⁺, Co²⁺, Ni²⁺, Zn²⁺, Hg²⁺, Pb²⁺, Fe²⁺, Mn²⁺, and Cd²⁺) in MeOH as a medium; b) titration of probe **5** (20 μ M) with incremental addition of Fe³⁺ ions form 0 – 2 equiv. was investigated using MeOH as a medium; c) CIE 1931 chromaticity diagram of probe **5** and its Fe³⁺ complex; Fluorescent changes in d) probe **5** on addition of Fe³⁺ ions, e) with increasing concentration of Fe³⁺ ions under long UV-

rays; e) f) A linear plot between F/F_0 v/s concentration of Fe^{3+} ions for the determination of LOD and LOQ; g) Stern-Volmer plot for the calculation of the Stern-Volmer quenching constant

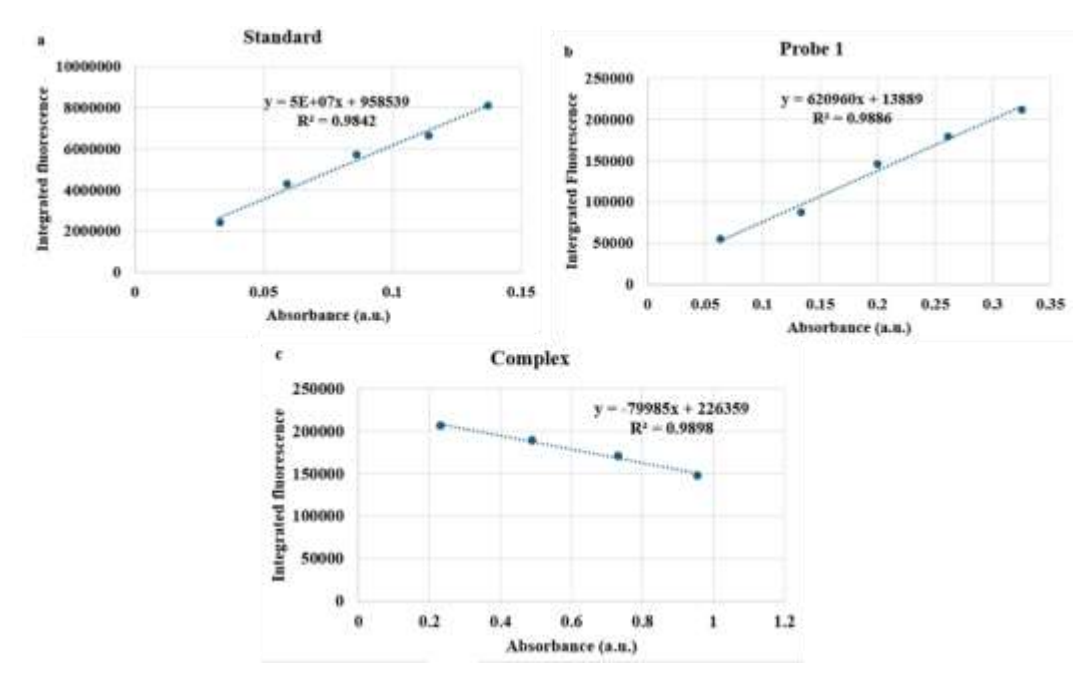


Figure 7.4: Graph of intergrated fluorescence v/s absorbance for determination of quantum yield **7.4. Reversibility Study**

The reversibility of probe **5** was examined with EDTA. It was noticed that the free solution of probe **5** revealed an absorption band at 400 nm. On the addition of Fe³⁺ ions, the absorption band of the probe shifts to 365 nm with an increase in intensity. By adding 10 µl of 1×10⁻¹ M solution of EDTA, the absorption band of probe **5** was regained, indicating the reversal reaction between probe **5** and Fe³⁺ ions. The newly emerged band at 365 nm disappeared with the reappearance of the original band at 400 nm, suggesting that EDTA successfully reversed the reaction. To further confirm this reversibility, several cycles were conducted with repeated additions of EDTA. Each cycle demonstrated consistent changes in the absorption spectrum, reinforcing the idea that EDTA acts as a reliable agent for reversing the reaction dynamics (**Figure 7.5**).

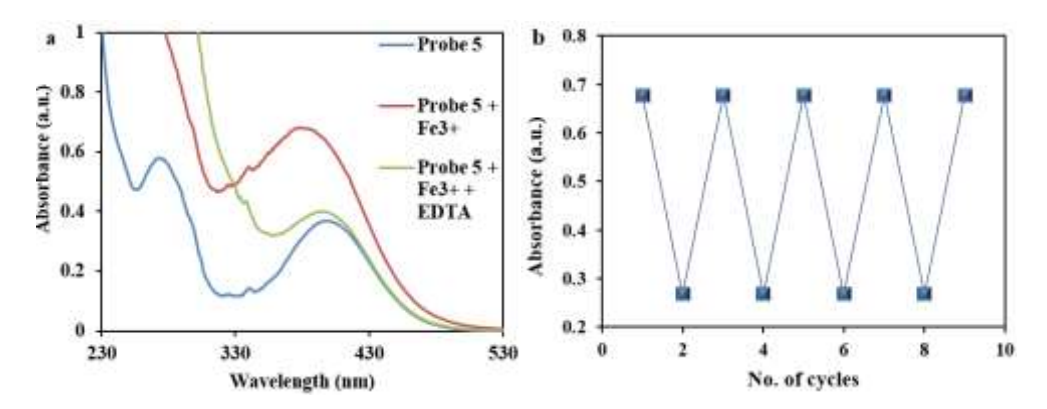
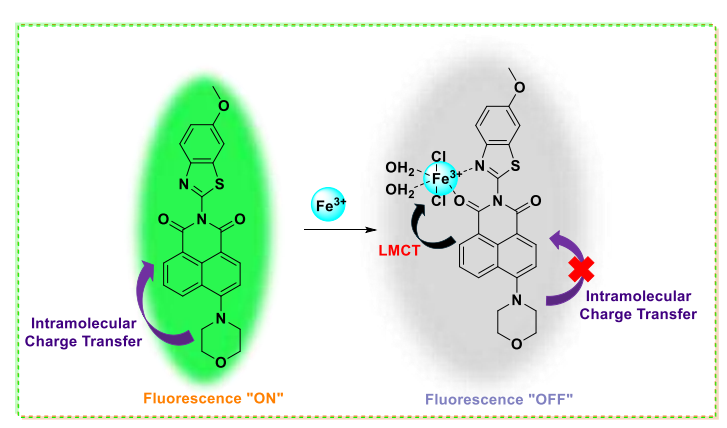


Figure 7.5: a) Reverse reaction of probe 5 (20 μ M) in MeOH in the presence of Fe³⁺ ion (2 μ l) and EDTA (0.12 mL); b) reversible absorbance signal at 400 nm of on repetitive addition of Fe³⁺ and EDTA

7.5. Binding Mechanism

The interaction between probe **5** and Fe³⁺ ions confers significant information about the probe's behavior towards the Fe³⁺ ions. The binding mechanism was investigated by using Job's plot, where the complexation ratio was exhibited by showing maximum absorbance at 0.5 mole fraction, indicating the 1:1 binding. Additionally, the linear curve exhibited by the B-H plot further confirmed the 1:1 stoichiometric ratio. The analysis proposed a plausible mechanism, as shown in **Scheme 7.2**. The HR-MS analysis was carried out to support complexation. The free probe **5** revealed the m/z ratio [probe **5** + H]⁺ peak at 446.1167. Further, on binding with Fe³⁺ ions, the m/z ratio of [probe **5** + H]⁺ was found at 609.6544 for the complex (**Figure S4**).



Scheme 7.2: Plausible binding mechanism of probe **5** for the detection of Fe³⁺ ions

7.6. Time-Dependent Study

To ensure the accuracy of the experiment, time-dependent absorption measurements were conducted on probe 1 and its complex with Fe³⁺ ions. A time course study was conducted in the

absence and presence of a metal ion, followed by the subsequent recording of UV-Visible data. It was then observed that the absorption of probe 1 and its complex remains consistent over time, ranging from 0 to 8 minutes. The outcome indicates that there is no significant difference in the intensity across different time periods, revealing the stability of the probe (**Figure 7.6**).

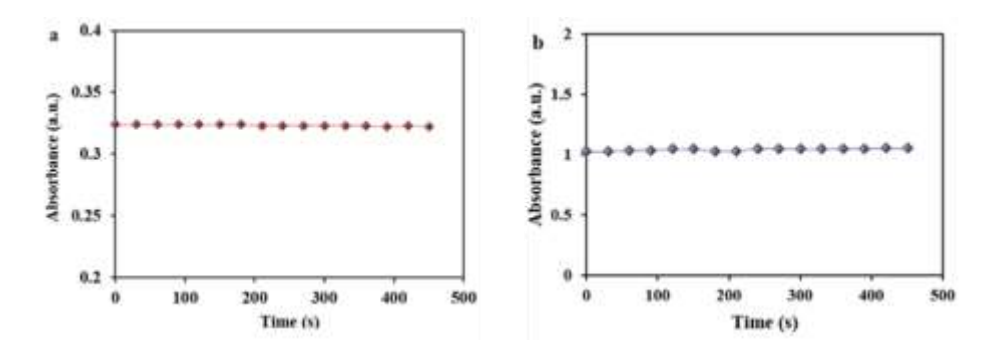


Figure 7.6: Time-dependent UV-Visible study of a) probe 1 and b) probe $1 + Fe^{3+}$ ions

7.7. Fluorescence Lifetime Analysis

Further to study the interaction between probe 1 and Fe³⁺ ions, fluorescence lifetime measurements of probe 1 in free form and in the presence of Fe³⁺ were investigated using time-resolved emission spectra (TRES) analysis. In the ground state quenching phenomenon, there is a negligible change in the quenching process, while it would cause perturbations in the excited state.

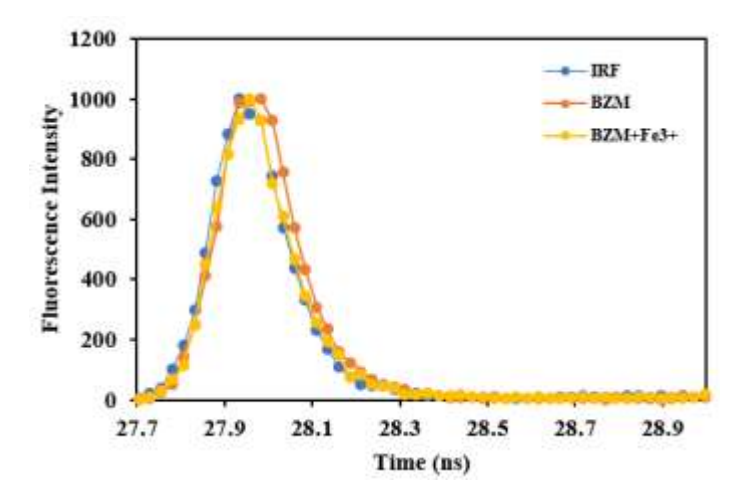


Figure 7.7: Fluorescence life-time spectra of probe 1 and probe $1 + Fe^{3+}$ ions

The value of the average decay time (**Table 7.1 and Figure 7.7**) was calculated with the help of equation 7. The fluorescence lifetime of probe 1 was found to be 0.16 ns, which significantly decreased to 0.09 ns on coordination with Fe³⁺ ions. This drastic decrease in the fluorescence lifetime suggests an efficient electron transfer process between probe 1 and Fe³⁺ ions, leading to

rapid deactivation of the excited state¹⁵⁵. Also, the decrease in average fluorescence decay could be attributed to the interaction between probe 1 and Fe^{3+} ion, leading to a decrease in radiative decay (k_r) and an increase in non-radiative (k_{nr}) decay compared to probe 1 (equation 8 and 9), as depicted in Table 7.2.

Table 7.1: Fluorescence lifetime decay probe 1 and probe $1 + Fe^{3+}$ ions

Compound	$\tau_1(ns)$	α_1	τ_2 (ns)	α_2	τ ₃ (ns)	α ₃	τ ₄ (ns)	α4	χ^2
Probe 1	0.06	0.00	0.17	0.00	0.16	0.50	0.16	-0.50	1.01
Probe 1 + Fe ³⁺	0.04	0.00	0.09	0.50	0.09	-0.50	12.06	0.00	1.69

 $[\]chi^2$ is the goodness of fit

Table 7.2: Average fluorescence decay time, quantum yield, radiative decay, and non-radiative decay of probe 1 and its complex

Compound	τ (ns)	ф	$\frac{k_r}{(\times 10^8 \text{ s}^{-1})}$	k_{nr} (× 10 ⁸ s ⁻¹)	χ^2
Probe 1	0.16	0.0069	23.18	6.24	1.01
Probe 1 + Fe ³⁺	0.09	0.0008	0.008	11.11	1.69

 $[\]chi^2$ is the goodness of fit

7.8. Density Functional Theory

7.8.1. Frontier Molecular Orbital Approach

The geometry optimization of probe **5** and its complex was done using Gaussian09W software. The structure optimization acknowledges the spatial arrangement of electrons and orbital energies of the Highest Occupied Molecular Orbitals (HOMO) and Lowest Unoccupied Molecular Orbitals (LUMO) for probe **5** and its Fe³⁺ complex were determined as illustrated in **Figure 7.8 a and b**. The HOMO of probe **5** was calculated to be -5.88 eV, while the LUMO was found to be -2.46 eV. On complexation with Fe³⁺ ion, the HOMO is mainly localized on the metal ion. At the same time, the electron intensity in the case of LUMO gets distributed over the probe, indicating intra-ligand charge transfer (ILCT) due to the partially filled *d* orbital of the Fe³⁺ ion. Also, the HOMO-LUMO energies of the probe **5**-Fe³⁺ complex were calculated to be -5.05 eV and -2.13 eV, respectively. The findings revealed that the HOMO-LUMO energy gap (ΔE_{gap}) of the probe, which was found

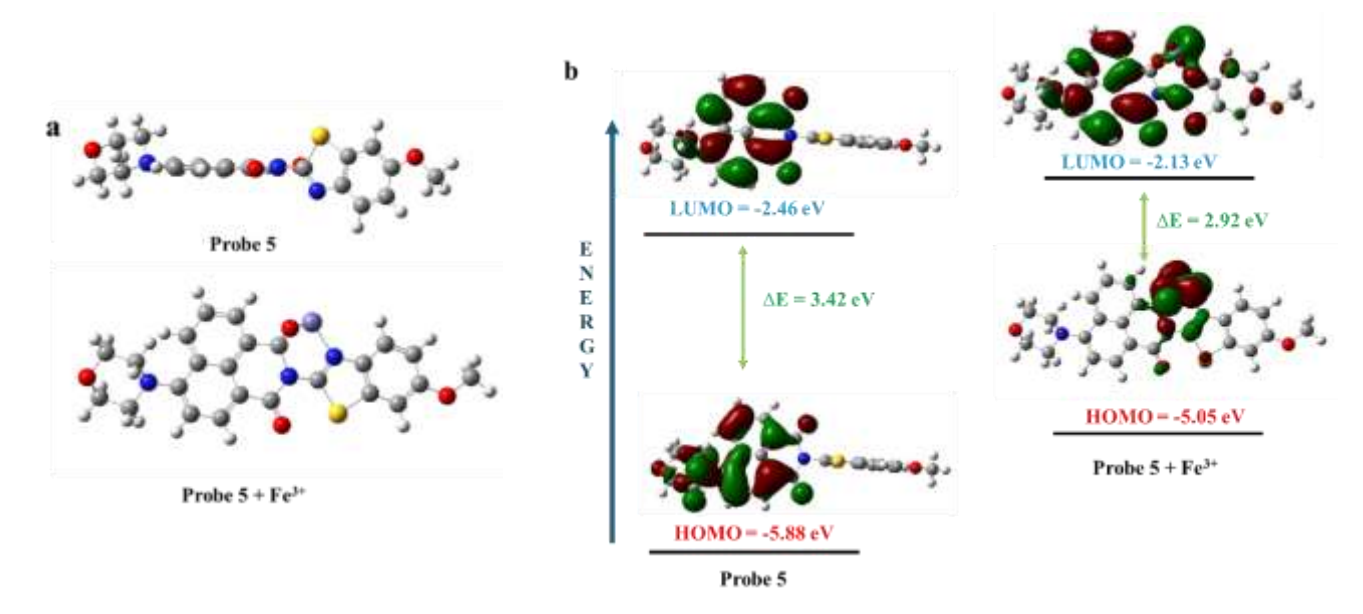


Figure 7.8: a) Optimized geometries and b) HOMO-LUMO energy gap of probe **5** and Fe³⁺ complex calculated by DFT through B3LYP/631-G(d,p) functional set

to be 3.42 eV, decreases to 2.92 eV in coordination with the Fe³⁺ ion, unveiling its most stable configuration. In addition, the theoretical results exhibited quenching in fluorescence intensity, which could be attributed to ligand to metal charge transfer (LMCT) effect. The fluorescence behavior of probe **5** primarily arises due to the electron-donating properties of the morpholine towards the electron-deficient naphthalimide moiety, leading to ICT. However, on complexation with Fe³⁺ ion, the electron density shifts towards the metal center, thereby inhibiting the ICT phenomenon and resulting in fluorescence quenching. The theoretical findings were found to corroborate with the experimental results therefore further validating the studies.

7.8.2. Non-linear optical (NLO) property analysis

The non-linear optical effect is a significant function for optical logic, switching, memory, and modulation. **Table 7.3** indicates the NLO results carried out using the DFT approach computed from the Gaussian 09W software, thereby calculating the first order of hyperpolarizability (β) of the probe describing the optical parameters. The dipole moments (μ) (equation 1), polarizabilities ($\langle \alpha \rangle$) (equation 2), anisotropy of the polarizabilities ($\langle \Delta \alpha \rangle$) (equation 3), and mean first-order hyperpolarizabilities (β) (equations 4 and 5) of the probe were calculated to investigate the impact of the DFT/B3LYP procedure on the NLO attributes of probe 5.

$$\mu = (\mu x^2 + \mu y^2 + \mu z^2)^{1/2} \tag{1}$$

$$\langle \alpha \rangle = \frac{\alpha x x + \alpha y y + \alpha z z}{3} \tag{2}$$

$$\langle \Delta \alpha \rangle = \frac{1}{\sqrt{2}} \sqrt{(\alpha x x - \alpha y y)^2 + (\alpha y y - \alpha z z)^2 + (\alpha z z - \alpha x x)^2 + 6(\alpha x y^2 + \alpha z x^2 + \alpha y z^2)}$$
(3)

$$\beta = \sqrt{\beta x^2 + \beta y^2 + \beta z^2} \tag{4}$$

$$\beta_i = \sum_{i \neq j} \beta i i i + \beta i j j + \beta i k k \tag{5}$$

The computed values obtained from the Gaussian 09W output file have been transformed into electrostatic units (esu) as the mean polarizabilities and mean first-order hyperpolarizability in the output file are presented in atomic units (a.u.), (α : 1 a.u. = 0.1482×10⁻²⁴ esu; β : 1 a.u. = 8.6393×10⁻³³ esu). Using the DFT/B3LYP level, the anisotropy of the polarizabilities ($\langle \Delta \alpha \rangle$) and mean first-order hyperpolarizability (β) in this investigation was determined to be 3.89×10⁻²⁴ and 4.02×10⁻³¹

 Table 7.3: Parameters for the calculation of non-linear optical (NLO) properties of probe 5

Parameters	Symbol	Value	Parameters	Symbol	Value	
(units)	Symbol	v aruc	(units)	Symbol	v aluc	
	μ_x	-5.3773		Bxxx	539.0986	
Dipole	μy	0.1083		Вууу	1.5785	
(Debye)	μΖ	-1.1539		Bzzz	4.5016	
	μ(D)	5.5008		Вхуу	-103.0239	
	Axx	44.5143		Bxxy	-28.7347	
	Ayy	-24.4602	Mean first-	Bxxz	-143.3692	
Polarizabilities	Azz	-20.0540	order hyper-	Bxzz	5.1428	
(α) (a.u.)	Axy	-7.0239	polarizabilities	Byzz	4.4346	
&	Axz	-8.2597	(β) (a.u.)	Вууг	-9.4338	
Anisotropy of	Ayz	3.3380		Bxyz	-10.2809	
the	A	0.0001		β total	466.02	
polarizabilities	$\alpha(e.s.u.)$	1.482×10 ⁻²⁹		β totat	4.02×10 ⁻³⁰	
(Δα)(a.u.)	α(ε.s.u.)	1.402^10		(e.s.u.)	4.02^10	
	Δα	26.30				
	$\Delta \alpha(e.s.u.)$	3.89×10 ⁻²⁴				

esu, respectively. One of the standard probes used to examine the NLO characteristics of molecular systems is urea. As a result, it is widely employed as a cutoff point in comparison analyses. The higher hyperpolarizability values of probe 5 are larger than those of the standard prototype NLO urea ($\langle \Delta \alpha \rangle = 3.8312 \times 10^{-24}$ esu; $\beta = 0.3728 \times 10^{-30}$ esu) (**Table 7.4**), indicating that the chosen probe 5 is showing virtuous NLO properties. The DFT/B3LYP method's β value indicated that the chemical under investigation is a viable option for further research on the characteristics of NLOs.

Therefore, we also built a combinatorial molecular circuit for INHIBIT (INH), which could be attributed to the reverse reactions of the probe **5** complex in the presence of EDTA. The logic circuit diagram, along with its corresponding truth table, is illustrated in **Figure 7.9**. The output signals at 380 nm were devised through absorbance signals. The addition of Fe³⁺ ions to the system leads to input I, while the addition of EDTA leads to input II. The binary codes '0' and '1' illustrate the chemical shift as input or output. For probe **5**, the absorbance threshold was determined to be 0.05. The ON-OFF switch correlates to the binary codes. In the non-availability of Fe³⁺ ion and

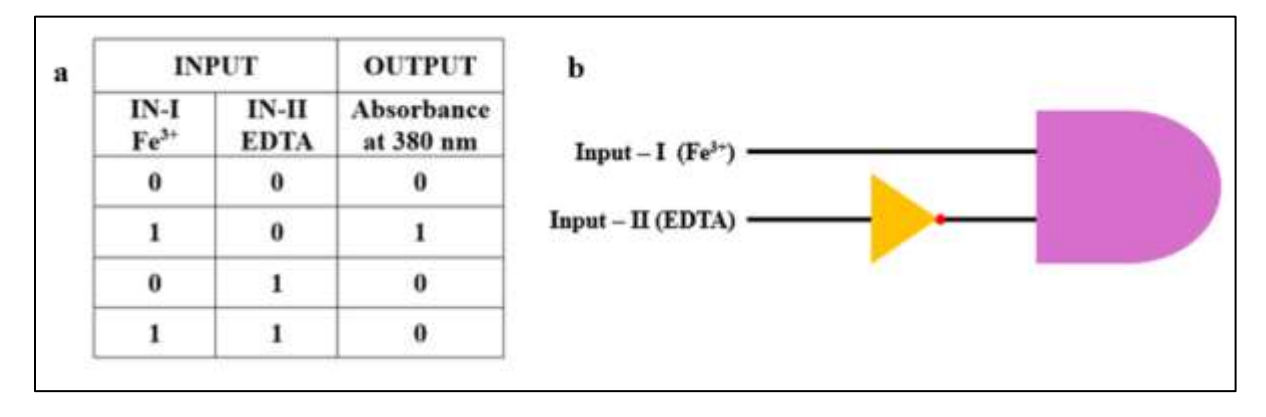


Figure 7.9: a) Truth table of absorbance output signals after various chemical inputs; b) "INHIBIT" logic gate circuit diagram

EDTA in the system *i.e.* no input I and input II, there is no absorbance at 380 nm, which turns "OFF" the system. On the other hand, in the presence of Fe³⁺ ion, when input I is 1 and input II is 0, there is absorbance at 380 nm, which switches "ON" the system, thereby exhibiting interaction between probe 5 and Fe³⁺ ion. An output signal 1 at 380 nm indicates that the system is turned "ON" while there is no input (0,0) or only one input II there (0,1). The system turns "ON" in the presence of input I (1,0) while in the presence of both inputs (1,1), it further switches "OFF". As a result, INHIBIT logic operations for probe 5 were successfully demonstrated, highlighting its potential application in molecular devices. These operations showcase the ability of probe 5 to

function as a molecular switch, effectively responding to the presence of the Fe³⁺ ion and enabling the manipulation of the output signals based on input signals. This capability underscores the versatility of the probe in the development of advanced molecular systems, paving the way for innovative applications in sensing and information processing.

7.8.3. Topological analysis

ELF and LOL study can be utilized to investigate the molecular orbital and its localization in the probe **5** and its complex¹³⁰. This topological analysis of explicit electrical characteristics, specifically the localization and delocalization of molecular structure accompanied by its stability¹³¹. In **Figures 7.10a**, the deep blue color in the background represents the absence of electrons, the red color indicates the localization of electrons, while the bright blue indicates the delocalization of the electrons¹³². The delocalized electrons exhibit stability as demonstrated by a greater number of resonance structures. The number ranging from 0.000 to 1.000, along with the color chart from deep blue to red serves as an indicator of the probability of electrons occupying specific orbitals. The electrons are mainly localized on the H atom indicated by the red color in probe **5**, while the delocalization between the morpholine and naphthalimide is represented by the green color of the heavy elements, including carbon, nitrogen, and oxygen atoms. On the other hand, this delocalization of electrons was found between the morpholine, naphthalimide, and benzothiazole moiety on its complexation with the Fe³⁺ ion (**Figure 7.10b**). Furthermore, the LOL

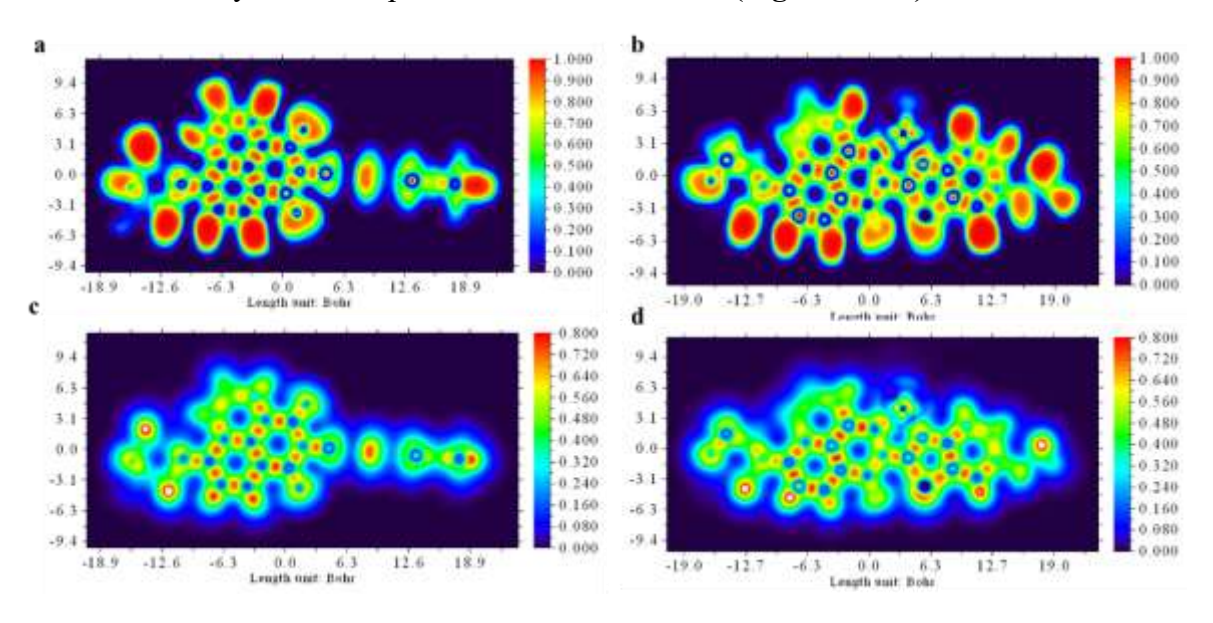


Figure 7.10: ELF diagram of a) probe **5** and b) probe **5** + Fe³⁺ complex; LOL diagram of c) probe **5** and d) probe **5** + Fe³⁺ complex

analysis revealed weak and strong π -delocalized orbitals indicated by blue and red colors respectively on the color map of the probe and complex, respectively $^{133,\,134}$. The scale ranging from 0.000 to 0.800 represents the extent of π orbital delocalization, with a color scale from blue to red depicting weak to strong delocalization (**Figure 7.10c and d**). In probe **5**, a strong π -delocalized orbital between the naphthalimide and morpholine unit is observed, while on complexation with Fe³⁺ ion, the electron delocalization was also spread onto the benzothiazole moiety, which was not the case in probe **5**.

7.8.4. Chemical parameters

The chemical parameters of probe 5 and its complex with Fe³⁺ provided valuable insights into the electronic structure, stability, and reactivity of the probe, which are crucial for its function as a selective Fe³⁺ sensor. Upon complexation with Fe³⁺, significant changes were observed in key parameters such as E_{HOMO} , E_{LUMO} , ΔE_{gap} , ionization potential (I), and electron affinity (A) as given in Table 7.4 156 . The E_{HOMO} and E_{LUMO} values for the free probe 5 and complex decreased from -5.88 eV to -5.05 eV and from -2.46 eV to -2.13 eV, respectively, indicating a shift of electron density towards the metal center, which stabilized the complex. Correspondingly, the energy gap (ΔEgap) reduced from 3.42 eV to 2.92 eV, suggesting enhanced stability of the metal-probe 5 interaction. The reduction in ionization potential and electron affinity upon binding indicated a decreased tendency for the complex to lose or accept electrons, reflecting a more stable electronic configuration. Additionally, the hardness (n) of the complex decreased from 1.7112 eV to 1.4595 eV, making it softer and more reactive, which could facilitate further interactions with metal ions. The dipole moment also decreased, suggesting a more localized charge distribution within the complex. The electronegativity (γ) of the complex decreased from 4.1670 eV to 3.5939 eV, further enhancing the stability of the complex. The electrophilicity index (O) also decreased, indicating a reduced reactivity toward nucleophilic attack. These electronic changes highlighted the enhanced stability and selective reactivity of probe 5 upon complexation with Fe³⁺, making it an effective sensor for Fe³⁺ detection.

Table 7.4: Comparison of global parameter index between probe **5** and its Fe³⁺ complex

Parameters	Symbol & Formula	Probe (eV)	Complex (eV)
E_{HOMO}	E_{H}	-5.88	-5.05
E_{LUMO}	E_L	-2.46	-2.13
Energy gap	$\Delta E_{gap} = (E_{H} - E_{L})$	3.42	2.92
Ionization Potential	$I = E_{\mathrm{H}} $	5.88	5.05
Electron Affinity	$A = E_L $	2.46	2.13
Global hardness	$\eta = (E_L - E_H)/2$	1.7112	1.4595
Softness	$s=1/2\eta$	0.2922	0.3426
Chemical potential	$\mu = (E_L + E_H)/2$	-4.1670	-3.5939
Electrophilicity	$\omega = \mu^2/2\eta$	5.0737	4.4250
Electronegativity	χ = - μ	4.1670	3.5939

7.9. Synthesis of Probe 5

7.9.1. Synthesis of compound 3

Probe **5** was synthesized following a previously reported procedure¹⁵². The compound **1** (1.00 g, 3.61 mmol) was added in 15 mL of ethanol, forming a suspension, to which 6-methoxybenzo[d]thiazol-2-amine (**2**) (0.97g, 5.41 mmol) was added. The reaction mixture was refluxed at 65 °C for 8 hours. Upon completion of the reaction, the mixture was allowed to cool to room temperature, leading to the formation of a precipitate. The resulting solid was collected by filtration, washed with hot ethanol, and dried in an oven at 55 °C for 4 hours, affording off-white precipitates of 6-bromo-2-(6-methoxybenzo[d]thiazol-2-yl)-1H-benzo[de]isoquinoline-1,3(2H)-dione (**3**). Yield: 89%.

7.9.2. Synthesis of probe 5

To compound 3 (0.50 g, 1,18 mmol) in a round-bottom flask, 2-methoxyethanol (10 mL) was added and allowed to stir at room temperature. To the solution, morpholine (0.18 g, 2.12 mmol) was added, and the reaction mixture was transferred to reflux at 110 °C for 13 hours. On the completion of the reaction, the mixture was allowed to cool at room temperature. The reaction mixture was poured into ice-cold water and was allowed to stir for 10 minutes. The yellow-colored precipitates formed and settled down at the bottom of the round-bottom flask and were filtered using a vacuum pump. The yellow-colored precipitate was then further recrystallized in ethanol

for the purity of the desired chemosensor, affording the desired probe 5, 2-(6-methoxybenzo[d]thiazol-2-yl)-6-morpholino-1H-benzo[de]isoquinoline-1,3(2H)-dione. Bright yellow solid, 79% yield; R $_f$ 0.3 (1% methanol in chloroform); mp 263-267 °C; ¹H-NMR (DMSO- d_6 , 500 MHz): 8.66 (d, J = 7.00 Hz, 1H, ArH), 8.61 (d, J = 8.00 Hz, 1H, ArH), 8.51 (d, J = 8.30 Hz, 1H, ArH,), 8.01 (d, J = 8.90 Hz, 1H, ArH,), 7.77 (t, J = 8.10 Hz, 1H, ArH), 7.38 (d, J = 2.40 Hz, 1H, ArH), 7.28 (d, J = 8.10 Hz, 1H, ArH), 7.16 (m, 1H, ArH), 4.05 (t, J = 4.45 Hz, 4H, CH), 3.91 (s, 3H, CH), 3.33 (t, J = 4.50 Hz, 4H, CH); ¹³C-NMR (DMSO- d_6 , 125 MHz): :158.32, 156.51 (CO), 144.90, 138.18, 133.46, 132.04, 131.14, 130.53, 126.34, 125.98, 124.83, 122.82, 116.32, 115.91, 115.13, 104.14 (ArC), 66.93 (CH₂-morph), 55.86 (OCH₃), 53.45 (CH₂-morph); Mass analysis: m/z ratio 446.1167 [M+H]⁺ (Figure A16-A18).

SUMMARY

Fluorescent probes are promising tools for detecting toxic ions pertaining in the environment. To achieve detection beyond the threshold limit, a series of 1,8-naphthalimide-based probes (1-5) were designed using various synthetic approaches to afford highly desirable sensing properties. These probes were synthesized through multi-step reactions and subsequently characterized by using spectroscopic techniques, including ¹H-NMR, ¹³C-NMR, and mass spectrometry, to confirm their structures. After structural validation, the photophysical properties of the probes were investigated through absorption and fluorescence spectroscopy. The solvatochromic behavior of the probes was examined in solvents of varying polarities, revealing a bathochromic shift on increasing polarity, which could be attributed to the prevalence of the ICT phenomenon. Additionally, their aggregation-induced emission (AIE) properties were evaluated in a binary solvent system of DMSO and water with varying water fractions. The enhancement in fluorescence or level off tail in the absorption spectra reveals the aggregation of the probe on increasing water content, since water is a poor solvent. The selectivity of the probes (1-5) sensed cations and anions, including Cu2+, Fe3+, F-, and CN- ions, which was assessed using UV-Visible and fluorescence spectroscopy. The probes (1-5) exhibit distinct naked-eye and ratiometric responses in the absorption spectra, which could be ascribed to the electronic perturbation on the introduction of ion(s). The fluorescence studies revealed both "turn-on" and "turn-off" responses upon interaction with specific ions. To determine the selectivity, the anti-interference study was performed in the presence of competitive ions, revealing no alterations. Furthermore, titration studies were conducted to determine key analytical parameters such as the limit of detection (LOD), limit of quantification (LOQ), association constant (K_a), and Stern-Volmer quenching constant (K_{sv}). The stoichiometry of the probe-ion complexes was validated using Job's plot, FT-IR analysis, HRMS, and ¹H-NMR titrations, and a plausible sensing mechanism was proposed. Additionally, the geometry optimization of the probe and its complexes was done by DFT calculations. FMO analysis was conducted to determine the HOMO-LUMO energy gap, while ELF and LOL studies provided insights into electronic distribution and localization within the probes and their complexes. The TD-DFT study was conducted to analyze the excited-state properties and orbital occupancy of the probe, and the simulated UV-Vis spectra were compared with the experimental results. In addition, the global reactivity parameters were also examined, and NLO properties of the probes were evaluated. Finally, the practical applications of these probes (1-5) were demonstrated through test strips, smartphone-based analysis, molecular logic gates, molecular keypad locks, and real-sample analysis.

Table 1: Summarization of spectroscopic response of probe(s) **(1-5)** with respective ion along with its practical application

Probe	Detecte d ions	Solvent medium & Optical response	Quantitative parameter	Mechanism Involved	Practical applications
но	Cu ²⁺	CH ₃ CN	LOD = $1.25 \times 10^{-5} \text{ M}$ LOQ = $4.16 \times 10^{-5} \text{ M}$ $K_a = 5.83 \times 10^4 \text{ M}^{-1}$ $K_{SV} = 9.24 \times 10^4 \text{ M}^{-1}$	MLCT	
O N O	F-	(Ratiometric, Colorimetric, and "Turn-off"	$\begin{aligned} \text{LOD} &= 1.07 \times 10^{\text{-}6} \text{M} \\ \text{LOQ} &= 3.57 \times 10^{\text{-}6} \text{M} \\ \text{K}_{\text{a}} &= 1.24 \times 10^{4} \text{M}^{\text{-}1} \\ \text{K}_{\text{SV}} &= 4.16 \times 10^{3} \text{M}^{\text{-}1} \end{aligned}$	ICT	Test strip development
(1)	CN-	fluorescence)	$LOD = 0.98 \times 10^{-6} M$ $LOQ = 3.31 \times 10^{-6} M$ $K_a = 1.24 \times 10^4 M^{-1}$ $K_{SV} = 1.03 \times 10^3 M^{-1}$	ICT	
S N O N O N O (2)	Cu ²⁺	MeOH: H2O (9:1, v/v) (Hyperchromic and "Turn-off" fluorescence)	$LOD = 1.22 \times 10^{-5} M$ $LOQ = 4.08 \times 10^{-5} M$ $K_a = 1.43 \times 10^2 M^{-1}$ $K_{SV} = 1.99 \times 10^2 M$	ICT	Logic gate

O N O N N NH (3)	CN ⁻	CH ₃ CN: H ₂ O (9:1, v/v) ("Turn-on" fluorescence)	$LOD = 4.2 \times 10^{-8} \text{ M}$ $LOQ = 1.39 \times 10^{-5} \text{ M}$ $Ka = 2.0 \times 10^{3} \text{ M}^{-1}$	ICT	Logic gate Real water sample analysis
0 N N NH N O (4)	CN-	DMSO: H ₂ O (4:1, v/v) (Ratiometric, Colorimetric, and "Turn-off" fluorescence)	$LOD = 5.47 \times 10^{-6} \text{ M}$ $LOQ = 1.82 \times 10^{-6} \text{ M}$ $Ka = 1.52 \times 10^{5} \text{ M}^{-1}$ $Ksv = 1.22 \times 10^{5} \text{ M}^{-1}$	ICT	Test stips Logic gate Smart-phone analysis Molecular keypad
0- N S O N O (5)	Fe ³⁺	MeOH (Ratiometric, colorimetric, and "Turn-off" Fluorescence)	$LOD = 1.05 \times 10^{-6} \text{M}$ $LOQ = 3.52 \times 10^{-6} \text{M}$ $Ka = 1.62 \times 10^{5} \text{M}^{-1}$ $Ksv = 6.87 \times 10^{5} \text{M}^{-1}$	ICT and LMCT	Logic gate

REFERENCES

- 1. Pundi, A.; Chang, C.-J., Recent developments in the preparation, characterization, and applications of chemosensors for environmental pollutants detection. *Journal of Environmental Chemical Engineering* **2023**, *11* (5), 110346.
- 2. Kaur, G.; Singh, I.; Tandon, N.; Tandon, R.; Bhat, A. A., 1, 8-Naphthalimide-Based Chemosensors: A Promising Strategy for Detection of Metal Ions in Environmental and Biological Systems. *ChemistrySelect* **2023**, *8* (44), e202301661.
- 3. Liu, Y.; Liang, P.; Guo, L., Nanometer titanium dioxide immobilized on silica gel as sorbent for preconcentration of metal ions prior to their determination by inductively coupled plasma atomic emission spectrometry. *Talanta* **2005**, *68* (1), 25-30.
- 4. Soylak, M.; Narin, I.; Dogan, M., Trace enrichment and atomic absorption spectrometric determination of lead, copper, cadmium and nickel in drinking water samples by use of an activated carbon column. *Analytical Letters* **1997**, *30* (15), 2801-2810.
- 5. Becker, J. S.; Matusch, A.; Depboylu, C.; Dobrowolska, J.; Zoriy, M., Quantitative imaging of selenium, copper, and zinc in thin sections of biological tissues (Slugs– Genus Arion) measured by laser ablation inductively coupled plasma mass spectrometry. *Analytical chemistry* **2007**, *79* (16), 6074-6080.
- 6. Thangphatthanarungruang, J.; Lomae, A.; Chailapakul, O.; Chaiyo, S.; Siangproh, W., A Low-cost Paper-based Diamond Electrode for Trace Copper Analysis at On-site Environmental Area. *Electroanalysis* **2021,** 33 (1), 226-232.
- 7. Kaur, K.; Saini, R.; Kumar, A.; Luxami, V.; Kaur, N.; Singh, P.; Kumar, S., Chemodosimeters: An approach for detection and estimation of biologically and medically relevant metal ions, anions and thiols. *Coordination Chemistry Reviews* **2012**, *2*56 (17-18), 1992-2028.
- 8. Gil, D.; Lee, J. J.; Kim, C., Detection of silver ions by a novel NBD-based colorimetric chemosensor with the intramolecular charge transfer character. *Polyhedron* **2023**, *240*, 116453.
- 9. Kim, G.; Gil, D.; Lee, J. J.; Kim, J.; Kim, K.-T.; Kim, C., An NBD-based fluorescent and colorimetric chemosensor for detecting S2–: Practical application to zebrafish and water samples. *Spectrochimica Acta Part A: Molecular and Biomolecular Spectroscopy* **2022**, *276*, 121207.
- 10. Lu, G.; Gao, Y.; Wang, X.; Zhang, D.; Meng, S.; Yu, S.; Zhuang, Y., A corrole-based fluorescent probe for detection of sulfur ion and its application in living cells. *Dyes and Pigments* **2022**, *197*, 109941.
- 11. Anand, T.; Sahoo, S. K., Cost-effective approach to detect Cu (II) and Hg (II) by integrating a smartphone with the colorimetric response from a NBD-benzimidazole based dyad. *Physical Chemistry Chemical Physics* **2019**, *21* (22), 11839-11845.
- 12. Oshchepkov, A. S.; Oshchepkov, M. S.; Oshchepkova, M. V.; Al-Hamry, A.; Kanoun, O.; Kataev, E. A., Naphthalimide-based fluorescent polymers for molecular detection. *Advanced Optical Materials* **2021,** 9 (6), 2001913.

- 13. Zhou, S.; Rong, Y.; Wang, H.; Liu, X.; Wei, L.; Song, X., A naphthalimide-indole fused chromophore-based fluorescent probe for instantaneous detection of thiophenol with a red emission and a large Stokes shift. *Sensors and Actuators B: Chemical* **2018**, *276*, 136-141.
- 14. Du, B.; Zhang, F. H.; Cao, W.; Wang, P. H.; Li, Z. J.; Ding, Z. J., A Naphthalimide-Based Fluorescent Turn-On Sensor for the Selective Detection of Diethyl Chlorophosphate. *ChemistrySelect* **2018**, *3* (47), 13470-13473.
- 15. Chung, J.; Li, H.; Lim, C. S.; Kim, H. M.; Yoon, J., Two-photon imaging of hydrogen polysulfides in living cells and hippocampal tissues. *Sensors and Actuators B: Chemical* **2020**, *322*, 128564.
- 16. Ou-Yang, J.; Jiang, W.-L.; Tan, K.-Y.; Liu, H.-W.; Li, S.-J.; Liu, J.; Li, Y.-F.; Li, C.-Y., Two-photon fluorescence probe for precisely detecting endogenous H2S in lysosome by employing a dual lock system. *Sensors and Actuators B: Chemical* **2018**, *260*, 264-273.
- 17. Zhu, J.-L.; Xu, Z.; Yang, Y.; Xu, L., Small-molecule fluorescent probes for specific detection and imaging of chemical species inside lysosomes. *Chemical Communications* **2019**, *55* (47), 6629-6671.
- 18. Shakya, S.; Khan, I. M.; Ahmad, M., Charge transfer complex based real-time colorimetric chemosensor for rapid recognition of dinitrobenzene and discriminative detection of Fe2+ ions in aqueous media and human hemoglobin. *Journal of Photochemistry and Photobiology A: Chemistry* **2020**, 392, 112402.
- 19. Yang, J. Y.; Gao, W. Y.; Wang, J. H.; Dong, Z. M.; Wang, Y.; Shuang, S. M., A new NBD-based probe for specific colorimetric and turn-on fluorescence sensing of Cu2+ and bio-imaging applications. *Journal of Luminescence* **2023**, *254*, 119549.
- 20. Zhao, J.; Zhang, J.; Hu, B.; Gao, C.; Li, Z.; Sun, Z.; You, J., A FRET-based ratiometric fluorescent probe for Hg2+ detection in aqueous solution and bioimaging in multiple samples. *Spectrochimica Acta Part A: Molecular and Biomolecular Spectroscopy* **2023**, 286, 121965.
- 21. Tigreros, A.; Portilla, J., Recent progress in chemosensors based on pyrazole derivatives. *RSC advances* **2020**, *10* (33), 19693-19712.
- 22. Duan, C.; Won, M.; Verwilst, P.; Xu, J.; Kim, H. S.; Zeng, L.; Kim, J. S., In vivo imaging of endogenously produced HClO in zebrafish and mice using a bright, photostable ratiometric fluorescent probe. *Analytical chemistry* **2019**, *91* (6), 4172-4178.
- 23. Espinar-Barranco, L.; Luque-Navarro, P.; Strnad, M. A.; Herrero-Foncubierta, P.; Crovetto, L.; Miguel, D.; Giron, M. D.; Orte, A.; Cuerva, J. M.; Salto, R., A solvatofluorochromic silicon-substituted xanthene dye useful in bioimaging. *Dyes and Pigments* **2019**, *168*, 264-272.
- 24. Bao, X.; Wu, X.; Berry, S. N.; Howe, E. N.; Chang, Y.-T.; Gale, P. A., Fluorescent squaramides as anion receptors and transmembrane anion transporters. *Chemical Communications* **2018**, *54* (11), 1363-1366.
- 25. Kumar, V.; Kumar, P.; Gupta, R., Detection of Al 3+ and Fe 3+ ions by nitrobenzoxadiazole bearing pyridine-2, 6-dicarboxamide based chemosensors: effect of solvents on detection. *New Journal of Chemistry* **2020**, *44* (31), 13285-13294.
- 26. Chen, X.; Pradhan, T.; Wang, F.; Kim, J. S.; Yoon, J., Fluorescent chemosensors based on spiroring-opening of xanthenes and related derivatives. *Chemical reviews* **2012**, *112* (3), 1910-1956.

- 27. Nguyen, V.-N.; Ha, J.; Cho, M.; Li, H.; Swamy, K.; Yoon, J., Recent developments of BODIPY-based colorimetric and fluorescent probes for the detection of reactive oxygen/nitrogen species and cancer diagnosis. *Coordination Chemistry Reviews* **2021**, *439*, 213936.
- 28. Qian, L.; Li, L.; Yao, S. Q., Two-photon small molecule enzymatic probes. *Accounts of Chemical Research* **2016**, *4*9 (4), 626-634.
- 29. Kim, H. M.; Cho, B. R., Small-molecule two-photon probes for bioimaging applications. *Chemical reviews* **2015**, *115* (11), 5014-5055.
- 30. Dong, H.-Q.; Wei, T.-B.; Ma, X.-Q.; Yang, Q.-Y.; Zhang, Y.-F.; Sun, Y.-J.; Shi, B.-B.; Yao, H.; Zhang, Y.-M.; Lin, Q., 1, 8-Naphthalimide-based fluorescent chemosensors: recent advances and perspectives. *Journal of Materials Chemistry C* **2020**, 8 (39), 13501-13529.
- 31. Wang, W.; Wen, Q.; Zhang, Y.; Fei, X.; Li, Y.; Yang, Q.; Xu, X., Simple naphthalimide-based fluorescent sensor for highly sensitive and selective detection of Cd 2+ and Cu 2+ in aqueous solution and living cells. *Dalton Transactions* **2013**, *42* (5), 1827-1833.
- 32. Dimov, S. M.; Georgiev, N. I.; Asiri, A. M.; Bojinov, V. B., Synthesis and sensor activity of a PET-based 1, 8-naphthalimide probe for Zn 2+ and pH determination. *Journal of fluorescence* **2014**, *24*, 1621-1628.
- 33. Kumar Das, S.; Kahali, S.; Kar, S.; Madhavan, N.; Datta, A., Naphthalimide-Based, Single-Chromophore, Emission Ratiometric Fluorescent Sensor for Tracking Intracellular pH. *ChemBioChem* **2024**, *25* (21), e202400538.
- 34. Huang, J.; Wu, D.; Ge, H.-J.; Liu, S.-H.; Yin, J., Fluorinated 1, 8-naphthalimides: Synthesis, solid structure and properties. *Chinese Chemical Letters* **2014**, *25* (10), 1399-1402.
- 35. Banerjee, S.; Veale, E. B.; Phelan, C. M.; Murphy, S. A.; Tocci, G. M.; Gillespie, L. J.; Frimannsson, D. O.; Kelly, J. M.; Gunnlaugsson, T., Recent advances in the development of 1, 8-naphthalimide based DNA targeting binders, anticancer and fluorescent cellular imaging agents. *Chemical Society Reviews* **2013**, *42* (4), 1601-1618.
- 36. Lee, J.-F.; Hsu, S. L.-C., Green polymer-light-emitting-diodes based on polyfluorenes containing N-aryl-1, 8-naphthalimide and 1, 8-naphthoilene-arylimidazole derivatives as color tuner. *Polymer* **2009**, *50* (24), 5668-5674.
- 37. Gautam, P.; Sharma, R.; Misra, R.; Keshtov, M.; Kuklin, S.; Sharma, G. D., Donor-acceptor-acceptor (D-A-A) type 1, 8-naphthalimides as non-fullerene small molecule acceptors for bulk heterojunction solar cells. *Chemical Science* **2017**, *8* (3).
- 38. Liu, S.; Bai, H.; Sun, Q.; Zhang, W.; Qian, J., Naphthalimide-based fluorescent photoinduced electron transfer sensors for saccharides. *RSC Advances* **2015**, *5* (4), 2837-2843.
- 39. Duke, R. M.; Gunnlaugsson, T., 3-Urea-1, 8-naphthalimides are good chemosensors: a highly selective dual colorimetric and fluorescent ICT based anion sensor for fluoride. *Tetrahedron letters* **2011**, *52* (13), 1503-1505.
- 40. Wang, C.; Zhang, D.; Huang, X.; Ding, P.; Wang, Z.; Zhao, Y.; Ye, Y., A ratiometric fluorescent chemosensor for Hg2+ based on FRET and its application in living cells. *Sensors and Actuators B: Chemical* **2014**, *198*, 33-40.

- 41. Gopikrishna, P.; Meher, N.; Iyer, P. K., Functional 1, 8-naphthalimide AIE/AIEEgens: recent advances and prospects. *ACS applied materials & interfaces* **2017**, *10* (15), 12081-12111.
- 42. Kamal, A.; Bolla, N. R.; Srikanth, P. S.; Srivastava, A. K., Naphthalimide derivatives with therapeutic characteristics: A patent review. *Expert opinion on therapeutic patents* **2013**, *23* (3), 299-317.
- 43. Roos, L.; Malan, F. P.; Landman, M., Naphthalimide-NHC complexes: Synthesis and properties in catalytic, biological and photophysical applications. *Coordination Chemistry Reviews* **2021**, *449*, 214201.
- 44. Zhu, H.; Liu, C.; Su, M.; Rong, X.; Zhang, Y.; Wang, X.; Wang, K.; Li, X.; Yu, Y.; Zhang, X., Recent advances in 4-hydroxy-1, 8-naphthalimide-based small-molecule fluorescent probes. *Coordination Chemistry Reviews* **2021**, *448*, 214153.
- 45. Zhou, L.; Xie, L.; Liu, C.; Xiao, Y., New trends of molecular probes based on the fluorophore 4-amino-1, 8-naphthalimide. *Chinese Chemical Letters* **2019**, *30* (10), 1799-1808.
- 46. Alam, P.; Leung, N. L.; Zhang, J.; Kwok, R. T.; Lam, J. W.; Tang, B. Z., AIE-based luminescence probes for metal ion detection. *Coordination Chemistry Reviews* **2021**, *429*, 213693.
- 47. Kang, L.; Liu, Y.-T.; Li, N.-N.; Dang, Q.-X.; Xing, Z.-Y.; Li, J.-L.; Zhang, Y., A schiff-base receptor based naphthalimide derivative: Highly selective and colorimetric fluorescent turn-on sensor for Al3+. *Journal of Luminescence* **2017**, *186*, 48-52.
- 48. Yu, H.; Guo, Y.; Zhu, W.; Havener, K.; Zheng, X., Recent advances in 1, 8-naphthalimide-based small-molecule fluorescent probes for organelles imaging and tracking in living cells. *Coordination Chemistry Reviews* **2021**, *444*, 214019.
- 49. Geraghty, C.; Wynne, C.; Elmes, R. B., 1, 8-Naphthalimide based fluorescent sensors for enzymes. *Coordination Chemistry Reviews* **2021**, *437*, 213713.
- 50. Turdean, G. L., Design and development of biosensors for the detection of heavy metal toxicity. *International Journal of Electrochemistry* **2011**, *2011* (1), 343125.
- 51. Bagal-Kestwal, D.; Karve, M. S.; Kakade, B.; Pillai, V. K., Invertase inhibition based electrochemical sensor for the detection of heavy metal ions in aqueous system: Application of ultra-microelectrode to enhance sucrose biosensor's sensitivity. *Biosensors and Bioelectronics* **2008**, *24* (4), 657-664.
- 52. Syed, A.; Zeyad, M. T.; Shahid, M.; Elgorban, A. M.; Alkhulaifi, M. M.; Ansari, I. A., Heavy metals induced modulations in growth, physiology, cellular viability, and biofilm formation of an identified bacterial isolate. *ACS omega* **2021**, 6 (38), 25076-25088.
- 53. Uchimiya, M.; Bannon, D.; Nakanishi, H.; McBride, M. B.; Williams, M. A.; Yoshihara, T., Chemical speciation, plant uptake, and toxicity of heavy metals in agricultural soils. *Journal of Agricultural and Food Chemistry* **2020**, *68* (46), 12856-12869.
- 54. Kaur, J.; Sengupta, P.; Mukhopadhyay, S., Critical review of bioadsorption on modified cellulose and removal of divalent heavy metals (Cd, Pb, and Cu). *Industrial & Engineering Chemistry Research* **2022**, *61* (5), 1921-1954.
- 55. Zhang, X.; Wei, H.; Guan, Q.; Yang, X.; Yu, Q.; Zhang, M.; Xia, Y., Maternal exposure to trace elements, toxic metals, and longitudinal changes in infancy anthropometry and

- growth trajectories: a prospective cohort study. *Environmental Science & Technology* **2023**, *57* (32), 11779-11791.
- 56. Kumar Jena, B.; Retna Raj, C., Gold nanoelectrode ensembles for the simultaneous electrochemical detection of ultratrace arsenic, mercury, and copper. *Analytical chemistry* **2008**, *80* (13), 4836-4844.
- 57. Steinmaus, C. M.; George, C. M.; Kalman, D. A.; Smith, A. H., Evaluation of two new arsenic field test kits capable of detecting arsenic water concentrations close to 10 µg/L. *Environmental science & technology* **2006**, *40* (10), 3362-3366.
- 58. Yantasee, W.; Lin, Y.; Hongsirikarn, K.; Fryxell, G. E.; Addleman, R.; Timchalk, C., Electrochemical sensors for the detection of lead and other toxic heavy metals: the next generation of personal exposure biomonitors. *Environmental health perspectives* **2007**, *115* (12), 1683-1690.
- 59. Aragay, G.; Pons, J.; Merkoçi, A., Recent trends in macro-, micro-, and nanomaterial-based tools and strategies for heavy-metal detection. *Chemical reviews* **2011**, *111* (5), 3433-3458.
- 60. Aggett, P., Present Knowledge in Nutrition. 10th. Erdman, J.; Macdonald, I.; Zeisel, S., editors. Wiley-Blackwell Washington, DC.:: 2012.
- 61. Mahata, S.; Kumar, S.; Dey, S.; Mandal, B. B.; Manivannan, V., A probe with hydrazinecarbothioamide and 1, 8-naphthalimide groups for "turn-on" fluorescence detection of Hg2+ and Ag+ ions and live-cell imaging studies. *Inorganica Chimica Acta* **2022**, 535, 120876.
- 62. Jothi, D.; Iyer, S. K., Recognition of Hg2+ ion in an organic semi-aqueous medium by a new napthalimide based fluorescent probe and its bioimaging applications. *Inorganic Chemistry Communications* **2022**, *143*, 109735.
- 63. Tian, M.; Wang, C.; Ma, Q.; Bai, Y.; Sun, J.; Ding, C., A highly selective fluorescent probe for Hg2+ based on a 1, 8-naphthalimide derivative. *Acs Omega* **2020**, *5* (29), 18176-18184.
- 64. Li, L.; Gao, S.; Yang, L.; Liu, Y.-L.; Li, P.; Ye, F.; Fu, Y., Cobalt (II) complex as a fluorescent sensing platform for the selective and sensitive detection of triketone HPPD inhibitors. *Journal of Hazardous Materials* **2021**, *404*, 124015.
- 65. Kumar, S.; Sharma, N.; Marok, S. S.; Kaur, S.; Singh, P., A 1, 8-naphthalimide based chemosensor for intracellular and biofluid detection of Pd 2+ ions: microscopic and anticounterfeiting studies. *Analytical Methods* **2023**, *15* (38), 5010-5017.
- 66. Jiang, C.; Yang, L.; Li, P.; Liu, Y.; Li, S.; Fu, Y.; Ye, F., A simple and rapid fluorescent approach for Pb2+ determination and application in water samples and living cells. *Spectrochimica Acta Part A: Molecular and Biomolecular Spectroscopy* **2021**, *2*63, 120168.
- 67. Treto-Suárez, M. A.; Hidalgo-Rosa, Y.; Schott, E.; Páez-Hernández, D.; Zarate, X., Fluorescence turn-on and turn-off mechanisms of a dual-selective chemosensor of Bi3+ and pH changes: Insights from a theoretical perspective. *Dyes and Pigments* **2021**, *185*, 108934.
- 68. Liu, Y.-L.; Yang, L.; Li, P.; Li, S.-J.; Li, L.; Pang, X.-X.; Ye, F.; Fu, Y., A novel colorimetric and "turn-off" fluorescent probe based on catalyzed hydrolysis reaction for detection of Cu2+ in real water and in living cells. *Spectrochimica Acta Part A: Molecular and Biomolecular Spectroscopy* **2020**, *227*, 117540.

- 69. Li, X.-H.; Yan, J.-L.; Zong, H.-T.; Wu, W.-N.; Wang, Y.; Zhao, X.-L.; Fan, Y.-C.; Xu, Z.-H., A 1, 8-naphthalimide-based turn-on fluorescent probe for imaging Cu2+ in lysosomes. *Inorganic Chemistry Communications* **2021**, *134*, 109026.
- 70. Arslan, F. N.; Aydin, D.; Elmas, S. N. K., Fast responsive colorimetric and ratiometric fluorescence chemoprobe based on a 1, 8–naphthalimide for nM recognition of Cu2+ and its application in real food and drinkable water samples. *Journal of Food Composition and Analysis* **2022**, *114*, 104824.
- 71. Zhang, S.; Wang, Y.; Xu, H., A new naphthalimide-picolinohydrazide derived fluorescent "turn-on" probe for hypersensitive detection of Al3+ ions and applications of real water analysis and bio-imaging. *Spectrochimica Acta Part A: Molecular and Biomolecular Spectroscopy* **2022**, *275*, 121193.
- 72. Xu, H.; Zhang, S.; Gu, Y.; Lu, H., Naphthalimide appended isoquinoline fluorescent probe for specific detection of Al3+ ions and its application in living cell imaging. Spectrochimica Acta Part A: Molecular and Biomolecular Spectroscopy **2022**, 265, 120364.
- 73. Xiang, D.; Zhang, S.; Wang, Y.; Sun, K.; Xu, H., A novel naphthalimide-based "turn-on" fluorescent chemosensor for highly selective detection of Zn2+. *Tetrahedron* **2022**, *106*, 132648.
- 74. Das, P. P.; Mohanty, P.; Barick, A. K.; Mohapatra, P.; Jali, B. R., A Versatile Molecular Probe of Napthalimide-Derivative for Zn (II) Sensor: A Mini-Review. *Trends in Sciences* **2023**, *20* (7), 5005-5005.
- 75. Chen, X.; Shao, H.; Zhu, T.; Chen, Z.; Hu, Y.; Zhang, H.; Liu, C., A new fluoride chemodosimeter based on 3-ether-substituted 1, 8-naphthalimide derivatives. *Journal of Fluorescence* **2022**, *32* (3), 921-926.
- 76. Xiao, L.; Ren, L.; Jing, X.; Li, Z.; Wu, S.; Guo, D., A selective naphthalimide-based colorimetric and fluorescent chemosensor for "naked-eye" detection of fluoride ion. *Inorganica Chimica Acta* **2020**, *500*, 119207.
- 77. Pati, C.; Raza, R.; Ghosh, K., Adenine-linked naphthalimide: A case of selective colorimetric as well as fluorometric sensing of F– and anion-activated moisture detection in organic solvents and CO2-sensing. Spectrochimica Acta Part A: Molecular and Biomolecular Spectroscopy 2020, 229, 117910.
- 78. Yang, L.; Liu, Y.-L.; Liu, C.-G.; Fu, Y.; Ye, F., A naked-eye visible colorimetric and ratiometric chemosensor based on Schiff base for fluoride anion detection. *Journal of Molecular Structure* **2021**, *1236*, 130343.
- 79. Yan, X.; Lan, H.; Li, Y.; Yan, X.; Xing, Q.; Wang, W.; Zhang, J.; Xiao, S., High-contrast colourimetric probes for fluoride and trace water based on tautomerization of naphthalimide and application in fingerprint imaging. *Spectrochimica Acta Part A: Molecular and Biomolecular Spectroscopy* **2021**, *254*, 119674.
- 80. Bi, W.; Zhao, X.; Yang, X.; Yuan, X.; Lin, Y.; Xu, K.; Liu, L.; Zeng, H.; Du, G.; Zhang, L., Ratiometric fluorescent probe with AIE characteristics for hypochlorite detection and biological imaging. *Spectrochimica Acta Part A: Molecular and Biomolecular Spectroscopy* **2024**, *323*, 124904.
- 81. Zhang, C.; Wang, Y.; Li, X.; Nie, S.; Liu, C.; Zhang, Y.; Guo, J., A fluorescent probe based on phenothiazine for detection of ClO- with naked-eye color change properties. *Analytical biochemistry* **2023**, 670, 115131.

- 82. Shiraishi, Y.; Nakatani, R.; Takagi, S.; Yamada, C.; Hirai, T., A naphthalimide–sulfonylhydrazine conjugate as a fluorescent chemodosimeter for hypochlorite. *Chemosensors* **2020**, *8* (4), 123.
- 83. She, Q.; Cao, Y.; Zhou, Y.; Tan, Y.; Kan, A.; Yang, J.; Yan, J.; Wu, J.; Liu, C., Novel förster resonance energy transfer (FRET)-based ratiometric fluorescent probe for detection of cyanides by nucleophilic substitution of aromatic hydrogen (SNArH). *Spectrochimica Acta Part A: Molecular and Biomolecular Spectroscopy* **2025**, *327*, 125339.
- 84. Zhang, C.-l.; Guo, J.-h.; Zhang, Y.; Liu, C., A naphthalimide-based bifunctional fluorescent probe for detecting CN- and alkaline pH and its application in food samples and living cells imaging. *Microchemical Journal* **2024**, *206*, 111594.
- 85. Williams, A. T. R.; Winfield, S. A.; Miller, J. N., Relative fluorescence quantum yields using a computer-controlled luminescence spectrometer. *Analyst* **1983**, *108* (1290), 1067-1071.
- 86. Singh, I.; Luxami, V.; Paul, K., Spectroscopy and molecular docking approach for investigation on the binding of nocodazole to human serum albumin. *Spectrochimica Acta Part A: Molecular and Biomolecular Spectroscopy* **2020**, *235*, 118289.
- 87. Frisch, M.; Clemente, F., MJ Frisch, GW Trucks, HB Schlegel, GE Scuseria, MA Robb, JR Cheeseman, G. Scalmani, V. Barone, B. Mennucci, GA Petersson, H. Nakatsuji, M. Caricato, X. Li, HP Hratchian, AF Izmaylov, J. Bloino and G. Zhe, Gaussian 9.
- 88. Aron, A. T.; Ramos-Torres, K. M.; Cotruvo Jr, J. A.; Chang, C. J., Recognition-and reactivity-based fluorescent probes for studying transition metal signaling in living systems. *Accounts of chemical research* **2015**, *48* (8), 2434-2442.
- 89. Pothulapadu, C. A. S.; Jayaraj, A.; N, S.; Priyanka, R. N.; Sivaraman, G., Novel benzothiazole-based highly selective ratiometric fluorescent turn-on sensors for Zn2+ and colorimetric chemosensors for Zn2+, Cu2+, and Ni2+ ions. *ACS omega* **2021**, 6 (38), 24473-24483.
- 90. Gray, H. B., Biological inorganic chemistry at the beginning of the 21st century. *Proceedings of the National Academy of Sciences* **2003**, *100* (7), 3563-3568.
- 91. Udhayakumari, D.; Naha, S.; Velmathi, S., Colorimetric and fluorescent chemosensors for Cu 2+. A comprehensive review from the years 2013–15. *Analytical Methods* **2017**, 9 (4), 552-578.
- 92. Lutsenko, S., Atp7b-/- mice as a model for studies of Wilson's disease. *Biochemical Society Transactions* **2008**, *36* (6), 1233-1238.
- 93. Ziegler, B. E.; Marta, R. A.; Burt, M. B.; McMahon, T. B., Insight into the gas-phase structure of a copper (II) l-histidine complex, the agent used to treat Menkes disease. *Inorganic Chemistry* **2014**, *53* (5), 2349-2351.
- 94. Borkow, G.; Gabbay, J., Copper as a biocidal tool. *Current medicinal chemistry* **2005**, *12* (18), 2163-2175.
- 95. Kiaune, L.; Singhasemanon, N., Pesticidal copper (I) oxide: environmental fate and aquatic toxicity. *Reviews of Environmental Contamination and Toxicology Volume 213* **2011**, 1-26.
- 96. S. Amuthakala, S. B., A. Kalilur Rahiman, Thiosemicarbazone-based bifunctional chemosensors for simultaneous detection of inorganic cations and fluoride anion. *Journal of Molecular Structure* **2020**, *1219*.

- 97. Baker, J. L.; Sudarsan, N.; Weinberg, Z.; Roth, A.; Stockbridge, R. B.; Breaker, R. R., Widespread genetic switches and toxicity resistance proteins for fluoride. *Science* **2012**, 335 (6065), 233-235.
- 98. Hu, Q.; Huang, Q.; Mao, Y.; Liu, X.; Tan, F.; Wang, Y.; Yin, Q.; Wu, X.; Wang, H., A near-infrared large Stokes shift probe based enhanced ICT strategy for F-detection in real samples and cell imaging. *Tetrahedron* **2019**, *75* (51), 130762.
- 99. Edition, F., Guidelines for drinking-water quality. WHO chronicle **2011**, 38 (4), 104-8.
- 100. Kulling, P., Hospital treatment of victims exposed to combustion products. *Toxicology letters* **1992**, *64*, 283-289.
- 101. Organization, W. H., *Guidelines for drinking-water quality*. World Health Organization: 2004; Vol. 1.
- 102. Sarkar, A.; Bhattacharyya, S.; Mukherjee, A., Colorimetric detection of fluoride ions by anthraimidazoledione based sensors in the presence of Cu (II) ions. *Dalton Transactions* **2016**, *45* (3), 1166-1175.
- 103. Georgiev, N. I.; Yaneva, I. S.; Surleva, A. R.; Asiri, A. M.; Bojinov, V. B., Synthesis, sensor activity and logic behavior of a highly water-soluble naphthalimide derivative. *Sensors and Actuators B: Chemical* **2013**, *184*, 54-63.
- 104. Chen, Z.; Wang, L.; Zou, G.; Cao, X.; Wu, Y.; Hu, P., A retrievable and highly selective fluorescent probe for monitoring dihydrogen phosphate ions based on a naphthalimide framework. *Spectrochimica Acta Part A: Molecular and Biomolecular Spectroscopy* **2013**, 114, 323-329.
- 105. Kumar, G.; Singh, I.; Goel, R.; Paul, K.; Luxami, V., Dual-channel ratiometric recognition of Al3+ and F- ions through an ESIPT-ESICT signalling mechanism. *Spectrochimica Acta Part A: Molecular and Biomolecular Spectroscopy* **2021**, *247*, 119112.
- 106. Jain, N.; Kaur, N., A comprehensive compendium of literature of 1, 8-Naphthalimide based chemosensors from 2017 to 2021. *Coordination Chemistry Reviews* **2022**, *4*59, 214454.
- 107. Uauy, R.; Olivares, M.; Gonzalez, M., Essentiality of copper in humans. *The American journal of clinical nutrition* **1998**, 67 (5), 952S-959S.
- 108. Danks, D., Copper deficiency in humans. *Annual review of nutrition* **1988,** 8.
- 109. Tapiero, H.; Tew, K. D., Trace elements in human physiology and pathology: zinc and metallothioneins. *Biomedicine & Pharmacotherapy* **2003**, *57* (9), 399-411.
- 110. Myint, Z. W.; Oo, T. H.; Thein, K. Z.; Tun, A. M.; Saeed, H., Copper deficiency anemia. *Annals of hematology* **2018**, *97*, 1527-1534.
- 111. Brewer, G. J., Copper toxicity in Alzheimer's disease: cognitive loss from ingestion of inorganic copper. *Journal of Trace Elements in Medicine and Biology* **2012**, *26* (2-3), 89-92.
- 112. Schilsky, M. L. In *Wilson disease: genetic basis of copper toxicity and natural history*, Seminars in liver disease, © 1996 by Thieme Medical Publishers, Inc.: 1996; pp 83-95.
- 113. Uriu-Adams, J. Y.; Keen, C. L., Copper, oxidative stress, and human health. *Molecular aspects of medicine* **2005**, *2*6 (4-5), 268-298.
- 114. Isangedighi, I. A.; David, G. S., Heavy metals contamination in fish: effects on human health. *Journal of Aquatic Science and Marine Biology* **2019**, *2* (4), 7-12.
- 115. Nor, Y. M., Ecotoxicity of copper to aquatic biota: a review. *Environmental research* **1987**, *43* (1), 274-282.

- 116. Gaggelli, E.; Kozlowski, H.; Valensin, D.; Valensin, G., Copper homeostasis and neurodegenerative disorders (Alzheimer's, prion, and Parkinson's diseases and amyotrophic lateral sclerosis). *Chemical reviews* **2006**, *106* (6), 1995-2044.
- 117. Jolliffe, K. K. A.; Gale, P. A., The supramolecular chemistry of anions. *Organic & Biomolecular Chemistry* **2022**, *20* (4), 713-714.
- 118. Gale, P. A., Anion receptor chemistry: highlights from 2008 and 2009. *Chemical Society Reviews* **2010**, 39 (10), 3746-3771.
- 119. Kuyucak, N.; Akcil, A., Cyanide and removal options from effluents in gold mining and metallurgical processes. *Minerals Engineering* **2013**, *50*, 13-29.
- 120. Bhattacharya, R.; Flora, S. J., Cyanide toxicity and its treatment. In *Handbook of toxicology of chemical warfare agents*, Elsevier: 2009; pp 255-270.
- 121. Bouali, W.; Yaman, M.; Seferoğlu, N.; Seferoğlu, Z., Colorimetric and fluorimetric detection of CN–ion using a highly selective and sensitive chemosensor derived from coumarin-hydrazone. *Journal of Photochemistry and Photobiology A: Chemistry* **2024**, *448*, 115227.
- 122. Laitos, J. G., Cyanide, mining, and the environment. Pace Envtl. L. Rev. 2012, 30, i.
- 123. Agency, U. E. P., Guidelines establishing test procedures for the analysis of pollutants. *Federal Register* **1979**, *44*, 69468-69483.
- 124. Singh, I.; Luxami, V.; Paul, K., Synthesis of naphthalimide-phenanthro [9, 10-d] imidazole derivatives: In vitro evaluation, binding interaction with DNA and topoisomerase inhibition. *Bioorganic Chemistry* **2020**, 96, 103631.
- 125. Gupta, A. S.; Paul, K.; Luxami, V., Benzimidazole based ratiometric chemosensor for detection of CN- and Cu2+ ions in protic/aqueous system: Elaboration as XOR logic operation. *Inorganica Chimica Acta* **2016**, *443*, 57-63.
- 126. Kaur, N.; Singh, J.; Dhaka, G.; Rani, R.; Luxami, V., Benzothiazole-based chemosensor for CN- and Cu2+: multi-logic operations within a single molecule. *Supramolecular Chemistry* **2015**, *27* (7-8), 453-459.
- 127. Zhang, Y.; Li, D.; Li, Y.; Yu, J., Solvatochromic AIE luminogens as supersensitive water detectors in organic solvents and highly efficient cyanide chemosensors in water. *Chemical Science* **2014**, *5* (7), 2710-2716.
- 128. Kaur, G.; Singh, I.; Tandon, R.; Tandon, N., Recent Advancements in Coumarin Based Colorimetric and Fluorescent Chemosensors. *Inorganic Chemistry Communications* **2023**, 111480.
- 129. Yang, Y.; Yin, C.; Huo, F.; Chao, J.; Zhang, Y.; Cheng, F., A new highly selective and turn-on fluorescence probe for detection of cyanide. *Sensors and Actuators B: Chemical* **2014**, *1*93, 220-224.
- 130. Saral, A.; Shahidha, R.; Thirunavukkarasu, M.; Muthu, S., Molecular structure, spectral, computational, IEFPCM investigation, and topological study on the biologically potent; cardiotonic drug 2-chloroquinolin-3-amine with structural optimization. *Chemical Physics Impact* **2023**, 6, 100193.
- 131. Geethapriya, J.; Shanthidevi, A.; Arivazhagan, M.; Elangovan, N.; Thomas, R., Synthesis, structural, DFT, quantum chemical modeling and molecular docking studies of (E)-4-(((5-methylfuran-2-yl) methylene) amino) benzenesulfonamide from 5-methyl-2-furaldehyde and sulfanilamide. *Journal of the Indian Chemical Society* **2022**, 99 (4), 100418.

- 132. Kanagathara, N.; Thirunavukkarasu, M.; Selvaraj, S.; Kumar, A. R.; Marchewka, M.; Janczak, J., Structural elucidation, solvent (polar and non-polar) effect on electronic characterization, non-covalent charge interaction nature, topology and pharmacological studies on NLO active l-argininium methanesufonate. *Journal of Molecular Liquids* **2023**, 385, 122315.
- 133. Jacobsen, H., Localized-orbital locator (LOL) profiles of chemical bonding. *Canadian Journal of Chemistry* **2008**, *86* (7), 695-702.
- 134. Al-Otaibi, J. S.; Sheena Mary, Y.; Shyma Mary, Y.; Soman, S.; Thirunavukkarasu, M., Solvation effects, reactivity studies and molecular dynamics of two phosphonic acids—theoretical investigation. *Polycyclic Aromatic Compounds* **2023**, *43* (8), 6804-6818.
- 135. Srisukjaroen, R.; Wechakorn, K.; Teepoo, S., A smartphone based-paper test strip chemosensor coupled with gold nanoparticles for the Pb2+ detection in highly contaminated meat samples. *Microchemical Journal* **2022**, *179*, 107438.
- 136. Batsaikhan, O.; Choi, B.; Nam, H.; Kim, C., Fluorescent and colorimetric dual-mode chemosensor for easy detection of Cu2+: Practical and smartphone-based application to test strip and water sample. *Inorganica Chimica Acta* **2024**, *571*, 122234.
- 137. Xu, Z.; Yang, X.; Liu, Z.; Zhang, M.-X., A 1, 8-naphthimide-based fluorescent probe for detection of formaldehyde in gaseous and application in living cells. *Journal of Photochemistry and Photobiology A: Chemistry* **2022**, *426*, 113731.
- 138. Ma, J.; Sun, R.; Xia, K.; Xia, Q.; Liu, Y.; Zhang, X., Design and application of fluorescent probes to detect cellular physical microenvironments. *Chemical Reviews* **2024**, *124* (4), 1738-1861.
- 139. Ackerman, C. M.; Lee, S.; Chang, C. J., Analytical methods for imaging metals in biology: from transition metal metabolism to transition metal signaling. *Analytical chemistry* **2017**, 89 (1), 22-41.
- 140. Carter, K. P.; Young, A. M.; Palmer, A. E., Fluorescent sensors for measuring metal ions in living systems. *Chemical reviews* **2014**, *114* (8), 4564-4601.
- 141. Afrin, A.; Pothulapadu, C. A. S.; Rose, A., Glowing discoveries: Schiff base-cyanostilbene probes illuminating metal ions and biological entities. *Analytical Methods* **2024**.
- 142. Bi, X.; Cao, N.; He, J., Recent advances in nanoenzymes for Alzheimer's disease treatment. *Colloids and Surfaces B: Biointerfaces* **2024**, 244, 114139.
- 143. Jin, B.; Zhang, Z.; Zhang, Y.; Yang, M.; Wang, C.; Xu, J.; Zhu, Y.; Mi, Y.; Jiang, J.; Sun, Z., Ferroptosis and myocardial ischemia-reperfusion: mechanistic insights and new therapeutic perspectives. *Frontiers in Pharmacology* **2024**, *15*, 1482986.
- 144. Wilson, M. T.; Reeder, B. J., The peroxidatic activities of Myoglobin and Hemoglobin, their pathological consequences and possible medical interventions. *Molecular Aspects of Medicine* **2022**, *84*, 101045.
- 145. Hsu, C. C.; Senussi, N. H.; Fertrin, K. Y.; Kowdley, K. V., Iron overload disorders. *Hepatology communications* **2022**, 6 (8), 1842-1854.
- 146. Pasricha, S.-R.; Tye-Din, J.; Muckenthaler, M. U.; Swinkels, D. W., Iron deficiency. *The Lancet* **2021**, *397* (10270), 233-248.

- 147. Gattermann, N.; Muckenthaler, M. U.; Kulozik, A. E.; Metzgeroth, G.; Hastka, J., The evaluation of iron deficiency and iron overload. *Deutsches Ärzteblatt International* **2021**, *118* (49), 847.
- 148. Sousa, L.; Oliveira, M. M.; Pessôa, M. T. C.; Barbosa, L. A., Iron overload: Effects on cellular biochemistry. *Clinica chimica acta* **2020**, *504*, 180-189.
- 149. Dos Santos, L.; Bertoli, S. R.; Ávila, R. A.; Marques, V. B., Iron overload, oxidative stress and vascular dysfunction: Evidences from clinical studies and animal models. *Biochimica et Biophysica Acta (BBA)-General Subjects* **2022**, *1866* (9), 130172.
- 150. Nan, X.; Huyan, Y.; Li, H.; Sun, S.; Xu, Y., Reaction-based fluorescent probes for Hg2+, Cu2+ and Fe3+/Fe2+. *Coordination Chemistry Reviews* **2021**, *426*, 213580.
- 151. Liu, L.; Zhou, T.; Li, Y.; Li, T., A Novel Rhodamine B Derivative as a "Turn-on" Fluorescent Sensor for Cu2+ with High Selectivity and Sensitivity. *Journal of Fluorescence* **2024**, 1-10.
- 152. Kaur, G.; Kumar, G.; Singh, I., A novel naphthalimide-derived "turn-off" chemosensor for the detection of Cu2+, F-and CN-ions. *Journal of Molecular Structure* **2025**, *1319*, 139252.
- 153. Homocianu, M., Exploring solvatochromism: A comprehensive analysis of research data. *Microchemical Journal* **2024**, *198*, 110166.
- 154. Kumar, Y.; Singh, N. K.; Mukhopadhyay, S.; Pandey, D. S., AIE active quinazoline based probes for selective detection of Fe3+ and acidochromism. *Inorganica Chimica Acta* **2023**, *546*, 121294.
- 155. Dathees, T. J.; Narmatha, G.; Prabhu, J.; Parvatham, K.; Kannan, V. R.; Nandhakumar, R., Thiourea-Derived Fluorescent Chemosensor for Ag⁺ Ions and Sequential Detection of Tryptophan with Practical Applications. *Journal of Molecular Structure* **2025**, 143836.
- 156. Mamad, D. M.; Azeez, Y. H.; Kaka, A. K.; Ahmed, K. M.; Omer, R. A.; Ahmed, L. O., The inhibitor activity of some azo compound derivatives using density functional theory and molecular dynamics simulations. *Computational and Theoretical Chemistry* **2024**, *1237*, 114645.

APPENDICES

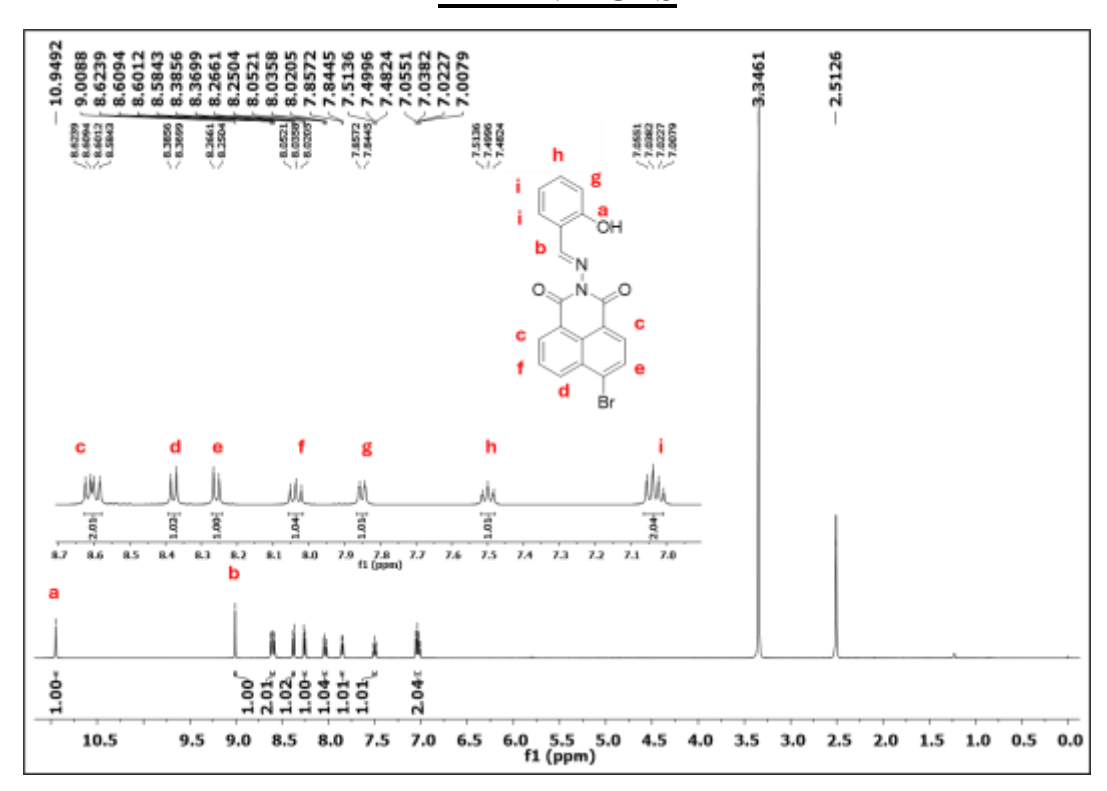


Figure A1: ¹H-NMR spectrum of probe 1

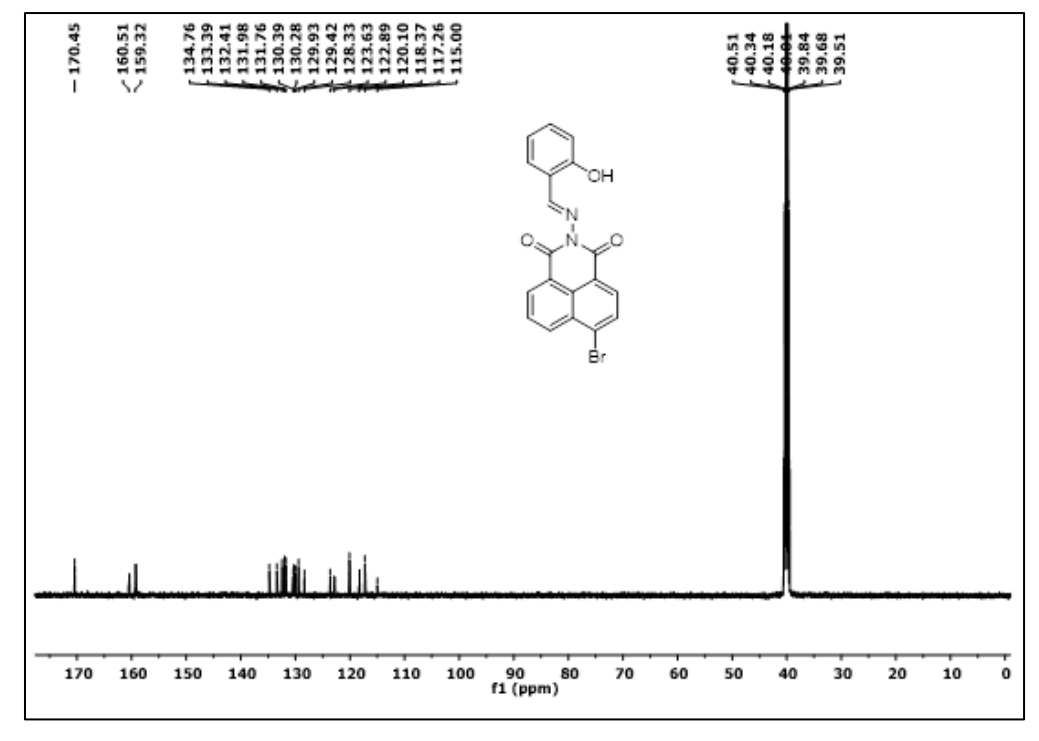


Figure A2: ¹³C-NMR spectrum of probe 1

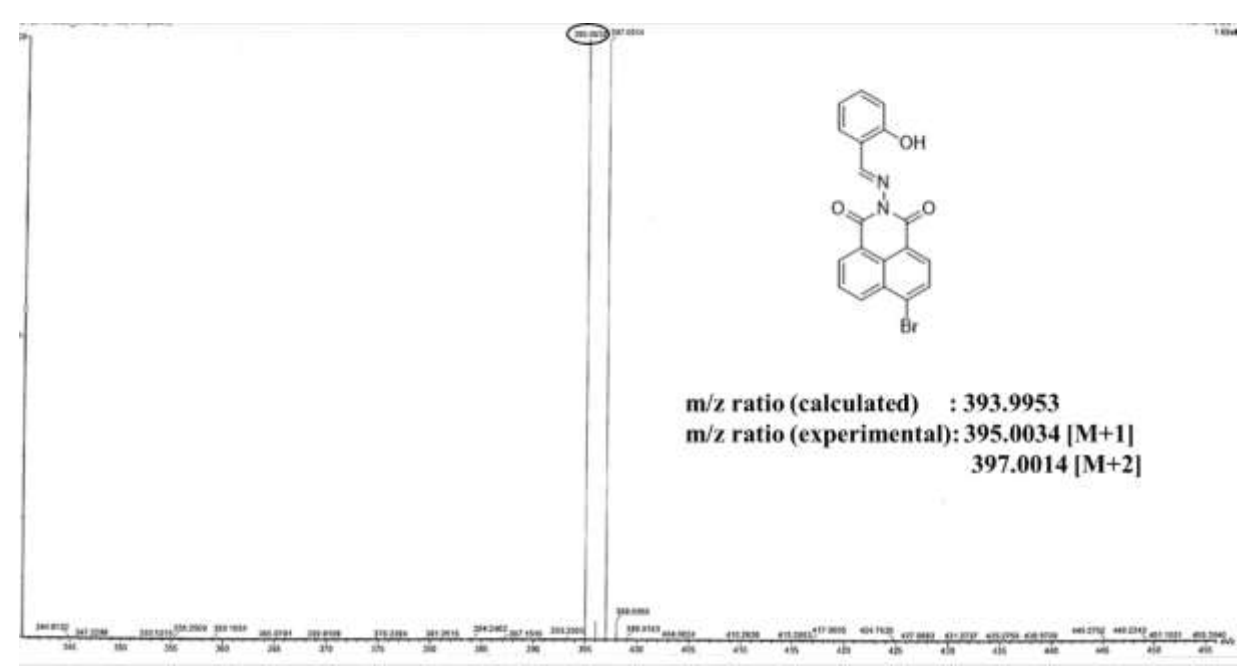


Figure A3: Mass spectrum of probe 1

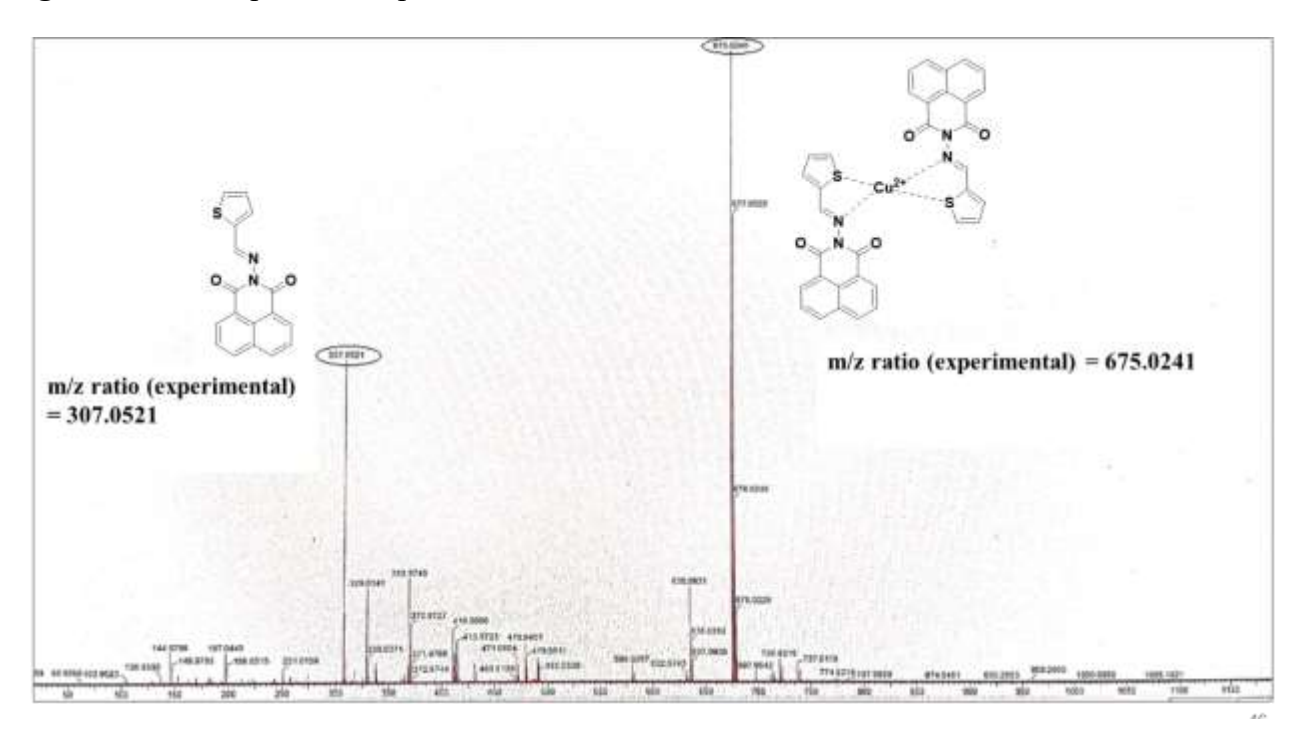


Figure A4: Mass spectrometry analysis of probe 2-Cu²⁺ complex

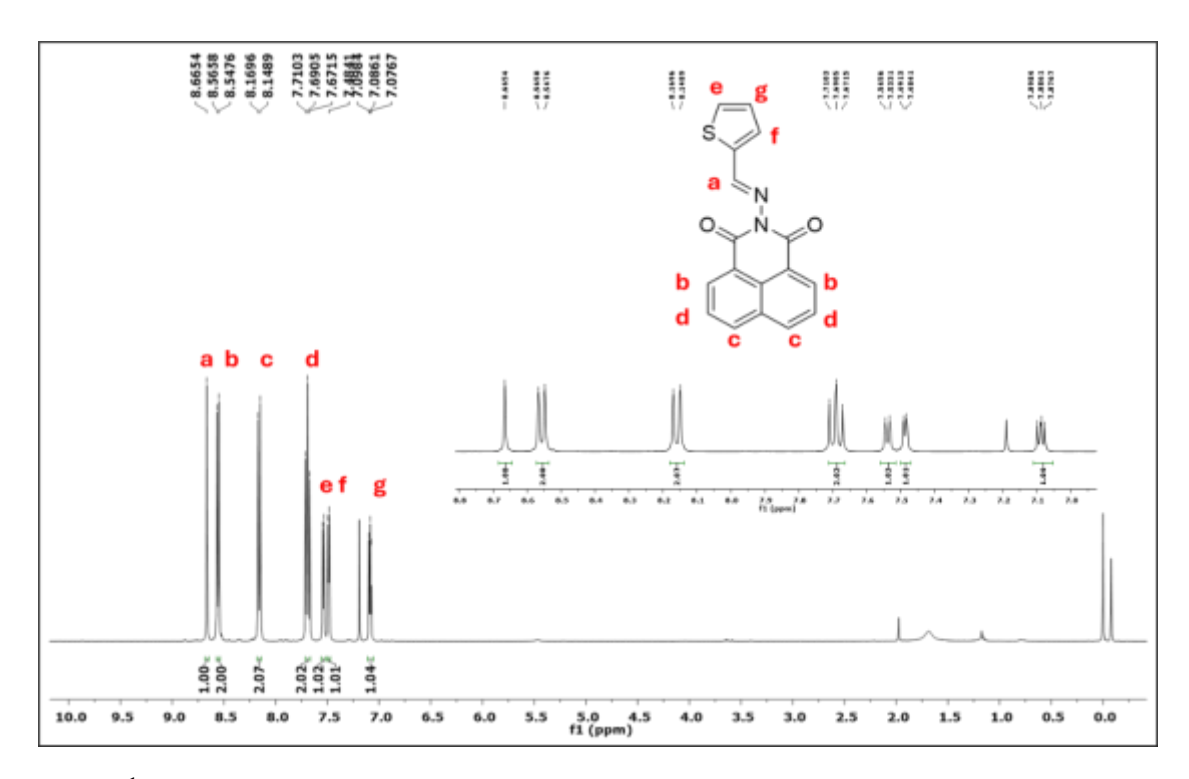


Figure A5: ¹H-NMR of probe 2

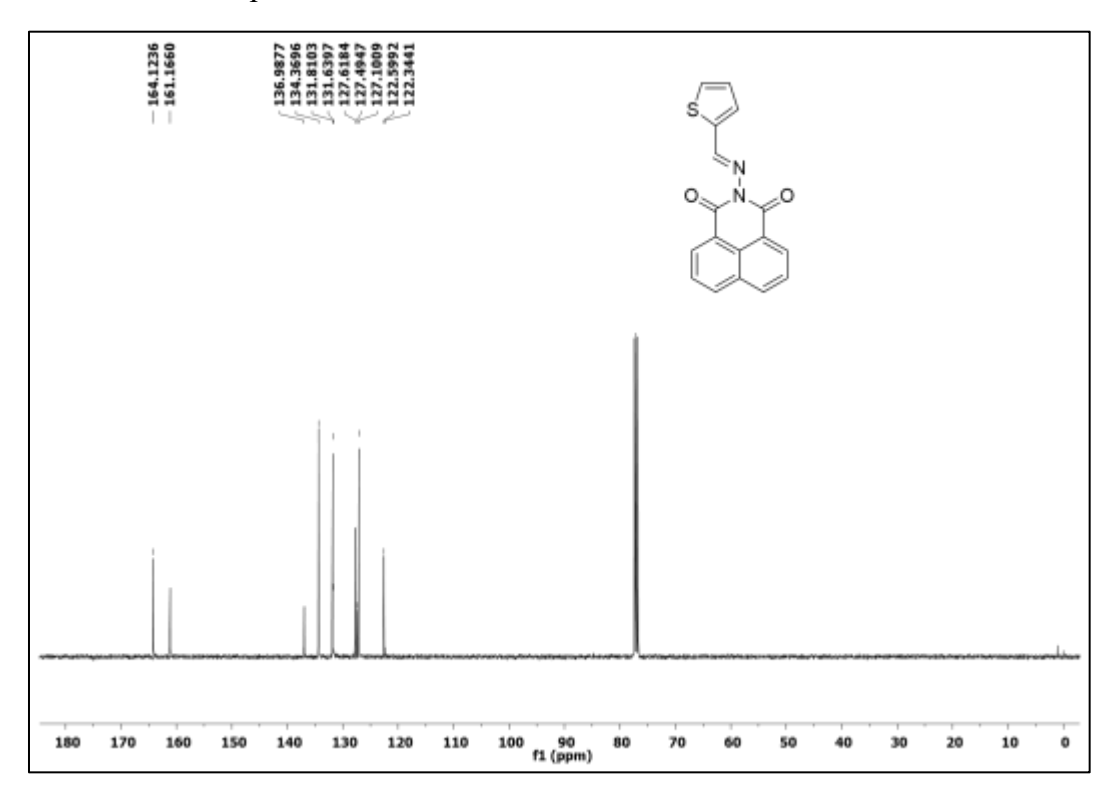


Figure A6: ¹³C-NMR of probe 2

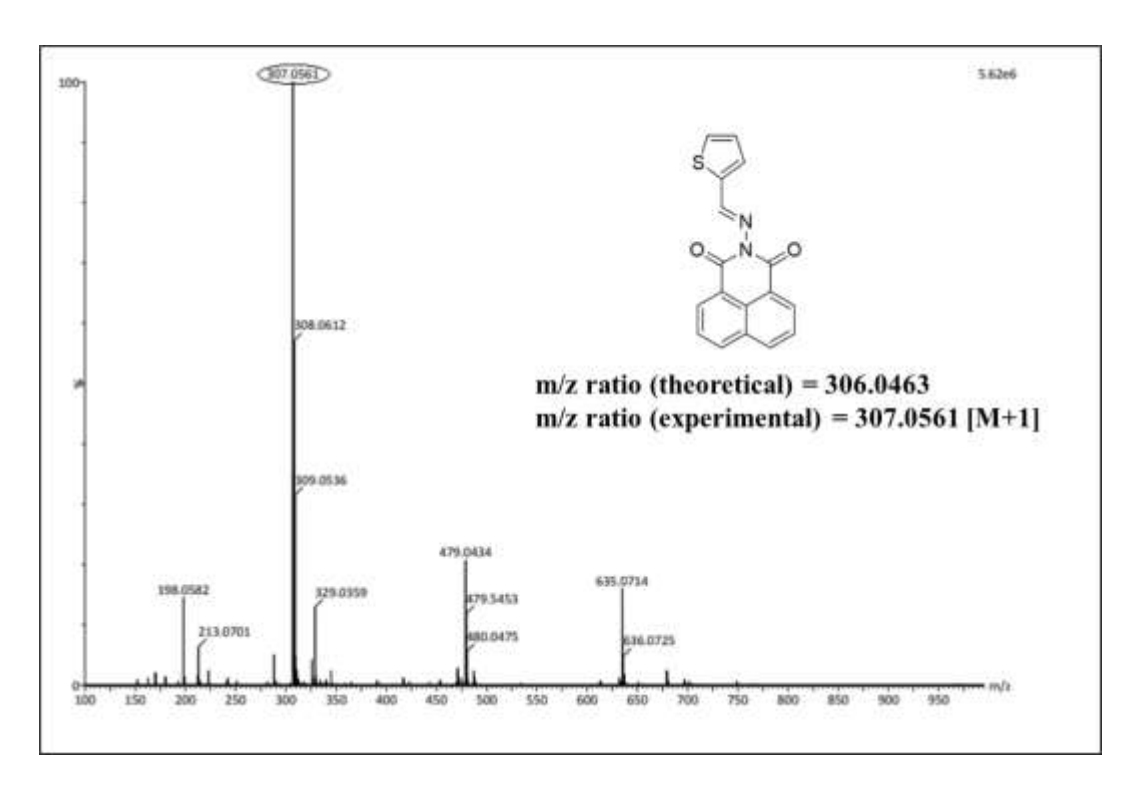


Figure A7: Mass spectra of probe 2

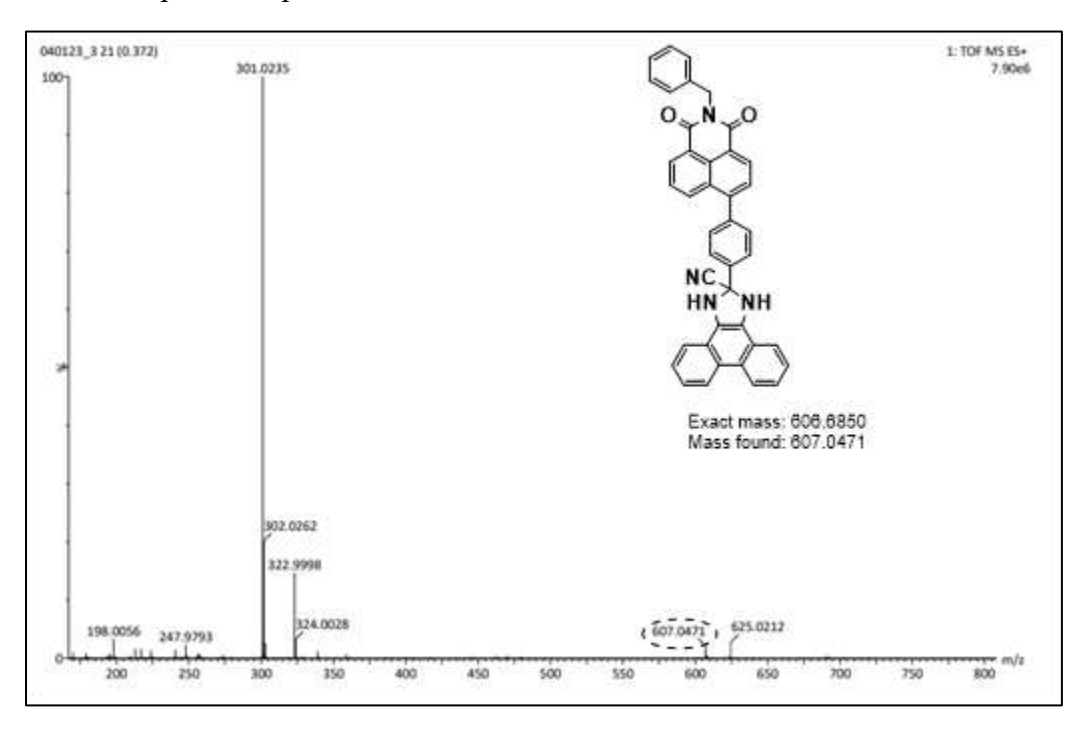


Figure A8: Mass spectra of probe 3+CN⁻ ion complex

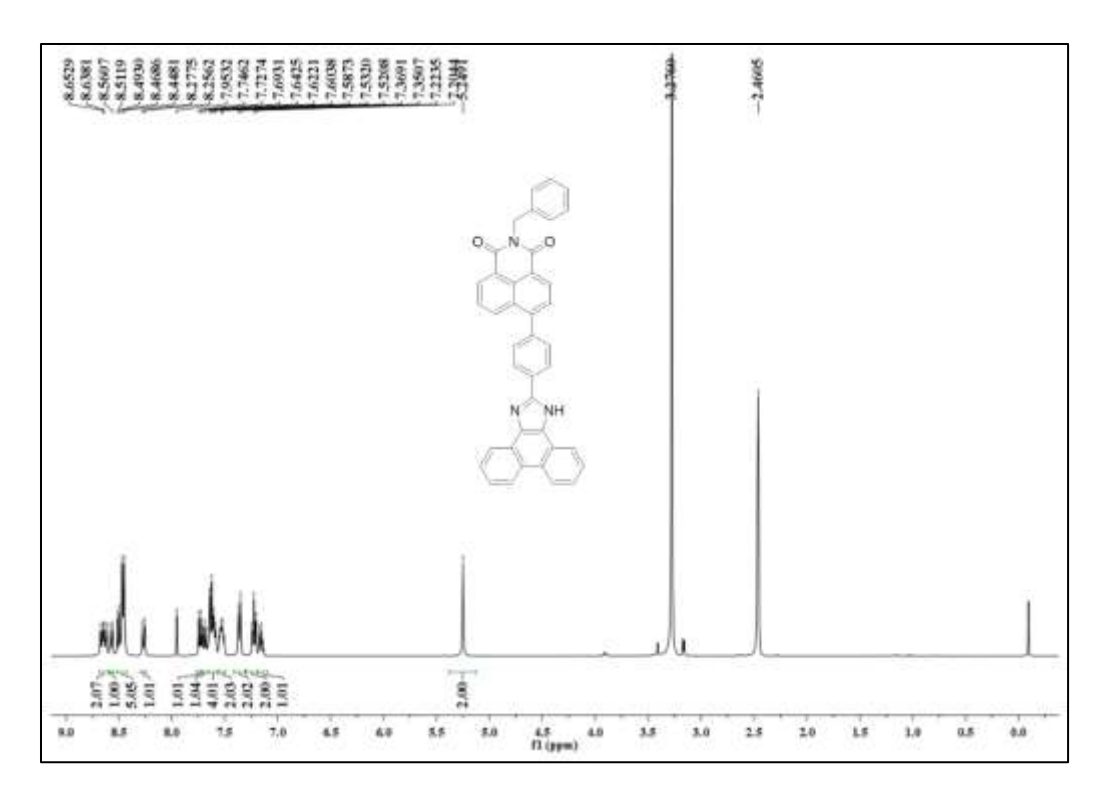


Figure A9: ¹H NMR spectrum of probe 3

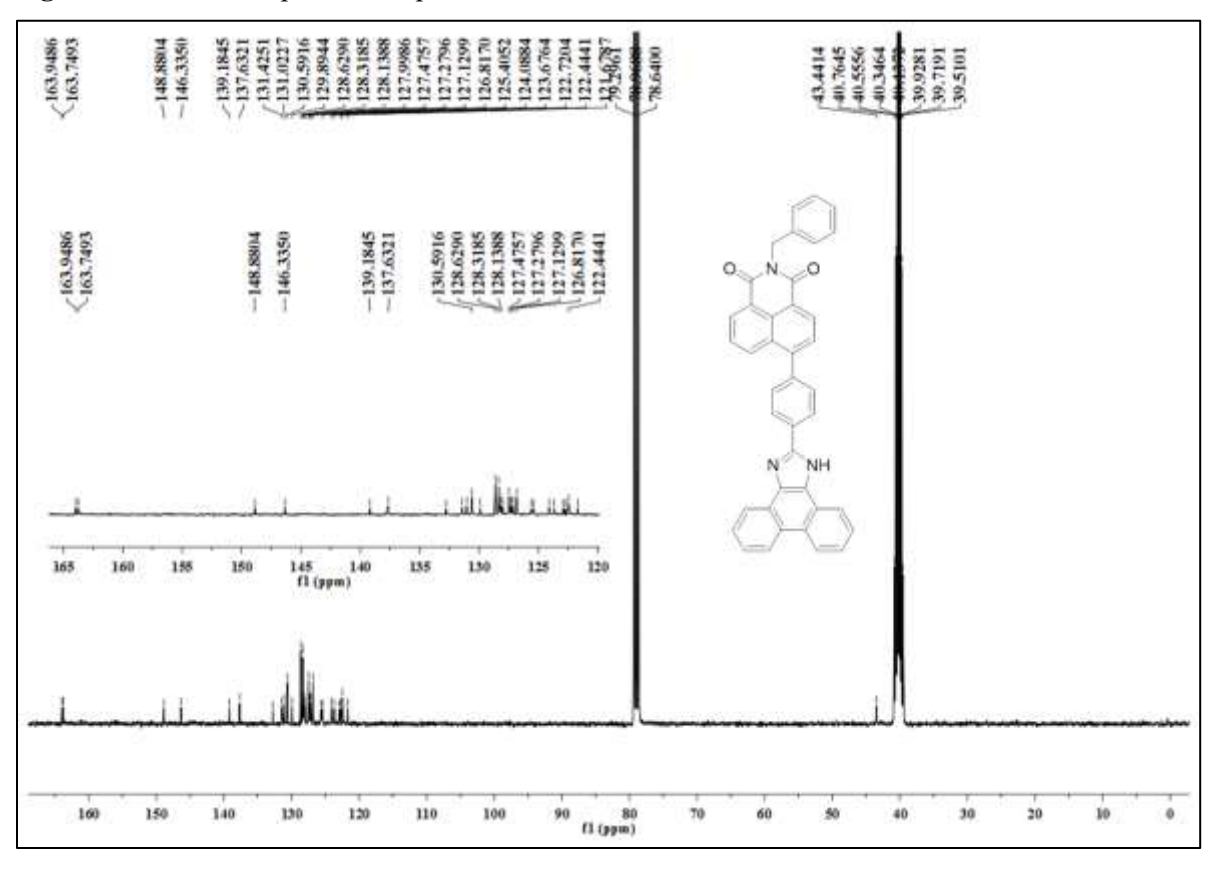


Figure A10: ¹³C NMR spectrum **of probe** 3

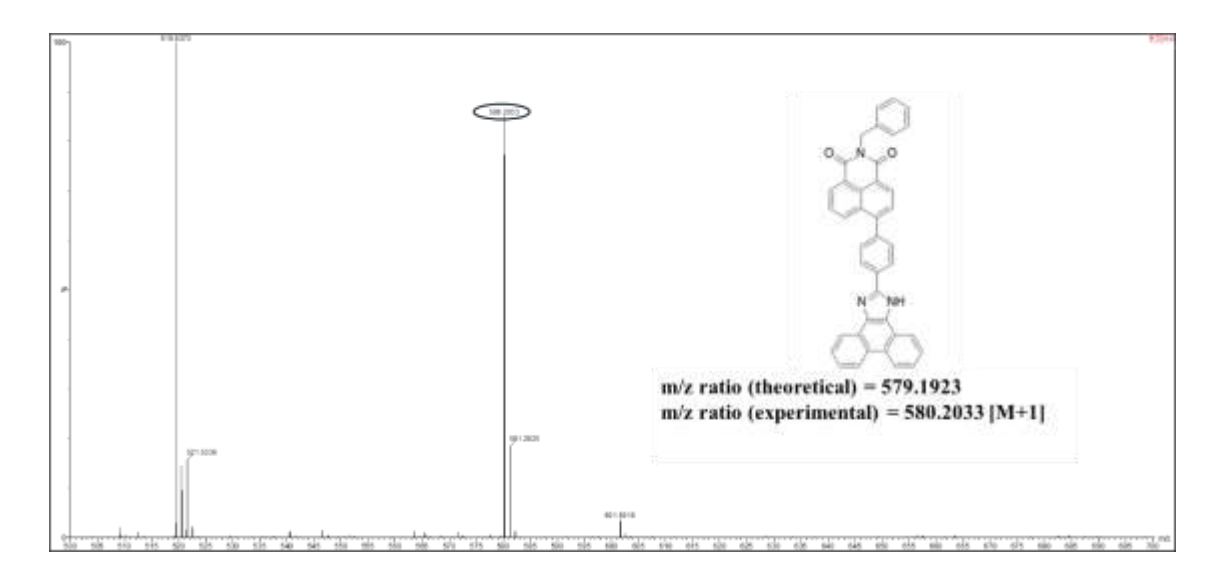


Figure A11: Mass spectrum of probe 3

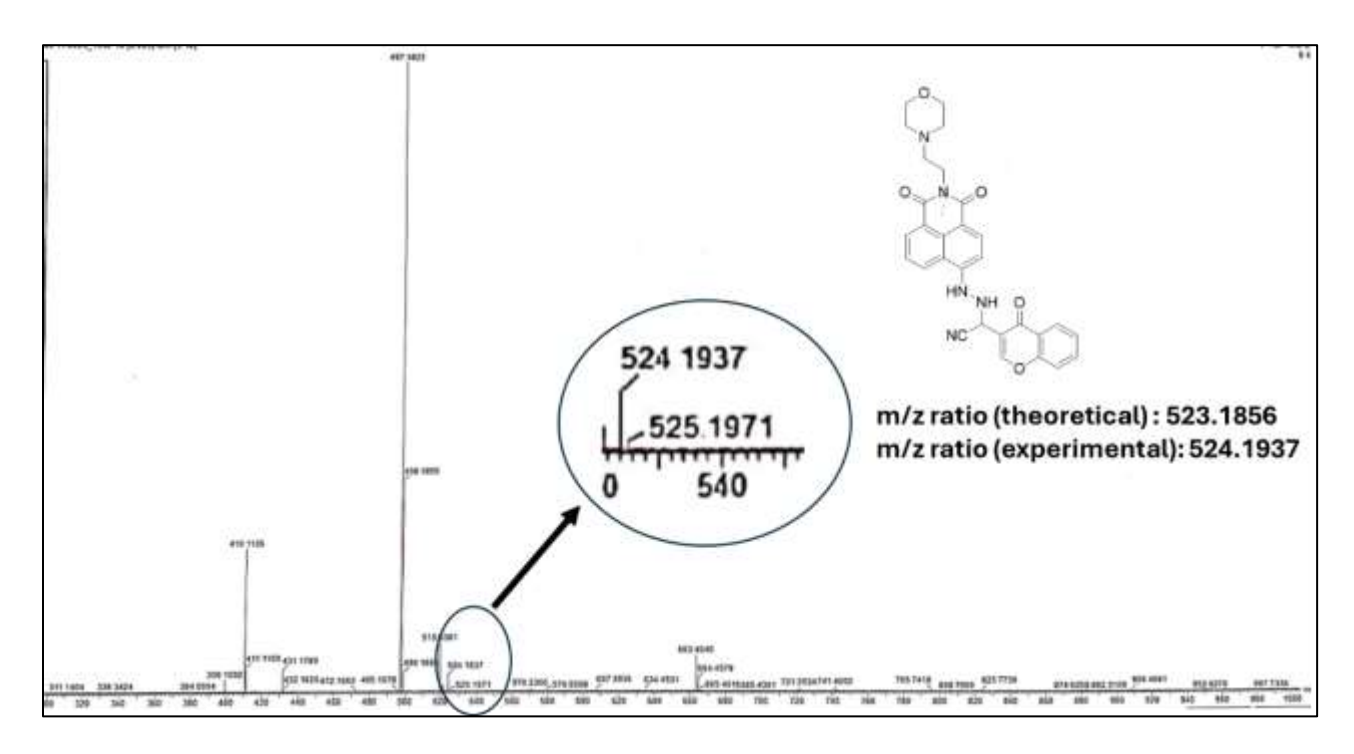


Figure A12: Mass spectra of probe 4 + CN⁻ complex

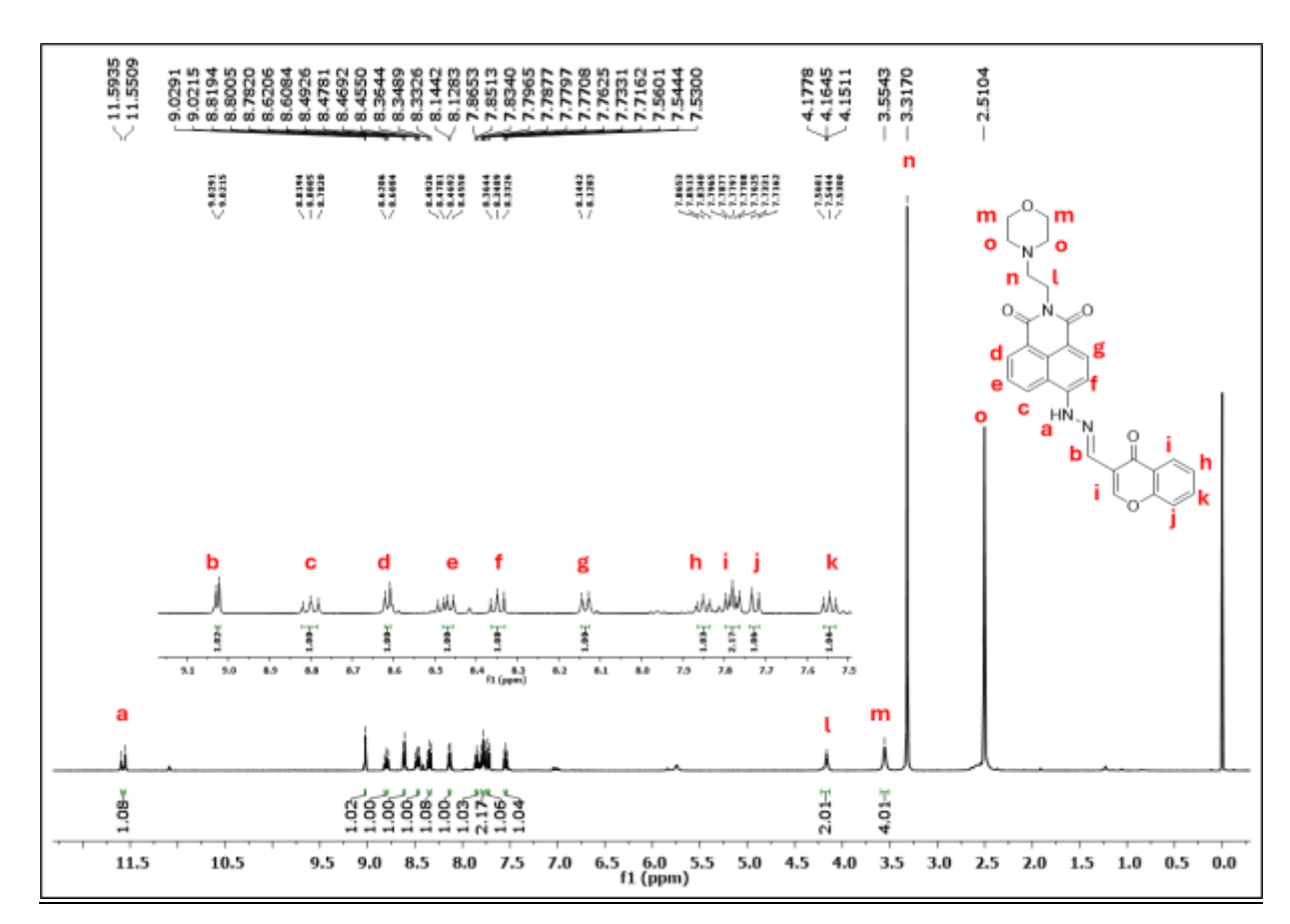


Figure A13: ¹H-NMR spectra of probe 4

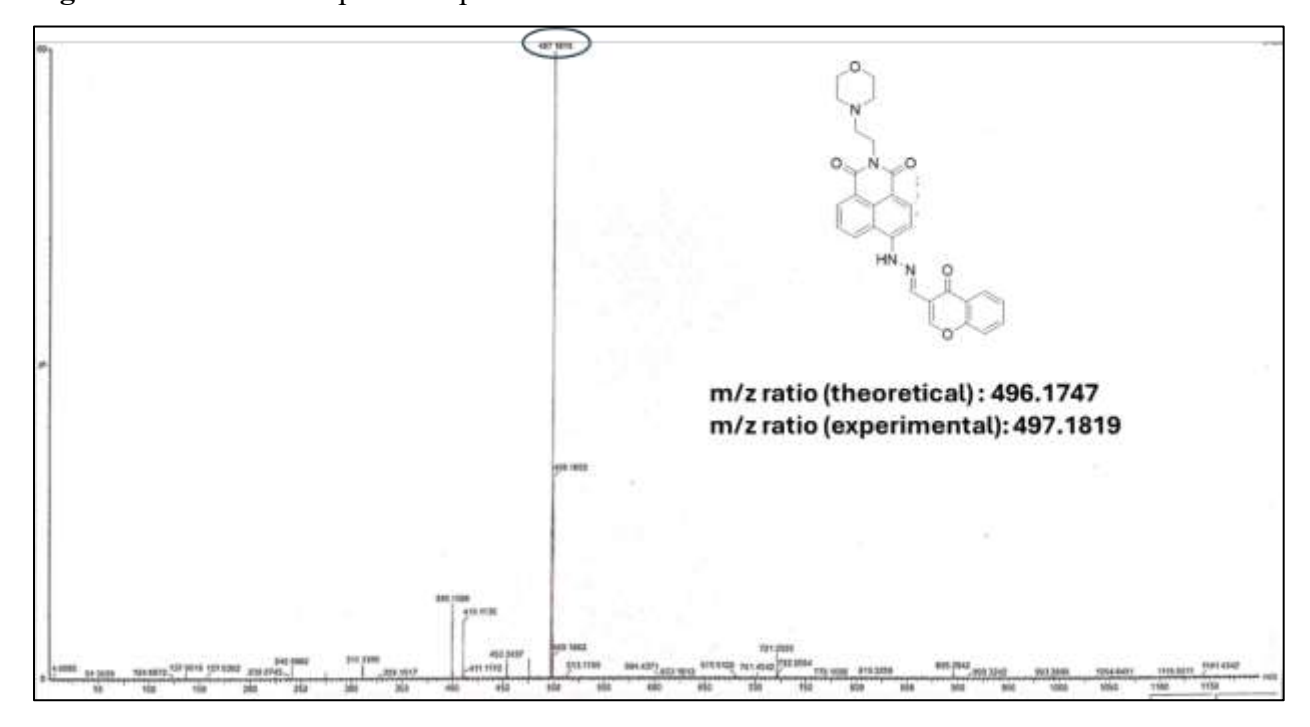


Figure A14: Mass spectra of probe

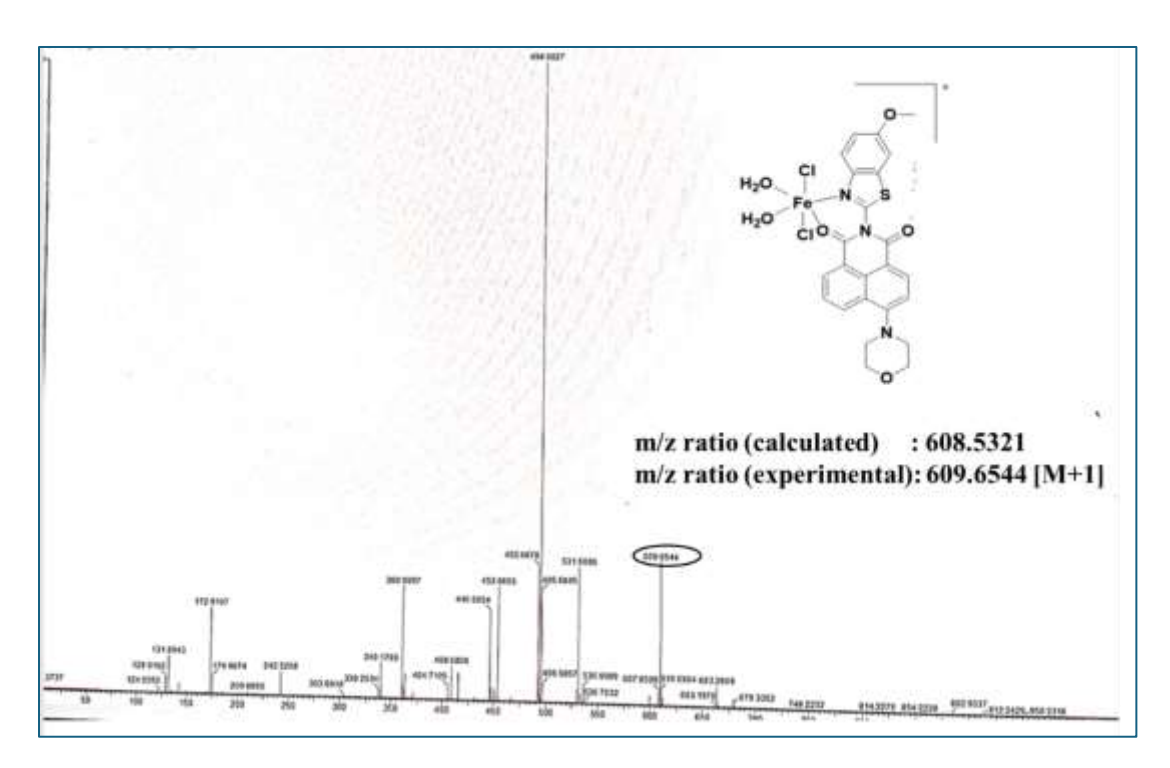


Figure A15: Mass spectra of probe $5 + Fe^{3+}$ ions

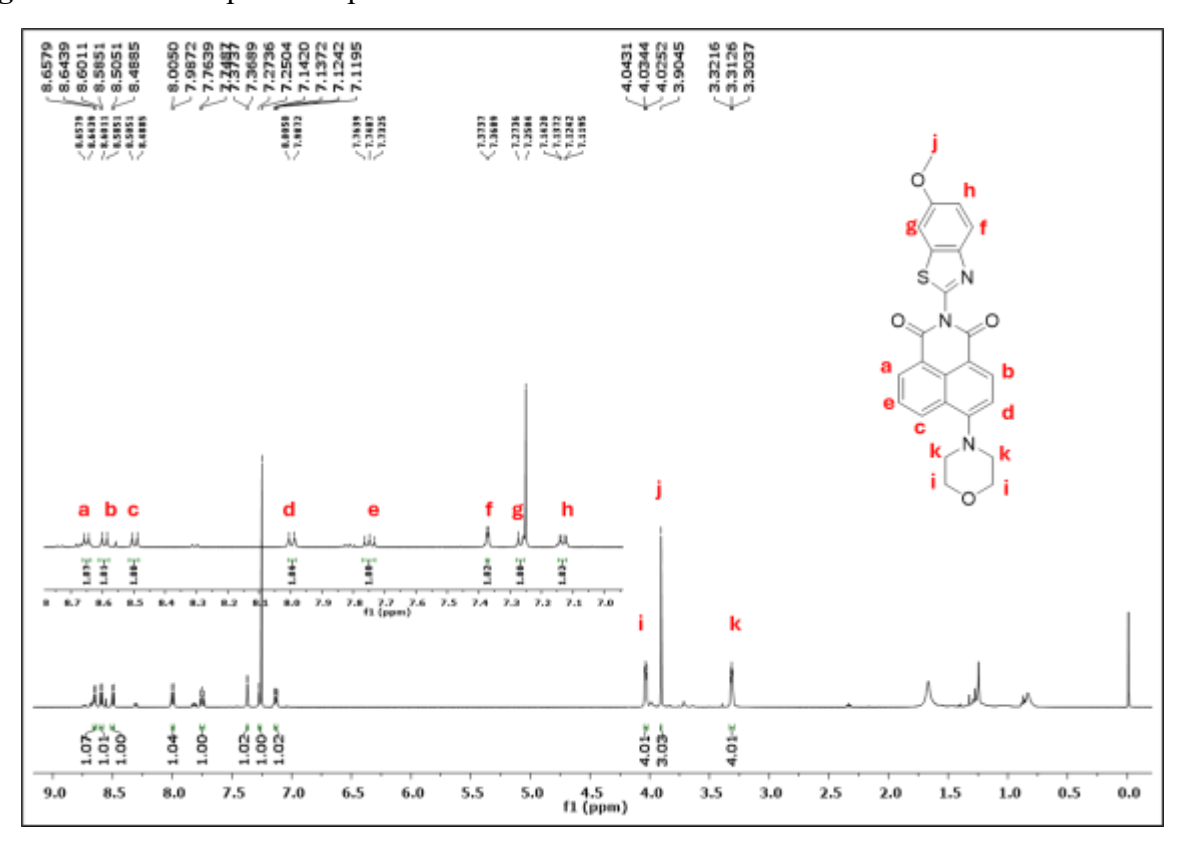


Figure A16: ¹H-NMR spectra of probe 5 in CDCl₃

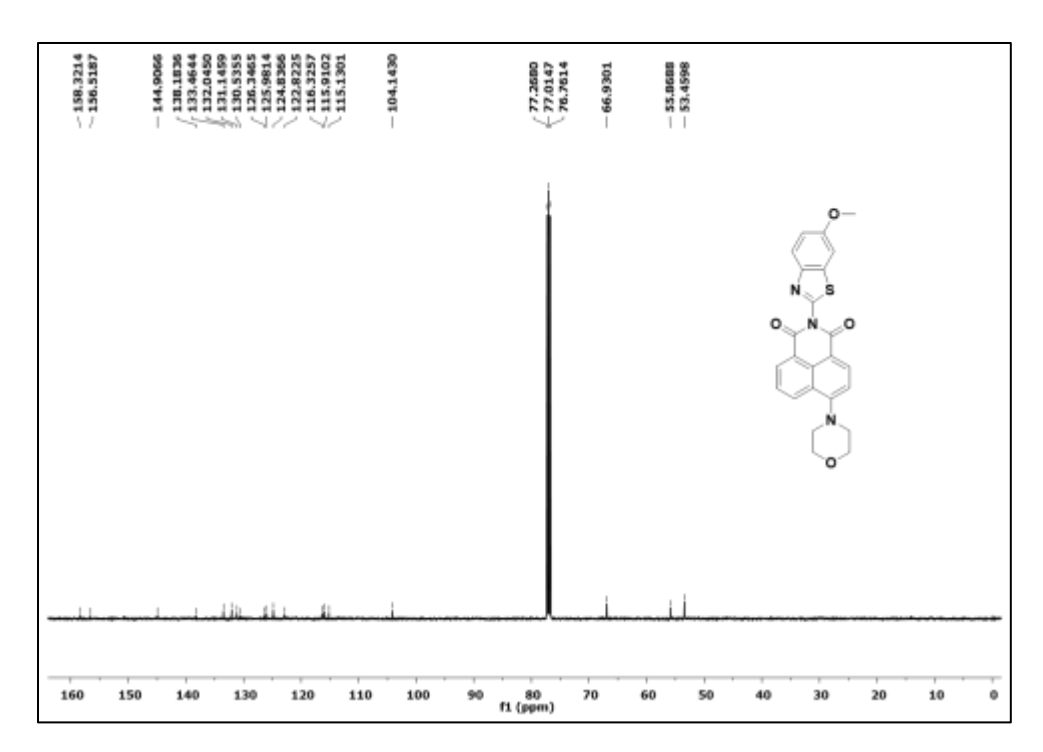


Figure A17: ¹³C-NMR spectra of probe 5 in CDCl₃

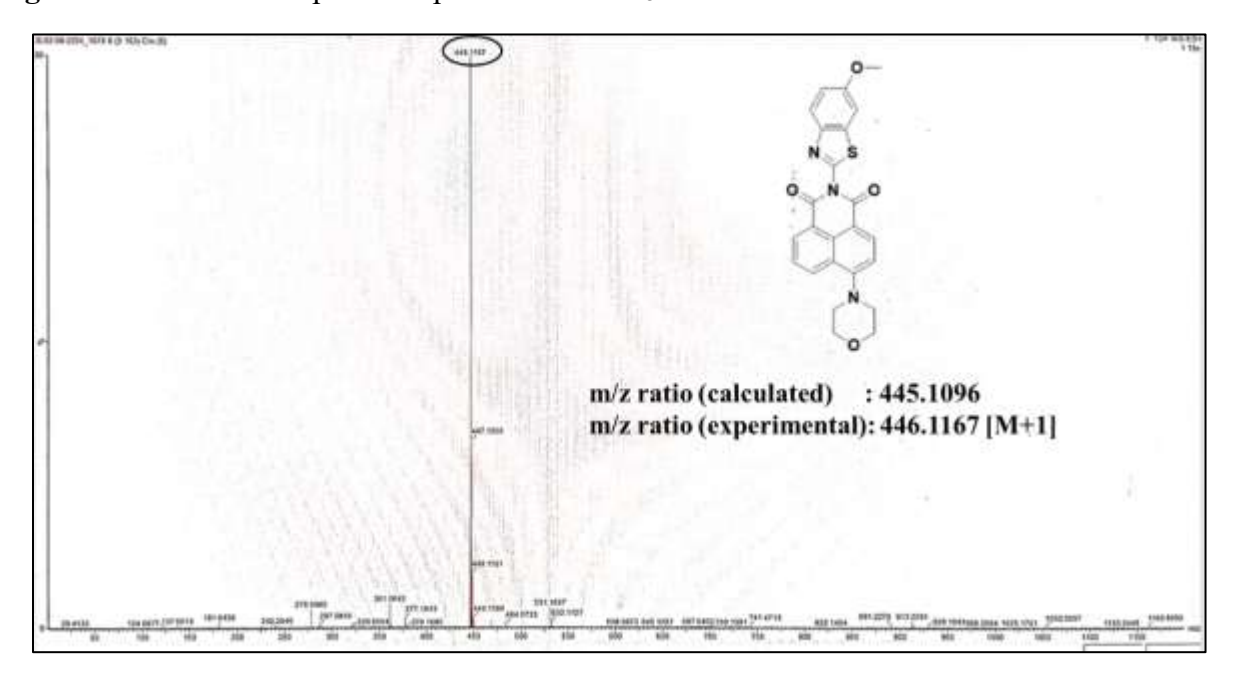


Figure A18: Mass spectra of probe 5

List of Publications, Conferences, and other achievements

Publications (Published)

- 1. <u>Kaur, G.</u>, Chaudhary, J., & Singh, I. (2025). Investigation of Naphthalimide-based Reversible Fluorescent Probe for the Selective Detection of Fe³⁺ ion: An Experimental and Computational (LOL/ ELF/ NLO/ DFT/ in silico) Approach. *Spectrochimica Acta Part A: Molecular and Biomolecular Spectroscopy* (Accepted)
- 2. Singh, M., <u>Kaur, G.</u>, Singh, I. (2025). Molecular self-assembly of peptides into supramolecular nano-architectures for target-specific drug delivery. **ACS Applied Bio Materials**. https://pubs.acs.org/doi/abs/10.1021/acsabm.5c00138
- 2. Bhat, A. A., Chaudhary, J., <u>Kaur, G.</u>, & Singh, I. (2025). Unlocking the Potential of Pyrrolidine Derivatives as Antidiabetic Agents: Insights from Computational Docking, ADME Profiling, and DFT Analysis. *ChemistrySelec*, 10(37), p.e00036.
- 3. <u>Kaur, G.</u>, Singh, I., & Kumar, G. (2025). A fluorescent "turn-off" naphthalimide-derived Schiff base for sensing Cu²⁺ ions: experimental and computational approach. **Photochemical & Photobiological Sciences**, 1-11.
- 4. <u>Kaur, G.</u>, Singh, I., Singh, G., & Kumar, D. (2025). A "naked-eye" Naphthalimide based Chemosensor for CN⁻ ion detection: Investigating its application as test-strips, Smartphone Analysis & Molecular Logic gate, and its TD-DFT study. **Inorganica Chimica Acta**, 581, 122615.
- 5. <u>Kaur, G.</u>, Palta, A., Kumar, G., Paul, K., & Singh, I. (2025). Fluorescent "turn-on" naphthalimide conjugate for the detection of CN⁻ ion with potential applications in real water samples and molecular logic gate. **Microchemical Journal**, 209, 112845.
- 6. <u>Kaur, G.</u>, Kumar, G., & Singh, I. (2025). A novel naphthalimide-derived "turn-off" chemosensor for the detection of Cu²⁺, F⁻, and CN⁻ ions. **Journal of Molecular Structure**, 1319, 139252.
- 7. Chaudhary, J., <u>Kaur, G.</u>, & Singh, I. (2024). Synthesis Strategies and Anti-parasitic Evaluation of Novel Compounds for Chagas Disease: Advancing Drug Discovery through Structure-Activity Relationships. European **Journal of Medicinal Chemistry**, 284, 117203.
- 8. <u>Kaur, G.</u>, Ahmad, A., & Singh, I. (2024). Recent Progress in Nanomaterial-based Electrochemical Biosensors for Hydrogen Peroxide Detection & their Biological Applications. **Talanta**, 286, 127447.
- 9. Raina, J., <u>Kaur, G.</u>, & Singh, I. (2024). Recent progress in nanomaterial-based aptamers as biosensors for point of care detection of Hg²⁺ ions and its environmental applications. **Talanta**, 277, 126372.

- 10. Bhat, A. A., <u>Kaur, G.</u>, Tandon, N., Tandon, R., & Singh, I. (2024). Current advancements in synthesis, anticancer activity, and structure–activity relationship (SAR) of coumarin derivatives. **Inorganic Chemistry Communications**, 167, 112605.
- 11. <u>Kaur, G.,</u> Rani, R., Raina, J., & Singh, I. (2024). Recent Advancements and Future Prospects in NBD-Based Fluorescent Chemosensors: Design Strategy, Sensing Mechanism, and Biological Applications. **Critical Reviews in Analytical Chemistry**, 1-41.
- 12. Singh, R., Shukla, A., <u>Kaur, G.,</u> Girdhar, M., Malik, T., & Mohan, A. (2024). Systemic analysis of glyphosate impact on environment and human health. **ACS omega**, 9(6), 6165-6183.
- 13. <u>Kaur, G.</u>, Singh, I., Tandon, N., Tandon, R., & Bhat, A. A. (2023). 1, 8-Naphthalimide-Based Chemosensors: A Promising Strategy for Detection of Metal Ions in Environmental and Biological Systems. **ChemistrySelect**, 8(44), e202301661.
- 14. <u>Kaur, G.</u>, Singh, I., Tandon, R., & Tandon, N. (2023). Recent advancements in coumarin based colorimetric and fluorescent chemosensors. **Inorganic Chemistry Communications**, 158, 111480.

Publications (Under Process)

- 1. <u>Kaur, G.,</u> Singh, M., & Singh, I. (2025). A 1,2,4-Triazole-Based ESIPT-Driven Ratiometric "Turn-On" Chemosensor for Selective Cyanide Detection with Test Strip Utility and Molecular Keypad Lock: An Experimental and Computational Exploration. **ACS Applied Bio Materials** (Under Revision)
- 2. Singh, S., <u>Kaur, G.</u>, & Singh, I. (2025). Supramolecular Self-Assembly of Virus Capsids into Functional Nanoarchitectures with Biological Relevance. **ACS Nano** (Under communication)
- 3. <u>Kaur, G.,</u> Elliot, P.I.P., & Singh, I. (2025). Synthesis of a novel 1,8-Naphthalimide derived chemosensor for sensing biologically significant metal ions Hg2+, Fe2+, and Fe3+ ions and its application in real water samples. **Inorganic Chemistry Communications** (Under communication).
- 4. Singh, S., <u>Kaur, G.</u>, & Singh, I. (2025). Mechanistic Understanding of Aggregation-Induced Emission: From Molecular Motion Restriction to Sensor Development. Elsevier- Book Chapter (Under communication)

List of Conferences & Workshops

- 1. Awarded Best Oral Presentation Award at 6th International Conference- Recent Advances in Fundamental and Applied Sciences, Lovely Professional University, India (2025).
- 2. Presented poster at National Symposium on Advanced Materials for Device Applications (DMA-2025), PU, India.
- 3. Presented poster at National Symposium on Catalysis on Sustainable Chemicals, Materials and Energy (CSCME-2025), TIET, India.
- 4. Presented a poster at the International Conference on Luminescent Materials: From Fundamentals to Applications (ICLMFA-2024, GNDU India (2024).
- Presented poster entitled Nitrobenzoxadiazole based chemosensor for the CNdetection and its application as XOR logic gate in the International Conference in Chemistry-2024 on Recent Advances In Applied Chemical Sciences by Maulana National Urdu University, India (2024).
- 6. Participated in a poster presentation on the topic entitled Design and synthesis of Rhodamine appended NBD derived fluorescent chemosensor for CN ion detection at the International Conference on Synthetic and Pharmaceutical Chemistry (2023).

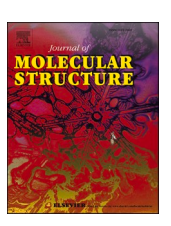
Other Achievements:

- 1. Patent (Published): Application No. 202411104856 A
 - The invention addresses the need for advanced, eco-friendly chemosensors with dual analytical and computational applications, paving the way for innovative solutions in environmental monitoring and molecular device development.
- 2. **Copyright (Published):** The copyright deals with the investigation methods and applicability of 1,8-Naphthalimide-based chemosensors

Contents lists available at ScienceDirect

Journal of Molecular Structure

journal homepage: www.elsevier.com/locate/molstr





A novel naphthalimide-derived "turn-off" chemosensor for the detection of Cu²⁺, F⁻ and CN⁻ ions

Gurdeep Kaur^a, Gulshan Kumar^b, Iqubal Singh^{c,*}

- a Department of Chemistry, School of Chemical Engineering & Physical Sciences, Lovely Professional University, Phagwara, 144411, India
- ^b Department of Chemistry, Banasthali University, Banasthali Newai, Rajasthan, 304022, India
- ^c School of Pharmaceutical Sciences, Lovely Professional University, Phagwara, 144411, India

ARTICLE INFO

Keywords: Napthalimide Absorbance Chemosensor Limit of detection TD- DFT

ABSTRACT

The development of selective chemosensor for the detection of detrimental analytes in the environment is crucial due to their catastrophic effects. In this study, a novel Schiff base derived from naphthalimide and salicylaldehyde was designed and prepared for the detection of Cu^{2+} , F, and CN^{-} ions in CH_3CN as medium. The chemosensor exhibits a red shift in the presence of Cu^{2+} , F^{-} , and CN^{-} ions accompanied by naked eye color change in the presence of F^{-} and CN^{-} ions. On the other hand, a "turn-off" response was observed in the presence of ion Cu^{2+} , F^{-} , and CN^{-} ions in the fluorescent spectrum. The good anti-interference characteristics, strong binding, and low limit of detection (LOD) of the chemosensor revealed its sensitivity against Cu^{2+} , F^{-} , and CN^{-} ions *i.e.* 1.25×10^{-5} M, 1.07×10^{-6} M, and 0.98×10^{-6} M, respectively. The binding ratio (1:1) was determined by Job's plot between the chemosensor and ions. In addition, the binding of ions with the chemosensor was proposed which was further supported by time-dependent density functional theory (TD-DFT) and IR spectrum data.

1. Introduction

The field of Supramolecular Chemistry has witnessed a tremendous revolution in recent years. The advanced properties of low cost, facile synthesis, excellent sensitivity, and good operability that are capable of detecting harmful analytes in the biological as well as environmental systems have gained significant attention in the research field. Ions play a crucial role in governing biological processes and affect human health [1]. Copper is one of the third most copious metals found in the human body responsible for various biological functions [2]. Cu²⁺ is the most common ionic form of copper that is present in the environment and responsible for various biological activities. Various physiological processes including enzyme-catalyzed procedures and redox reactions depend severely on Cu²⁺ ions [3]. It possesses wide application in different areas such as electrical wires, fertilizers, pesticides, water pipes, machinery parts, used in valves, feeds used for animals or birds, and the release of industrial effluents is the major cause of water contamination [4]. The augmented level of Cu²⁺ ions can be the cause of severe diseases like Wilson's disease [5], Alzheimer's disease, Menkes syndrome [6], Parkinson's disease [7], etc. The wide-ranging application of this metal in different spheres including agriculture, domestic, construction, and industry, is the primary cause of metal pollutants globally [8]. The permissible amount of copper ions in the human body usually ranges from 1-5 mg/day. Amongst anions, fluoride and cyanide have been widely studied due to their wide use in chemical and industrial fields. Fluoride ion (F) is one of the imperative anions posessing a significant role in numerous activities like water fluoridation, dental care, and chemical components in medical systems [9]. It is also used in various materials like toothpaste, medicine, tea, and food [10]. Its ingestion in minute amounts can avert bone deformity and various other dental problems [11]. However, as per the World Health Organization, the level of fluoride should be less than 1.5 ppm in drinking water [12]. Also, the presence of a high level of cyanide ions in the biological systems can lead to disruption of various processes due to its ability to bind with Fe³⁺ ions [13]. It can cause severe damage and in certain cases death if ingested more than 0.05mg/kg body weight. As per the WHO guidelines, the acceptable amount of cyanide in drinking water is $1.6\,\mu M$ due to its acute toxicity [14]. Therefore, it has become essential to monitor the level of anions by developing such effective methods.

The conventional sensing techniques like ion sensing, fluorescence sensing, and ¹⁹F NMR, etc. are quite expensive and require technical operators limiting its use. Therefore, the development of fluorescent chemosensors is a reliable and inexpensive approach for sensing ions and is easy to handle. They possess advantages such as low cost and

^{*} Corresponding author.

Contents lists available at ScienceDirect

Microchemical Journal

journal homepage: www.elsevier.com/locate/microc





Fluorescent "turn-on" naphthalimide conjugate for the detection of CN⁻ ion with potential applications in real water samples and molecular logic gate

Gurdeep Kaur^a, Aastha Palta^b, Gulshan Kumar^c, Kamaldeep Paul^b, Iqubal Singh^{d,*}

- a Department of Chemistry, School of Chemical Engineering & Physical Sciences, Lovely Professional University, Phagwara, India
- ^b Department of Chemistry and Biochemistry, Thapar Institute of Engineering and Technology, Patiala, India
- ^c Department of Chemistry, Banasthali University, Banasthali Newai, Rajasthan, India
- d School of Pharmaceutical Sciences, Lovely Professional University, Phagwara, India

ARTICLE INFO

Keywords: Chemosensor Suzuki–Miyaura Fluorescence Detection limit 1H NMR titration Practical applicability

ABSTRACT

A naphthalimide-based chemosensor was synthesized via a Suzuki–Miyaura cross-coupling reaction followed by amination yielding the desired chemosensor. The free probe itself exhibits feeble emission while in the presence of CN $^-$ ion, a "turn-on" response was observed in the fluorescent spectra. Also, the solvatochromic behaviour of the chemosensor was studied with different solvents of increasing polarity revealing the presence of Intra-molecular Charge Transfer (ICT) phenomenon specifically between the naphthalimide and phenanthroimidazole units. Further, the chemosensor exhibited remarkable selectivity and sensitivity towards CN $^-$ ion with a detection limit as low as $4.2\times10^{-8}\,\mathrm{M}$. At the same time, the sensor-ion ensemble was found to have a reversible effect in the presence of Fe $^{3+}$ ions (LOD $=8.9\,\mathrm{nM}$) which led to the construction of molecular logic INHIBIT gate. In addition, the plausible binding mechanism was studied through Job's plot, $^1\mathrm{H}\,\mathrm{NMR}$ titrations, and DFT studies revealing a 1:1 binding ratio between the chemosensor and ion. Further, the sensor found its practical applicability in detecting CN $^-$ ions in real-field water samples.

1. Introduction

In past years, there has been a burgeoning attention in the detection of anions because of their significant role in biological, chemical, and environmental processes [1]. However, the challenge is generally faced in terms of its diffused charges in comparison to cations while the interaction between the receptor and anion is generally weak and electrostatic [2,3]. Amongst various anions, one of the most hazardous ions is cyanide ion (CN⁻). The presence of CN⁻ ion is abundant in nature as well in synthetic materials. It is not just limited to industries but also has entered the normal supplies, for instance, the seed of various fruits, and enters into the environment as by-product of the combustion of various materials. Also, it is widely used by industries in electroplating, resin production, pharmaceuticals, gold mining, and textiles [4,5]. Further, accidental leaks, inappropriate discarding of industrial waste containing CN ion, and the breakdown of cyanide-based chemical warfare agents pose potential threats to the environment [6]. Immoderate contact with CN⁻ anion can cause various health issues acting as poison for the lungs, stomach, and skin. According to the Environmental Protection Agency (EPA), the suggested tolerable level of CN⁻ ion in drinking water is 0.2 ppm [7]. Therefore, developing a competent, quick-to-respond, and highly selective ${\rm CN^-}$ sensor holds immense significance for the environment.

Although there are numerous techniques including Inductively Coupled Plasma Atomic Emission Spectroscopy, Voltammetry, Inductively Coupled Plasma Mass Spectrometry, and Atomic Absorption Spectroscopy but sophisticated tools are laborious and expensive, therefore the optical chemosensors boast of being inexpensive and rapid response [8]. In addition, chromogenic and fluorogenic chemosensors offer facile preparation, fast response, high selectivity, visual detection, and accurate quantification [9]. Further, the strategy for CN⁻ ion sensing is usually based on coordination bonding and nucleophilic addition [5]. The hydrogen bonding method involves CN⁻ interaction with the binding unit, resulting in hydrogen bond formation thereby causing significant changes in color or fluorescence signals [10,11]. However, this method suffers from poor selectivity and inhibition in protic solvents. In addition, the chromogenic approach involves a chemical reaction where reactive sites are selectively attacked by CNnucleophiles, exhibiting improved selectivity and sensitivity towards CN⁻ ion [12]. Photophysical properties of organic fluorophores are

^{*} Corresponding author.

Contents lists available at ScienceDirect

Inorganica Chimica Acta

journal homepage: www.elsevier.com/locate/ica



Research paper



A "naked-eye" Naphthalimide based Chemosensor for CN⁻ ion detection: Investigating its application as test-strips, Smartphone Analysis & Molecular Logic gate and its TD-DFT study

Gurdeep Kaur^a, Iqubal Singh^{b,*}, Gurpinder Singh^a, Deepak Kumar^a

- a Department of Chemistry, School of Chemical Engineering and Physical Sciences, Lovely Professional University, Phagwara 144411, India
- b School of Pharmaceutical Sciences, Lovely Professional University, Phagwara 144411, India

ARTICLE INFO

Keywords: Naphthalimide Cyanide sensing Naked eye detection Limit of detection TD-DFT Logic gate

ABSTRACT

It is unanimously known that cyanide (CN $^-$) is one of the most toxic ions because it can interfere with the body's physiological phenomenon causing endocrine disorders, respiratory failure, hypoxia, vascular necrosis, and even death. Therefore, it is essential to develop cost-effective, sensitive, rapid, and efficient methods for sensing CN $^-$ ions. The naphthalimide-based highly selective probe 1 was successfully synthesized in a multi-step process. Probe 1 displayed high selectivity and specificity against cyanide (CN $^-$) ion and exhibited naked eye changes accompanied by "turn-off' fluorescence behavior. The introduction of CN $^-$ ion into the probe solution shows a visible color change from yellow to blue. Further, the optical methods were employed to determine the sensing performance of probe 1 towards CN $^-$ ion. The CN $^-$ ion detection limit was 5.47 μ M with a binding constant of 1.52 \times 10 5 M $^{-1}$. The fluorescence quenching efficiency towards cyanide ion was found to be 73.21 %, with the Stern-Volmer quenching constant to be 1.22 \times 10 5 M $^{-1}$. Job's plot analysis revealed 1:1 stoichiometric binding between probe 1 and CN $^-$ ion, further supported by FT-IR analysis, mass analysis, ¹H NMR titrations, and TD-DFT study. Probe 1 finds its practical application for detecting CN $^-$ ion using the test strip method. In addition, chemically switchable fluorescent dyes provide helpful building blocks for developing intricate molecular devices that communicate via adjustments in their emission characteristics; therefore, probe 1 was also used to establish molecular logic gates.

1. Introduction

The past few years have observed the inclination of researchers towards the recognition of ions because of their significant role in biological, chemical, and environmental processes [1]. However, the challenge is generally faced in terms of its diffused charges, such as anions in comparison to cations, while the interaction between the receptor and anion is usually weak and electrostatic [2,3]. Amongst various anions, one of the most hazardous ions is cyanide ion (CN⁻). The presence of CN⁻ ion is abundant in nature as well as in synthetic materials. It is not just limited to the industries but also has entered the ordinary sources, for instance, the seed of various fruits, and enters into the environment as a by-product of the combustion of various materials. Also, it is widely used by industries in electroplating, resin production, pharmaceuticals, gold mining, and textiles [4,5]. Further, accidental leaks, inappropriate discarding of industrial waste containing CN⁻ ion,

and the breakdown of cyanide-based chemical warfare agents pose potential threats to the environment [6]. Extreme contact with CN^- ion can result in various health issues, such as poisoning the lungs, stomach, and skin. As per the Environmental Protection Agency (EPA), the suggested tolerable extent of CN^- ion in drinking water is 0.2 ppm [7]. Therefore, developing a highly selective, rapidly responsive, and efficient CN sensor is of immense significance for the environment.

Although there are numerous sophisticated tools for detection but are quite laborious and expensive, so the optical chemosensors offer the advantage of being inexpensive and rapid response [8]. In addition, chromogenic and fluorogenic chemosensors offer simplified facile preparation, fast response, high selectivity, visual detection, and accurate quantification [9]. Further, the strategy for CN⁻ ion sensing is usually based on coordination bonding and nucleophilic addition [5]. The hydrogen bonding method involves CN⁻ association with the binding unit, resulting in the formation of hydrogen bonds thereby

^{*} Corresponding author.

ORIGINAL PAPERS



A fluorescent "turn-off" naphthalimide-derived Schiff base for sensing Cu²⁺ ions: experimental and computational approach

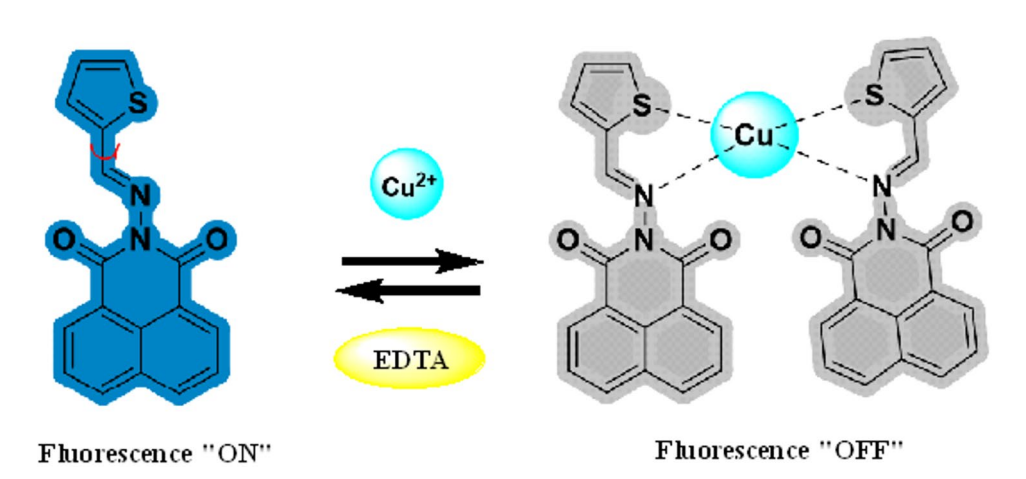
Gurdeep Kaur¹ · Iqubal Singh² · Gulshan Kumar³

Received: 24 January 2025 / Accepted: 12 May 2025 © The Author(s), under exclusive licence to the European Photochemistry Association, European Society for Photobiology 2025

Abstract

A naphthalimide-based Schiff base (probe 1) was synthesized for the selective detection of Cu^{2+} ions in a MeOH: H_2O (9:1, v/v) solvent system. The optical properties of the probe were investigated using UV–visible and fluorescence spectroscopy. In the UV–visible spectrum, probe 1 displayed absorption bands at 260 nm and 330 nm. Fluorescence measurements revealed an emission peak at 445 nm, accompanied by a shoulder at 470 nm. Upon the addition of Cu^{2+} ions, a significant quenching of the fluorescence intensity was observed, whereas other metal ions showed negligible interference. Quantitative analysis revealed a limit of detection (LOD) of 1.22×10^{-5} M and a limit of quantification (LOQ) of 4.08×10^{-5} M for Cu^{2+} . The association constant was calculated from the B–H plot which was determined to be 1.43×10^2 M⁻¹ with the quenching constant of 1.99×10^2 M calculated from the Stern–Volmer plot. Also, the binding stoichiometry of 2:1 was determined by Job's plot between the probe 1 and Cu^{2+} ions, respectively. Further, the results were validated by HR-MS, DLS, and computational studies. The DFT studies revealed a charge transfer from the thiophene ring towards the naphthalimide moiety which was significantly inhibited in the presence of Cu^{2+} ions.

Graphical abstract



Keywords Naphthalimide · Emission · Quenching · Stern-Volmer plot · Computational studies

1 Introduction

Published online: 23 May 2025

Copper is a vital metal ion, that plays essential roles in various biological processes across living organisms, including bacteria, fungi, plants, and animals [1]. In humans, copper

is crucial for blood clotting, hormone maturation, cellular energy processing, red blood cell formation, and bone health [2–4]. It also functions as an oxidant, protecting cells from oxidative damage caused by free radicals. Moreover, copper contributes to brain energy production and neurotransmitter regulation, influencing cognitive function and neurological

Extended author information available on the last page of the article





www.chemistryselect.org

Unlocking the Potential of Pyrrolidine Derivatives as Antidiabetic Agents: Insights from Physicochemical Analysis, Molecular Docking, ADMET, and DFT Studies

Aeyaz Ahmad Bhat, [a] Jitendra Chaudhary, [b] Gurdeep Kaur, [a] and Iqubal Singh*[b]

This study investigates the antidiabetic potential of pyrrolidinebased derivatives using an integrated computational approach comprising molecular docking, physicochemical profiling, ADMET analysis, DFT, and topological evaluations. Out of 65 hypothesized derivatives, 27 adhered to Lipinski's Rule, demonstrating the oral drug-likeness. ADMET screening further shortlisted 7 compounds (6l, 8l, 9e, 9h, 9k, 9l, and 9n) that exhibited favorable absorption (HIA: 0.708-0.996), moderate plasma protein binding (23.82-76.37%), non-inhibition of major CYP450 isoforms (1A2, 2C19, 2C9, 2D6, and 3A4), and nontoxic profiles with no predicted carcinogenicity, mutagenicity, or cardiotoxicity. Docking studies revealed that three derivatives exhibited the strongest binding affinities: 9h: -8.01, -7.06, -8.1 kcal/mol; **9k**: -8.2, -7.88, -8.2 kcal/mol and **9l**: -8.03, -7.4, -7.39 kcal/mol, for α -amylase, α -glucosidase, DPP-IV, respectively, all of which surpassed the standards acarbose and vildagliptin. NCI and docking pose analysis highlighted stable hydrogen bonding, $\pi-\pi$ stacking, and π -alkyl interactions, reinforcing their strong binding stabilities. Moreover, DFT calculations were performed for the three top-ranked derivatives (**9h**, **9k**, and **9l**). Overall, these three derivatives developed as the most promising candidates amid all the assessed pyrrolidine derivatives for their binding affinity for all, results showed lower Δ Egap values (**9h**: 3.2920 eV, **9k**: 5.1475 eV, **9l**: 5.4148 eV) than vildagliptin (6.5511 eV), indicating higher polarizability, reactivity, and charge transfer potential. Electrophilicity indices (ω) of 0.0030, 0.0115, and 0.0138 for **9h**, **9k**, and **9l**, respectively, suggested significant biological potential. Topological analyses revealed electron localization at electrophilic sites and delocalization over π -systems, supporting reactivity and structural stability. Collectively, these findings highlight **9h**, **9k**, and **9l** as promising antidiabetic candidates.

1. Introduction

Diabetes mellitus (DM) is a chronic metabolic disorder characterized by elevated blood glucose levels resulting from defects in insulin secretion, insulin action, or both. Among its types, type 2 diabetes mellitus (T2DM) is the most prevalent, accounting for approximately 90%–95% of global diabetes cases. Deput a global burden of T2DM is rising rapidly due to ageing populations, sedentary lifestyles, and poor dietary habits. It is estimated that over 415 million individuals were affected by diabetes in 2015, with projections reaching 642 million by 2040. According to the World Health Organization, diabetes will likely become the seventh leading cause of death by 2030. Current antidiabetic therapies include α -glucosidase inhibitors (e.g., acarbose), DPP-4 inhibitors (e.g., vildagliptin), and insulin sensitizers.

As we all know, the use of medications has been increasing rapidly nowadays, which in turn is causing various side effects

- [a] A. Ahmad Bhat, G. Kaur

 Department of Chemistry, School of Chemical Engineering and Physical
 Sciences. Lovely Professional University. Phaawara 144411. India
- [b] J. Chaudhary, I. Singh School of Pharmaceutical Sciences, Lovely Professional University, Phagwara 144411, India E-mail: brar.iqubal@gmail.com
- Supporting information for this article is available on the WWW under https://doi.org/10.1002/slct.202500036

in our bodies. For example, antidiabetic therapies are frequently associated with a range of adverse effects that can negatively impact patient compliance and long-term health outcomes.^[6] Biguanides, such as metformin, often lead to gastrointestinal issues including nausea and diarrhea, and in rare cases, may cause lactic acidosis or vitamin B12 deficiency with long-term use.[7] Sulfonylureas are known to cause hypoglycemia, weight gain, and increase the risk of cardiovascular events.[8] Thiazolidinediones, like pioglitazone and rosiglitazone, may result in fluid retention, weight gain, heart failure, bone fractures, and potentially bladder cancer.^[9] DPP-4 inhibitors, including sitagliptin and vildagliptin, have been associated with side effects such as nasopharyngitis, joint pain, and rare cases of pancreatitis. [10] α -Glucosidase inhibitors like acarbose commonly cause gastrointestinal discomfort including flatulence, bloating, and diarrhea.[11] SGLT2 inhibitors, such as canagliflozin and dapagliflozin, may lead to urinary tract infections, dehydration, diabetic ketoacidosis, and, in some cases, an increased risk of lower-limb amputation.^[12] Insulin therapy, while essential in many cases, is also linked to hypoglycemia, weight gain, and injection site complications such as lipodystrophy. These side effects highlight the urgent need to develop safer and more tolerable antidiabetic treatments.[13]

If we look at recent advancements and medications used for the treatment of T2DM as shown in Figure 1,^[14] pyrrolidine-based compounds have emerged as promising therapeutic agents due to their ability to inhibit key enzymes involved in carbohy-



www.acsabm.org Review

Molecular Self-Assembly of Peptides into Supramolecular Nanoarchitectures for Target-Specific Drug Delivery

Mohan Singh, Gurdeep Kaur, and Iqubal Singh*



Cite This: https://doi.org/10.1021/acsabm.5c00138

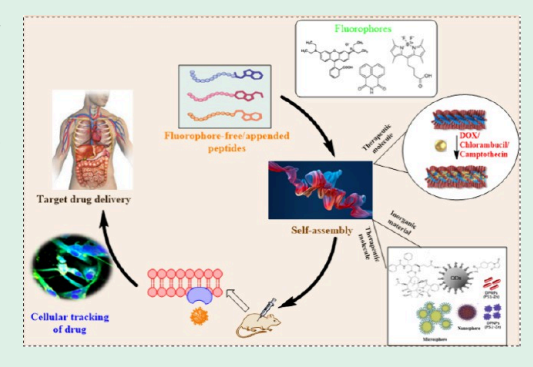


ACCESS I

Metrics & More

Article Recommendations

ABSTRACT: Self-assembled fluorescent peptides are promising drug-delivery vehicles targeting cancer cells and enhancing the precision of therapeutic agents. Several systems have been developed including fluorescent peptides as cysteine-core peptides, cyclic peptides, nanostructures and peptide polymer conjugates specifically designed for targeted drug delivery. Further, these supramolecular carriers aid in targeted drug transport by using different cargos like doxorubicin (Dox), paclitaxel (PTX), etc. Additionally, dipeptides such as tryptophan-phenylalanine self-assemble via zinc ion chelation, facilitating the endosomal escape thereby enhancing the drug efficacy within multifunctional nanoparticle systems. Furthermore, pH-activatable and enzyme-responsive peptide nanostructures have been engineered to exhibit potential for controlled drug release. These self-assembled peptide systems not only enable targeted drug delivery but also provide controlled release, with applications extending to ocular drug delivery



and the treatment of retinal diseases. These systems possess intrinsic fluorescence properties that allow real-time tracking of drug release and cellular uptake, making them highly useful for theranostic applications. Moreover, fluorescently tagged cell-penetrating peptides (CPPs) are widely used to explore how these systems enter cells, revealing multiple ways they are taken up, like endocytosis, micropinocytosis, direct membrane crossing, and counterion-assisted transport. This versatility adds real value to peptide-based approaches in cancer therapy. Further research advancements should enhance stability, explore combination therapies, and improve clinical translation for broader therapeutic applications.

KEYWORDS: Self-assembly, Fluorescent peptides, Cancer cells, Cell-penetrating peptides, Targeted drug delivery

1. INTRODUCTION

Molecular self-assembly happens naturally, guided by several noncovalent forces like electrostatic and hydrophobic interactions, π - π stacking, hydrogen bonds, and coordination.^{1,2} Self-assembly occurs when various macromolecules or fragments interact under physiological conditions, either as identical or different components. These interactions usually start in a disorganized state but gradually result in a wellordered final structure, such as distinct structured or crystal macromolecules.^{3,4} Self-assembly is a prevalent and fundamental process that is crucial for the biological functions of cells. For instance, the construction of the cytoskeleton is facilitated by the self-assembly of actin and tubulin proteins, while the configuration of the double-helix structure of DNA exemplifies another instance of molecular self-assembly. In particular, the self-assembly of peptides involves the creation of molecular aggregates with specific arrangements through noncovalent interactions.⁶ Nanotechnology, particularly in drug delivery, has leveraged self-assembly due to its ability to generate nanoscale systems that can encapsulate and deliver therapeutic agents. Nanodrug delivery systems have demonstrated immense potential in overcoming challenges associated

with traditional cancer therapies by improving targeted drug delivery, reducing side effects, and enhancing therapeutic efficacy.^{7,8}

Peptides, which are short chains of amino acids (2–50 residues), exhibit a wide range of biological functions by acting as hormones, enzymes, and signaling molecules. Owing to their specificity and efficacy, peptides play a significant role in medical research and drug development. Peptide self-assembly is a spontaneous process driven by both kinetic and thermodynamic factors. This process typically arises from the effects of various forces discussed above, which contribute to the formation of ordered and complex nanostructures. These forces involved in peptide self-assembly are crucial in facilitating the assembly process thereby promoting the formation of thermodynamically stable supramolecular struc-

Received: January 23, 2025 Revised: May 1, 2025 Accepted: May 2, 2025



Contents lists available at ScienceDirect

Talanta

journal homepage: www.elsevier.com/locate/talanta



Recent progress in nanomaterial-based electrochemical biosensors for hydrogen peroxide detection & their biological applications

Gurdeep Kaur^a, Aftab Ahmad^b, Iqubal Singh^{b,*}

- ^a School of Chemical Engineering and Physical Sciences, Lovely Professional University, Phagwara, 144411, India
- ^b School of Pharmaceutical Sciences, Lovely Professional University, Phagwara, 144411, India

ARTICLE INFO

Keywords: Electrochemical Metal oxides Nanomaterials Nanocomposites Hydrogen peroxide

ABSTRACT

The electrochemical biosensor has brought a paradigm shift in the field of sensing due to its fast response and easy operability. The performance of electrochemical sensors can be modified by coupling them with various metal oxides, nanomaterials, and nanocomposites. Hydrogen peroxide is a short-lived reactive oxygen species that plays a crucial role in various physiological and biological processes. Therefore, its monitoring is of paramount importance. With this, the research fraternity has developed various nanomaterial-based superlative sensors that have enhanced the sensing performance towards H₂O₂ in terms of sensitivity, detection limit, and linear range. The integration of nanocomposite materials has allowed for the synergistic combination of different components, leading to improved sensor stability, selectivity, and detection limits. The precious metal alloys, metal oxides, semiconductor nanomaterials, carbon cloth, multi-walled carbon nanotubes, graphene oxide, and nanoparticles demonstrate effective catalytic performance for detecting H₂O₂ electrochemically. These advanced materials possess extraordinary properties and structures, rendering them highly advantageous for diverse applications. These biosensors aid in monitoring H₂O₂ levels secreted by MCF-7, HeLa cells, NIH-3T3, and A549 cells in real-time. Further, this type of biosensor identified alterations in H2O2 levels in the lungs, bronchoalveolar lavage fluid (BALF) of mice with pulmonary fibrosis, activated hepatic stellate cells, and the livers of mice with liver fibrosis. The current review highlights the recent advancements in compositions, morphology, limit of detection, sensitivity, biological applications, etc. properties of the electrochemical biosensors for H_2O_2 detection.

1. Introduction

Hydrogen peroxide (H_2O_2) , a reactive oxygen species (ROS), is a crucial biological molecule for internal immune activity and transmission of signals [1,2]. H_2O_2 is a short-lived reactive oxygen species present both in water as well in the atmosphere due to its various ongoing biological processes [3]. In aquatic ecosystems, it is formed due to the irradiation of UV rays in dark conditions [4–7]. H_2O_2 plays a crucial function in different physiochemical and biological operations, like breaking down pollutants, self-cleaning, transforming metabolites, etc. Within organisms such as plants, the production of H_2O_2 is facilitated by enzymes (superoxide and superoxide dismutase) during the electron transport chain process in chloroplasts and mitochondria, as well as plasma NADH oxidase and other apoplastic oxidases [8]. The transportation in plants is helped by aquaporins with the assistance of enzymes like catalase, peroxiredoxin, glutathione peroxidase-like

enzymes, and ascorbate peroxidase [9–11]. In humans, it is produced in vivo both enzymatically and non-enzymatically by dismutation of superoxide radicals (Oʻʻʻ). Also, H_2O_2 is directly formed with the help of various oxidase enzymes and β -oxidation of fatty acids [12–15]. Though chemically it is poorly reactive, it becomes highly dangerous when it readily converts into reactive hydroxyl radicals (OHʻ) on exposure to UV radiations or when it interacts with transition metal ions, probably iron due to its in vivo presence e.g. by liberating Fe²⁺ ions from heme proteins [16].

Further, it has been extensively used in medications, textiles, mining, etc., and as a food preservative for controlling microbial growth [17]. H_2O_2 has garnered the interest of numerous researchers because of its pivotal role in biological signaling and as a by-product in cellular oxidative reactions [18,19]. Excessive build-up of H_2O_2 within cells can result in severe ailments like Alzheimer's, heart disease, and cancer, and disrupt normal cell functions, leading to cell death and making it

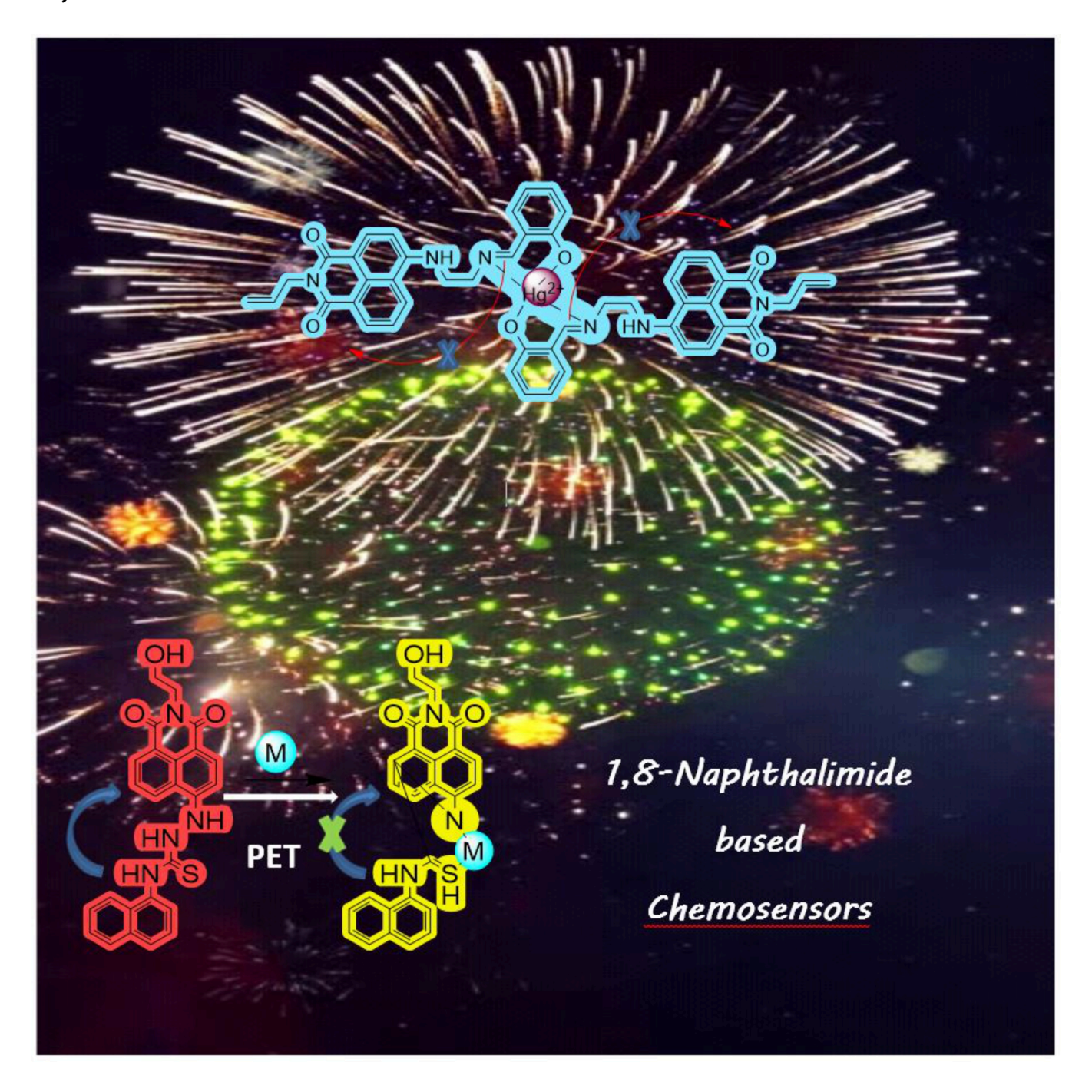
^{*} Corresponding author.



www.chemistryselect.org

1,8-Naphthalimide-Based Chemosensors: A Promising Strategy for Detection of Metal Ions in Environmental and Biological Systems

Gurdeep Kaur, $^{[a]}$ Iqubal Singh, $^{[b]}$ Nitin Tandon, $^{*[a]}$ Runjhun Tandon, $^{[a]}$ and Aeyaz Ahmad Bhat $^{[a]}$



Contents lists available at ScienceDirect

Inorganic Chemistry Communications

journal homepage: www.elsevier.com/locate/inoche



Recent advancements in coumarin based colorimetric and fluorescent chemosensors

Gurdeep Kaur^a, Iqubal Singh^b, Runjhun Tandon^a, Nitin Tandon^{a,*}

- ^a Department of Chemistry, School of Chemical Engineering & Physical Sciences, Lovely Professional University, Phagwara 144411, India
- ^b School of Pharmaceutical Sciences, Lovely Professional University, Phagwara 144411, India

ARTICLE INFO

Keywords:
Coumarin
Cations
Anions
Chemosensor
Fluorescence
Sensing mechanism

ABSTRACT

Coumarin comprises of large number of organic compounds displaying diverse electronic and structural features enabling their application in the field of supramolecular chemistry. The presence of heteroatom and other groups including semicarbizide, pyrimidine, ester linkages, tetraphenylethylene, etc. in the coumarin-derived motif acts as a ligand by offering coordination sites to the selected ions thereby perturbing the optical properties, thus emerging as chemosensors. These sensors can detect an array of substances, including hazardous gases, metal ions, anions, reactive oxygen and nitrogen species, and biothiols. The coumarin probe appended with benzothiazole selectively recognizes Cu²⁺ ions with a detection limit of 4 ppb among the pool of ions, while amongst anions coumarin derived malononitrile-based sensor detected ClO⁻ ions with the least LOD recorded at 5.7 nM. A general trend of 1:1 stochiometric ratio between the metal and ion complexes was found in most of the cases. This review emphasizes the recent advancements in coumarin-based chemosensors for sensing cations and anions during the period 2019-2022. Also, it provides insight into the design of probes, analytical performance, sensing mechanism, and complexation of probes with their respective ions. The probes' colorimetric and fluorescent approach is sophisticatedly elaborated with pictorial representation along with its detection limit, the stoichiometric ratio of the metal-ligand complex, and its performance in optimum pH conditions. This extensive review may facilitate and intrigue the research fraternity to develop more efficient chemosensors for sensing harmful ions possessing broad applications and challenge the researchers for its commercial utility.

1. Introduction

All life forms require various ions to perform vital functions and to regulate fundamental processes like metabolism, signaling, osmotic regulation, catalysis, biomineralization, generation of gradient potential across the membrane, nerve conduction, and a unique manner to store energy. Transition metal ions often referred to as trace elements like zinc, chromium, copper, cobalt, manganese, chromium, nickel, vanadium, etc. play a significant role in biological processes [1]. Though often present in substantial amounts their characterization is occasionally misleading. The genomic studies have suggested that elements such as zinc and iron are extensively used in biology; on the other hand, metals like cobalt, copper, nickel, and molybdenum are used broadly

across various organisms [2] while the use of ions such as cadmium, mercury, uranium, and arsenic are regarded as detrimental biometals [3]. Still, the microbial metalloproteomes remain uncharacterized. The initial step to characterize the metal ion in an organism is to quantify the metal content of cells and tissues. Biometals exist in various forms including tightly bound metal-like cofactors, and hydrated ions, in a loosely bound form such as in heterogeneous buffers and as labile species. The total content is an aggregate of all these diverse forms [4]. Nowadays, rising interest in ionic activities in biological systems and their legal requirements for water, food, medical substances, and environmental monitoring is of great significance. Moreover, the foremost importance of anions (cyanide, fluoride, hypochlorite, hydroxide, acetate, etc.) in diverse biological fields inspired us to develop selective and

Abbreviations: ICP-AES, Inductively Coupled Plasma Atomic Emission Spectroscopy; AAS, Atomic Absorption Spectroscopy; ICP-MS, Inductively Coupled Plasma Mass Spectrometry; AIE, Aggregation Induced Emission; TICT, Twisted Intramolecular Charge Transfer; CHEF, Chelation Enhanced Fluorescence; PET, Photoinduced Electron Transfer; LOD, Limit of Detection; LOQ, Limit of Quantitation; ICT, Intramolecular Charge Transfer; GSH, Glutathione; DLS, Dynamic light scattering; EPA, Environment Protection Agency; PPi, Pyrophosphate Ions; WHO, World Health Organisation; CHQF, Chelating Quenched Fluorescence.

E-mail address: tandonnitin12004@gmail.com (N. Tandon).

^{*} Corresponding author.



Critical Reviews in Analytical Chemistry



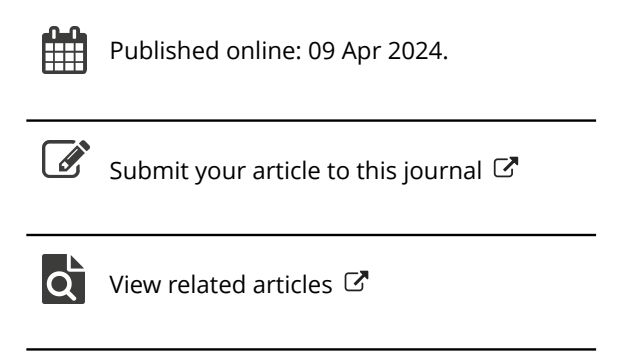
ISSN: (Print) (Online) Journal homepage: www.tandfonline.com/journals/batc20

Recent Advancements and Future Prospects in NBD-Based Fluorescent Chemosensors: Design Strategy, Sensing Mechanism, and Biological Applications

Gurdeep Kaur, Richa Rani, Jeevika Raina & Iqubal Singh

To cite this article: Gurdeep Kaur, Richa Rani, Jeevika Raina & Iqubal Singh (09 Apr 2024): Recent Advancements and Future Prospects in NBD-Based Fluorescent Chemosensors: Design Strategy, Sensing Mechanism, and Biological Applications, Critical Reviews in Analytical Chemistry, DOI: 10.1080/10408347.2024.2337869

To link to this article: https://doi.org/10.1080/10408347.2024.2337869





Contents lists available at ScienceDirect

Talanta

journal homepage: www.elsevier.com/locate/talanta





Recent progress in nanomaterial-based aptamers as biosensors for point of care detection of ${\rm Hg}^{2+}$ ions and its environmental applications

Jeevika Raina^a, Gurdeep Kaur^b, Iqubal Singh^{a,*}

- ^a School of Pharmaceutical Sciences, Loyely Professional University, Phagwara, India, 144411
- ^b School of Chemical Engineering and Physical Sciences, Lovely Professional University, Phagwara, India, 144411

ARTICLE INFO

Keywords: Aptamer Biosensor Mercury Electrochemical Fluorescent Colorimetric

ABSTRACT

Among the foremost persistent heavy metal ions in the ecosystem, mercury (Hg^{2+}) remains intimidating to the environment by producing a catastrophic effect on the environment as well as on mankind due to the exacerbation of anthropogenic activities. Therefore, it has become necessary to develop superlative techniques for its detection even at low concentrations. The conventional approaches for Hg^{2+} ions are quite laborious, and expensive, and require expertise in operating sophisticated instruments. To overcome these limitations, aptamer-based biosensors emerged as a promising tool for its detection. DNA-based aptamers have evolved as a significant technique by detecting them even in ppb levels. This review outlines the progress in aptamer-based biosensors from the year 2019–2023 by inducing changes in the electrochemical signal or by fluorescent/colorimetric approaches. The electrochemical sensors used nanomaterial electrodes or increasing the sensitivity whereas fluorescent and colorimetric sensors exhibit quenching or strong fluorescence in the presence of Hg^{2+} ions depending upon the prevailing mechanism or visible color changes. This perturbation in the signals could be attributed to the formation of the T- Hg^{2+} -T complex with the aptamers in the presence of ions revealing its real-time and biological applications in living or cancerous cells. Furthermore, next-generation biosensors are suggested to bring a paradigm shift to the integration of high-end smartphones, machine learning, artificial intelligence, etc.

1. Introduction

Heavy metal pollutants in the environment remain a persisting issue in modern life with aggrandizing modernization and industrialization. One such detrimental pollutant is mercury (Hg²⁺) which causes a serious nuisance to the ecosystem [1]. Mercury occurs naturally in the Earth's environment as inorganic, metallic, and organic forms and broadly exists in water, soil, and air [2]. It enters into the natural environment by degassing Earth's crust by volcanic eruptions whereas excessive burning of fossil fuels has further increased its abundance in the atmosphere [3]. This metallic contaminant is toxic to mankind as well as to the environment in numerous ways. Its exposure to humans can cause failure of vital organs such as lungs, brain, and kidneys; serious immune system diseases; and even induce severe disorders like Minamata disease, Hunter-Russell syndrome, and Pink disease [4-7] According to the World Health Organization (WHO) and the USA Environmental Protection Treaty (EPA), the maximum permissible limit of mercury in water is 30 nM and 10 nM respectively [8,9]. Therefore, the requirement

of high sensitivity and selectivity to detect mercury ions in real samples and their quantification is still arduous. However, to tackle this problem various conventional methods including Inductively Induced Plasma (ICP), Atomic Absorption Spectrometry (AAS), mass spectrometry (MS) Atomic Spectrometry, etc. were used [10,11]. However, these costly instruments and their time-consuming procedures make them unsuitable for online use. To combat these challenges, some promising techniques such as colorimetry, fluorescence, electrochemistry, electro-chemiluminescence, and surface plasmon resonance were adopted to monitor the levels of ${\rm Hg}^{2+}$ ions (see Tables 1–3).

In the present scenario, the application of single-stranded oligonucleotides known as aptamers has been exploited to detect the target analytes in the sample. They are synthesized by an *in vitro* technique commonly known as SELEX (Systematic Evolution of Ligands by Exponential Enrichment) for targeting specific molecules [50,51]. During the entire procedure, the modification of the molar ratio that is between the target and the library is done for the adjustment of the selection stringency, effectively enhancing the enrichment of high-affinity aptamers.

^{*} Corresponding author.

Contents lists available at ScienceDirect

European Journal of Medicinal Chemistry

journal homepage: www.elsevier.com/locate/ejmech



Review article

Synthesis strategies and anti-parasitic evaluation of novel compounds for chagas disease: Advancing drug discovery through structure-activity relationships

Jitendra Chaudhary ^a, Gurdeep Kaur ^b, Iqubal Singh ^{a,*} o

- ^a School of Pharmaceutical Sciences, Lovely Professional University, Phagwara, 144411, India
- ^b School of Chemical Engineering and Physical Sciences, Lovely Professional University, Phagwara, 144411, India

ARTICLE INFO

Keywords: Chagas disease Trypanosoma cruzi Structure-activity relationships Amastigotes Trypomastigotes

ABSTRACT

This study presents a comprehensive exploration of the synthesis of novel compounds targeting Chagas Disease (CD) caused by *Trypanosoma cruzi*. It is a global health threat with over 6–7 million infections worldwide. Addressing challenges in current treatments, the investigation explores diverse compound classes, including thiazoles, thiazolidinone, imidazole, pyrazole, 1,6-diphenyl-1*H*-pyrazolo[3,4-*b*] pyridine, pyrrole, naphthoquinone, neolignan, benzeneacyl hydrazones, and chalcones-based compounds. Highlighting compounds with superior trypanocidal activity compared to standard drugs. The study elucidates structure-activity relationships, emphasizing the impact of substituents, fluorine presence, and substitution patterns. Noteworthy findings include neolignan derivatives demonstrating efficacy against intracellular amastigotes and free-moving trypomastigotes, with unsaturated side chains. Benzeneacylhydrazones and chalcones, as novel classes, showed varied efficacy, with certain compounds surpassing benznidazole. A novel series of triketone compounds exhibited strong anti-parasitic activity, outperforming standard drugs. Docking study revealed that the halogen and methoxy substituted phenyl ring, thiazole, thiazolidine-4-one, quinoline, isoindoline-1,3-dione, pyrrole heterocyclic motifs can play the key role in the designing of effective inhibitors of *T. cruzi.* Mutually, these insights placed the foundation for the development of innovative and effective treatments for CD, addressing the urgent need for improved therapeutic options.

1. Introduction

Chagas disease (CD), also referred to as American trypanosomiasis, was first identified by the Brazilian physician Carlos chagas in 1909 [1–3]. This debilitating multi-systemic disorder is due to the *paras*itic protozoan *Trypanosoma cruzi* (*T. cruzi*) [4,5]. It presents a substantial threat to human health [6], with the potential to be life-threatening [7]. It is primarily transmitted through the excrement of infected triatomine bugs, also referred to as kissing bugs [8,9]. However, it can also spread through blood donations, organ transplants, and perinatal transmission as well as through laboratory accidents. The impact of this disease is most profoundly felt in impoverished rural communities, where access to healthcare is limited [10]. The CD has a significant geographical footprint, with endemic regions spanning more than 21 continental Latin American countries [11]. However, its reach extends beyond regions where the disease is prevalent due to population movement and

travel, making it a global concern. CD shows a broad range of clinical manifestations, affecting various organ systems, such as the heart, digestive tract, and nervous system. Around 6 to 7 million people worldwide are infected with CD, with 9000 to 15,000 new cases reported per year [12]. Globally, trypanosomiasis contributes to an estimated 10,000-14,000 death yearly [13]. It affects impoverished communities living in areas with restricted healthcare availability. More than 90 % of global cases are concentrated in Argentina (1.5 million), Brazil (1.2 million), and Mexico (0.88 million), Bolivia has the greatest number of cases, totalling 0.61 million. Colombia (0.44 million) and Venezuela (0.31 million) also have significant cases, where it is endemic [14]. The CD is linked to poor nutrition, compromised immune systems, and concurrent infections. The manifestations of CD initially include fever, site swelling, rash, eyelid swelling, and spleen/liver enlargement. Later stages can lead to complications like irregular heartbeat, heart esophagus, and failure. colon enlargement, and

^{*} Corresponding author.

Contents lists available at ScienceDirect

Inorganic Chemistry Communications

journal homepage: www.elsevier.com/locate/inoche





Current advancements in synthesis, anticancer activity, and structure–activity relationship (SAR) of coumarin derivatives

Aeyaz Ahmad Bhat a, Gurdeep Kaur a, Nitin Tandon a, Runjhun Tandon a, Iqubal Singh b,*

- a Department of Chemistry, School of Physical Sciences, Lovely Professional University, Phagwara 144411, India
- ^b School of Pharmaceutical Sciences, Lovely Professional University, Phagwara 144411, India

ARTICLE INFO

Keywords:
Anticancer
Coumarin
Synthesis
Cancer cell lines
Structure-activity relationship

ABSTRACT

Within the realm of cancer therapeutics, coumarin derivatives stand out as a promising class of compounds, exhibiting a wide array of biological effects and demonstrating significant potential for anticancer activity while minimizing detrimental side effects. This comprehensive study endeavours to navigate through the broad spectrum of coumarin derivatives, offering a thorough exploration of their synthetic methodologies, target cancer cell lines and the intricate interplay between chemical structure and biological activity. Through an unbiased analysis, this research aims to unravel the complex structure–activity relationships that govern the anticancer efficacy of coumarin derivatives, shedding light on their underlying mechanisms of action within cellular pathways. By highlighting the recent research findings it provides a holistic understanding of the therapeutic potential of coumarin derivatives, offering insights that could pave the way for their future application in cancer therapy.

1. Introduction

According to a World Health Organization (WHO), report, more than 13 million cancer-related deaths will occur worldwide in 2030 [1,2]. The majority of cancers can be identified by their uncontrolled growth of cells without differentiation. According to estimates, one in five individuals will develop cancer before the age of 75 [3]. Generally, the occurrence of cancer is due to the dysregulation of crucial enzymes and other proteins regulating cell division and proliferation [4,5]. Even though there have been numerous efforts made to treat cancer diseases and much progress has been made from cancer diagnosis to treatment, some cancer patients do not respond to therapy or experience recurrence after an initial response. Chemotherapy, however, is a fundamental method of treatment but drug resistance to many anticancer agents is one of the biggest challenges in chemotherapy [6]. To overcome drug resistance, high doses of chemotherapeutic agents had to be

administered after drug-induced toxicities [7,8]. Therefore, there is a pressing need to find new anticancer agents with promising activity and high therapeutic index [9].

The coumarin (2*H*-chromen-2-one or 2*H*-1-benzopyran-2-one, 1) nucleus is a bicyclic heterocycle made up of benzene and 2-pyrone rings. Coumarins are prompting a biological investigation to assess their potential therapeutic significance. It belongs to the flavonoid group of plant secondary metabolites and is a diverse class of natural and synthetic compounds with a variety of pharmacological properties, including anti-inflammatory [10], free radical scavenging [11], antinociceptive [12], cardioprotective [13], antithrombotic [14], antiviral [15], antimicrobial [16,17], antituberculosis [18], anti-carcinogenic [19], antidepressant [20], antihyperlipidemic [21] and anticholinesterase [22] activities. Numerous heterocyclic compounds were reported to have coumarin moiety with wide varieties of biological activities. Hymecromone (4-methylumbelliferone, 2) was used, for instance, as a

Abbreviations: SAR, Structure-activity relationship; WHO, World Health DaiOrganization; 5-FU, 5-Fluorouracil; HDAC, Histone deacetylase inhibitors; ER, Estrogen receptor; HSP90, Heat shock protein; POCl₃, Phosphorus oxychloride; DMF, Dimethylformamide; RT, Room temperature; DEAD, Diethyl azodicarboxylate; 7-IP, 7-Isopenthenyloxycoumarin; CS, Collateral sensitivity; MDR, Multidrug resistance; HOBT, Hydroxybenzotriazole; EDCI, [1-Ethyl-3-(3-dimethylaminopropyl) carbodiimide hydrochloride]; DIEA, Diisopropylethylamine; O-THP, O-Tetrahydropyranyl protected hydroxylamine; SAHA, Suberoylanilide hydroxamic acid; EDG, Electron donating group; EWG, Electron withdrawing group; EAC, Ehrlich ascites carcinoma cells; MCT1, Monocarboxylate transporter 1; THF, Tetrahydrofuran; DEC, Diethyl carbonate; PI, Propidium iodide; CHHD, Coumarin-substituted hydrazide-hydrazone derivatives; TEA, Triethyl amine; SRB, Sulforhodamine B; GI, growth inhibition; DCM, Dichloromethane; TBAB, Tetrabutylammonium bromide.

^{*} Corresponding author.

http://pubs.acs.org/journal/acsodf

Review

Systemic Analysis of Glyphosate Impact on Environment and **Human Health**

Reenu Singh, Akanksha Shukla, Gurdeep Kaur, Madhuri Girdhar, Tabarak Malik,* and Anand Mohan*



See https://pubs.acs.org/sharingguidelines for options on how to legitimately share published articles.

Downloaded via 49.43.90.31 on February 4, 2024 at 12:04:49 (UTC).

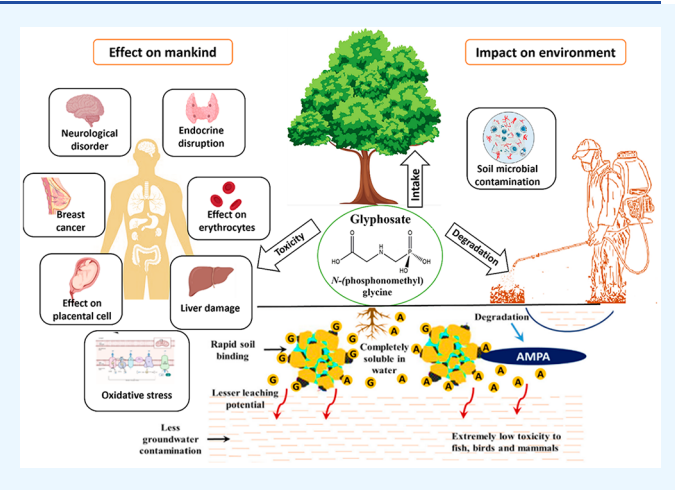
Cite This: https://doi.org/10.1021/acsomega.3c08080



ACCESS |

Metrics & More

ABSTRACT: With a growing global population, agricultural scientists are focusing on crop production management and the creation of new strategies for a higher agricultural output. However, the growth of undesirable plants besides the primary crop poses a significant challenge in agriculture, necessitating the massive application of herbicides to eradicate this problem. Several synthetic herbicides are widely utilized, with glyphosate emerging as a potential molecule for solving this emerging issue; however, it has several environmental and health consequences. Several weed species have evolved resistance to this herbicide, therefore lowering agricultural yield. The persistence of glyphosate residue in the environment, such as in water and soil systems, is due to the misuse of glyphosate in agricultural regions, which causes its percolation into groundwater via the vertical soil profile. As a result, it endangers many nontarget organisms existing in the natural environment, which comprises both soil and water. The



Article Recommendations

current Review aims to provide a systemic analysis of glyphosate, its various effects on the environment, its subsequent impact on human health and animals, which will lead us toward a better understanding of the issues about herbicide usage and aid in managing it wisely, as in the near the future glyphosate market is aiming for a positive forecast until 2035.

1. INTRODUCTION

Over the past decade, the usage of synthetic chemicals in the agricultural sector has proven to have a catastrophic impact on the environment, leading to the accumulation of harmful residues in the biosphere. The imprudent utilization of pesticides in agricultural fields has led to a paradigm shift in the environment. Though the shear exploitation of agrochemicals has led to an enhancement in agricultural produce by effectively managing the pests, rodents, and microbial infections, such haphazard usage of synthetic chemicals and excessive spraying of these chemicals in the fields has adverse impacts not only on the environment but also to human health and other nontargeted organisms. The modern cultivation practices exploit various synthetic chemicals such as herbicides, insecticides, and pesticides to increase agricultural efficiency. The advent of "agricultural evolution" and the use of pesticides and herbicides was mainly started for mankind, but growing human demands and avidity to increase crop yields has gradually led to their overuse. The discovery of N-(phosphonomethyl)glycine was among the dynamic revolutions in agriculture, making it one of the extensively employed herbicides all over the globe. It is typically administered to plants in the form of complicated formulations that promote absorption, with an approximate worldwide demand of half a

million tons per annum.³ This broad-spectrum synthetic organophosphonate herbicide is extensively utilized to destroy undesired plants in agriculture as well as the nonagriculture sector.4

For over a decade, glyphosate has been considered as the most effective farming tool and safest herbicide employed in the agriculture industry. In the beginning, glyphosate was observed to exhibit low toxicity to human beings, as there were barely indications of genotoxicity or carcinogenicity in mammals.⁵ In 1950, Henri Martin of Swiss pharmaceutical company was among the first one to synthesize N-(phosphonomethyl)glycine, and its herbicidal activity on perennial weeds was further tested and confirmed by Monsanto in 1970 and Baird in 1971, respectively.⁷ Due to the competition among other herbicides in the market, glyphosate use in agricultural applications was modest in the

Received: October 15, 2023 Revised: December 15, 2023 Accepted: December 29, 2023

